UNIVERSITAT POLITÈCNICA DE VALÈNCIA

INSTITUTO DE TECNOLOGÍA QUÍMICA

(UPV-CSIC)

Structural, promotion, and metal-support interaction effects in Co/TiO_2 catalysts for Fischer-Tropsch synthesis

DOCTORAL THESIS

Presented by

Francine Bertella

Supervisor:

Prof. Agustín Martínez Feliu

Valencia, July 2018

“Look up at the stars and not down at your feet. Try to make sense of
what you see, and wonder about what makes the universe exist.
Be curious.”

Stephen Hawking

Abstract

The present doctoral thesis focused on the investigation of the structural parameters that can determine the ultimate catalytic properties for Fischer-Tropsch synthesis (FTS) of TiO_2-supported cobalt catalysts. On the one hand, the study of the influence of the titania polymorph (rutile vs. anatase) as support for Ru-promoted Co and Ru nanoparticles (NPs) has allowed to identify some correlations between the TiO_2 crystalline phase, the SMSI (strong metal-support interaction) effect, and the catalytic performance for FTS of the catalysts. On the other hand, by preparing CoRu catalysts supported on TiO_2-anatase with low, medium, and high surface area, further insights into the SMSI effect and its dependence on the textural properties of the TiO_2-anatase support have been gained. Besides, the consequences of increasing the surface area of the support on the activity and selectivity of the catalysts for FTS have been explained based on the established structure-SMSI relationships. Moreover, a detailed study involving the use of *in situ* synchrotron-based spectroscopic characterizations at pressures higher than the ambient pressure usually applied in most previous works, has been carried out aiming at explaining the role of Ru addition and concentration as promoter in Co/TiO_2 catalysts. Finally, reduction-oxidation-reduction (ROR) treatments have been applied on $CoRu/TiO_2$ catalysts to revert the SMSI effect as a feasible strategy to enhance their catalytic activity.

Overall, the results reported in this thesis provide grounds for designing TiO_2-supported Co catalysts with improved activity and selectivity for FTS.

Resumen

La presente tesis doctoral está centrada en la investigación de los parámetros estructurales que determinan las propiedades catalíticas en la síntesis de Fischer-Tropsch (SFT) de catalizadores de cobalto soportados en TiO_2. Por un lado, el estudio de la influencia del polimorfo de óxido de titanio (rutilo vs. anatasa) utilizado como soporte en catalizadores de Co promovidos con Ru ha permitido obtener correlaciones entre la estructura cristalina del soporte, la extensión del efecto SMSI (interacción fuerte metal-soporte) y los resultados catalíticos. Por otro lado, mediante la modificación de las propiedades texturales del soporte TiO_2-anatasa con el objetivo de obtener catalizadores con baja, media y alta área superficial se ha podido avanzar en el conocimiento del efecto SMSI y su correlación con las propiedades texturales del soporte. Además, las consecuencias del aumento en área superficial del soporte en la actividad y selectividad de catalizadores $CoRu/TiO_2$ para la SFT se han podido explicar en base a las relaciones establecidas entre estructura y efecto SMSI. Adicionalmente, el uso de técnicas de luz sincrotrón junto con caracterización espectroscópica *in situ* realizada a presiones superiores a la atmosférica, ha permitido explicar el papel de la adición y concentración de Ru como promotor en catalizadores $CoRu/TiO_2$. Finalmente, se han estudiado tratamientos de reducción-oxidación-reducción (ROR) en catalizadores $CoRu/TiO_2$ con el objetivo de mejorar su actividad catalítica.

Como conclusión general, los conocimientos derivados de los resultados obtenidos en esta tesis doctoral pueden aportar estrategias

adecuadas para el diseño de catalizadores de FT mejorados basados en Co empleando TiO_2 como soporte.

Resum

La present tesi doctoral està centrada en la investigació dels paràmetres estructurals que poden tenir influència en les propietats catalítiques dels catalitzadors que s'han aplicat a la reacció de síntesi de Fischer-Tropsch (SFT). S'ha estudiat la influència del polimorf de titani (rutil o anatasa) utilitzat com a suport de nanopartícules (NPs) de Co i Ru, observant correlacions entre l'estructura cristal·lina del suport, l'efecte SMSI (forta interacció metall-suport) i els resultats catalítics. D'altra banda, es va fer un estudi modificant les propietats texturals de la anatasa amb l'objectiu d'obtenir catalitzadors amb diferent àrea superficial, i s'ha pogut establir un coneixement més profund de l'efecte SMSI i la seua correlació amb les propietats texturals del suport. A més, la influència de l'augment de l'àrea superficial del suport per a la reacció de SFT, en termes d'activitat i selectivitat, han sigut explicats d'acord a les relacions establides entre l'estructura i l'efecte SMSI. Addicionalment, fent ús de tècniques de llum sincrotró juntament amb caracterització in situ realitzada a altes pressions, ha sigut possible explicar el paper de l'addició i concentració de Ru com a promotor en catalitzadors CoRu/TiO_2. Finalment, s'han estudiat els tractaments de reducció-oxidació-reducció (ROR) en catalitzadors CoRu/TiO_2 amb l'objectiu de millorar la seua activitat catalítica.

En resum, els coneixements derivats dels resultats obtinguts en esta tesi doctoral permeten establir estratègies per al disseny de catalitzadors millorats per a la síntesi de FT basats en cobalt utilitzant TiO_2 com a suport.

Acronyms

|FT| – Modulus of Fourier Transform

ASF - Anderson-Schulz-Flory

BE – Binding Energy

BET – Brunauer-Emmett-Teller

BJH - Barrett-Joyner-Halenda

BTL – Biomass-To-Liquids

CN – Coordination Number

CTL – Coal-To-Liquids

CTY – Cobalt Time Yield

DFT – Density Functional Theory

DOR – Degree of Reduction

EDS – Energy Dispersive X-Ray Spectroscopy

EXAFS – Extended X-ray Absorption Fine Structure

fcc – Face Centered Cubic crystal structure

FEFF – Effective curved wave scattering amplitude in the modern EXAFS equation

FESEM – Field Emission Scanning Electron Microscopy

FID – Flame Ionization Detector

FTIR – Fourier Transform Infrared Spectroscopy

FTS – Fischer-Tropsch Synthesis

GC – Gas Chromatograph

GHSV – Gas Hourly Space Velocity

GTL – Gas-To-Liquids

HAADF – High-Angle Annular Dark Field detector

hcp – Hexagonal Close Packed crystal structure

HRTEM – High Resolution Transmission Electron Microscopy
HTFT – High Temperature Fischer-Tropsch
ICP-OES – Inductively Coupled Plasma – Optical Emission Spectroscopy
JCPDS - Joint Committee on Powder Diffraction Standards
LTFT – Low Temperature Fischer-Tropsch
NP – Nanoparticle
PID - Proportional–Integral–Derivative controller
SMSI – Strong Metal-Support Interaction
STEM – Scanning Transmission Electron Microscopy
TCD - Thermal Conductivity Detector
TEM – Transmission Electron Microscopy
TOF – Turnover Frequency
TOS – Time-On-Stream
TPR – Temperature Programmed Reduction
TPV – Total Pore Volume
WGSR – Water-Gas-Shift Reaction
XANES – X-ray Absorption Near Edge Structure
XAS – X-ray Absorption Spectroscopy
XPS – X-ray Photoemission Spectroscopy
XRD – X-ray Diffraction
α' – Auger parameter
ΔE_0 – correction to the energy origin or threshold energy shift
σ^2 – Debye-Waller factor or mean square relative displacement (MSRD)
χ – Structural parameter
Φ – Work function

Acknowledgements

These acknowledgements are written in different languages, otherwise it wouldn’t be fair to everyone. Primeramente, me gustaría agradecer a mi director de tesis, el Prof. Agustín Martínez, por haberme aceptado en su grupo, por sus enseñamientos y paciencia. He aprendido mucho contigo. Agradezco también a la Dra. Patricia Concepción por su interés en mi trabajo, colaboración y por su enorme ayuda.

Tengo que agradecer, y mucho, a Raúl, por su gigantesca paciencia principalmente cuando empecé y no hablaba muy bien el castellano y le pedía que me repitiera una y otra vez cómo funcionaba el reactor, el croma y los análisis. Muchísimas gracias por toda la ayuda (que no ha sido poca). También quiero agradecer a Yannick que, así como Raúl, me ha “salvado la vida” muchas veces en el cubo. Gracias también por recordarme que una cerveza después de un día “pleno” de trabajo en el ITQ viene muy bien.

Gracias a todos que me han ayudado con los turnos en los sincrotrones (Raúl, Mariam, Sara, Dani, Jorge y Chris); vuestra ayuda ha sido esencial para mi trabajo. Mi especial agradecimiento a José Miguel por todos los análisis de infrarrojo. Soy consciente de la dificultad adicional que presentaban los materiales que he estudiado, así que tengo que agradecerte mucho por toda tu dedicación, especialmente en los análisis a presión. A mis compañeros en el ITQ, Natalia, Ledys, Cristina, Ximo, Nuria y Sara, muchas gracias por todas las conversaciones y risas, espero poder volver a veros a todos muy pronto. En general, quiero agradecer a todas las personas, desde técnicos a personal de administración que han contribuido de alguna u otra manera al desarrollo de esa tesis doctoral.

Agora em português, o meu maior agradecimento é para ti Chris, muito obrigada por toda a ajuda, e não somente na parte científica, mas também por estar sempre disposto a me ajudar, teu esforço e dedicação sempre foram um exemplo a ser seguido. Ter você sempre por perto, sendo meu porto seguro, foi essencial.

Meus sinceros agradecimentos a Profa. Sibele Pergher, por sempre acreditar em mim, sem você eu não teria chegado até aqui e por isso, sou eternamente grata.

Agradeço de coração a minha família, meus pais e minha irmã, por nunca medirem esforços e por todo amor e incentivo ao longo desses anos. O apoio de vocês foi fundamental. Um especial agradecimento as minhas amigas, Suelen e Cleisi, que mesmo com um oceano de distância, sempre me incentivaram e estiveram presentes.

A todos os brasileiros que passaram pelo ITQ, meu muito obrigada. A companhia de vocês me fez sentir “em casa” mesmo estando em outro país.

Back to English, I would like to express my gratitude to Dr. Giovanni Agostini for the collaboration with the EXAFS data. Last but not least I would like to thank my “international friends” Andrew, Ledys, Jan and Natalia, for the great moments that we have experienced in Valencia, your friendship is really important to me and has certainly contributed to make my stay here much easier.

CAPES (Program Science without Borders) is acknowledged for the doctoral scholarship.

Table of contents

Abstract .... **i**

Resumen .... **ii**

Resum .... **iv**

Acronyms .... **v**

Acknowledgements .... **vii**

Chapter 1. Introduction 1

1.1. Setting the scene 2

1.2. Brief historical background and current prospects 5

1.3. Fischer-Tropsch synthesis 7

1.4. Catalysts for Fischer-Tropsch synthesis 8

1.4.1. Co-based catalysts 9

1.4.1.1. Activity of Co-based catalysts 12

1.4.1.2. Selectivity in Co-based catalysts 14

1.4.1.3. Titania-supported Co FTS catalysts 17

1.5. References 25

Chapter 2. Objectives 29

Chapter 3. TiO_2 polymorph dependent SMSI effect in Co-Ru/TiO_2 catalysts and its relevance to Fischer-Tropsch synthesis 33

3.1. Introduction 35

3.2. Experimental 37

3.2.1. Materials 37

3.2.2. Synthesis of pure anatase and rutile TiO_2 phases 37

3.2.3. Synthesis of Co-Ru/TiO_2 catalysts 38

3.2.4. Characterization techniques 39

3.2.5. Fischer–Tropsch synthesis experiments 42

3.3. Results and discussion 43

3.3.1. Characterization of the TiO_2 supports 43

3.3.2. Characterization of the Co-Ru/TiO_2 catalysts 46

3.3.2.1. Structural and textural properties 46

3.3.2.2. Reducibility and particle size of cobalt 49

3.3.2.3. Surface properties of cobalt 54

3.3.3. Fischer-Tropsch synthesis on Co-Ru/TiO_2 catalysts 57

3.3.3.1. FTS activity 57

3.3.3.2. In situ IR-CO under syngas reaction conditions 61

3.3.3.3. Product distribution 63

3.4. Conclusions 65

3.5. References 68

3.6. Supporting Information 72

3.6.1. Raman spectroscopy of calcined Co-Ru/TiO_2 catalysts 72

3.6.1.1. Experimental 72

3.6.1.2. Discussion of Raman results 72

3.6.2. Crystalline phases in the H_2-reduced catalysts 74

3.6.2.1. Experimental 74

3.6.2.2. XRD patterns of as-reduced catalysts 74

3.6.3. TiO_2 phases in spent catalysts 76

Chapter 4. The impact of support surface area on the SMSI decoration effect and catalytic performance for Fischer-Tropsch synthesis of Co-Ru/TiO_2-anatase catalysts 77

4.1. Introduction 79

4.2. Experimental 81

4.2.1. Synthesis of TiO_2-anatase supports 81

4.2.2. Synthesis of Co-Ru/TiO_2 catalysts 82

4.2.3. Characterization techniques 83

4.2.4. Fischer–Tropsch synthesis experiments 86

4.3. Results and discussion 87

4.3.1. Characterization of TiO_2-anatase supports 87

4.3.2. Characterization of the Co-Ru/TiO_2 catalysts 91

4.3.3. Fischer-Tropsch synthesis on Co-Ru/TiO_2 catalysts 102

4.4. Conclusions 109

4.5. References 112

4.6. Supporting Information 114

4.6.1. Crystalline Co phases in the H_2-reduced catalysts studied by in situ H_2-XRD 114

4.6.1.1. Experimental 114

4.6.1.2. XRD patterns of as-reduced catalysts 114

Chapter 5. Influence of Ru promotion on Co/TiO_2 catalysts for Fischer-Tropsch synthesis 117

5.1. Introduction 119

5.2. Experimental 123

5.2.1. Synthesis of anatase support 123

5.2.2. Synthesis of CoRu/TiO_2 catalysts 123

5.2.3. Characterization techniques 124

5.2.4. Fischer-Tropsch synthesis experiments 130

5.3. Results and discussion 131

5.3.1. Characterization of the TiO_2-anatase support 131

5.3.2. Characterization of CoRu/TiO_2 catalysts 133

5.3.3. In situ characterization of as-reduced CoRu/Ti catalysts by XAS 142

5.3.4. Catalytic behavior of Co/TiO$_2$ and CoRu/TiO$_2$ catalysts in Fischer-Tropsch synthesis 148

5.3.5. In situ XAS characterization of CoRu/Ti catalysts during FTS at atmospheric pressure 157

5.3.6. In situ CO-FTIR characterization of Co/Ti and CoRu/Ti catalysts during FTS at atmospheric pressure 159

5.3.7. In situ CO-FTIR characterization of Co/Ti and CoRu/Ti catalysts during FTS at high pressure 166

5.3.8. In situ XPS characterization of Co/Ti and CoRu/Ti catalysts during FTS at high pressure 169

5.4. Conclusion 179

5.5. References 182

5.6. Supporting Information 186

Chapter 6. Improving the catalytic activity of CoRu/TiO$_2$ catalysts for Fischer-Tropsch synthesis by reduction-oxidation-reduction (ROR) treatments 187

6.1. Introduction 189

6.2. Experimental 192

6.2.1. Synthesis of TiO$_2$-anatase support 192

6.2.2. Synthesis of CoRu/TiO$_2$ catalysts 193

6.2.3. Reduction, oxidation, re-reduction (ROR) treatments 193

6.2.4. Characterization techniques 194

6.2.5. Fischer-Tropsch synthesis experiments 199

6.3. Results and discussion 200

6.3.1. Characterization of TiO$_2$-support 200

6.3.2. Characterization of Co/Ti-C catalyst 202

6.3.3. Reduction, oxidation and re-reduction (ROR) treatments 206

6.3.4. In situ characterization of Co/Ti catalysts submitted to ROR treatments by XAS under operational conditions 211

6.3.5. CO-FTIR characterization of Co/Ti catalysts submitted to ROR treatments 218

6.3.6. Characterization by AP-XPS of Co/Ti catalysts submitted to ROR treatments 221

6.3.7. Catalytic behavior of Co/Ti catalysts submitted to ROR treatments in Fischer-Tropsch synthesis 225

6.4. Conclusion 230

6.5. References 231

Chapter 7. General conclusions 235

CHAPTER 1

INTRODUCTION

1.1. Setting the scene

Achieving an alternative and clean source of energy supply has been one of the biggest challenges of humanity. Among all energy sources, crude oil remains as the most used resource for both liquid fuels and raw materials, accounting to approx. 34 % of the world energy consumption (Figure 1.1) [1].

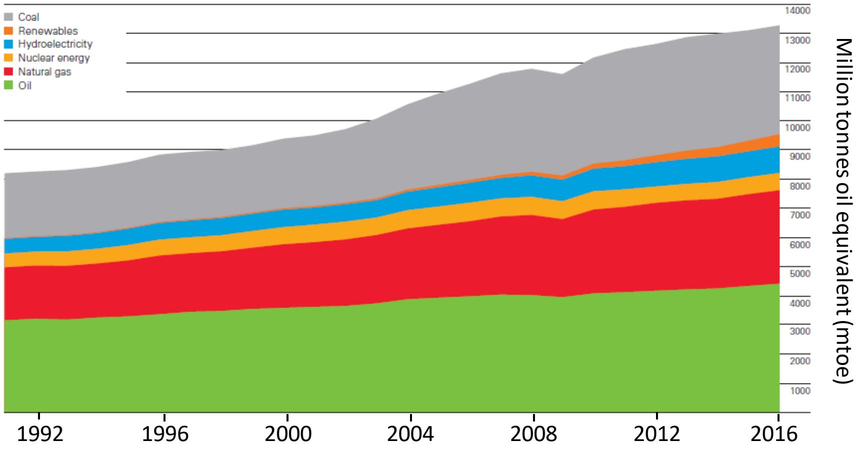

Figure 1.1. World primary energy consumption in million tonnes oil equivalent from 1991 to 2016. Adapted from ref. [1].

The global oil consumption growth averaged 1.6 million barrels per day in 2016, which is above the 10-year average of 1 million barrels per day. Considering the same consumption of 2016, current perspectives predict that global oil reserves would last for 50.6 years [1]. Among all services dependent of oil, the transportation section is highly dominated by oil-derived fuels. Figure 1.2a depicts the trends in oil demand according to new polices scenario, which incorporates existing energy policies as well as an assessment of the results likely to stem from the implementation of announced policy intentions, while Figure 1.2b shows a sustainable scenario, which outlines an integrated approach to achieving internationally agreed objectives on climate change, air quality and universal access to modern energy [2].

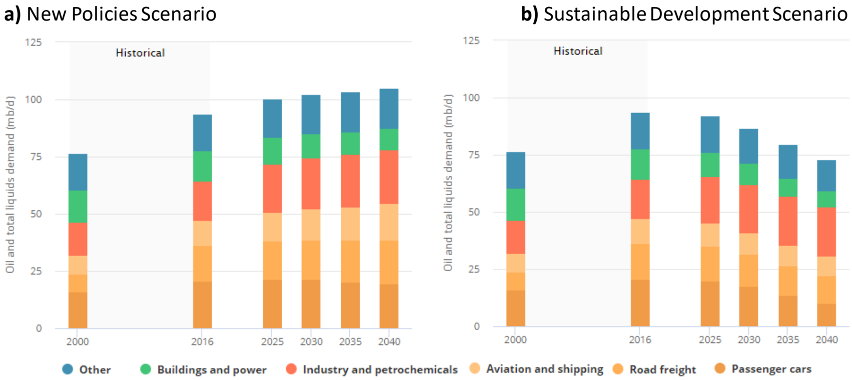

Figure 1.2. Oil demand growth to 2040 according to new policies scenario (a) and sustainable development scenario (b). Adapted from ref. [2].

A closer look to the oil demand growth trends, considering the new policies scenario, reveals that petrochemicals, aviation and shipping, and road freight account for the bulk of the growth in oil demand, offsetting declines in other sectors. However, in the sustainable development scenario, the majority of the decline in oil demand comes from transport, which is the largest oil consumer today [2].

These trends underline the major importance of seeking alternative renewable feedstocks to produce transportation fuels in order to attain a more sustainable scenario, especially due to the environmental problems related to the use of oil-derived transportation fuels, such as the release of greenhouse gas emissions (mainly CO_2). Moreover, the combustion of fossil fuels results in the emission of environmentally harmful compounds, such as SO_2 and NO_x. These issues have been encouraging governments to invest in renewable energies (solar, hydroelectric, wind) in order to develop a more independent, sustainable and environmentally friendly energy system.

Therefore, biofuels produced from renewable resources could help to minimize the fossil fuel burning and, consequently, CO_2 emissions. First-generation biofuels (i.e. biodiesel and bioethanol) are obtained from feedstocks that are also food resources, which can present several drawbacks, such as competition with food crops, impact on biodiversity and land use [3].

In this context, there are great expectations regarding the second-generation biofuels. They are produced from lignocellulosic feedstocks, which are cheap and abundant non-food materials available from plants. Examples of 2nd generation biofuels are cellulosic ethanol and Fischer–Tropsch fuels. By this way, biomass is expected to play a prominent role in the future of the energy system.

The Fischer-Tropsch synthesis is an important part of XTL technologies, where “X” refers to the employed feedstock: natural gas (GTL, gas-to-liquids), coal (CTL, coal-to-liquids) or biomass (BTL, biomass-to-liquids). Independently from the carbon source, the XTL technology typically comprises three main steps: (i) syngas production, (ii) Fischer-Tropsch synthesis, and (iii) product separation and upgrading (i.e. diesel, gasoline, jet fuel, oxygenates, among others) [4, 5]. The abundant reserves of natural gas, incremented in the last years by the discovery and exploitation of large stranded gas fields, can be a driving force to the further implementation of GTL processes, and in consequence, to improvements in the Fischer-Tropsch synthesis technology.

1.2. Brief historical background and current prospects

The Fischer-Tropsch synthesis is an industrial process used to convert synthesis gas (or syngas, a mixture of CO and H_2) into higher hydrocarbons for use as fuels and chemicals. Sabatier and Senderens were the pioneers (in 1902) to produce hydrocarbons (mostly methane) from syngas, using metallic catalysts based on Co and Ni at atmospheric pressure [6]. Then, in 1913, a patent from BASF reported the conversion of syngas into hydrocarbons at higher temperatures and pressures [7]. Continuing the effort to produce hydrocarbons, in the 1920's, the German researchers Hans Fischer and Franz Tropsch succeeded to convert syngas into higher hydrocarbons that could be used as fuels, using catalysts based on Fe and Co [8]. Further research in Germany led in 1936 to the first commercial plant of Fischer-Tropsch synthesis (FTS) and within a short period of time, nine FTS plants were built in Germany [9]. Later, with the end of the World War II, several plants had to shut down due to the uncompetitive prices of the produced fuels compared with those obtained from crude oil. However, the FTS technology became known all over the world and was extensively investigated by other countries. In the 1950s, small plants were built and operated in the USA [4].

Based on substantial coal reserves, large scale HTFT (high temperature Fischer-Tropsch) and LTFT (low temperature Fischer-Tropsch) coal-based FTS plants were developed by Sasol in South Africa between the years 1950-1980s. These plants ultimately helped the Apartheid regime to reduce oil dependencies during the embargos in the late 1980s [10].

In the subsequent years, several other companies have invested in FTS technology, as shown in Table 1.1.

Table 1.1. Some current commercial FTS plants. Adapted from ref. [4].

Company	Location	Start-up date	Capacity [a]
Shell	Bintulu, Malaysia	1992	14500
Sasol	Sasolburg, South Africa	1993	5000
PetroSA	Mosselbay, South Africa	1993	22000
Sasol-QP (Oryx)	Ras Laffan, Qatar	2007	34000
Shell (Pearl)	Ras Laffan, Qatar	2011	140000
Chevron-Sasol	Escravos, Nigeria	2013	34000

[a] Approximate plant capacity (barrels per day)

The interest in the Fischer-Tropsch synthesis has been highly dependent on the crude oil price. However, this catalytic process has experienced a renaissance in the last few decades not only due to the rise in crude oil prices, but also to legislative concerns about fuel quality. In this respect, the diesel obtained via FTS is practically free from nitrogen, sulphur and aromatics contaminants, in addition to its high cetane number (normally more than 70), leading to reduced harmful emissions in comparison with a conventional oil-derived diesel fuel (cetane number usually lower than 50) [11-13].

Moreover, the increasing interest in the Fischer-Tropsch synthesis has been reflected in the number of publications over the years (Figure 1.3). The data was collected from two search engines: Web of Science (a) and Scopus (b) using “Fischer-Tropsch” as keyword.

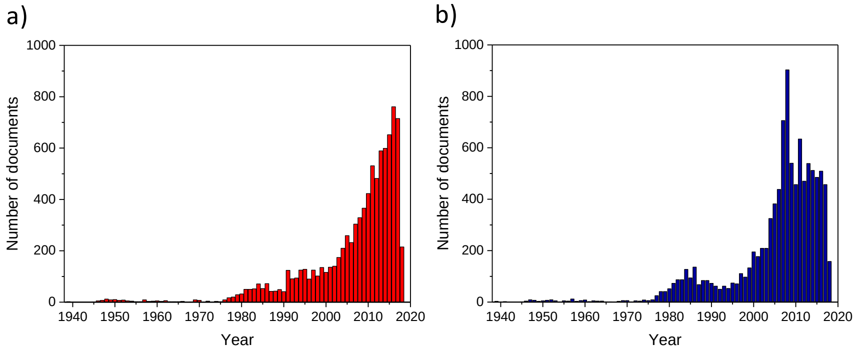

Figure 1.3. Number of documents related to Fischer-Tropsch over the years searched on Web of Science (a) and Scopus (b).

It is thus clear that the Fischer-Tropsch synthesis, which is at the core of XTL processes, is gaining more and more interest at both industrial (Table 1.1) and academic (Figure 1.3) levels, especially in the last 20 years.

1.3. Fischer-Tropsch synthesis

The FTS reaction is a surface catalyzed polymerization reaction comprising the steps of CO and H_2 adsorption and dissociation on the active sites, chain initiation, chain growth and termination with final product desorption [14, 15]. The reaction products are mainly n-paraffins and α-olefins (equations 1.1 and 1.2, respectively) and, in a much lesser amount, oxygenates such as alcohols (equation 1.3).

$$(2n+1)H_2 + nCO \rightarrow C_nH_{2n+2} + nH_2O \qquad \text{(Eq.1.1)}$$

$$2nH_2 + nCO \rightarrow C_nH_{2n} + nH_2O \qquad \text{(Eq.1.2)}$$

$$2nH_2 + nCO \rightarrow C_nH_{2n+1} + (n-1)H_2O \qquad \text{(Eq.1.3)}$$

Other side reactions, considered as undesired, can take place during FTS, such as the water-gas-shift reaction (WGSR) and the

Boudouard or CO disproportionation reaction, as shown in equations 1.4 and 1.5, respectively. The later reaction produces carbon that gradually deposits on the catalyst promoting its deactivation. The extent of these side reactions depends on both the type of catalyst and reaction conditions.

$$CO + H_2O \rightarrow CO_2 + H_2 \qquad \text{(Eq.1.4)}$$

$$2CO \rightarrow C + CO_2 \qquad \text{(Eq.1.5)}$$

In spite that more than 90 years passed since the researchers Fischer and Tropsch made their discovery, the fundaments behind the FTS chemistry are not yet fully understood and are still controversial subjects of debate in the literature [14, 16-18].

1.4. Catalysts for Fischer-Tropsch synthesis

Several transition metals from group VIII can catalyze the hydrogenation of CO to hydrocarbons. Among them, only Ni, Co, Fe and Ru have sufficient FTS activity for commercial utilization [19]. Ruthenium is the most active metal; however, its high cost and low availability makes it unsuitable for commercial application. On the other hand, the high hydrogenation activity of nickel promotes the excessive formation of methane, besides the fact that volatile nickel carbonyls can be formed depending on reaction conditions with the consequent loss of catalyst from the reactor [20]. As a result, only cobalt and iron are used in the formulation of commercial FTS catalysts.

The choice of active metal influences deeply the product selectivity and the catalyst cost. Iron catalysts are cheaper than those based on cobalt but usually produce more olefins and oxygenates as well as more CO_2 due to their higher activity for the WGSR [4, 19, 21]. On the other hand, cobalt catalysts are more active and selective towards long chain hydrocarbons than iron catalysts which, besides their low WGS activity, make them the preferred option for producing high-quality diesel fuel [4, 19, 22].

1.4.1. Co-based catalysts

The typical composition of a commercial Co-based FTS catalyst is presented in Figure 1.4 [4, 23].

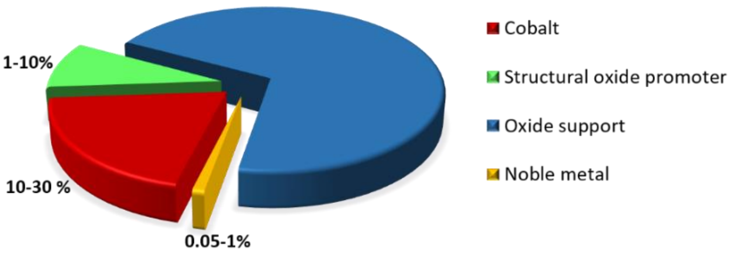

Figure 1.4. Typical formulation of Co-based catalysts for commercial FTS.

The active phase of Co catalysts for CO hydrogenation is metallic cobalt. However, due to its high cost, it needs to be well dispersed on a support in order to increase the amount of exposed cobalt metal sites. A great effort has been made to prepare catalysts with adequate Co dispersion, in which the chemical nature of the support plays a major role. For industrial purposes, oxide supports with high surface area are preferred, such as SiO_2, Al_2O_3 and TiO_2 [20, 23]. Apart from dispersing the Co nanoparticles (NPs), the support also provides mechanical strength and thermal stability to the catalyst.

Besides the main active Co phase and the support, different metal oxides are typically included in the catalyst formulation as promoters in order to improve the activity and hydrocarbon selectivity. The most used oxide promoters reported in literature are ZrO_2, La_2O_3, CeO_2 and MnO [23-26]. Among other attributes, the use of these oxide promoters can increase the dispersion and reducibility of cobalt and enhance the mechanical and attrition resistance of the catalyst [19, 24].

Small cobalt particles supported on traditional porous oxide supports are rather difficult to reduce due to strong interactions with the carrier that may lead to the formation of mixed compounds such as cobalt silicates or cobalt aluminates. These mixed species are barely reducible and should be avoided since they result in inactive sites for FT synthesis and, hence, in a less efficient use of cobalt [23].

In this respect, small amounts of noble metals (mainly Ru, Re, and Pt) can be added to the catalyst in order to decrease the reduction temperature of cobalt, preventing or minimizing the formation of mixed compounds with the support. The improvement in cobalt reduction is attributed to faster hydrogen activation in the presence of noble metals and subsequent spillover of hydrogen to cobalt oxides promoting their reduction [27]. In addition to improving cobalt reduction [28, 29], the incorporation of noble metals in the catalyst composition can increase the cobalt dispersion [30, 31], inhibit catalyst deactivation, and form bimetallic particles by alloying with cobalt that may enhance its intrinsic reactivity through synergic effects [32]. In most cases, the use of small amounts of noble metals results in a higher concentration of accessible Co^0 sites leading to significant improvements in catalytic activity [27, 28].

The hydrocarbon selectivity can also be modified upon promotion with noble metals [33].

The chemical identity and textural characteristics of the support also play a crucial role in determining the final catalytic performance of the cobalt catalyst. In this sense, by controlling the porous structure and morphology of the support, the size (dispersion) of the supported Co nanoparticles can be adjusted. In the literature, it has been reported that the mesoporosity of meso-macroporous silica supports deeply influences the size, reducibility and dispersion of the supported Co NPs [34]. These authors showed, by tuning the size of mesopores, a superior catalytic activity for an optimum size of mesopores of 8.5 nm. Besides, the hydrocarbon product distribution is highly dependent on the mesopore diameter, which influences both the size of Co crystallites and the H_2/CO ratio inside the pores (due to diffusional restrictions of CO inside small pores) [34]. Besides pore diameter, the pore length in mesoporous SBA-15 silicas also affects the dispersion of Co NPs [35]. It was shown that the use of SBA-15 with short pores leads to higher Co metal dispersions with respect to conventional SBA-15 morphology with long and highly curved pores [35].

The importance of controlling the textural properties and morphology of the support in order to improve Co dispersion has also been highlighted for Al_2O_3-supported Co catalysts [36-38]. Borg and co-workers reported that increasing the pore diameter of ɣ- Al_2O_3 support leads to larger Co metal crystallites [36]. Such positive correlation between support pore diameter and Co particle size generally applies for supports with conventional morphologies (3D, intra-particle pores). However, by comparing Ru-promoted Co catalysts supported on conventional ɣ- Al_2O_3 materials spanning a wide range of pore sizes and surface areas and on a nanofibrous ɣ-Al_2O_3 (1D morphology, extra-particle porosity), it was demonstrated that the final cobalt dispersion is mainly dictated by the specific surface area of the support rather than by its pore size [37]. Recently, Liu and co-workers reported for nanofibrous ɣ-Al_2O_3 supports that the aspect ratio of the nanofibers (i.e. the length/diameter ratio) also influences the size of the supported Co_3O_4 crystallites in the calcined catalysts. Interestingly, their results showed that the support with larger aspect ratio inhibited migration and coalescence of cobalt nanoparticles resulting in a significant improvement in the stability of the catalyst during FTS [38].

Besides from the morphology, the crystalline phase of the support can also influence the final properties of the catalyst. For instance, Borg and co-workers reported a higher selectivity to C_{5+} hydrocarbons for similarly sized cobalt NPs supported on α-Al_2O_3 with respect to those supported on ɣ-Al_2O_3 [39]. In the same line, Rane and co-workers showed a higher C_{5+} selectivity for Co supported on α-Al_2O_3 with respect to ɣ-Al_2O_3 and δ-Al_2O_3 supports [40].

According to the previous studies, one may anticipate that the final FTS performance of TiO_2-supported Co catalysts will also be influenced by parameters like the TiO_2 crystalline phase, morphology, and porosity as well as by the strong metal-support interaction (SMSI) effect. The study of these aspects constitutes the basis of the present thesis.

1.4.1.1. Activity of Co-based catalysts

The activity of Co-based catalysts can be influenced by several parameters, such as metal loading, size of the supported cobalt particles (i.e. dispersion), and degree of cobalt reduction (DOR). These parameters can be tuned in different extents by controlling the texture, morphology, and chemical identity of the support, and by the addition of metal and/or metal oxide promoters [23, 28, 41].

Since the active phase of Co-based catalysts for FTS is metallic cobalt, it seems logical that maximizing the dispersion of Co^0 NPs sites (i.e. decreasing its crystallite size) would lead, at constant metal loading, to catalysts exhibiting the maximum activity. This, however, implies that all exposed Co^0 sites display the same intrinsic activity (TOF) irrespective of the Co^0 particle size. In this respect, Iglesia and co-workers [42, 43] observed a constant TOF for Co catalysts supported on SiO_2, Al_2O_3, and TiO_2 materials at industrially relevant FTS conditions. However, the catalysts prepared in that study exhibited moderate Co dispersions below ca. 10%, corresponding to Co^0 particle sizes above ca. 10 nm. Therefore, the question remained as to whether the same trend would apply to more dispersed catalysts, that is, with Co^0 particle sizes below 10 nm.

This question has been addressed more recently by preparing model Co catalysts with controlled Co particle size in the range of interest (< 10 nm) supported on carbon nanofibers (CNF) [44] and on surface-modified silica-type materials (i.e. ITQ-2 zeolite) [45]. Both studies demonstrated a drastic reduction in TOF for Co particles sizing below a critical size of 6-8 nm, as depicted in Figure 1.5a and 1.5b for Co/CNF and Co/ITQ-2 catalysts, respectively. In addition, both groups presented evidences that surface reconstruction of cobalt nanoparticles occur in the presence of syngas under conventional FTS conditions, especially for the smaller nanoparticles. Moreover, the above studies also indicated a gradual increase in C_{5+} selectivity with increasing Co^0 particle size, even for sizes beyond the critical value of 6-8 nm [44, 45]. The reasons for this are not completely understood, although it has been suggested that chain growth (leading to longer hydrocarbon chains) is favored on the large Co ensembles that are more abundant in the terraces of larger Co^0 nanoparticles [46]. Thus, the analysis of the literature suggests that a precise control of the cobalt nanoparticle size is essential to design supported Co FTS catalysts with improved activity and selectivity.

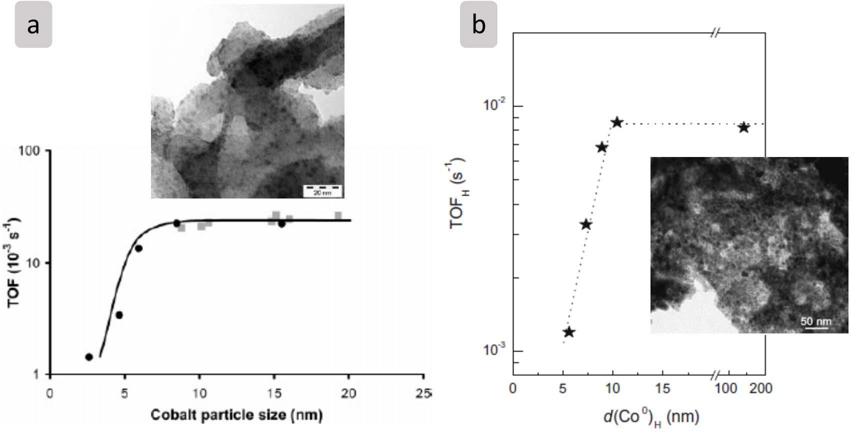

Figure 1.5. Dependence of the intrinsic activity (TOF) of cobalt with Co particle size for model catalysts supported on carbon nanofibers (a) and on all-silica ITQ-2 zeolite (b). Adapted from ref. [44, 45].

1.4.1.2. Selectivity in Co-based catalysts

The Fischer-Tropsch synthesis is driven by a polymerization mechanism, in which the products generally follow a statistical hydrocarbon distribution known as the Anderson-Schulz-Flory (ASF) distribution [14, 47] (Figure 1.6). According to this model, the FTS selectivity can be represented by a single parameter, the chain growth probability (α), which depends on the rates of chain growth (r_p) and chain termination (r_t) as expressed in equation 1.6.

$$\alpha = {}^{r_p}/_{r_p + r_t} \qquad \text{(Eq.1.6)}$$

In this ideal model, the chain growth probability is assumed to be independent of the hydrocarbon chain length, resulting in a product distribution that can be obtained as described in equation 1.7, where Wn is the weight fraction of products with n number of carbons.

$$^{W_n}/_{n} = \alpha^{n-1} \cdot (1-\alpha)^2 \qquad \text{(Eq.1.7)}$$

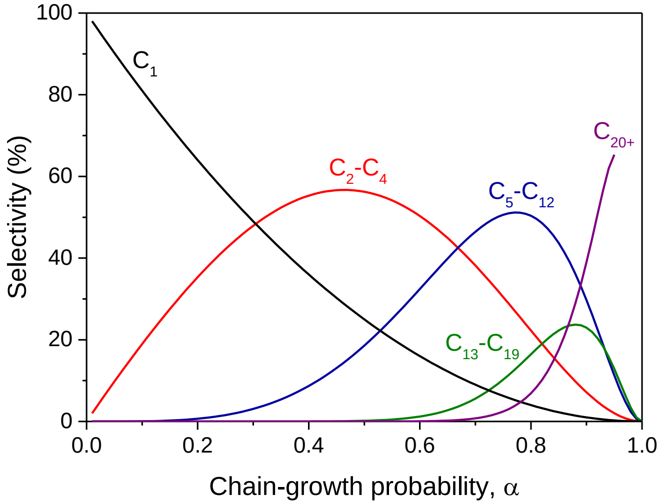

Figure 1.6. Anderson-Schulz-Flory distribution for products obtained by the Fischer-Tropsch synthesis.

As observed in Figure 1.6, the polymerization-type kinetics of the FTS reaction yields hydrocarbons spanning a wide range of carbon atoms from methane (C_1) to waxes (C_{20+}). After separation, the wax fraction is upgraded, typically via hydrocracking, to produce the target liquid FTS fuels, particularly diesel [4, 12].

Experimentally, however, the hydrocarbon distribution obtained under industrially relevant FTS conditions typically shows some deviations from the ideal ASF distribution. For instance, an increase in the α value is commonly observed above a certain carbon number (generally above C_{10}) resulting in a selectivity to C_{5+} hydrocarbons higher than that predicted by the ASF model. This effect has been explained by Iglesia and co-workers [42, 43] according to their α-olefin re-adsorption model, by which highly reactive primary α-olefin products re-adsorb on Co sites during their diffusion through the catalyst pores (filled with liquid hydrocarbons under realistic FTS conditions) and participate in chain growth events increasing the average chain length of the formed hydrocarbons. These authors demonstrated that the hydrocarbon selectivity is largely determined by diffusional restrictions of reactants and/or products within the catalyst pellets, and proposed a structural parameter (χ) that correlates the selectivity to C_{5+} with mass transfer limitations (Figure 1.7). This parameter, defined according to equation 1.8, depends on the average radius of catalyst pellets (R_0), the density of Co^0 sites per unit area (θ_{Co}), the void fraction (ε), and the average pore radius (r_p) of the metal oxide support. Therefore, higher χ values imply more severe mass transport limitations.

$$\chi = \frac{{R_0}^2 \cdot \varepsilon \cdot \theta_{Co}}{r_p} \qquad \text{(Eq.1.8)}$$

As observed in Figure 1.7, the C_{5+} selectivity initially increases with increasing χ, reaches a maximum at a χ value of approx. $200 \cdot 10^{-16}$ m, and then decreases at higher χ values. According to Iglesia and co-workers, the initial increase in C_{5+} selectivity with χ is related to an enhanced re-adsorption of α-olefins, as discussed before, while the decline in selectivity in the higher range of χ (i.e. high diffusion severity) is attributed to an impeded diffusion of CO in the catalyst pores that increased the true H_2/CO ratio around the Co particles promoting the formation of lighter hydrocarbons.

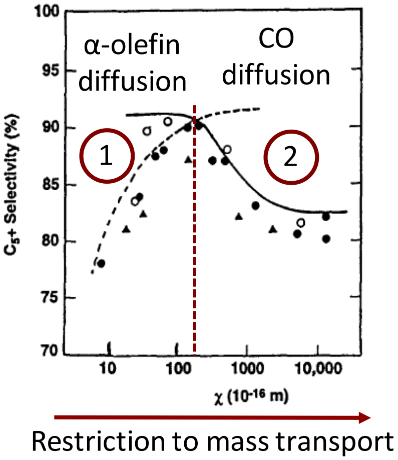

Figure 1.7. Change in selectivity to C_{5+} hydrocarbons as a function of the structural parameter χ. Adapted from ref. [43].

Therefore, given the strong dependence of the hydrocarbon selectivity on mass transport limitations (χ), the textural properties of the support (e.g. surface area and pore diameter) will be key parameters to designing Co FTS catalysts with enhanced selectivity to the target C_{5+} hydrocarbon fraction.

1.4.1.3. Titania-supported Co FTS catalysts

Titania stands, besides SiO_2 and Al_2O_3, among the most employed supports for preparing Co-based FTS catalysts. Apart from its low cost and high thermal stability, TiO_2-supported Co catalysts were reported to exhibit high activity and selectivity to the desired liquid hydrocarbon fraction (C_{5+}) [4, 48]. In spite of this, the amount of studies using TiO_2 as support is considerably low with respect to those using SiO_2 or Al_2O_3. One possible cause for this is the low specific surface area (for instance, ca. 50 m^2/g for the widely employed commercial P25 TiO_2 from Evonik Degussa) and pore volume of TiO_2 materials, which limits the maximum amount of cobalt that can be incorporated in these supports with appropriate dispersion.

The interaction strength between cobalt NPs and titania, alumina and silica supports increases in the following order: $Co/SiO_2<Co/TiO_2<Co/Al_2O_3$ [28]; therefore, the use of titania as carrier can afford a good compromise between cobalt dispersion and reducibility. Nonetheless, the addition of small amounts of noble metal to Co/TiO_2 catalysts is frequently accomplished in order to ensure good dispersion and high reducibility of the supported Co phases.

Iglesia and co-workers [32] have demonstrated a higher TOF (2-4 times) and higher C_{5+} selectivity for Ru-promoted Co/TiO_2 catalysts in comparison to the unpromoted counterpart. They attributed the increase in activity to a synergy between Co and Ru atoms in bimetallic Co-Ru particles, in which Ru assist in removing C and O species from the catalyst surface that could promote catalyst deactivation during the initial stages of the FTS reaction.

Storsæter and co-workers [49], on the other hand, reported an increase in activity and selectivity to C_{5+} for Re-promoted Co/TiO_2 catalysts that was mainly attributed to the increase in the degree of cobalt reduction due to the presence of Re without significantly changing the metal dispersion.

The effect of promotion of Co/TiO_2 catalysts with different noble metals (Ag, Ru, Pt and Re) has been studied by Eschemann and co-workers [50]. In that work, catalysts promoted with Ru and Ag exhibited higher TOFs than those promoted with the other noble metals. The higher intrinsic activity for the Ag-promoted catalyst was attributed to the presence of some *hcp* Co^0 phases, which were previously reported to show higher reactivity than *fcc* Co^0 [51]. On the other hand, the superior activity of Ru-promoted Co/TiO_2 catalyst was assigned to an accelerated water formation (and removal) and/or to hydrogen-assisted CO dissociation due to the higher hydrogenation activity of metallic Ru atoms.

The concentration of noble metal promoters in supported Co catalysts has a large impact on the final catalytic performance, although contradictory results have been reported in different studies when varying the amount of added noble metal. For instance, some authors reported slight improvements in CO conversion when increasing the Ru loading from 0.17 to 1.64 wt% (corresponding to Ru/Co atomic ratios from 0.0049 to 0.0478) in $RuCo/SiO_2$ catalysts (20 wt% Co) [29]. Others, however, observed that the CO conversion passes through a maximum, decreasing at Ru concentrations above 1.0 wt% in Al_2O_3-supported Co catalysts containing 20 wt% Co (Ru/Co= 0.0291) [52], and above 0.05 wt% Ru for catalysts loaded with 5 wt% Co (Ru/Co= 0.0058) [53]. In the case of TiO_2-based materials, where low amounts of noble metal promoter ($\leq$ 0.5 wt%) have been used [28, 50], no studies addressing the influence of the concentration of noble metal promoters have been so far reported to the best of our knowledge.

Additionally, TiO_2 can crystallize mainly in three different polymorphs, namely anatase, rutile, and brookite (Figure 1.8). However, a great deal of the studies in literature using Co supported on TiO_2 employed the commercial P25 TiO_2 material [28, 54, 55] that consists in a mixture of anatase (70-80 %) and rutile (30-20 %) crystalline phases [56].

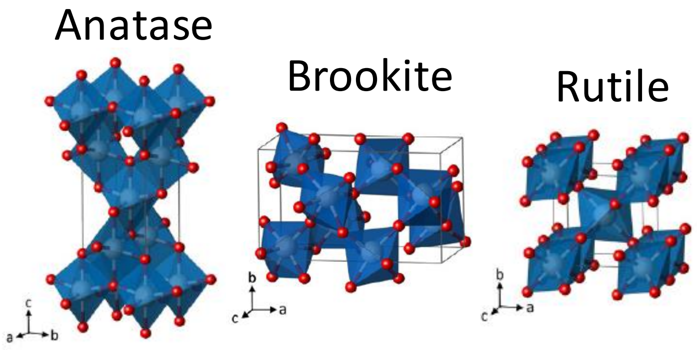

Figure 1.8. Anatase, brookite and rutile TiO_2 crystalline phases. Adapted from ref. [57].

Furthermore, a particular characteristic of the Co-titania system is the possible occurrence of the well-known SMSI (strong metal-support interaction) effect. This term was used first by Tauster and co-workers [58] to characterize the suppression of H_2 and CO chemisorption capacity of metals supported on TiO_2 when submitted to high temperate treatments under reducing environments.

The SMSI effect has been shown to occur for metals from group VIII supported on reducible oxides such as TiO_2, CeO_2, and Nb_2O_5 among others [59]. During reduction at high temperatures (usually above 300 °C), the support (titania in this case) is partially reduced to form mobile TiO_x species (with $x<2$) that migrate and partially cover the surface of the supported metal nanoparticles (decoration effect), inhibiting their capacity to chemisorb CO and H_2 [60]. A schematic representation of the decoration effect is shown in Figure 1.9.

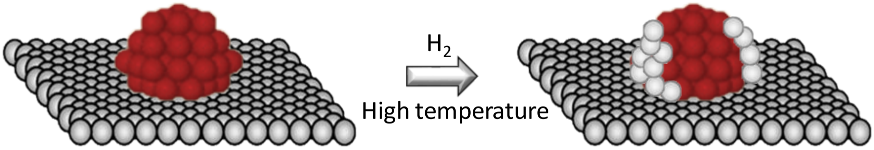

Figure 1.9. Schematic representation of the decoration effect experienced by a group VIII metal supported on a reducible oxide (e.g. Co/TiO_2 system).

Two mechanisms have been proposed to explain the suppression of H_2 and CO chemisorption capacity experienced by the metal under the SMSI state: (i) decoration of the supported metal NPs by partially reduced TiO_x moieties (geometric effect), and (ii) change in the electronic structure of the metal due to charge transfer from the support to the supported NPs (electronic effect) [61, 62].

A sufficiently high temperature and a source of H_2 are prerequisites for the decoration effect to occur. To start the migration, Ti^{3+}/lattice oxide vacancies must be created to generate the partially reduced TiO_x species [59]. According to Fu and Wagner, the propensity of a given metal to undergo decoration by TiO_x species is determined by its work function (Φ), concluding that metals with higher Φ than titania are more prone to undergo decoration (or even encapsulation in extreme cases) [63]. For instance, the decoration effect has been observed for Co, Ru, Pd, and Ir metals, all of them presenting higher Φ than titania [64-67].

In some cases, the TiO_x overlayer decorating metal NPs as the result of the SMSI effect has been directly observed by electron microscopy [64, 68], as exemplified in Figure 1.10 for Co/TiO_2 (a) [64] and Ir/TiO_2 (b) [69] systems. In the former case, the decoration effect was observed as "moiré" fringes (Figure 1.10a), while in the case of Ir/TiO_2 this effect manifests as a very thin TiO_x overlayer covering the surface of the metallic Ir NPs (Figure 1.10b).

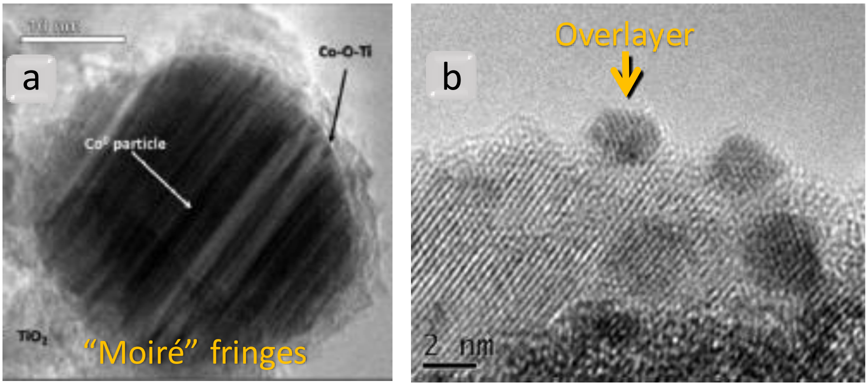

Figure 1.10. HRTEM images of Co/TiO_2 (a) and Ir/TiO_2 (b) catalysts exhibiting decoration by TiO_x species as a consequence of the SMSI effect. Adapted from ref. [64, 69].

Since the SMSI effect inhibits the CO and H_2 chemisorption capacity of titania-supported metal nanoparticles, it can directly influence the performance of the catalyst in the FTS reaction. However, the possible influence of the SMSI effect on the FTS performance of TiO_2-supported Co catalysts is generally not considered in most of the previous works. For instance, Jongsomjit and co-workers [70, 71] have observed higher CO conversion for Co catalysts based on rutile. They ascribed the enhanced catalytic activity to a weaker interaction of Co NPs with rutile with respect to anatase, which inhibited the formation of barely reducible mixed cobalt-support compounds due to water generated during the H_2 reduction treatment [70]. On the other side, Shimura and co-workers [72] attributed the higher CO conversion to a stronger interaction of Co NPs with the rutile polymorph, which suppressed cobalt aggregation leading to a highly dispersed Co catalyst. While Jongsomjit and co-workers did not take into account the SMSI effect to explain their results, a more pronounced SMSI effect for anatase-supported catalysts with respect to those based on rutile was suggested in the study by Shimura and co-workers [72].

Moreover, a decreased degree of the SMSI effect for the rutile phase has been stated in the literature for other systems, e.g. for Pd/TiO_2 [66] and Rh/TiO_2 [73], in order to explain differences in catalytic behavior with respect to equivalent anatase-supported materials. Besides the type of TiO_2 polymorph, the textural properties of the TiO_2 support have also been claimed to influence the extent of the SMSI effect and, consequently, the catalytic activity. For instance, Abdel-Mageed and co-workers [65] observed a decrease in TOF for CO methanation of Ru NPs supported on anatase with the increase in support surface area. Similarly, other authors [74] have reported a higher SMSI effect for Pt/TiO_2 catalysts comprising smaller TiO_2 particles (consequently, higher surface area) tested in the cyclohexane dehydrogenation reaction.

Nevertheless, no clear correlations between the titania properties (e.g. crystalline phase and textural properties) and the ultimate catalytic behavior of Co/TiO_2 catalysts for FTS have been established. This can be attributed, at least in part, to the reversibility of the SMSI effect as water generated during the FTS reaction can re-oxidize the TiO_x moieties back to TiO_2 recovering part of the initially exposed metal surface sites [42] and, consequently, altering the catalytic performance. Moreover, the SMSI effect can hamper the determination of cobalt dispersion measured by hydrogen chemisorption or the degree of cobalt reduction determined by temperature programmed reduction (H_2-TPR) [50, 75]. In addition, the low contrast between cobalt and titania in conventional electron microscopy makes the measurements highly laborious. Due to these difficulties, the use of synchrotron-based spectroscopy techniques (e.g. XANES and EXAFS) has been applied which, in combination with conventional characterization techniques, can provide valuable insights about the degree of reduction, the influence of promoters, and deactivation effects [76, 77].

1.5. References

[1] BP Statistical Review of World Energy, https://www.bp.com/en/global/corporate/energy-economics/statistical-review-of-world-energy.html, (accessed 2018/04/27).

[2] International Energy Agency, http://www.iea.org/weo/, (accessed 2018/04/27).

[3] S.N. Naik, V.V. Goud, P.K. Rout, A.K. Dalai, Renew. Sust. Energ. Rev. 14 (2010) 578-597.

[4] J. van de Loosdrecht, F.G. Botes, I.M. Ciobîcă, A. Ferreira, P. Gibson, D. Moodley, A. Saib, J. Visagie, C. Weststrate, H. Niemantsverdriet, Fischer–Tropsch Synthesis: Catalysts and Chemistry, in: J. Reedijk, K. Poeppelmeier (Eds.), Comprehensive Inorganic Chemistry II, Elsevier, 2013, pp. 525-557.

[5] H. Jahangiri, J. Bennett, P. Mahjoubi, K. Wilson, S. Gu, Catal. Sci. Technol. 4 (2014) 2210-2229.

[6] P. Sabatier, J.B. Senderens, C. R. Hebd. Seances Acad. Sci. 134 (1902) 514-516.

[7] A. Mittasch, C. Schneider, German Patent 293 787, 1913.

[8] F. Fischer, H. Tropsch, Brennst.-Chem. (1923) 276-285.

[9] J.L. Casci, C.M. Lok, M.D. Shannon, Catal. Today 145 (2009) 38-44.

[10] M.E. Dry, Catal. Today 71 (2002) 227-241.

[11] J.H. Gregor, Catal. Lett. 7 (1991) 317-331.

[12] M.E. Dry, J. Chem. Technol. Biot. 77 (2002) 43-50.

[13] D. Leckel, Energ. Fuel 23 (2009) 2342-2358.

[14] G.P. Van Der Laan, A.A.C.M. Beenackers, Cataly. Rev. 41 (1999) 255-318.

[15] B.H. Davis, Fuel Process. Technol. 71 (2001) 157-166.

[16] H. Schulz, E. van Steen, M. Claeys, Top. Catal. 2 (1995) 223-234.

[17] P.M. Maitlis, R. Quyoum, H.C. Long, M.L. Turner, Appl. Catal. A Gen. 186 (1999) 363-374.

[18] W. Chen, I.A.W. Filot, R. Pestman, E.J.M. Hensen, ACS Catal. 7 (2017) 8061-8071.

[19] A.Y. Khodakov, W. Chu, P. Fongarland, Chem. Rev. 107 (2007) 1692-1744.

[20] M.E. Dry, The Fischer–Tropsch (FT) Synthesis Processes, in: G. Ertl, H. Knözinger, F. Schüth, J. Weitkamp (Eds.) Handbook of Heterogeneous Catalysis 2008.

[21] B.H. Davis, Ind. Eng. Chem. Res. 46 (2007) 8938-8945.

[22] A.P. Vogel, B. van Dyk, A.M. Saib, Catal. Today 259 (2016) 323-330.

[23] A.Y. Khodakov, Catal. Today 144 (2009) 251-257.
[24] F. Morales, B.M. Weckhuysen, Promotion Effects in Co-based Fischer–Tropsch Catalysis, in: J. J. Spivey, K. M. Dooley (Eds.), Catalysis: Volume 19, RSC Publishing, 2006, pp. 1-40.
[25] G.R. Johnson, A.T. Bell, ACS Catal. 6 (2016) 100-114.
[26] G.R. Johnson, A.T. Bell, J. Catal. 338 (2016) 250-264.
[27] F. Diehl, A.Y. Khodakov, Oil Gas Sci. Technol. 64 (2008) 11-24.
[28] G. Jacobs, T.K. Das, Y. Zhang, J. Li, G. Racoillet, B.H. Davis, Appl. Catal. A Gen. 233 (2002) 263-281.
[29] S.-H. Song, S.-B. Lee, J.W. Bae, P.S. Sai Prasad, K.-W. Jun, Catal. Commun. 9 (2008) 2282-2286.
[30] A. Kogelbauer, J.J.G. Goodwin, R. Oukaci, J. Catal. 160 (1996) 125-133.
[31] N. Tsubaki, S. Sun, K. Fujimoto, J. Catal. 199 (2001) 236-246.
[32] E. Iglesia, S.L. Soled, R.A. Fiato, G.H. Via, J. Catal. 143 (1993) 345-368.
[33] W. Ma, G. Jacobs, R.A. Keogh, D.B. Bukur, B.H. Davis, Appl. Catal. A Gen. 437-438 (2012) 1-9.
[34] H. Li, B. Hou, J. Wang, X. Huang, C. Chen, Z. Ma, J. Cui, L. Jia, D. Sun, D. Li, Catal. Sci. Technol. 7 (2017) 3812-3822.
[35] G. Prieto, A. Martínez, R. Murciano, M.A. Arribas, Appl. Catal. A Gen. 367 (2009) 146-156.
[36] O. Borg, S. Eri, E. Blekkan, S. Storsater, H. Wigum, E. Rytter, A. Holmen, J. Catal. 248 (2007) 89-100.
[37] A. Martínez, G. Prieto, J. Rollán, J. Catal. 263 (2009) 292-305.
[38] C. Liu, Y. Zhang, Y. Zhao, L. Wei, J. Hong, L. Wang, S. Chen, G. Wang, J. Li, Nanoscale 9 (2017) 570-581.
[39] O. Borg, P. Dietzel, A. Spjelkavik, E. Tveten, J. Walmsley, S. Diplas, S. Eri, A. Holmen, E. Rytter, J. Catal. 259 (2008) 161-164.
[40] S. Rane, Ø. Borg, J. Yang, E. Rytter, A. Holmen, Appl. Catal. A Gen. 388 (2010) 160-167.
[41] G. Prieto, M.I.S. De Mello, P. Concepción, R. Murciano, S.B.C. Pergher, A. Martínez, ACS Catal. 5 (2015) 3323-3335.
[42] E. Iglesia, S.L. Soled, R.A. Fiato, J. Catal. 137 (1992) 212-224.
[43] E. Iglesia, Appl. Catal. A Gen. 161 (1997) 59-78.
[44] G.L. Bezemer, J.H. Bitter, H.P. Kuipers, H. Oosterbeek, J.E. Holewijn, X. Xu, F. Kapteijn, A.J. van Dillen, K.P. de Jong, J. Am. Chem. Soc. 128 (2006) 3956-3964.
[45] G. Prieto, A. Martínez, P. Concepción, R. Moreno-Tost, J. Catal. 266 (2009) 129-144.
[46] C.J. Weststrate, P. van Helden, J.W. Niemantsverdriet, Catal. Today 275 (2016) 100-110.
[47] Q. Zhang, J. Kang, Y. Wang, ChemCatChem 2 (2010) 1030-1058.

[48] R.C. Reuel, C.H. Bartholomew, J. Catal. 85 (1984) 78-88.

[49] S. Storsater, B. Totdal, J. Walmsley, B. Tanem, A. Holmen, J. Catal. 236 (2005) 139-152.

[50] T.O. Eschemann, J. Oenema, K.P. de Jong, Catal. Today 261 (2016) 60-66.

[51] H. Karaca, O.V. Safonova, S. Chambrey, P. Fongarland, P. Roussel, A. Griboval-Constant, M. Lacroix, A.Y. Khodakov, J. Catal. 277 (2011) 14-26.

[52] S.A. Hosseini, A. Taeb, F. Feyzi, F. Yaripour, Catal. Commun. 5 (2004) 137-143.

[53] J.-Y. Park, Y.-J. Lee, P.R. Karandikar, K.-W. Jun, J.W. Bae, K.-S. Ha, J. Mol. Catal. A: Chem. 344 (2011) 153-160.

[54] T.O. Eschemann, J.H. Bitter, K.P. de Jong, Catal. Today 228 (2014) 89-95.

[55] T.O. Eschemann, K.P. de Jong, ACS Catal. 5 (2015) 3181-3188.

[56] B. Ohtani, O.O. Prieto-Mahaney, D. Li, R. Abe, J. Photoch. Photobio. A Chem. 216 (2010) 179-182.

[57] M. Landmann, E. Rauls, W.G. Schmidt, J. Phys. Condens. Matter. 24 (2012) 195503.

[58] S.J. Tauster, S.C. Fung, R.T. Baker, J.A. Horsley, Science 211 (1981) 1121-1125.

[59] G.L. Haller, D.E. Resasco, Metal-Support Interaction: Group VIII Metals and Reducible Oxides, in: D. Eley (Series Volume Editor), H. Pines, P. B. Weisz (Serial Editors), Advances in Catalysis, Volume 36, 1st Edition, Academic Press, 1989, pp. 173-235.

[60] S.J. Tauster, Acc. Chem. Res. 20 (1987) 389-394.

[61] M. Ahmadi, H. Mistry, B. Roldan Cuenya, J. Phys. Chem. Lett. 7 (2016) 3519-3533.

[62] C.-J. Pan, M.-C. Tsai, W.-N. Su, J. Rick, N.G. Akalework, A.K. Agegnehu, S.-Y. Cheng, B.-J. Hwang, J. Taiwan Inst. Chem. E. 74 (2017) 154-186.

[63] Q. Fu, T. Wagner, Surf. Sci. Rep. 62 (2007) 431-498.

[64] V.A. O'Shea, M.C. Galvan, A.E. Prats, J.M. Campos-Martin, J.L. Fierro, Chem. Commun. 47 (2011) 7131-7133.

[65] A.M. Abdel-Mageed, D. Widmann, S.E. Olesen, I. Chorkendorff, J. Biskupek, R.J. Behm, ACS Catal. 5 (2015) 6753-6763.

[66] Y. Li, B. Xu, Y. Fan, N. Feng, A. Qiu, J.M.J. He, H. Yang, Y. Chen, J. Mol. Catal. A Chem. 216 (2004) 107-114.

[67] E.W. Zhao, H. Zheng, K. Ludden, Y. Xin, H.E. Hagelin-Weaver, C.R. Bowers, ACS Catal. 6 (2016) 974-978.

[68] X.Y. Shi, W. Zhang, C. Zhang, W.T. Zheng, H. Chen, J.G. Qi, J. Microsc. 262 (2016) 203-215.

[69] O. Hernández-Cristóbal, J. Arenas-Alatorre, G. Díaz, D. Bahena, M. J. Yacamán, J. Phys. Chem. C 119 (2015) 11672-11678.
[70] B. Jongsomjit, C. Sakdamnuson, P. Praserthdam, Mater. Chem. Phys. 89 (2005) 395-401.
[71] B. Jongsomjit, T. Wongsalee, P. Praserthdam, Catal. Commun. 6 (2005) 705-710.
[72] K. Shimura, T. Miyazawa, T. Hanaoka, S. Hirata, Appl. Catal. A Gen. 460-461 (2013) 8-14.
[73] A. Yamamoto, J. Ohyama, K. Teramura, T. Shishido, T. Tanaka, Catal. Today 232 (2014) 165-170.
[74] M. Bonne, P. Samoila, T. Ekou, C. Especel, F. Epron, P. Marécot, S. Royer, D. Duprez, Catal. Commun. 12 (2010) 86-91.
[75] M. Voß, D. Borgmann, G. Wedler, J. Catal. 212 (2002) 10-21.
[76] G. Jacobs, Y. Ji, B.H. Davis, D. Cronauer, A.J. Kropf, C.L. Marshall, Appl. Catal. A Gen. 333 (2007) 177-191.
[77] G. Jacobs, W. Ma, P. Gao, B. Todic, T. Bhatelia, D.B. Bukur, B.H. Davis, Catal. Today 214 (2013) 100-139.

CHAPTER 2

OBJECTIVES

The major goal of this doctoral thesis is to elucidate the influence of structural characteristics of the support, Ru promotion, and redox treatments of CoRu/TiO_2 catalysts on the Fischer-Tropsch synthesis (FTS). After a succinct introduction to the topic (Chapter 1) and description of the main objectives of the thesis (Chapter 2), the results of the present investigation are reported in the following four chapters, each of one addressing specific subjects of the FTS reaction catalyzed by TiO_2-supported Co catalysts.

More specifically, Chapter 3 focuses on the study of different titania polymorphs (anatase and rutile) as supports for CoRu-based catalysts, highlighting the consequences in the activity and selectivity for FTS of the titania crystalline phase. Similarly, the influence of the textural properties (i.e. surface area) of anatase-TiO_2 supports on the FTS performance of CoRu/TiO_2 catalysts is addressed in Chapter 4. In both chapters, the impact of the SMSI (strong metal-support interaction) effect on the physicochemical and catalytic properties of CoRu/TiO_2 catalysts is discussed.

In Chapter 5, the effect of Ru promotion in CoRu/TiO_2-anatase catalysts is studied by varying the Ru loading with the aim of clarifying the role of Ru as promoter of cobalt. Finally, in Chapter 6 the application of redox (reduction-oxidation-reduction, ROR) treatments is investigated as a possible strategy to improving the catalytic performance of CoRu/TiO_2 catalysts for FTS.

Overall, the outcome of the research gathered in this thesis may provide grounds for a more rational design of better TiO_2-supported Co FTS catalysts.

CHAPTER 3

TiO_2 POLYMORPH DEPENDENT SMSI EFFECT IN CO-RU/TiO_2 CATALYSTS AND ITS RELEVANCE TO FISCHER-TROPSCH SYNTHESIS

In this chapter the influence of titania polymorph (anatase or rutile) in Co-Ru/TiO_2 catalysts and its consequences on activity and selectivity for the Fischer-Tropsch synthesis is presented in the form of scientific article:

TiO_2 polymorph dependent SMSI effect in Co-Ru/TiO_2 catalysts and its relevance to Fischer-Tropsch synthesis

Francine Bertella, Patricia Concepción, Agustín Martínez.

Reproduced with permission from *Catalysis Today 289 (2017) 181-191*.

https://doi.org/10.1016/j.cattod.2016.08.008

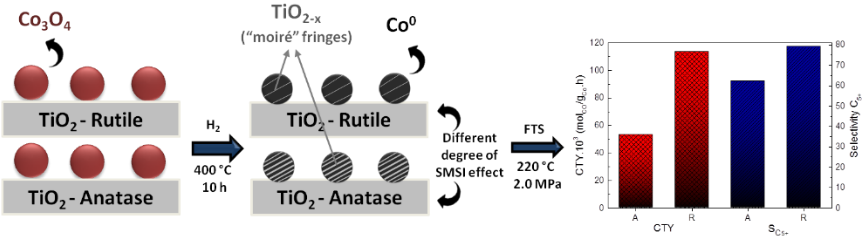

3.1. Introduction

Fischer-Tropsch synthesis (FTS) is at the core of XTL processes allowing a variety of liquid fuels and chemicals to be produced from oil-alternative carbon resources such as natural gas (GTL), coal (CTL), and biomass (BTL) via syngas (H_2+CO). Of particular interest is the Co-catalyzed low-temperature FTS in which syngas is selectively converted to long-chain *n*-paraffins (waxes) that are then hydrocracked to produce high-quality diesel [1, 2].

Preparation of Co-based FTS catalysts commonly involves dispersion (via impregnation) of a cobalt salt precursor, most frequently cobalt nitrate, on a high surface area porous inorganic oxide carrier, among which SiO_2, Al_2O_3, and TiO_2 are the most widely employed, followed by drying, calcination, and H_2-reduction to generate the active metallic Co sites on the catalyst surface [1]. Commonly, some metals (e.g. Ru, Re, Pt) and/or metal oxides are included in the catalyst formulation in order to promote the reduction and dispersion of the supported Co particles [3, 4]. The final catalytic performance of Co-based FTS catalysts becomes mainly dictated by the metal content, the dispersion (i.e. Co particle size), and the degree of Co reduction which ultimately determine the concentration of surface metal Co sites. These properties are affected by a number of factors such as the nature of the cobalt precursor and loading method [1], the chemical identity and porosity of the oxide carrier [1, 5, 6], and the so-called thermal history (i.e. the drying, calcination, and reduction conditions) [7].

As for the chemical nature of the support, TiO_2 has proven to be particularly beneficial from the standpoint of both catalyst activity and selectivity to the targeted liquid (C_{5+}) hydrocarbon fraction [6, 8, 9]. As a support, TiO_2 is known to exhibit the SMSI (strong metal-support interaction) decoration effect by virtue of which TiO_{2-x} sub-oxides form during H_2 reduction and migrate on top of the supported metal nanoparticles inhibiting their H_2 and CO chemisorption capability [10-14]. For Co/TiO_2, partial encapsulation of Co nanoparticles by a few atomic layers of thick TiO_{2-x} phase during reduction was directly imaged by HRTEM [15]. In nature, TiO_2 exists in three distinct crystallographic forms, namely anatase, rutile, and brookite. Previous studies have shown that the TiO_2 crystal phase composition is highly influential to the ultimate FTS performance of Co/TiO_2 catalysts, albeit with controversial results. For instance, by supporting 20 wt% Co on TiO_2 with different anatase:rutile ratios, Jongsomjit et al. observed a maximum CO conversion rate under methanation conditions (H_2/CO= 10) for the catalyst comprising 19% rutile and 81% anatase which also exhibited the highest H_2 chemisorption capacity [16]. This behavior was ascribed to a weaker interaction of Co with rutile in comparison to anatase that prevented the formation of barely reducible mixed Co-O-Ti compounds assisted by water generated during the H_2 reduction treatment thus increasing the amount of available surface Co^0 atoms [17]. Other authors also reported higher CO conversion rates for Co/TiO_2 catalysts prepared from TiO_2 with more than 15% rutile in comparison to those based on pure anatase [18, 19]. However, in contrast with the previous study, the effect was related to a stronger Co-support interaction in presence of rutile that inhibited the aggregation of Co particles during reduction improving the final Co^0 dispersion, although the possibility of a suppressed SMSI effect over rutile was not excluded [18].

It is apparent from the previous discussion that further work is required to clarify the role of the TiO_2 crystalline phase, with a special focus on the little studied phase-dependent SMSI effect, in determining the FTS performance of Co/TiO_2 catalysts. To this aim, we synthesized 100% pure anatase and rutile TiO_2 phases and used them as supports for preparing Ru-promoted Co/TiO_2 catalysts (nominal loadings of 10 wt% Co and 0.5 wt% Ru). The prepared catalysts display alike mean Co^0 particle sizes (5-6 nm) and particle size distributions as well as high and similar extents of cobalt reduction (ca. 90%), enabling a fair study of the TiO_2 crystalline phase dependent SMSI effect and its consequences on the catalytic behavior for FTS under industrially relevant conditions (220 °C, 2.0 MPa, H_2/CO= 2).

3.2. Experimental

3.2.1. Materials

Triton X-100 [(*tert*-octylphenoxy)polyethoxyethanol] (Aldrich), titanium(IV) butoxide (99+%, Alfa Aesar), 1-hexanol (>98% GC, Fluka Chemika), cyclohexane (99%, Aldrich), hydrochloric acid (37%, Aldrich), and acetic acid (99,5%, Aldrich) were used as received.

3.2.2. Synthesis of pure anatase and rutile TiO_2 phases

Pure anatase and rutile TiO_2 phases were synthesized by thermal treatment of reverse microemulsions following a procedure similar to that reported in [20]. In short, an aqueous solution containing the acid (acetic acid for anatase and hydrochloric acid for rutile) and the Ti source (titanium(IV) butoxide) was added to an organic mixture containing the surfactant (Triton X-100), cosurfactant (1-hexanol), and solvent (cyclohexane) under stirring at room temperature (r.t.). The formed microemulsion was then either heated at 40 °C for 24 h under reflux (for rutile) or introduced into a Teflon-lined stainless steel autoclave and hydrothermally treated at 120 °C for 5 h (for anatase). After the thermal treatments the solids were recovered by centrifugation, washed 5 times in ethanol in a process involving redispersion and centrifugation, dried at 60 °C overnight, and finally calcined in flowing air at 400 °C for 8 h. The obtained TiO_2 anatase and rutile supports are labeled as Ti-A and Ti-R, respectively. The conditions and composition of the microemulsions employed for the syntheses of pure anatase and rutile phases are gathered in Table 3.1.

Table 3.1. Nomenclature and conditions employed for the synthesis of pure TiO_2 anatase and rutile phases.

Support	Acid	Temp. (°C)	Time (h)	w = [H_2O]/[Triton] (mol/mol)	h = [H_2O]/[Ti] (mol/mol)
Ti-A	CH_3COOH	120	5	19.4	33.8
Ti-R	HCl	40	24	15.0	18.8

3.2.3. Synthesis of Co-Ru/TiO_2 catalysts

Co-Ru/TiO_2 catalysts with nominal loadings of 10 wt% Co and 0.5 wt% Ru (added as reduction promoter) were prepared by incipient wetness co-impregnation of the calcined TiO_2 carriers with an aqueous solution of $Co(NO_3)_2{\cdot}6H_2O$ (Aldrich) and ruthenium(III) nitrosyl nitrate (Aldrich) as metal precursors, followed by drying at 100 °C overnight and calcination in flowing air at 300 °C for 3 h. The catalysts based on anatase and rutile are denoted as Co-Ru/Ti-A and Co-Ru/Ti-R, respectively.

3.2.4. Characterization techniques

X-ray powder diffraction (XRD) patterns were recorded on a Philips X'Pert diffractometer using monochromatic Cu Kα radiation (λ= 0.15406 nm). The average TiO_2 crystallite size was estimated by the Scherrer's equation applied to the most intense reflections (1 1 0) for rutile (2θ= 27.44°) and (1 0 1) for anatase (2θ= 25.28°), assuming a shape factor k= 0.9.

Textural properties were derived from the N_2 adsorption isotherms measured at -196 °C in an ASAP-2420 equipment (Micromeritics). Specific surface areas were calculated following the Brunauer–Emmett–Teller (BET) method, total pore volumes (TPV) were determined at a relative pressure of 0.98, and the pore size distributions were obtained by applying the Barrett–Joyner–Halenda (BJH) approach. Prior to the adsorption measurements, the samples were degassed at 300 °C and vacuum overnight.

The morphology of the samples were studied by field emission scanning electron microscopy (FESEM) using a ZEISS Ultra-55 microscope.

The Co and Ru contents were determined by ICP-OES (Inductively Coupled Plasma-Optical Emission Spectrometry) in a Varian 715-ES spectrometer after dissolution of the solids in an acid mixture of 20%HNO_3:20%HF:60%HCl (% volume).

The reduction behavior of the oxidized Co-Ru/TiO_2 catalysts was studied by hydrogen temperature-programmed reduction (H_2-TPR) in a Micromeritics Autochem 2910 equipment. The samples were initially flushed with an Ar flow at r.t. for 30 min, and then the gas was switched to 10 vol% H_2 in Ar and the temperature linearly increased up to 900 °C at a heating rate of 10 °C/min. A downstream 2-propanol/N_2(liq) trap was used to retain the water generated during the reduction. The H_2 consumption rate was monitored in a thermal conductivity detector (TCD) previously calibrated using the reduction of a standard CuO sample. This setup was also used to measure the degree of cobalt reduction (DR) after submitting the catalysts to the same reduction protocol applied in-reactor prior to the FTS experiments (400 °C in H_2 flow for 10 h).

Cobalt dispersions were determined by H_2 chemisorption at 100 °C in an ASAP 2010C Micromeritics equipment by extrapolating the total H_2 uptake to zero pressure [21]. Metal particle sizes ($d(Co^0)_{H2}$) were estimated from the total amount of chemisorbed H_2, the Co content (from ICP-OES) and the degree of cobalt reduction by assuming a chemisorption stoichiometry H/Co= 1 and a surface atomic density for Co^0 of 14.6 atoms/nm^{-2}.

Cobalt particle sizes were studied by electron microscopy in a JEOL-JEM-2100F microscope operating at 200 kV in scanning-transmission mode (STEM) using a High-Angle Annular Dark Field (HAADF) detector. Prior to microscopy observation, the samples were suspended in ethanol and submitted to ultrasonication for one minute. Afterwards, the suspension was let to slowly decant for two minutes and a drop was extracted from the top side and placed on a carbon-coated copper grid. The catalysts were previously *ex situ* reduced under a flow of H_2 at 400 °C, passivated at r.t. under a flow of 0.5% O_2/N_2, and stored at r.t. until the sample preparation for microscopy. Metal particle size histograms were generated upon measurement of 150–200 particles from several micrographs taken at different positions on the TEM grid. Metallic cobalt particle sizes ($d(Co^0)_{TEM}$) were corrected for a 3 nm thick CoO passivation outlayer [22].

X-ray photoelectron spectra (XPS) were collected using a SPECS spectrometer with a 150MCD-9 detector and using a non-monochromatic Mg Kα (1253.6 eV) X-ray source. Spectra were recorded using an analyzer pass energy of 30 eV, an X-ray power of 200 W, and an operating pressure of 10^{-9} mbar. During data processing of the XPS spectra, binding energy (BE) values were referenced to the Ti2p peak (458.6 eV). Spectra treatment was performed using the CASA software. The samples were analyzed in their calcined state as well as after H_2 reduction (20 cm^3/min) at 400 °C for 2 h in a micro-reactor directly connected to the UHV of the XPS analyze chamber to avoid contact with air after the sample treatment.

IR-CO spectra were recorded with a Nexus 8700 FTIR spectrometer using a DTGS detector and acquiring at 4 cm^{-1} resolution. An IR cell allowing *in situ* treatments in controlled atmospheres and temperatures in the 25-500 °C range was connected to a vacuum system with gas dosing facility. For IR studies, previously reduced (at 400 °C for 10 h) and passivated samples were pressed into self-supported wafers of 10 mg/cm^2 and reduced again in the IR cell at 400 °C in H_2 flow (20 cm^3/min) for 2 h, followed by vacuum treatment at 450 °C for 1 h. Afterwards, the samples were cooled down to 25 °C under dynamic vacuum and CO was dosed at increasing pressures (1.9-30 mbar). IR spectra were recorded after each dosage. Additional *in situ* IR experiments were performed by exposing the reduced catalysts to a flow of syngas (50 cm^3/min) at r.t. for 1 h to ensure homogeneous atmosphere in the IR cell. Next, the temperature was increased up to the FTS reaction temperature of 220 °C and the spectra recorded after 4 h of reaction at this condition. Spectra analysis was done using the Origin software.

3.2.5. Fischer–Tropsch synthesis experiments

Fischer–Tropsch synthesis (FTS) experiments were performed in a down-flow fixed bed stainless steel reactor with i.d. of 10 mm and length of 40 cm. The reactor was loaded with 0.5 g of catalyst (0.25–0.42 mm pellet size) diluted with SiC granules (0.6–0.8 mm) until a total bed volume of 6.4 cm^3. The catalysts were reduced *in situ* in flowing H_2 at 400 °C for 10 h at ambient pressure. After reduction, the temperature was decreased to 100 °C under flow of H_2 and then syngas with H_2/CO molar ratio of 2 (CO:H_2:Ar volume ratio of 3:6:1, Ar as internal standard for gas chromatography) was flowed through the reactor at the desired flow rate, the reaction pressure increased up to 2.0 MPa, and the temperature raised up to 220 °C at a rate of 2 °C/min. The temperature in the catalytic bed was controlled by two thermocouples connected to independent PID controllers, while a third vertically sliding thermocouple was used to verify the absence of temperature gradients (T= 220 ± 1 °C) along the catalyst bed. Initial FTS activities were determined at *quasi*-differential CO conversions (< 10%) using a constant gas hourly space velocity (GHSV) of 11.7 $L_{syngas}/(g_{cat}\cdot h)$ to ensure a low water partial pressure in the catalytic bed. This condition was maintained during ca. 7 h on stream, after which the GHSV was adjusted for each catalyst so as to attain a constant CO conversion of 10 ± 2% in the *pseudo*-steady state. Heavier hydrocarbons were condensed in two consecutive traps located at the reactor outlet and kept, respectively, at 150 °C and 100 °C, both at the reaction pressure (2.0 MPa). The stream leaving the second trap was depressurized and regularly analyzed on line in a Varian 450 gas chromatograph (GC) equipped with three columns and TCD and FID detectors. After separation of the water co-product, the hydrocarbon fractions collected in the traps were weighted, diluted with CS_2, and analyzed off line in the same GC. The combination of the on line and off line GC analyses through the common product methane resulted in carbon mass balances in the 98-102% range. Product selectivities are expressed on a carbon basis.

3.3. Results and discussion

3.3.1. *Characterization of the TiO_2 supports*

The XRD patterns of the calcined supports (Figure 3.1) confirm the successful synthesis of 100% pure anatase (JCPDS 00-021-1272) and rutile (JCPDS 00-021-1276) phases at the specific microemulsion conditions employed. This phase selectivity is closely related to the type of acid used [23-25], and originates from the different affinities of the acids with the octahedral TiO_6 units during the phase transformation from anatase to rutile. Hence, CH_3COO^- anions coordinate stronger to titanium than Cl^- anions, preventing the transformation of the metastable anatase phase to the thermodynamically more stable rutile form [25, 26]. No other crystalline phases were detected. Line broadening analysis of the most intense reflections using the Scherrer's approach reveals a lower mean particle size for anatase (9.5 nm) compared to rutile (13.6 nm), as shown in Table 3.2.

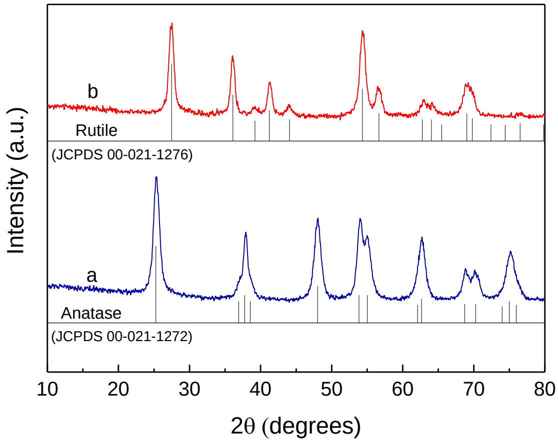

Figure 3.1. X-ray diffraction patterns of calcined TiO_2 supports. Diffraction lines for pure anatase (JCPDS 00-021-1272) and rutile (JCPDS 00-021-1276) phases are also shown as reference.

Table 3.2. Main physicochemical properties of TiO_2 supports.

Support	BET area (m^2/g)	TPV[a] (cm^3/g)	APD[b] (nm)	d(TiO_2)[c] (nm)
Ti-A	164	0.30	6.4	9.5
Ti-R	59	0.17	7.3	13.6

[a] TPV= Total pore volume. [b] APD= Average pore diameter (BJH). [c] Mean TiO_2 crystallite size.

The N_2 adsorption isotherms and the pore size distributions for the TiO_2 carriers are shown in Figure 3.2, and the derived textural properties are summarized in Table 3.2. The Ti-A sample presents a type IV adsorption isotherm characteristic of mesoporous solids, while Ti-R exhibits type III adsorption isotherm typical for non-porous or macroporous solids (Figure 3.2a) [27]. At high relative pressures (> 0.95) both samples show a rapid increase in the amount of N_2 adsorbed that signs for the presence of large interparticle mesopores and macropores, particularly in the rutile Ti-R sample. The N_2 uptake capacity is much higher for the anatase sample which, accordingly, displays notably higher specific surface area (BET= 164 m^2/g) and total pore volume (TPV= 0.30 cm^3/g) than rutile (BET= 59 m^2/g, TPV= 0.17 cm^3/g, Table 3.2). In turn, the anatase support shows a relatively narrow unimodal pore size distribution in the mesopore range (2-20 nm) with a maximum centered at 8.8 nm. Differently, the rutile sample displays a very broad pore size distribution with a maximum at 7.4 nm and a profile extending beyond the range of mesopores that can be reliably measured by N_2 physisorption (Figure 3.2b). This reflects the presence of large mesopores and macropores in this sample already inferred from the shape of the N_2 adsorption isotherm at high P/P_0 values. The average pore diameter (BJH) is 6.4 nm for Ti-A and 7.3 nm for Ti-R (Table 3.2). However, the total pore volume and average pore diameter for the rutile sample are probably underestimated due to the inadequacy of N_2 to measure the larger mesopores and macropores present in this material.

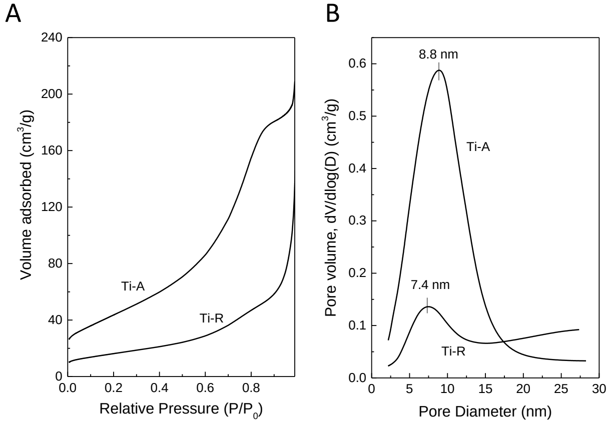

Figure 3.2. N_2 adsorption isotherms (A) and BJH-derived pore size distributions (B) for the calcined anatase (Ti-A) and rutile (Ti-R) samples.

As for the morphology, the FESEM images in Figure 3.3 show irregularly-shaped agglomerates of small rice-like crystallites sizing about 10-30 nm for anatase (Figure 3.3a) and *pseudo*-spherical agglomerates (0.2-0.5 µm) of slightly elongated crystallites (10-20 nm) for rutile (Figure 3.3b). The observed differences in morphology are mainly dictated by the type of acid employed in the syntheses [28], although other factors like the concentration of the Ti source in the microemulsion may be also influential [29, 30].

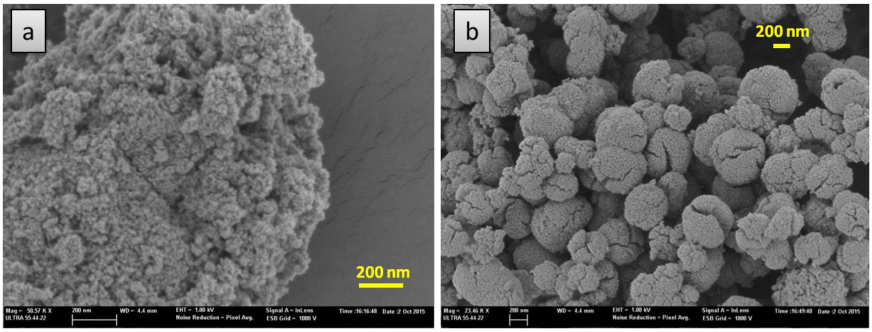

Figure 3.3. FESEM images for: a) anatase (Ti-A) and b) rutile (Ti-R) TiO_2 samples.

3.3.2. Characterization of the Co-Ru/TiO_2 catalysts

3.3.2.1. Structural and textural properties

The XRD patterns of the calcined Co-Ru/TiO_2 catalysts are shown in Figure 3.4. The mean particle size of the TiO_2 supports did not experience significant variations upon impregnation with the metal precursors and calcination. Besides TiO_2 peaks, reflections belonging to the Co_3O_4 spinel phase (JCPDS 00-042-1467) are clearly perceived in the calcined catalysts, with no signs for the presence of other crystalline cobalt phases. However, the relatively low intensity of the spinel peaks and overlapping with TiO_2 diffractions prevent an accurate estimation of the Co_3O_4 crystallite sizes by line broadening analysis. Moreover, formation of mixed Co-Ti compounds (e.g. $CoTiO_3$) was not evidenced by Raman spectroscopy for any of the two studied catalysts, as shown in Figure 3.S1 of the Supplementary Material, although their presence cannot be completely excluded.

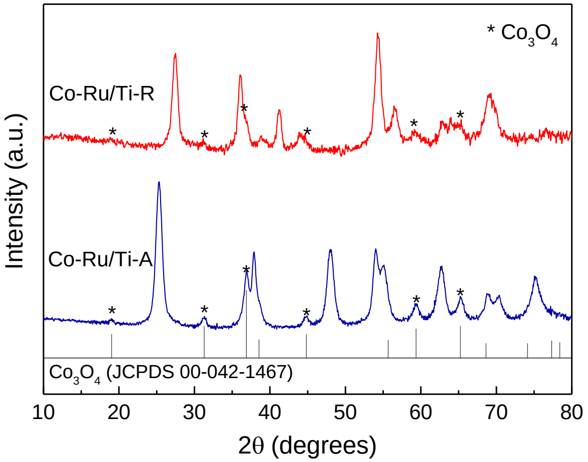

Figure 3.4. X-ray diffraction patterns of calcined Co-Ru/Ti-A and Co-Ru/Ti-R catalysts.

The Co content in the catalysts determined by ICP-OES slightly exceeds the nominal value (11-12 wt%) while the concentration of Ru (0.3-0.4 wt%) is 20-40% lower than the expected value (Table 3.3). The partial loss of Ru upon air-calcination has been previously reported and is attributed to the formation of volatile suboxide RuO_x species under oxidizing atmospheres [31-33].

The Co-Ru/TiO_2 catalysts exhibit N_2 adsorption isotherms similar to the respective supports, albeit with a decreased N_2 adsorption capacity due to the deposited metal oxide phases (Figure 3.5a). Analogously to the respective supports, the catalyst based on rutile shows a much broader pore size distribution than that based on anatase which, differently, displays a rather narrow distribution with a maximum for pores sizing ca. 8.1 nm (Figure 3.5b). The textural properties derived from the N_2 adsorption isotherms are collected in Table 3.3. The BET area of the catalysts decreases by 23-28% and the total pore volume (TPV) by 18-23% relative to the pristine supports. However, when calculated per mass of TiO_2 support (Table 3.3) the relative decreases in BET area and TPV are, respectively, 8% and 10% for the anatase-based catalyst and 15% and 6%, respectively, for the catalyst supported on rutile. Therefore, considering the dilution effect, these results suggest a minor pore blockage (≤ 10%) by the supported metal oxides, particularly in the rutile-based catalyst presenting wider pores. In turn, no significant variations in the mean pore diameter are noticed for the catalysts with respect to the corresponding supports (Table 3.3).

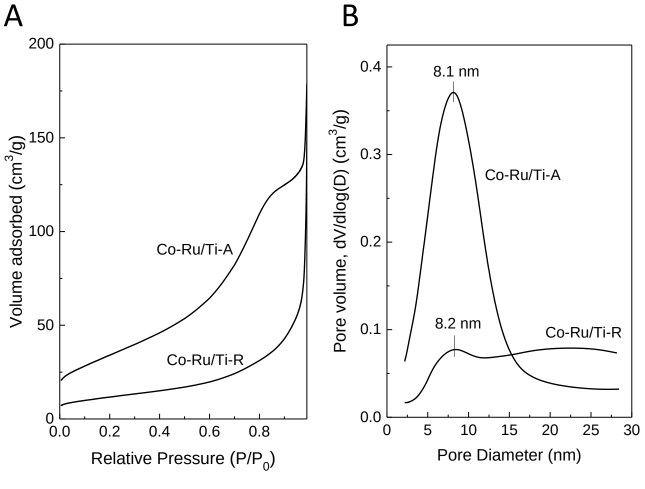

Figure 3.5. N_2 adsorption isotherms (A) and BJH-derived pore size distributions (B) for the calcined Co-Ru/Ti-A and Co-Ru/Ti-R catalysts.

Table 3.3. Chemical composition and textural properties of the calcined CoRu/TiO_2 catalysts.

Catalyst	Metal content		BET area		TPV[a]		APD[b]
	wt%Co	wt%Ru	$(\frac{m^2}{g_{cat}})$	$(\frac{m^2}{g_{TiO2}})$	$(\frac{cm^3}{g_{cat}})$	$(\frac{cm^3}{g_{TiO2}})$	(nm)
Co-Ru/Ti-A	11.7	0.3	126	151	0.23	0.27	6.1
Co-Ru/Ti-R	11.1	0.4	42	50	0.14	0.16	8.4

[a] TPV= Total pore volume. [b] APD= Average pore diameter (BJH).

3.3.2.2. Reducibility and particle size of cobalt

The reduction behavior of the Co-Ru/TiO_2 catalysts was studied by H_2-TPR, and the corresponding reduction profiles are shown in Figure 3.6. No appreciable H_2 consumption was observed for the pristine Ti-A and Ti-R supports, in agreement with previous reports [16, 34, 35]. Both catalysts display two main reduction features with maximum H_2 consumptions (T_{max}) at ca. 120-190 °C and 260-350 °C, respectively, that correspond to the stepwise reduction of Co_3O_4 to metallic Co ($Co_3O_4 \rightarrow CoO \rightarrow Co^0$) as commonly observed for ex-nitrate supported Co catalysts [5, 33, 36]. Besides, an additional reduction with lower H_2 consumption is perceived at higher temperatures (T_{max} at 390 °C for Co-Ru/Ti-A and 425 °C for Co-Ru/Ti-R) which can be ascribed to the reduction of oxidic Co phases presenting a stronger interaction with the TiO_2 support. Moreover, a relatively small H_2 consumption extending over a broad temperature range (500-700 °C) is inferred for the Co-Ru/Ti-A sample. This feature might be related to the reduction of minor amounts of mixed Co-O-Ti compounds, although a contribution from the partial reduction of anatase TiO_2 assisted by metallic Co (and Ru) species via H_2 spillover is not discarded. It is clearly seen in Figure 3.6 that the T_{max} for the main reductions are downward shifted by ca. 70-90 °C in the Co-Ru/Ti-A sample in comparison to Co-Ru/Ti-R, signing for an enhanced reducibility of cobalt when supported on anatase. An easier reducibility, hence a weaker Co-support, for Co oxides supported on anatase was also concluded by Shimura et al. in previous studies using TiO_2 supports with different % fraction of rutile phase [18, 19], although the opposite trend (i.e. a weaker Co-support interaction for rutile) was reported by others [16, 17, 37]. Nonetheless, a high degree of cobalt reduction can be anticipated after the pre-catalysis reduction treatment with pure H_2 at 400 °C for 10 h at the view of the corresponding profiles, as expected from the presence of the Ru reduction promoter [38-43]. In fact, degrees of cobalt reduction (DR) of 89-93% were obtained from the H_2 consumed in H_2-TPR experiments performed on catalysts pre-reduced at 400 °C for 10 h in pure H_2 (see section 2.4), as shown in Table 3.4. Such high and alike DR values are desirable not only to maximize the amount of active Co^0 sites but also to avoid potential side effects on the FTS activity and selectivity due to the presence of oxidic Co species supported on TiO_2, as recently reported [44]. A high extent of reduction of Co_3O_4 to Co^0 in the Co-Ru/TiO_2 catalysts is also concluded from *in situ* H_2-XRD experiments, which indicated the presence of both *hcp*- and *fcc*-Co^0 with no evidence for Co_3O_4 or CoO crystalline phases after the *in situ* treatment at 400 °C (7 h) in flowing H_2 (see Figure 3.S2 in Supplementary Material). Additionally, no signs for the formation of Co-Ti alloys or mixed oxides were found in these experiments.

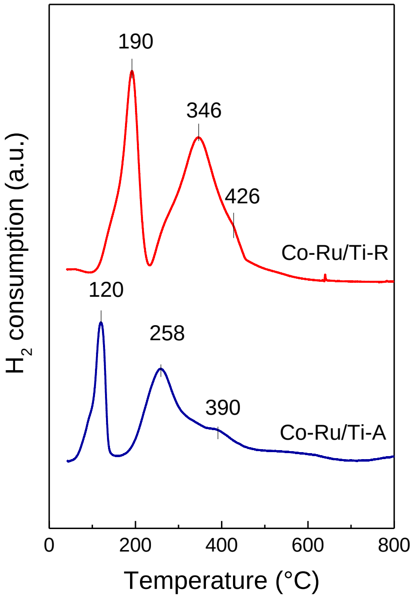

Figure 3.6. H_2-TPR profiles for the Co-Ru/TiO_2 catalysts.

Table 3.4. Properties of cobalt in the Co-Ru/TiO_2 catalysts.

Catalyst	DR[a] (%)	H_2 uptake (μmol/g_{cat})	Co^0 particle size (nm) d(Co^0)$_{H2}$	d(Co^0)$_{TEM}$	Atomic (Co/Ti)$_{surf}$ ratio[b] Calc.	H_2-red.
Co-Ru/Ti-A	93	13.8	64.7	5.2	0.08	0.32
Co-Ru/Ti-R	89	27.3	29.5	6.0	0.24	0.30

[a] Percentage degree of cobalt reduction upon treatment in pure H_2 at 400 °C for 10 h.

[b] Atomic Co/Ti surface ratio in calcined and as-reduced catalysts determined by XPS.

The H_2 uptakes obtained from H_2 chemisorption and the mean Co^0 particle sizes estimated from both H_2 chemisorption (d(Co^0)$_{H2}$) and TEM (d(Co^0)$_{TEM}$) are also included in Table 3.4. As seen there, the H_2 uptake for Co-Ru/Ti-A is about 50% that of Co-Ru/Ti-R. The obtained H_2

uptakes translate into "apparent" Co^0 particle sizes ($d(Co^0)_{H2}$) of ca. 65 nm and 30 nm for the catalysts supported on, respectively, anatase and rutile phases. On the other hand, the size of the supported Co^0 nanoparticles was also obtained by direct electron microscopy imaging of as-reduced samples. Representative HAADF-STEM images and the corresponding particle size histograms are shown in Figure 3.7. Metallic Co nanoparticles, appearing as bright spots in the micrographs, look relatively well distributed over the two TiO_2 supports, although some clustered regions can be perceived, as commonly observed for supported Co catalysts prepared by impregnation using cobalt nitrate precursor [45, 46]. The histograms reveal similar Co^0 particle size distributions spanning from ca. 2 to 14 nm, with predominance of nanoparticles sizing 4-6 nm. Nonetheless, the rutile-based catalyst presents a somewhat greater contribution from particles above 8 nm in diameter (Figure 3.7d) which results in a slightly higher average Co^0 particle size (6.0 nm) in comparison to the anatase-supported sample (5.2 nm), as seen in Table 3.4. The formation of some larger Co^0 nanoparticles in Co-Ru/Ti-R can be related to the presence of wider pores in the rutile support (Figure 3.2) in which the nanoparticles may grow in a less constrained environment [47-52].

The significantly greater "apparent" Co^0 particle sizes obtained from H_2 chemisorption measurements with respect to those derived from statistical TEM analysis is a clear sign for the occurrence of the SMSI effect during the H_2 reduction treatment at 400 °C, as it is well documented for cobalt (as well as other metals) supported on TiO_2 [10-15]. As a consequence, the H_2 (and CO) chemisorption capacity of metallic cobalt is suppressed by TiO_{2-x} species that migrate from the support and decorate the nanoparticles. The remarkably lower H_2 uptake observed for Co-

Ru/Ti-A hence indicates that the SMSI decoration effect occurred to a greater extent when Co is supported on anatase in comparison to rutile. This conforms with earlier studies which reported the occurrence of SMSI in Pd supported on anatase but not on rutile after reduction in H_2 at a relatively low temperature of 200 °C [53].

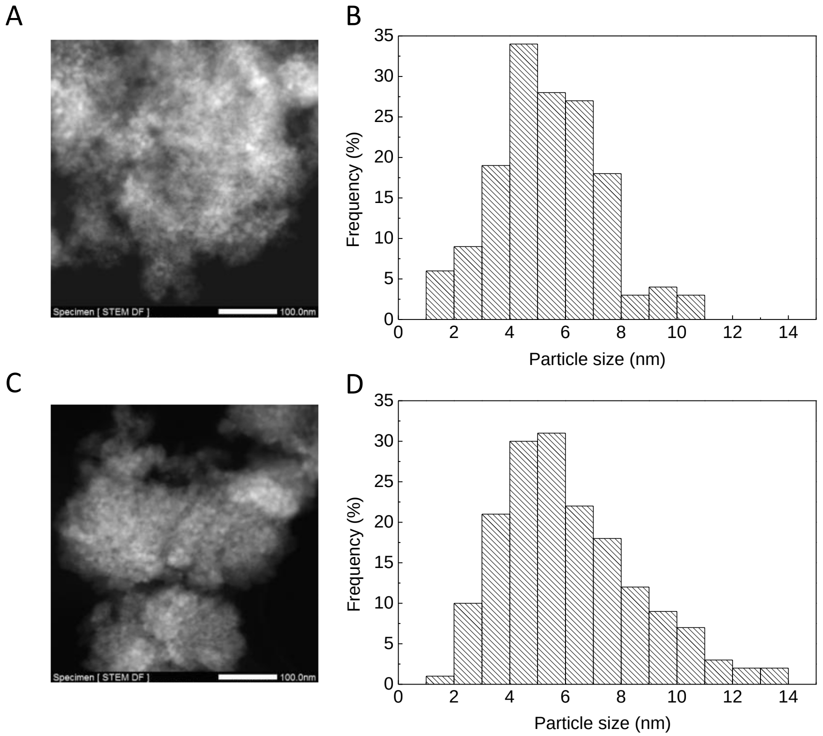

Figure 3.7. Representative HAADF-STEM images (A, C) and the derived metallic cobalt particle size histograms (B, D) for the H_2-reduced Co-Ru/Ti-A (A, B) and Co-Ru/Ti-R (C, D) catalysts. Co^0 particle sizes have been corrected by a 3 nm thick CoO outlayer.

3.3.2.3. Surface properties of cobalt

The surface properties of cobalt in the Co-Ru/Ti-A and Co-Ru/Ti-R catalysts have been studied by XPS and IR of adsorbed CO. The surface Co/Ti atomic ratio in the calcined samples as measured by XPS is 0.08 for Co-Ru/Ti-A and 0.24 for Co-Ru/Ti-R (Table 3.4), evidencing a higher dispersion of the Co_3O_4 oxide phase in the catalyst supported on rutile TiO_2. The $Co2p_{3/2}$ XP spectra for the calcined catalysts are presented in Figure 3.8a. Deconvolution of the $Co2p_{3/2}$ core level in the spectrum of the calcined Co-Ru/Ti-A sample shows two main components at 779.0 and 780.7 eV with a broad satellite structure at 786.3 eV characteristic for the spinel Co_3O_4 oxide [54]. These peaks appear shifted to higher binding energies (780.0 and 781.7 eV, with a satellite structure at 786.9 eV) in the Co-Ru/Ti-R sample. Moreover, the intensity of the satellite peak (distinctive of paramagnetic Co^{2+} species [55-57]) relative to the main peak is higher in Co-Ru/Ti-R (s/m= 0.383) than in Co-Ru/Ti-A (s/m= 0.215). Thus, both the lower BE of the $Co2p_{3/2}$ peaks and the lower s/m ratio obtained for the catalyst supported on TiO_2-anatase suggest a higher fraction of surface Co^{3+} sites (i.e. surface defects) in this catalyst relative to that supported on TiO_2-rutile. Unlike the oxidized samples, analogous $Co2p_{3/2}$ core level profiles (Figure 3.8b) and surface Co/Ti atomic ratios (ca. 0.3, Table 3.4) were observed for Co-Ru/Ti-A and Co-Ru/Ti-R after H_2 reduction. The much higher increase in the surface Co/Ti atomic ratio observed for the anatase-based catalyst upon H_2 reduction is indicative of a higher mobility of the titanium species in this polymorph. The deconvoluted spectra in Figure 3.8b show components at 777.5 eV, 779.1 eV, 780.8 eV, 783.2 eV, and 786.8 eV. The 777.5 eV peak is ascribed to metallic cobalt. In turn, the presence of the peak at 780.8 eV of oxidized cobalt species (and the corresponding shake-up satellite structures at 783.2 and 786.8 eV) evidences a less effective reduction of Co_3O_4 to Co^0 in the *in situ* H_2 treatment at 400 °C for 2 h (ca. 25% of Co^0 in both samples) in comparison to the high reduction degrees (~90%) achieved in the pre-catalysis H_2 reduction at 400 °C for 10 h. The assignment of the component at 779.1 eV exhibiting a BE intermediate between Co^0 and Co^{2+} is less straightforward. De la Peña O'Shea et al. attributed a similar component in Co/TiO_2 samples to the formation of Co-O-Ti linkages during the reduction treatment arising from the SMSI decoration effect [15]. However, the comparable relative contribution of this component in the XPS spectra of the as-reduced catalysts (Figure 3.8b) seems inconsistent with its attribution to Co-O-Ti species originated only from the SMSI effect which occurs to a much greater extent in the catalyst supported on anatase TiO_2. Thus, we suggest that the component at 779.1 eV is contributed not only from the SMSI effect but also from cobalt species at the perimeter of the nanoparticles in close contact with the TiO_2 support.

The fact that XPS, with a penetration depth of ca. 6 nm, did not reveal appreciable differences in the state of the cobalt in the as-reduced samples suggests that the SMSI effect should occur on the uppermost layers of the Co^0 nanoparticles. Therefore, we studied the properties of the surface Co^0 sites by means of a more surface-sensitive technique such as IR spectroscopy of adsorbed CO. The IR-CO spectra recorded at r.t. for increasing CO doses are presented in Figure 3.9. In the case of Co-Ru/Ti-R, IR bands at 2073, 2063, 2047, and 2014 cm^{-1} are clearly observed (Figure 3.9a), which are assigned to CO interacting with both *fcc* and *hpc* Co^0 crystal phases (bands in the 2073-2047 cm^{-1} range [58]) and with coordinatively unsaturated Co^0 sites in defects of the metal crystallites such as edges, steps, and corners (band at 2014 cm^{-1}) [22]. Differently, the reduced Co-Ru/Ti-A sample features much less intense bands at a lower frequency (2057 and 1994 cm^{-1}, Figure 3.9b) that have been associated to defected Co^0 sites in a less extended surface crystal phase or to CO interacting in a *tilted* configuration with surface species at the metal-oxide interface [59]. In our case, the low frequency of the IR bands observed in the Co-Ru/Ti-A sample coupled to their low intensity is consistent with the presence of cobalt sites partially covered by TiO_{2-x} species and, thus, with a higher extent of the SMSI effect in this catalyst, as also concluded from other characterizations previously discussed.

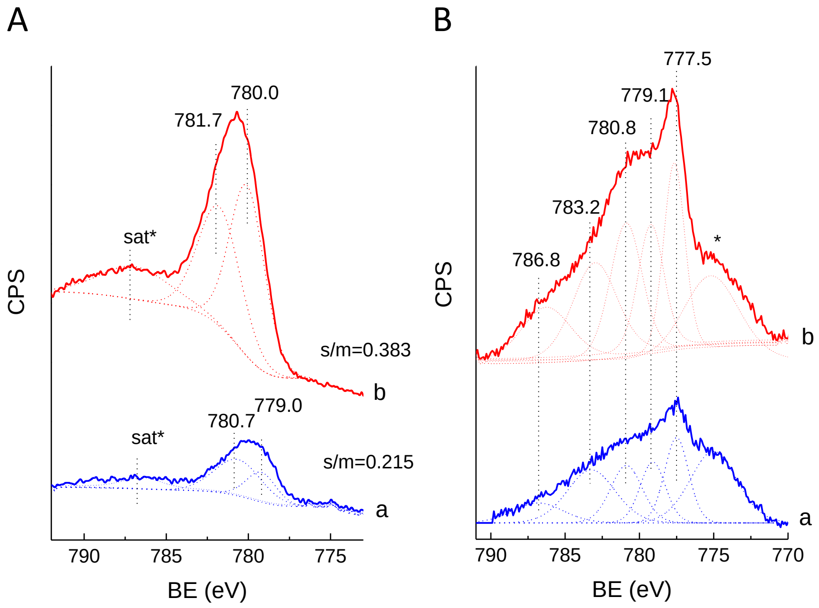

Figure 3.8. $Co2p_{3/2}$ XPS core level spectra for calcined (A) and H_2-reduced (B) catalysts: a) Co-Ru/Ti-A, b) Co-Ru/Ti-R. Sat* is the satellite peak associated to Co^{2+}.

Therefore, the different extent of the SMSI effect arising from the distinct TiO_2 crystal phase leads not only to a different concentration of exposed Co^0 sites but also to a dissimilar surface topology of the supported Co^0 nanoparticles. The implications of these effects on the catalytic performance of the Co-Ru/TiO_2 catalysts for FTS are discussed in the next section.

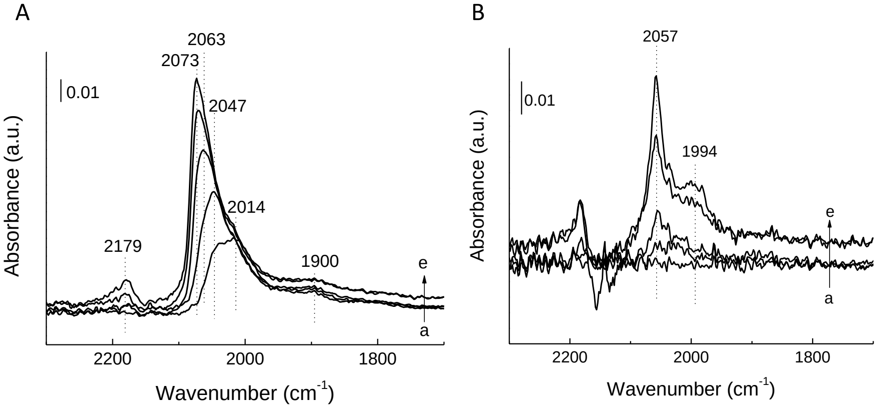

Figure 3.9. IR-CO spectra at r.t. and increasing CO doses (1.9 → 30 mbar) for H_2-reduced Co-Ru/Ti-R (A) and Co-Ru/Ti-A (B) samples.

3.3.3. Fischer-Tropsch synthesis on Co-Ru/TiO_2 catalysts

3.3.3.1. FTS activity

The initial and *pseudo*-steady state CO conversions, cobalt-time-yields (CTYs), and turnover frequencies (TOFs) of the catalysts are presented in Table 3.5. The initial activities were estimated by extrapolation of the conversion-TOS curves at TOS= 0 (not shown). Clearly, the rutile-based catalyst displays a notably higher (by a factor of ca. 1.7) initial CO conversion and CTY than that supported on anatase. In the *pseudo*-steady state, the $CTY_{rutile}/CTY_{anatase}$ ratio at similar CO conversion (10 ± 1%) increases further to 2.1 (Table 3.5). Other authors also found a higher CO hydrogenation activity for rutile-containing Co/TiO_2 catalysts in comparison to those based on pure anatase [18, 19]. The enhanced activity in the presence of rutile phase was ascribed to an increase in the concentration of metallic surface Co sites (i.e. of Co^0 surface area) upon H_2 reduction, although with conflicting explanations. Thus, while some authors attributed the increase in the amount of accessible Co^0 sites in rutile-containing catalysts to a weaker Co-support interaction that increased the reducibility of Co [17], others indicated a stronger Co-support interaction that inhibited Co aggregation during the H_2 reduction process [18]. Our characterization results clearly evidenced an easier reduction of Co oxides to metallic Co in the anatase-supported catalyst (Figure 3.6). Nonetheless, the promotion of Co with Ru ensured a high and homogeneous degree of cobalt reduction (ca. 90%) for both catalysts after the H_2 reduction treatment at 400 °C for 10 h. Taking into account the similar TEM-derived Co^0 particle sizes (5-6 nm, Table 3.4) and degrees of cobalt reduction, the higher FTS activity of Co-Ru/Ti-R with respect to Co-Ru/Ti-A can be mainly ascribed to the higher H_2 chemisorption capacity (hence, higher amount of active surface Co^0 sites) of the rutile-based sample (Table 3.4) due to a suppressed SMSI decoration effect.

Moreover, it can be observed in Table 3.5 that both catalysts exhibit similar TOFs (based on H_2 chemisorption) both at initial (ca. 9-11·10^{-2} s^{-1}) and steady state (ca. 6.5·10^{-2} s^{-1}) conditions. These values are in the range of TOFs reported for ex-nitrate Co catalysts supported on SiO_2 [7], γ-Al_2O_3 [5, 33], and TiO_2 [5, 60, 61] at equivalent reaction conditions

(220 °C, 2.0 MPa). In the cobalt-catalyzed FTS, a dependence of TOF with Co^0 particle size has been unambiguously proved for Co supported on carbon nanofibers [62] and silica [22] materials by which TOF drastically drops for metal particle sizes below 6-8 nm and remains invariable for larger particle sizes. In the case of TiO_2-supported catalysts, the effect of Co^0 particle size on TOF is less clear, probably due to the difficulty for preparing appropriate model catalysts. For instance, Delgado et al. observed an increase in TOF when decreasing the particle size from 7 to 1.7 nm in TiO_2-supported colloidal cobalt nanoparticles synthesized in water by chemical reduction with $NaBH_4$ [63]. Liu et al. also suggested a higher intrinsic activity for Co^0 nanoparticles sizing less than 10 nm when supported on β-SiC coated with TiO_2 [64]. The results from these studies appear thus to contradict the TOF-particle size trend reported for small (< 10 nm) cobalt nanoparticles supported on carbon and silica materials, and advises for further studies to elucidate Co particle size effects in TiO_2-supported catalysts. Nonetheless, the rather similar TEM-derived Co^0 particle sizes and size distributions in both Co-Ru/Ti-R and Co-Ru/Ti-A catalysts (Figure 3.7, Table 3.4) discard any significant contribution of this factor to the observed catalytic performance. Other authors also found a constant TOF of ca. 0.20 s^{-1} for Co/TiO_2 samples with different TiO_2 phase compositions, which is about twice the TOF obtained in the present work albeit at a higher reaction temperature (230 °C) [18].

Table 3.5. Initial and *pseudo*-steady state activities (SS) of Co-Ru/TiO_2 catalysts for Fischer-Tropsch synthesis (FTS). Reaction conditions: T= 220 °C, P= 2.0 MPa, H_2/CO= 2 mol/mol. Initial activities were obtained by extrapolating the CO conversion-TOS curves at TOS= 0 at constant GHSV of 11.7 $L_{syngas}/(g_{cat}\cdot h)$, while SS activities were averaged for the next 8 h of reaction after adjusting the GHSV for each catalyst so as to obtain a CO conversion of ~10%.

Catalyst	CO conversion (%)		$CTY\cdot 10^3$ $(mol_{CO}/g_{Co}/h)^a$		$TOF\cdot 10^2$ $(s^{-1})^b$	
	Initial	SS	Initial	SS	Initial	SS
Co-Ru/Ti-A	6.6	8.8	89.3	53.2	10.5	6.3
Co-Ru/Ti-R	11.0	10.9	156.8	113.5	8.9	6.5

[a] CTY= cobalt-time-yield (activity per total mass of cobalt).

[b] TOF= turnover frequency (activity per surface Co^0 sites as measured by H_2 chemisorption).

The apparently similar TOFs obtained in this work for the anatase- and rutile-supported catalysts contrasts with the significantly distinct electronic character of the Co^0 sites exposed on surface of the H_2 reduced catalysts according to the previous IR-CO results (Figure 3.9). Indeed, a different reactivity towards CO dissociation for Co^0 sites in defects such as corners, edges, and steps and in terraces of the nanoparticles has been postulated on the basis of DFT calculations [65, 66]. However, metal cobalt nanoparticles are known to experience surface reconstruction under syngas atmosphere at typical FTS temperatures that produces a change in their surface topology and hence in the type of exposed Co^0 sites [22, 62]. Therefore, we performed additional *in situ* IR experiments in order to elucidate the nature of the surface Co^0 sites in the two catalysts when exposed to syngas conversion conditions at the FTS temperature of 220 °C. The results are discussed in the following section.

3.3.3.2. In situ IR-CO under syngas reaction conditions

The IR-CO spectra at CO saturation coverage after H_2 reduction and after reaction with syngas at 220 °C for 4 h are shown in Figure 3.10. A shift of the main Co-carbonyl band towards lower frequencies is observed for both catalysts, which clearly evidences surface reconstruction of the Co^0 nanoparticles towards more open planes when exposed to syngas at FTS conditions [22]. Interestingly, the amount of surface Co^0 sites titrated by CO for the anatase-based catalyst substantially increased after syngas reaction with respect to the as-reduced state (Figure 3.10a,b). This fact reveals that the significant SMSI effect experienced by this catalyst during the reduction process was at least partially reversed during reaction with syngas. A certain recovery of the normal (non-SMSI) state has also been reported for other metals like Pt and Rh supported on TiO_2 when exposed to a CO/H_2 mixture at 275 °C [67]. According to these authors, the water produced during the syngas conversion was responsible for the observed partial reversibility of the SMSI effect [67]. As a consequence of the dynamic character of the SMSI effect, the surface state of the supported Co^0 nanoparticles under syngas conversion conditions turns similar for the two Co-Ru/TiO_2 catalysts, as indicated by the alike frequency of their main CO-Co^0 IR band (2041 and 2050 cm^{-1} for the anatase- and rutile-supported catalysts, Figure 3.10b,d). It should be noted that the anatase and rutile phases remained 100% pure without appreciable variation in the mean TiO_2 crystallite size in the corresponding catalysts after being exposed to FTS reaction at high pressure conditions (see Figure 3.S3 and Table 3.S1 in Supplementary Material).

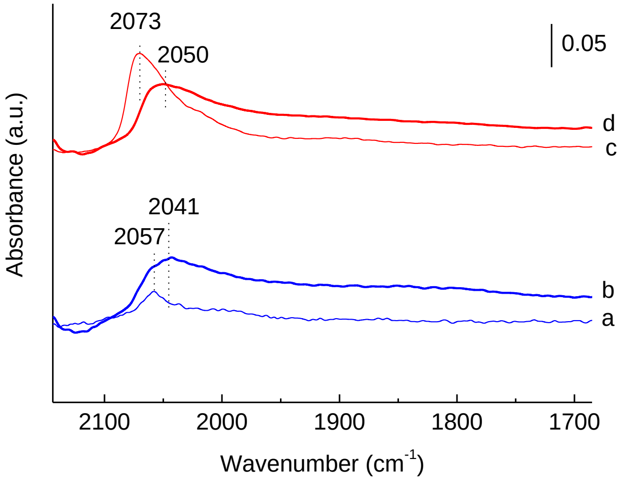

Figure 3.10. IR-CO spectra at saturation CO coverage recorded after H_2 reduction (a,c) and after *in situ* reaction with syngas at 220 °C for 4 h (b,d) for Co-Ru/Ti-A (a,b) and Co-Ru/Ti-R (c,d) catalysts.

The above at work IR results might thus account for the comparable TOFs obtained for the two catalysts (Table 3.5). However, the fact that the SMSI effect was partially reversed for the anatase-based catalyst implies a higher amount of active surface Co^0 sites under working conditions compared to that measured for the as-reduced sample and, consequently, a lower TOF than that calculated from H_2 chemisorption. Taking this into account, a dependence of TOF on the TiO_2 crystal phase may be inferred, although additional work is advised to reach a definitive conclusion on this issue.

3.3.3.3. Product distribution

As for the product distribution (Table 3.6), both catalysts show low selectivity to CO_2 (< 1 %C) as expected from the well known low activity of Co^0 for catalyzing the competing water-gas-shift reaction (WGSR). The distribution of hydrocarbons indicate, at similar CO conversion (10 ± 1%), a higher selectivity to the desired C_{5+} liquid fraction (79.1%) and lower selectivity to methane (9.5%) for Co-Ru/Ti-R in comparison to Co-Ru/Ti-A (S_{C1}= 14.9%, S_{C5+}= 62.0%).

Table 3.6. Product selectivities obtained in the steady state over Co-Ru/TiO_2 catalysts at similar CO conversion (10 ± 1%). Reaction conditions: T= 220 °C, P= 2.0 MPa, H_2/CO= 2 mol/mol, GHSV= 5.2 (for Co-Ru/Ti-A) and 8.5 (for Co-Ru/Ti-R) $L_{syngas}/g_{cat}/h$.

Catalyst	S_{CO2} (%C)	Hydrocarbons (%C)			O/P ratio[a] (wt/wt)	$2\text{-}C_4^=/1\text{-}C_4^=$ ratio
		C_1	C_2-C_4	C_{5+}		
Co-Ru/Ti-A	1.0	14.9	23.1	62.0	1.6	0.20
Co-Ru/Ti-R	0.6	9.5	11.4	79.1	2.0	0.16

[a] Olefin-to-paraffin weight ratio for the C_2-C_4 hydrocarbon fraction.

Based on surface science studies, it has been proposed that activation of CO and monomer (CH_x) formation is favored on under-coordinated Co^0 sites at step edges while chain growth requires rather large ensembles of Co^0 atoms in close-packed terraces of cobalt crystallites [68]. Considering this, the SMSI decoration effect is expected to reduce the size of the surface ensembles at the terraces and, consequently, to disfavor chain growth processes. Thus, the more pronounced SMSI effect found for the anatase-based catalyst might account, in principle, for its lower C_{5+} selectivity in comparison to the rutile-based one. However, our at work IR-CO results clearly evidenced the partial reversibility of the SMSI effect by which most of the decorated Co^0 sites in CoRu/Ti-A were uncovered under syngas reaction conditions. In turn, the IR-CO results also indicated an analogous electronic nature of the surface Co^0 atoms (i.e. similar frequency for the CO-Co^0 bands) in both catalysts under reaction conditions. Therefore, a clear impact of the SMSI effect on product selectivity, although not discarded, cannot be definitively concluded from our study.

On the other hand, mass transfer limitations are known to significantly impact the selectivity of Co catalysts under realistic FTS conditions where the pores are filled with liquid hydrocarbons. This effect is particularly relevant for catalysts with relatively small pores and pellet sizes typically applied for fixed bed reactor operations [69]. Under this situation, the H_2/CO ratio around the Co particles located within the pores increases with respect to that in the gas phase favoring the hydrogenation of intermediates and shifting the product distribution towards lighter hydrocarbons. As observed in Table 3.6, the olefin-to-paraffin (O/P) weight ratio in the analyzed C_2-C_4 fraction is 1.6 for Co-Ru/Ti-A and 2.0 for Co-Ru/Ti-R. Thus, the more paraffinic nature of the hydrocarbons in the anatase-based catalyst points towards a higher extent of hydrogenation of the primary α-olefins that aligns with a more impeded diffusion of CO in this catalyst than in the rutile-based sample. Accordingly, the higher C_{5+} selectivity of the Co-Ru/Ti-R sample is likely ascribed to an enhanced mass transfer rate for CO in the larger pores of the rutile TiO_2 support. Besides secondary hydrogenation, the primary α-olefins may also undergo double-bond and skeletal isomerizations during FTS. Although the relevance of α-olefin re-adsorption on the ultimate product selectivity remains controversial, α-olefin isomerization reactions would prevent their participation in chain growth processes and, hence, lower the selectivity to long-chain hydrocarbons. In our case, the analysis of the C_4 fraction revealed the absence of isobutane and isobutene products, indicating that branching isomerization did not occur on the Co-Ru/TiO_2 catalysts at the investigated conditions. Differently, the formation of *cis-* and *trans-*2-butene was observed on both catalysts, though in different extents. Hence, 2-butene/1-butene ratios of 0.20 and 0.16 were obtained for, respectively, the anatase- and rutile-based catalysts (Table 3.6), indicating that olefin double-bond migration is more favored on the former polymorph. Recently, by using monolayer-type model Co catalysts we have demonstrated the significance of the surface acid-base character of the oxide support in determining the extent of secondary α-olefin reactions during FTS and, consequently, the final product selectivity [5]. Despite large variations in surface acidity are not expected for the different TiO_2 polymorphs, anatase has been experimentally proved to contain stronger surface Lewis acid sites (associated to coordinatively unsaturated Ti^{4+} ions) than rutile [70, 71]. Therefore, it is sensible that the higher surface acidity of TiO_2 anatase accounts for the favored α-olefin double-bond isomerization observed for Co-Ru/Ti-A, and that this may contribute to the lower C_{5+} selectivity displayed by this catalyst (Table 3.6).

3.4. Conclusions

The following main conclusions can be withdrawn from the present study:

1) Ru-promoted Co catalysts (10 wt% Co-0.5 wt% Ru nominal loadings) supported on 100% pure anatase (CoRu/Ti-A) and rutile (CoRu/Ti-R) TiO_2 polymorphs experienced the SMSI decoration effect during the H_2 reduction treatment at 400 °C performed prior to catalysis.

2) The extent of the SMSI effect was much more pronounced for CoRu/Ti-A leading to much lower H_2 and CO chemisorption capacities for the supported Co^0 nanoparticles (NPs) compared to CoRu/Ti-R.

3) The higher extent of the SMSI effect in CoRu/Ti-A resulted in a decreased activity (by about 50%) for Fischer-Tropsch synthesis (FTS) with respect to CoRu/Ti-R in terms of both CO conversion and cobalt-time-yield (CTY) at 220 °C, 2.0 MPa, and H_2/CO= 2.

4) Conversely, the two catalysts showed comparable TOFs (based on H_2 chemisorption) at both initial ($9\text{-}10\cdot10^{-2}$ s^{-1}) and *pseudo*-steady state (ca. $6.5\cdot10^{-2}$ s^{-1}) conditions.

5) A similar extent of surface reconstruction (towards more defected planes) leading to an alike electronic nature of the accessible Co^0 sites for both the anatase- and rutile-supported catalysts was found by *in situ* IR-CO spectroscopy after exposing the reduced samples to syngas flow at 220 °C (0.1 MPa) for 4 h.

6) The SMSI effect was seen to be partially reversible under syngas reaction conditions significantly increasing the amount of surface Co^0 sites available for reaction in the anatase-based catalyst. This observation questions TOFs calculated from H_2 chemisorption in TiO_2-supported catalysts and points towards a dependence of TOF on the TiO_2 polymorph, advising for further studies to definitively elucidate this issue.

7) At constant CO conversion the rutile-based catalyst displayed higher C_{5+} selectivity than that based on anatase, which was ascribed to an

enhanced mass transfer (due to its larger pores) as well as to a lower surface acidity (inhibiting α-olefins double bond migration) of rutile relative to anatase. A clear impact of the SMSI effect on product selectivity, although not discarded, could not be definitively concluded from our work.

Acknowledgments

Financial support by the MINECO of Spain through the Severo Ochoa project (SEV 2012-0267) is gratefully acknowledged. The authors also thank the Microscopy Service of the Universitat Politècnica de València for its assistance in microscopy characterization. F. Bertella (Science without Frontiers – Process no.13705/13-0) thanks CAPES for a predoctoral fellowship.

3.5. References

[1] A.Y. Khodakov, W. Chu, P. Fongarland, Chem. Rev. 107 (2007) 1692-1744.
[2] M.E. Dry, J. Chem. Technol. Biotechnol. 77 (2002) 43-50.
[3] R. Oukaci, A.H. Singleton, J.G. Goodwin Jr., Appl. Catal. A: Gen. 186 (1999) 129-144.
[4] A.Y. Khodakov, Catal. Today 144 (2009) 251-257.
[5] G. Prieto, M.I.S. De Mello, P. Concepción, R. Murciano, S.B.C. Pergher, A. Martínez, ACS Catal. 5 (2015) 3323-3335.
[6] E. Iglesia, S.L. Soled, R.A. Fiato, J. Catal. 137 (1992) 212-224.
[7] G. Prieto, P. Concepción, R. Murciano, A. Martínez, J. Catal. 302 (2013) 37-48.
[8] R.C. Reuel, C.H. Bartholomew, J. Catal. 85 (1984) 78-88.
[9] E. Iglesia, S.L. Soled, R.A. Fiato, G.H. Via, J. Catal. 143 (1993) 345-368.
[10] S.J. Tauster, S.C. Fung, R.L. Garten, J. Am. Chem. Soc. 100 (1978) 170-175.
[11] J. Van De Loosdrecht, A.M. Van Der Kraan, A.J. Van Dillen, J.W. Geus, J. Catal. 170 (1997) 217-226.
[12] A. Dandekar, M.A. Vannice, J. Catal. 183 (1999) 344-354.
[13] J.C. Colmenares, A. Magdziarz, M.A. Aramendia, A. Marinas, J.M. Marinas, F.J. Urbano, J.A. Navio, Catal, Commun. 16 (2011) 1-6.
[14] S.J. Tauster, S.C. Fung, R.T.K. Baker, J.A. Horsley, Science 211 (1981) 1121-1125.
[15] V.A. De La Peña O'Shea, M. Consuelo Álvarez Galván, A.E. Platero Prats, J.M. Campos-Martin, J.L.G. Fierro, Chem. Commun. 47 (2011) 7131-7133.
[16] B. Jongsomjit, T. Wongsalee, P. Praserthdam, Catal. Commun. 6 (2005) 705-710.
[17] B. Jongsomjit, C. Sakdamnuson, P. Praserthdam, Mater. Chem. Phys. 89 (2005) 395-401.
[18] K. Shimura, T. Miyazawa, T. Hanaoka, S. Hirata, Appl. Catal. A: Gen. 460-461 (2013) 8-14.
[19] K. Shimura, T. Miyazawa, T. Hanaoka, S. Hirata, Catal. Today, 232 (2014) 2-10.
[20] M. Andersson, A. Kiselev, L. Österlund, A.E.C. Palmqvist, J. Phys. Chem. C 111 (2007) 6789-6797.
[21] R.C. Reuel, C.H. Bartholomew, J. Catal. 85 (1984) 63-77.
[22] G. Prieto, A. Martínez, P. Concepción, R. Moreno-Tost, J. Catal. 266 (2009) 129-144.

[23] M. Wu, J. Long, A. Huang, Y. Luo, S. Feng, R. Xu, Langmuir 15 (1999) 8822-8825.

[24] D. Zhang, L. Qi, J. Ma, H. Cheng, J. Mater. Chem. 12 (2002) 3677-3680.

[25] M. Wu, G. Lin, D. Chen, G. Wang, D. He, S. Feng, R. Xu, Chem. Mater. 14 (2002) 1974-1980.

[26] C. Sanchez, J. Livage, M. Henry, F. Babonneau, J. Non-Crystal. Solids 100 (1988) 65-76.

[27] M. Thommes, K. Kaneko, A.V. Neimark, J.P. Olivier, F. Rodriguez-Reinoso, J. Rouquerol, K.S.W. Sing, Pure Appl. Chem. 87 (2015) 1051-1069.

[28] M. Andersson, L. Österlund, S. Ljungström, A. Palmqvist, J. Phys. Chem. B 106 (2002) 10674-10679.

[29] Q. Chen, C. Chen, H. Ji, W. Ma, J. Zhao, RSC Adv. 3 (2013) 17559-17566.

[30] Y. Wang, L. Zhang, K. Deng, X. Chen, Z. Zou, J. Phys. Chem. C 111 (2007) 2709-2714.

[31] T. Lopez, L. Herrera, R. Gomez, W. Zou, K. Robinson, R.D. Gonzalez, J. Catal. 136 (1992) 621-625.

[32] J.S. Girardon, E. Quinet, A. Griboval-Constant, P.A. Chernavskii, L. Gengembre, A.Y. Khodakov, J. Catal. 248 (2007) 143-157.

[33] A. Martínez, G. Prieto, J. Rollán, J. Catal. 263 (2009) 292-305.

[34] B. Jongsomjit, C. Sakdamnuson, J.G. Goodwin Jr, P. Praserthdam, Catal. Lett. 94 (2004) 209-215.

[35] I. Florea, Y. Liu, O. Ersen, C. Meny, C. Pham-Huu, ChemCatChem 5 (2013) 2610-2620.

[36] D. Schanke, S. Vada, E.A. Blekkan, A.M. Hilmen, A. Hoff, A. Holmen, J. Catal. 156 (1995) 85-95.

[37] Y. Li, Y. Fan, H. Yang, B. Xu, L. Feng, M. Yang, Y. Chen, Chem. Phys. Lett. 372 (2003) 160-165.

[38] Q. Cai, J. Li, Catal. Commun. 9 (2008) 2003-2006.

[39] K.M. Cook, S. Poudyal, J.T. Miller, C.H. Bartholomew, W.C. Hecker, Appl. Catal. A: Gen. 449 (2012) 69-80.

[40] T.O. Eschemann, J. Oenema, K.P. De Jong, Catal. Today 261 (2016) 60-66.

[41] G. Jacobs, T.K. Das, Y. Zhang, J. Li, G. Racoillet, B.H. Davis, App. Catal. A: Gen. 233 (2002) 263-281.

[42] P. Li, J. Liu, N. Nag, P.A. Crozier, App. Catal. A: Gen. 307 (2006) 212-221.

[43] J.Y. Park, Y.J. Lee, P.R. Karandikar, K.W. Jun, J.W. Bae, K.S. Ha, J. Mol. Catal. A: Chem. 344 (2011) 153-160.

[44] G. Melaet, W.T. Ralston, C.S. Li, S. Alayoglu, K. An, N. Musselwhite, B. Kalkan, G.A. Somorjai, J. Am. Chem. Soc. 136 (2014) 2260-2263.
[45] A.M. Saib, D.J. Moodley, I.M. Ciobîc, M.M. Hauman, B.H. Sigwebela, C.J. Weststrate, J.W. Niemantsverdriet, J. Van De Loosdrecht, Catal. Today 154 (2010) 271-282.
[46] K.H. Cats, I.D. Gonzalez-Jimenez, Y. Liu, J. Nelson, D. Van Campen, F. Meirer, A.M.J. Van Der Eerden, F.M.F. De Groot, J.C. Andrews, B.M. Weckhuysen, Chem. Commun. 49 (2013) 4622-4624.
[47] S. Storsæter, B. Tøtdal, J.C. Walmsley, B.S. Tanem, A. Holmen, J. Catal. 236 (2005) 139-152.
[48] Ø. Borg, S. Eri, E.A. Blekkan, S. Storsæter, H. Wigum, E. Rytter, A. Holmen, J. Catal. 248 (2007) 89-100.
[49] A.Y. Khodakov, A. Griboval-Constant, R. Bechara, V.L. Zholobenko, J. Catal. 206 (2002) 230-241.
[50] Y. Liu, K. Fang, J. Chen, Y. Sun, Green Chem., 9 (2007) 611-615.
[51] D. Song, J. Li, J. Mol. Catal. A: Chem. 247 (2006) 206-212.
[52] H. Xiong, Y. Zhang, K. Liew, J. Li, J. Mol. Catal. A: Chem. 295 (2008) 68-76.
[53] Y. Li, B. Xu, Y. Fan, N. Feng, A. Qiu, J.M.J. He, H. Yang, Y. Chen, J. Mol. Catal. A: Chem. 216 (2004) 107-114.
[54] D.G. Castner, P.R. Watson, I.Y. Chan, J. Phys. Chem. 93 (1989) 3188-3194.
[55] I. Jirka, J. Phys. Chem. B 105 (2001) 1140-1148.
[56] J.G. Dillard, M.H. Koppelman, J. Coll. Interf. Sci. 87 (1982) 46-55.
[57] Z. Zsoldos, L. Guczi, J. Phys. Chem. 96 (1992) 9393-9400.
[58] D. Song, J. Li, Q. Cai, J. Phys. Chem. C 111 (2007) 18970-18979.
[59] P. Concepción, A. Corma, J. Silvestre-Albero, V. Franco, J.Y. Chane-Ching, J. Am. Chem. Soc. 126 (2004) 5523-5532.
[60] T.O. Eschemann, K.P. De Jong, ACS Catal. 5 (2015) 3181-3188.
[61] T.O. Eschemann, J.H. Bitter, K.P. De Jong, Catal. Today 228 (2014) 89-95.
[62] G.L. Bezemer, J.H. Bitter, H.P.C.E. Kuipers, H. Oosterbeek, J.E. Holewijn, X. Xu, F. Kapteijn, A.J. Van Diilen, K.P. De Jong, J. Am. Chem. Soc. 128 (2006) 3956-3964.
[63] J.A. Delgado, C. Claver, S. Castillón, D. Curulla-Ferré, V.V. Ordomsky, C. Godard, Appl. Catal. A: Gen. 513 (2016) 39-46.
[64] Y. Liu, I. Florea, O. Ersen, C. Pham-Huu, C. Meny, Chem. Commun. 51 (2015) 145-148.
[65] S. Shetty, A.P.J. Jansen, R.A. Van Santen, J. Am. Chem. Soc. 131 (2009) 12874-12875.

[66] R.A. Van Santen, M.M. Ghouri, S. Shetty, E.M.H. Hensen, Catal. Sci. and Technol. 1 (2011) 891-911.
[67] J.B.F. Anderson, R. Burch, J.A. Cairns, Appl. Catal. 21 (1986) 179-185.
[68] C.J. Weststrate, P. van Helden, J.W. Niemantsverdriet, Catal. Today, 2016, doi: 10.1016/j.cattod.2016.04.004.
[69] E. Iglesia, Appl. Catal. A: Gen. 161 (1997) 59-78.
[70] H. Li, M. Vrinat, G. Berhault, D. Li, H. Nie, P. Afanasiev, Mater. Res. Bull. 48 (2013) 3374-3382.
[71] M. Addamo, M. Del Arco, M. Bellardita, D. Carriazo, A. Di Paola, E. García-López, G. Marcì, C. Martín, L. Palmisano, V. Rives, Res. Chem. Interm. 33 (2007) 465-479.

3.6. Supporting Information

3.6.1. Raman spectroscopy of calcined Co-Ru/TiO_2 catalysts

3.6.1.1. Experimental

Raman spectra of calcined samples were acquired in a Renishaw in Via Raman spectrometer equipped with a Leica DMLM microscope. A 50x objective of 1 mm optical length was used to focus the depolarized laser beam onto a 3–5 µm spot on the sample surface and collect the backscattered light. As an excitation source a 514 nm HPNIR diode laser was used and the laser power at the sample was 25 mW. The Raman scattering was collected in a static-scan mode in the 100–800 cm^{-1} spectral region with resolution > 4 cm^{-1}.

3.6.1.2. Discussion of Raman results

The Raman spectra for the calcined Co-Ru/Ti-A and Co-Ru/Ti-R catalysts are presented, along with those of the respective TiO_2 supports, in Figure 3.S1.

The calcined Co-Ru/Ti-A sample (Figure 3.S1A-b) displays Raman bands at 147, 197, 399, 515, and 639 cm^{-1} characteristic of the anatase TiO_2 polymorph (Figure 3.S1A-a) [1], along with active bands at 481, 523, and 690 cm^{-1} assigned to the spinel Co_3O_4 phase [2]. As for Co-Ru/Ti-R (Figure 3.S1B-b), the characteristic Raman bands of the rutile phase at 235, 447, and 611 cm^{-1} (Figure 3.S1B-a) [1] as well as those of Co_3O_4 (481, 523, and 690 cm^{-1}) are clearly identified. No Raman bands related to the $CoTiO_3$ mixed oxide, for which the strongest and most representative Raman active band peaks at 696 cm-1 [3], are evidenced in none of the calcined catalysts.

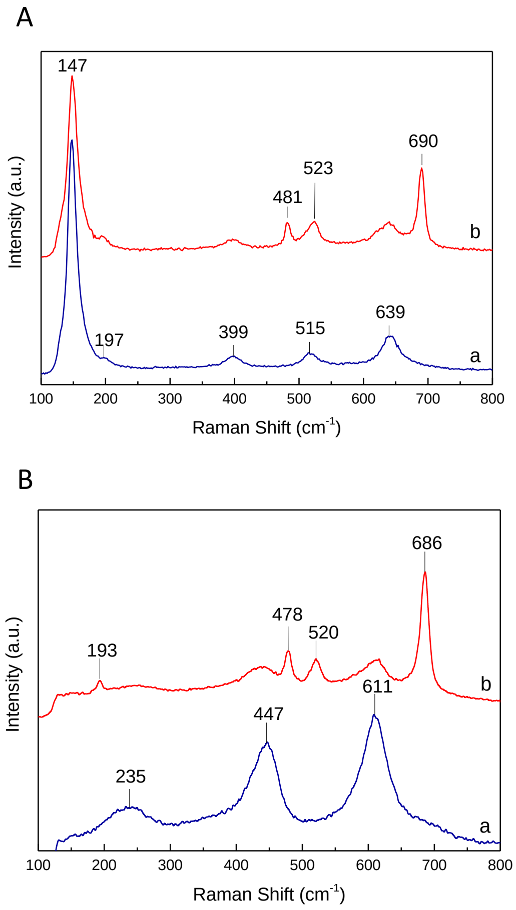

Figure 3.S1. Raman spectra of the TiO_2 supports and corresponding CoRu/TiO_2 catalysts: A) Ti-A (a) and Co-Ru/Ti-A (b), and B) Ti-R (a) and Co-Ru/Ti-R (b).

References

[1] J. Zhang, M. Li, Z. Feng, J. Chen, C. Li, J. Phys. Chem. B 110 (2006) 927.
[2] V.G. Hadjiev, M.N. Iliev, I. V Vergilov, J. Phys. C: Solid State Phys. 21 (1988) L199.
[3] M.A. Ehsan, R. Naeem, H. Khaledi, M. Sohail, A. Hakeem Saeed, M. Mazhar, Dalton Trans. 45 (2016) 10222.

3.6.2. Crystalline phases in the H_2-reduced catalysts

3.6.2.1. Experimental

In situ H_2-XRD measurements were performed to assess the crystalline phases present in the as-reduced catalysts. The measurements were performed in a Panalytical X'Pert PRO diffractometer using monochromatized CuKα radiation and operated at 45 kV and 40 mA. The samples were loaded in a XRK-900 Anton Paar cell and flushed with a gas stream comprising 5 vol% H_2 diluted in N_2. In these experiments, the X-ray diffractograms were first recorded at 30 °C (corresponding to the calcined state of the catalysts) and then the temperature was raised to 400 °C under the diluted H_2 flow. Once the reduction temperature was reached, patterns were recorded every hour until a constant diffractogram was observed (typically after 7 h).

3.6.2.2. XRD patterns of as-reduced catalysts

The XRD patterns of the catalysts after *in situ* reduction in H_2 at 400 °C for 7 h are shown in Figure 3.S2. A clear identification of the crystalline cobalt phases present in the reduced catalysts is not feasible due to overlapping with the intense TiO_2 peaks. Nevertheless, weak peaks at 44.2° and 47.5° (2θ) corresponding to the most intense reflections of, respectively, fcc-Co^0 (JCPDS 00-15-0806) and hcp-Co^0 (JCPDS 00-005-0727) crystalline phases are evidenced in both catalysts. Moreover, the reflections associated to the spinel Co_3O_4 oxide present in the calcined materials (Figure 3.4) are not longer evidenced in the H_2-reduced samples, signing for a high degree of $Co_3O_4 \rightarrow Co^0$ reduction, in agreement with the obtained H_2-TPR profiles. In turn, no crystalline phases related to Co-Ti alloys or mixed oxides are perceived for any of the as-reduced catalysts.

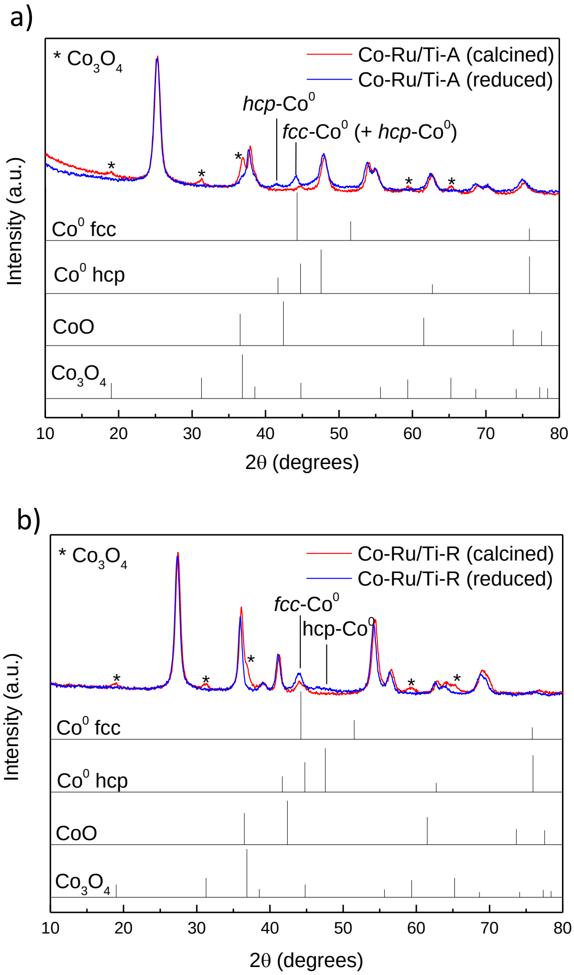

Figure 3.S2. XRD patterns recorded after *in situ* reduction for 7 h in diluted H_2 flow (5 vol% H_2 in N_2) at 400 °C for CoRu/Ti-A (a) and CoRu/Ti-R (b) catalysts. For each catalyst, the XRD pattern recorded at 30 °C is also included for comparative purposes as representative of the as-calcined state. The patterns of reference cobalt compounds are shown for an easier identification of the crystalline phases.

3.6.3. TiO_2 phases in spent catalysts

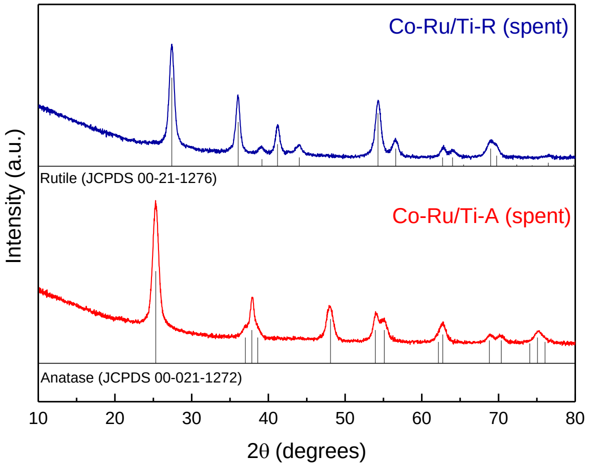

Figure 3.S3. XRD patterns for the Co-Ru/TiO_2 catalysts after being used in FTS for ca. 15 h at 220 °C, 2.0 MPa, and $H_2/CO= 2$. Diffraction lines for pure anatase (JCPDS 00-021-1272) and rutile (JCPDS 00-021-1276) phases are included to facilitate identification of TiO_2 phases.

Table 3.S1. Mean size of TiO_2 crystallites in the Co-Ru/TiO_2 catalysts before (as-calcined) and after FTS reaction (conditions as in Figure 3.S3) calculated by the Scherrer equation applied to the most intense reflections for anatase ($2\theta= 25.28°$) and rutile ($2\theta= 27.44°$) phases.

Catalyst	Mean TiO_2 crystallite size (nm)	
	Before reaction	After reaction
CoRu/Ti-A	11.2	11.5
CoRu/Ti-R	12.0	13.2

These data show negligible variation in the average TiO_2 crystallite size (within ± 10% error) during the FTS catalytic tests for the studied catalysts.

CHAPTER 4

THE IMPACT OF SUPPORT SURFACE AREA ON THE SMSI DECORATION EFFECT AND CATALYTIC PERFORMANCE FOR FISCHER-TROPSCH SYNTHESIS OF CO-RU/TIO$_2$-ANATASE CATALYSTS

In Chapter 3, the influence of titania polymorph (anatase vs. rutile) was studied. Since the anatase crystalline phase was shown to be more prone to undergo the SMSI effect, in this chapter the influence of the textural properties of TiO_2-anatase support of Co-Ru/TiO_2 catalysts has been investigated to shed light on the SMSI effect and its repercussion on activity and selectivity for the Fischer-Tropsch synthesis. The results are presented in the form of scientific article:

The impact of support surface area on the SMSI decoration effect and catalytic performance for Fischer-Tropsch synthesis of Co-Ru/TiO_2-anatase catalysts

Francine Bertella, Patricia Concepción, Agustín Martínez.

Reproduced with permission from *Catalysis Today 296 (2017) 170-180*.

https://doi.org/10.1016/j.cattod.2017.05.001

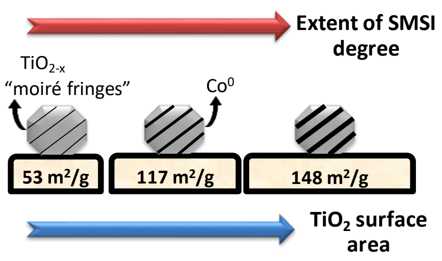

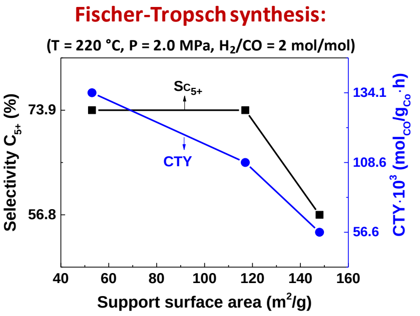

4.1. Introduction

Cobalt catalysts supported on porous metal oxides (e.g. SiO_2, Al_2O_3, and TiO_2) are commercially employed in Fischer-Tropsch synthesis (FTS) processes to produce high-performance clean-burning fuels, particularly diesel, from fossil carbon sources alternative to oil such as natural gas and coal as well as, more recently, from renewable biomass via the intermediate synthesis of *syngas* (mixture of CO and H_2) [1,2]. The catalytic performance of Co-based FTS catalysts under industrially-relevant conditions is determined by the combination of multiple parameters among which the dispersion (i.e. particle size) and distribution of the metallic cobalt nanoparticles on the support surface [3-5], the texture, morphology, and chemical nature of the support [6-8], the presence of metal and/or metal oxide promoters [9-12], and the so-called thermal history (the conditions of the thermal treatments given to the catalyst prior to FTS) [13] are probably the most influencing ones. A strong dependence of the intrinsic activity (turnover frequency or TOF) for FTS on Co^0 particle size by which the TOF drastically decreases below a critical size of 6-9 nm (depending on catalyst and reaction conditions) has been unequivocally reported for model cobalt catalysts supported on weakly interacting materials, favoring the reduction of small cobalt nanoparticles, such as carbon nanofibers [3] and surface-silylated pure silica ITQ-2 zeolite [4]. For more interacting supports like Al_2O_3 and TiO_2, however, discrepancies regarding the Co^0 particle size-TOF dependence can be the found in earlier works [14-16] which probably arise from to the difficulty to prepare appropriate model catalysts with narrow cobalt particle size distribution and high reducibility in the size range of interest (< 10 nm). On the other hand, the porous structure of the support is known to affect the FTS performance by influencing the metal dispersion [6] and the transport rate of CO and products (i.e. α-olefins) through the catalyst pores under industrially-relevant conditions [17].

Among the main supports employed in the preparation of industrial Co-based catalysts, TiO_2 is particularly attractive from the viewpoint of both activity and selectivity to the targeted liquid (C_{5+}) hydrocarbons [18]. Nonetheless, in spite of their obvious interest, TiO_2-supported cobalt catalysts have been less investigated than those comprising SiO_2 or Al_2O_3. This can be probably ascribed to a higher complexity of the Co/TiO_2 systems that originates from the particular features of titania exhibiting different crystallographic polymorphs (anatase, rutile, brookite) and the well known strong metal-support interaction (SMSI) effect by which partially reduced TiO_x species generated during the reduction treatment migrate and decorate the surface of the supported metal nanoparticles inhibiting their CO and H_2 chemisorption capacity. In a recent study, we demonstrated that Ru-promoted cobalt catalysts supported on pure TiO_2-anatase experienced a more pronounced SMSI effect and, in consequence, a decreased cobalt-mass-based activity during FTS in comparison to those supported on pure TiO_2-rutile [19]. Besides crystalline phase and phase composition, other TiO_2 properties might also affect the SMSI effect and, hence, the catalytic behavior of TiO_2-supported catalysts. To this respect, Abdel-Mageed et al. [20] have recently observed an enhanced SMSI decoration effect when increasing the surface area of TiO_2 in Ru/TiO_2 catalysts. The decrease in the concentration of surface metallic Ru sites resulting from the more pronounced SMSI effect overcompensated the higher metal dispersion of the catalyts based on TiO_2 with higher surface areas producing a decrease in the overall catalytic activity for selective CO methanation in CO_2-rich reformate gases [20]. Similarly, Bonne et al. [21] observed a higher SMSI effect in Pt/TiO_2-SiO_2 nanocomposites comprising small TiO_2 crystallites compared to a conventional Pt/TiO_2 (P25) catalyst, and proposed tuning the TiO_2 crystal size (by varying the TiO_2 content in the nanocomposites) as an effective means of controlling the SMSI effect. However, none of these works provided a rationale for the observed variation in the SMSI extent with the crystallite size (i.e. surface area) of the TiO_2 carrier.

According to the previous discussions, we here investigated the impact of the surface area of 100% pure TiO_2-anatase supports on the extent of SMSI and the catalytic performance of Ru-promoted Co/TiO_2 catalysts for Fischer-Tropsch synthesis at typical reaction conditions of 220 °C, 2.0 MPa, and H_2/CO molar ratio of 2.

4.2. Experimental

4.2.1. Synthesis of TiO_2-anatase supports

Pure TiO_2-anatase supports with different surface areas were synthesized by a hydrothermal method using titanium(IV) *n*-butoxide (99+%, Alfa Aesar) as titanium source and acetic acid (99.5%, Aldrich). Briefly, titanium(IV) *n*-butoxide was added dropwise to an acetic acid solution under magnetic stirring at room temperature. Subsequently, the mixture was introduced into a Teflon-lined stainless steel autoclave and hydrothermally treated at selected temperatures for 24 h. Afterwards, the solid was recovered by centrifugation, washed 5 times with ethanol in a process involving redispersion and centrifugation, dried at 60°C overnight, and finally calcined. In this way, three TiO_2-anatase samples with surface areas ranging from 53 to 148 m^2/g were obtained by varying the concentration of the acetic acid solution, the synthesis temperature, and the calcination conditions, as summarized in Table 4.1. The TiO_2-anatase supports with high, medium, and low surface area were labeled as Ti-H, Ti-M, and Ti-L, respectively. As seen in Table 4.1, samples with lower surface area were obtained by using higher acetic acid concentrations, higher synthesis temperatures, and by applying higher temperatures, static conditions, and higher heating rates during the final calcination step.

Table 4.1. Nomenclature and conditions employed for the hydrothermal synthesis of pure TiO_2-anatase with different specific surface areas.

	Acetic acid		Synthesis	Calcination		
Support	Conc. (mol/L)	Vol. (mL)	temp. (°C)	T (°C)	Air condition[a]	Heating rate (°C/min)
Ti-H	1.5	28	120	400	Air flow	1
Ti-M	10	20	150	400	Static air[a]	5
Ti-L	Pure	20	200	500	Static air[a]	5

[a] Calcined in a muffle furnace.

4.2.2. Synthesis of Co-Ru/TiO_2 catalysts

Co-Ru/TiO_2 catalysts were prepared by incipient wetness co-impregnation of the calcined TiO_2 supports with an aqueous solution containing the required amounts of $Co(NO_3)_2.6H_2O$ (Aldrich) and ruthenium(III) nitrosyl nitrate (Aldrich) precursors to achieve a nominal composition of 10 wt% Co and 0.5 wt% Ru. Next, the catalysts were dried at 100 °C overnight and calcined in flowing air at 300 °C for 3 h. The catalysts supported on high, medium, and low surface area TiO_2-anatase were labeled as Co-Ru/Ti-H, Co-Ru/Ti-M, and Co-Ru/Ti-L, respectively.

4.2.3. Characterization techniques

Chemical compositions were obtained by Inductively Coupled Plasma-Optical Emission Spectrometry (ICP-OES) in a Varian 715-ES spectrometer after digestion of the solids in an acid mixture of HNO_3:HF:HCl (1:1:3 volume ratio).

X-ray powder diffraction (XRD) patterns were recorded on a Philips X'Pert diffractometer using monochromatized Cu-K_α radiation (λ = 0.15406 nm). The average diameter of the TiO_2 crystallites were obtained by line broadening analysis applied to the most intense (1 0 1) reflection of anatase (2θ = 25.28°) using the Scherrer's equation and assuming a shape factor k = 0.9.

The N_2 adsorption isotherms were measured at -196 °C in a Micromeritics ASAP-2420 equipment after degassing the samples at 300 °C under vacuum overnight. Specific surface areas were obtained following the Brunauer-Emmett-Teller (BET) method, total pore volumes were determined at a relative pressure of 0.98, and pore size distributions were derived by applying the Barrett-Joyner-Halenda (BJH) approach to the adsorption branch of the isotherms.

The morphology of the samples were studied by field emission scanning electron microscopy (FESEM) using a ZEISS Ultra-55 microscope.

Raman spectra for the pristine high surface area (Ti-H) and low surface area (Ti-L) anatase-TiO_2 samples and after reduction in flowing H_2 at 400°C for 10 h were acquired in a Renishaw in Via Raman spectrometer equipped with a Leica DMLM microscope. A 50x objective of 1 mm optical length was used to focus the depolarized laser beam onto a 3–5 µm spot on the sample surface and collect the backscattered light. As an excitation source a 514 nm HPNIR diode laser was used and the laser power at the sample was 25 mW. The Raman scattering was collected in a static-scan mode in the 100-800 cm^{-1} spectral region with resolution > 4 cm^{-1}.

Reduction profiles for the Co-Ru/TiO_2 catalysts were measured by hydrogen temperature-programmed reduction (H_2-TPR) in a Micromeritics Autochem 2910 device. The samples (ca. 100 mg) were flushed with an Ar flow at room temperature for 30 min, and then the gas was switched to a gas mixture of H_2 diluted (10 vol%) in Ar. Next, the temperature was linearly increased up to 900 °C at a heating rate of 10 °C/min while monitoring the H_2 consumption in a thermal conductivity detector (TCD) pre-calibrated using the reduction of a standard CuO sample as reference. Water generated during the reduction was retained in a 2-propanol/$N_{2(liq)}$ trap located downstream the analyzer to ensure that only H_2 is detected in the TCD. Additional experiments were performed in the same equipment in order to determine the degree of cobalt reduction (DR). To this purpose, the catalysts were first reduced in pure flowing H_2 at 400 °C for 10 h (the same conditions applied prior to the FTS reactions). Then, the gas was switched to the diluted H_2 stream (10 vol% H_2 in Ar) and the temperature increased from 400 °C to 800 °C at a rate of 10 °C/min while registering the signal of H_2 in the TCD. DR values were calculated assuming that the H_2 consumed in this last step corresponds to the reduction of cobalt oxide (in the form of CoO) remaining after the 400 °C reduction treatment.

Cobalt dispersions were determined by H_2 chemisorption at 100 °C in an ASAP 2010C Micromeritics equipment by extrapolating the total gas uptakes in the adsorption isotherms at zero pressure [18]. Prior to the measurements the samples (about 300 mg) were reduced under flowing pure H_2 at 400 °C for 10 h. Metal particle sizes ($d(Co^0)_{H2}$) were estimated from the total amount of chemisorbed H_2, assuming an adsorption stoichiometry H/Co of 1, the Co content (from ICP-OES), the degree of cobalt reduction, and considering spherical particle geometry with a surface atomic density of 14.6 atoms/nm^2.

Cobalt particle sizes were also determined by transmission electron microscopy in a JEOL-JEM-2100 F microscope operating at 200 kV in scanning transmission mode (STEM) using a High-Angle Annular Dark Field (HAADF) detector. Before microscopy observation, the samples were prepared by suspending the solid in dichloromethane and submitting the suspension to ultrasonication for one minute. Afterwards, the suspension was let to slowly decant for two minutes and a drop was extracted from the top side and placed on a carbon- coated copper grid. The catalysts were previously reduced *ex situ* under a flow of H_2 at 400 °C, passivated at r.t. under a flow of 0.5 vol% O_2/N_2 and stored at r.t. until the sample preparation for microscopy. Metal particle size histograms were generated upon measurement of 150–200 particles from several micrographs taken at different positions on the TEM grid. Average cobalt particle sizes ($d(Co^0)_{TEM}$) were corrected for a 2.5 nm thick CoO passivation outlayer as measured by high-resolution transmission electron microscopy (HR-TEM).

IR-CO spectra were recorded with a Nexus 8700 FTIR spectrometer using a DTGS detector and acquiring at 4 cm^{-1} resolution. An IR cell allowing *in situ* treatments in controlled atmospheres and temperatures in the 25-500 °C range was connected to a vacuum system with gas dosing facility. For IR studies, the samples (pre-reduced *ex situ* at 400 °C for 10 h in pure H_2 flow and subsequently passivated) were pressed into self-supported wafers of 10 mg/cm^2, reduced again in the cell at 400 °C for 2 h in flowing H_2, and submitted to a vacuum treatment at 450 °C for 1 h. Afterwards, the samples were cooled down to 25 °C under dynamic vacuum and CO was then dosed at increasing pressures (1.9-30 mbar). IR spectra were recorded after each dosage. Spectra analysis was done using the Origin software.

4.2.4. Fischer–Tropsch synthesis experiments

Catalytic experiments were performed in a down-flow fixed-bed stainless steel reactor with internal diameter of 10 mm and length of 40 cm. The reactor was loaded with 0.5 g of catalyst (0.25-0.42 mm pellet size) diluted with SiC granules (0.6-0.8 mm) until a total bed volume of 6.4 cm^3. Prior to reaction, the catalysts were reduced *in situ* in flowing H_2 at 400 °C for 10 h at ambient pressure. After reduction, the temperature was decreased to 100 °C under flowing H_2 and then *syngas* with H_2/CO molar ratio of 2 (CO:H_2:Ar volume ratio of 3:6:1, Ar used as internal standard for GC analyses) was passed through the reactor at the desired flow rate, the reaction pressure increased up to 2.0 MPa, and the temperature raised up to 220 °C at a rate of 2 °C/min. The temperature in the catalytic bed was controlled by two thermocouples connected to independent PID controllers. A third vertically sliding thermocouple was used to verify the absence of temperature gradients (T = 220 ± 1 °C) after the reaction temperature was established. Initial FTS activities were determined at quasi-differential CO conversions (<10%) using a constant gas hourly space velocity (GHSV) of 11.7 $L_{syngas}/(g_{cat}\cdot h)$ to ensure a low water partial pressure in the catalytic bed. This condition was maintained during ca. 7-

8 h on stream, after which the GHSV was adjusted for each catalyst so as to achieve a constant CO conversion of 10 ± 2% in the *pseudo*-steady state. Heavier hydrocarbons and water were condensed in two consecutive traps located at the reactor outlet and kept, respectively, at 150 °C and 100 °C, both at the reaction pressure (2.0 MPa). The stream leaving the second trap was depressurized and regularly analyzed on line by gas chromatography (GC) in a Varian 450 chromatograph equipped with three columns and TCD and FID detectors. After separation of the water co-product, the hydrocarbon fractions collected in the traps were weighted, diluted with CS_2, and analyzed off line in the same GC. The combination of the on line and off line GC analyses through the common product methane resulted in carbon mass balances in the 98-102% range. Product selectivities are expressed on a carbon basis.

4.3. Results and discussion

4.3.1. *Characterization of TiO_2-anatase supports*

The XRD patterns of the calcined supports (Figure 4.1) confirm that anatase (JCPDS 00-021-1272) is the only crystalline TiO_2 phase in all three synthesized supports. It is known from previous studies that the crystallization as anatase or rutile polymorphs is closely related to the type of acid used during the synthesis [22,23]. In the presence of acetic acid, as applied in this work, the CH_3COO^- anions coordinate strongly to titanium preventing the transformation of the metastable anatase to the thermodynamically favored rutile phase [22,24]. The XRD-derived mean particle sizes for the calcined TiO_2-anatase materials are shown in Table 4.2. As previously commented, materials with larger TiO_2 particle size could be obtained by using higher temperatures and acetic acid concentrations during the hydrothermal syntheses as well as more severe calcination conditions. Hence, the mean TiO_2 particle size increased from 11 nm for Ti-H to 14 nm for Ti-M and further to 27 nm for Ti-L.

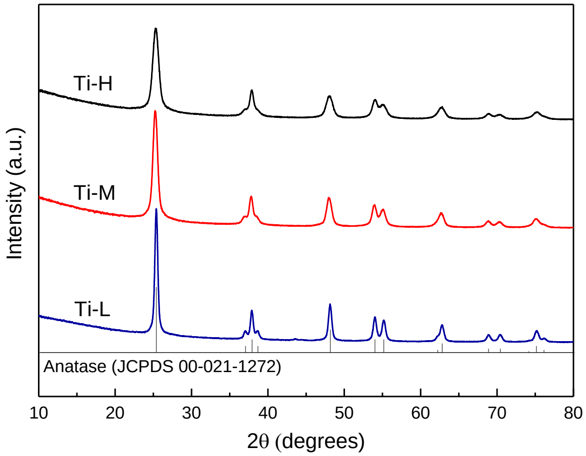

Figure 4.1. X-ray diffraction patterns of calcined TiO_2 supports exhibiting the characteristic diffraction peaks of the anatase phase (JCPDS 00-021-1272).

The N_2 adsorption-desorption isotherms and corresponding pore size distributions for calcined TiO_2 samples are shown in Figure 4.2, and the derived textural properties are gathered in Table 4.2. All TiO_2 supports present type IV adsorption isotherms (Figure 4.2a) characteristic of mesoporous solids with a large hysteresis loop at high relative pressure related to capillary condensation [25], similar to those previously reported for mesoporous TiO_2 synthesized using triblock copolymers as mesoporogens [26,27]. It is worth noting that in spite of having used distinct acid concentrations and temperatures in the syntheses, the type of pores, as indicated by the shape of the hysteresis loop, is similar for all three TiO_2-anatase samples. According to the N_2 uptakes, the BET areas follow, as expected, the reverse trend of TiO_2 particle sizes, decreasing from 148 m^2/g for Ti-H to 53 m^2/g for Ti-L, with Ti-M presenting an intermediate BET value of 117 m^2/g (Table 4.2). Moreover, all TiO_2 supports display unimodal pore size distributions with maxima at 8.8, 11.7, and 11.8 nm for Ti-H, Ti-M, and Ti-L, respectively (Figure 4.2b). Note, however, that the sample with medium surface area, Ti-M, exhibits a broader distribution of pore sizes in comparison to Ti-H and Ti-L. Nevertheless, the average pore diameter follows an opposite trend to the specific surface areas, progressively increasing from 6.1 to 8.4 nm with decreasing the BET area of the TiO_2-anatase material from 148 to 53 m^2/g (Table 4.2). In turn, it can be seen in Table 4.2 that the Ti-L sample with the lowest surface area also presents the lowest total pore volume (0.13 cm^3/g), while both Ti-H and Ti-M samples show higher and alike total pore volumes (0.26 ± 0.01 cm^3/g).

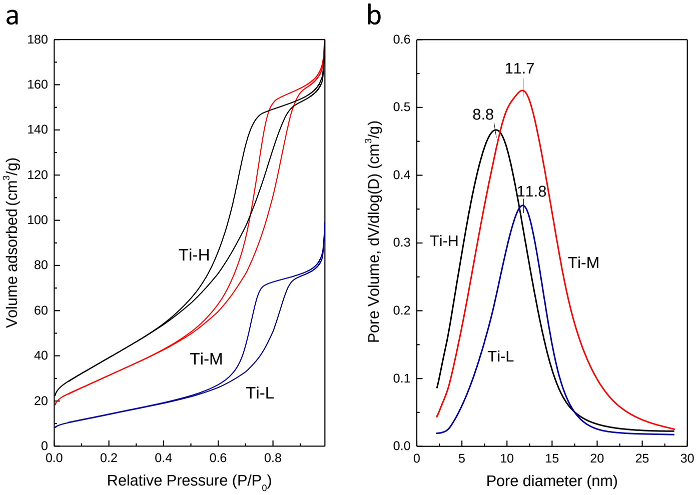

Figure 4.2. N_2 adsorption-desorption isotherms (a) and corresponding pore size distributions (b) for calcined TiO_2-anatase carriers.

Table 4.2. TiO_2 particle size (XRD) and textural properties of TiO_2-anatase supports derived from N_2 physisorption.

Support	TiO_2 particle size (nm)	BET area (m^2/g)	Total pore volume (cm^3/g)	Average pore diameter (nm)
Ti-H	11	148	0.25	6.1
Ti-M	14	117	0.27	7.8
Ti-L	27	53	0.13	8.4

Differences in particle size among the prepared TiO_2 supports were also clearly perceived by electron microscopy, as seen in the representative FESEM images shown in Figure 4.3. In all cases agglomerated particles comprised of small rice-like crystallites of distinct sizes were found, indicating that the morphology of the TiO_2 crystallites becomes mainly dictated by the nature of the acid employed in the synthesis, in agreement with earlier observations [22]. The size of the crystallites, however, evidently increased with the decrease of the specific surface area, ranging 10-30 nm for Ti-H, 15-35 nm for Ti-M, and 20-50 nm for Ti-L.

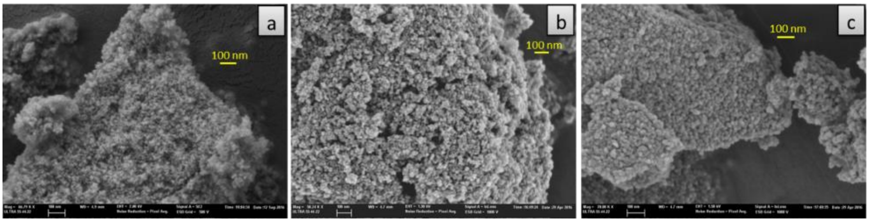

Figure 4.3. Representative FESEM images for calcined TiO_2-anatase supports: Ti-H (a), Ti-M (b), and Ti-L (c).

4.3.2. Characterization of the Co-Ru/TiO_2 catalysts

The XRD patterns of the Co-Ru/TiO_2 catalysts in their oxidized state are presented in Figure 4.4. Peaks corresponding to the Co_3O_4 spinel phase (JCPDS 00-042-1467) were detected for all three samples besides the characteristic reflections of the TiO_2-anatase phase. No additional crystalline phases related to cobalt or TiO_2 were perceived. Moreover, line broadening analysis of the TiO_2 peaks indicated no practical differences in the mean TiO_2 particle size between the catalysts and the corresponding supports. An accurate estimation of the Co_3O_4 mean particle size was, however, not feasible due to the relative low intensity of the Co_3O_4 spinel reflections and overlapping with TiO_2 diffractions.

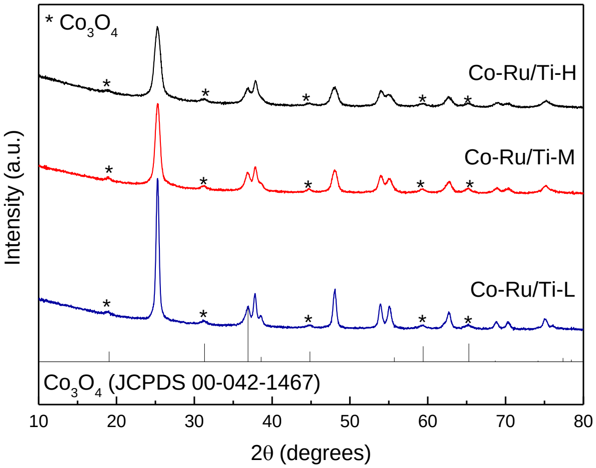

Figure 4.4. X-ray diffraction patterns of calcined Co-Ru/TiO_2 catalysts. The characteristic diffraction lines of Co_3O_4 spinel (JCPDS 00-042-1467) are also shown for an easier visualization of the Co_3O_4-related diffractions in the catalysts.

As observed in Figure 4.5a, the calcined Co-Ru/TiO_2 catalysts exhibit type IV N_2 adsorption-desorption isotherms characteristic of mesoporous solids similar to those of the corresponding supports. The BJH pore size distributions (Figure 4.5b) are, also, alike to the TiO_2 supports, with maxima at 10.6, 11.8, and 9.5 nm for Co-Ru/Ti-L, Co-Ru/Ti-M, and Co-Ru/Ti-H, respectively. The derived textural properties are given in Table 4.3. The BET surface area and total pore volume of the catalysts decreased by about 15-25% with respect to the values of the corresponding supports. This reduction is mostly ascribed to the dilution effect caused by the presence of the metal oxide phases. Indeed, BET areas and total pore volumes recalculated per mass of support (Table 4.3) are only less than 7% lower than those of the carriers (Table 4.2), indicating negligible pore blockage by the supported metal oxides. This is more evident for the catalyst based on the low surface area Ti-L sample comprising larger mesopores, for which the values of BET area and total pore volume recalculated per mass of TiO_2 are identical to those of the bare support. Moreover, the average pore diameters of the catalysts (Table 4.3) do not show significant variations with respect to those of the pristine carriers.

Table 4.3. Chemical composition and textural properties of calcined Co-Ru/TiO_2 catalysts.

Catalyst	Metal content (wt%)		BET area[a]	TPV[a]	APD[b]
	Co	Ru	(m^2/g)	(cm^3/g)	(nm)
Co-Ru/Ti-H	11.8	0.2	113 (135)	0.20 (0.24)	6.4
Co-Ru/Ti-M	11.8	0.4	99 (118)	0.21 (0.25)	7.5
Co-Ru/Ti-L	11.1	0.2	45 (53)	0.11 (0.13)	7.9

[a] TPV= total pore volume, data in parentheses correspond to the values recalculated per mass of TiO_2 support. [b] APD= average pore diameter.

The Co and Ru contents measured by ICP-OES are presented in Table 4.3. The concentration of cobalt slightly exceeds the targeted value (10 wt%) by about 10%. However, ruthenium contents are notably lower (by 20-60%) than the nominal content (0.5 wt%) due the formation of volatile sub-oxide RuO_x species during calcination under oxidizing atmosphere [28].

The reducibility of the Co-Ru/TiO_2 catalysts was studied by H_2-TPR and the corresponding reduction profiles are presented in Figure 4.6. All catalysts display two main reduction features with maximum H_2 consumptions at temperatures of ca. 125-170 °C ($T1_{max}$) and ca. 275-320 °C ($T2_{max}$). The low-temperature and high-temperature reduction features are ascribed, respectively, to the well-known two-step reduction of Co_3O_4 to Co^0 (T1: $Co_3O_4 \rightarrow CoO$; T2: $CoO \rightarrow Co^0$). The broad temperature range of the $T2_{max}$ reduction peak signs for the presence of CoO with different degrees of interaction with the TiO_2 support [29]. Additionally, a relatively small reduction feature at higher temperatures ($T3_{max}$= 392-425 °C) is perceived for the three catalysts, indicative of Co^{2+} species displaying a stronger interaction with the TiO_2 carrier. It is worth noting that the maximum temperatures for these three reduction peaks gradually shift towards higher values when decreasing the surface area of the TiO_2-anatase support (Figure 4.6). This trend could be related to an increasing mean size of the Co^0 nanoparticles with the decrease in support surface area, as will be discussed next based on TEM data. Previous studies did also found higher reduction temperatures for larger cobalt nanoparticles in Co/TiO_2 catalysts [30]. Nonetheless, at the view of the obtained H_2-TPR profiles, a high extent of cobalt reduction might be inferred for all three Co-Ru/TiO_2 catalysts upon reduction in pure H_2 at 400 °C for 10 h, as performed prior to catalysis. This is confirmed by the high (and similar) degrees of cobalt reduction (87- 91%) obtained in the additional H_2-TPR experiments on pre-reduced catalysts, as seen in Table 4.4. The high degrees of cobalt reduction achieved are attributable to the presence of Ru in the catalysts and its well known role as reduction promoter [9,28,31]. Moreover, *in situ* H_2-XRD measurements did not reveal diffractions related to cobalt oxide (Co_3O_4 and/or CoO) phases upon reducing the catalysts in flowing H_2 at 400°C, supporting the high degree of cobalt reduction concluded from the H_2-TPR experiments (see Figure 4.S1 in Supplementary Material). Conversely, the H_2-XRD results indicated the coexistence of both *fcc*-Co^0 (JCPDS 00-15-0806) and *hcp*-Co^0 (JCPDS 00-005-0727) crystalline phases in the reduced catalysts (Figure 4.S1).

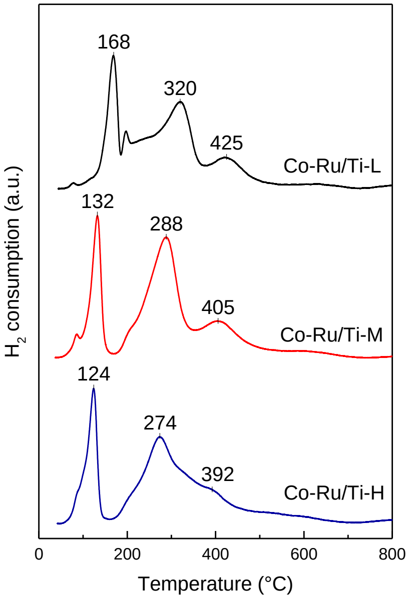

Figure 4.6. H_2-TPR profiles for Co-Ru/TiO_2 catalysts.

Table 4.4 summarizes the main properties of cobalt in the Co-Ru/TiO_2 catalysts. Hydrogen chemisorption experiments revealed increasing H_2 uptakes with decreasing the TiO_2 surface area, going from 17.6 µmol/g_{cat} for Co-Ru/Ti-H to 24.5 µmol/g_{cat} for Co-Ru/Ti-L. Such H_2 uptakes translate into apparent cobalt particle sizes ($d(Co^0)_{H2}$ in Table 4.4) of 48.2 nm for Co-Ru/Ti-H, 39.5 nm for Co-Ru/Ti-M, and 33.7 nm for Co-Ru/Ti-L.

Table 4.4. Properties of cobalt in the Co-Ru/TiO_2 catalysts.

Catalyst	H_2 uptake (µmol/g_{cat})	DR [a] (%)	Co^0 particle size (nm)		$d(Co^0)_{H2}$/ $d(Co^0)_{TEM}$ ratio
			$d(Co^0)_{H2}$	$d(Co^0)_{TEM}$	
Co-Ru/Ti-H	17.6	88.3	48.2	7.2	6.7
Co-Ru/Ti-M	21.2	87.1	39.5	7.4	5.3
Co-Ru/Ti-L	24.5	91.2	33.7	9.1	3.7

[a] DR= degree of cobalt reduction.

Metal cobalt particle sizes were also measured by STEM after reduction in H_2 at 400 °C and passivation. Representative HAADF-STEM images and their corresponding particle size histograms are shown in Figure 4.7. In all Co-Ru/TiO_2 catalysts metallic cobalt nanoparticles, visible as bright spots in the images, appear well dispersed over the TiO_2-anatase supports, although some clustered regions are also evidenced, as frequently observed in catalysts prepared by impregnation with cobalt nitrate precursor [6]. It is observed in the histograms that the size of cobalt nanoparticles extends over a broader range in the low surface area Co-Ru/Ti-L catalyst (3-27 nm) in comparison to the medium and high surface area ones (3-18 nm). The particle size values presented in the histograms were previously corrected by a 2.5 nm thick CoO outlayer resulting from the passivation treatment, according to the representative HR-TEM image shown in Figure 4.8 corresponding to the as-reduced and passivated Co-Ru/Ti-L sample. In the image, the Co^0 particle, identified by the lattice spacing of 0.19 nm related to the (1 0 1) plane of *hcp*-Co^0, appears covered by a 2.5 nm thick layer presenting a lattice spacing of 0.21 nm characteristic of the (2 0 0) crystallographic plane of CoO. As seen in Table 4.4, the corrected STEM-derived average Co^0 particle sizes, $d(Co^0)_{TEM}$, present an inverse relationship with the support surface area, with values of 7.2, 7.4, and 9.1 nm for Co-Ru/Ti-H, Co-Ru/Ti-M, and Co-Ru/Ti-L, respectively.

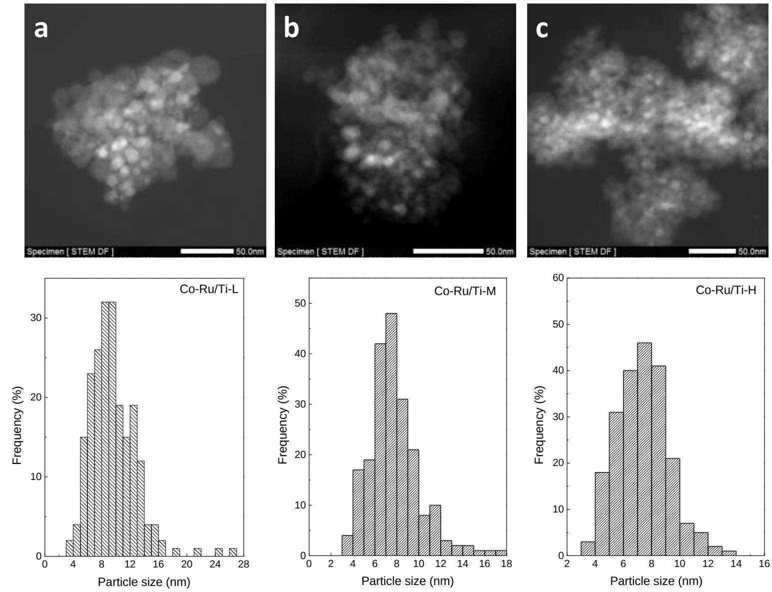

Figure 4.7. HAADF-STEM micrographs (top) for H_2-reduced and passivated Co-Ru/Ti-L (a), Co-Ru/Ti-M (b), and Co-Ru/Ti-H (c) catalysts. The respective Co^0 particle size histograms are shown at the bottom of each image.

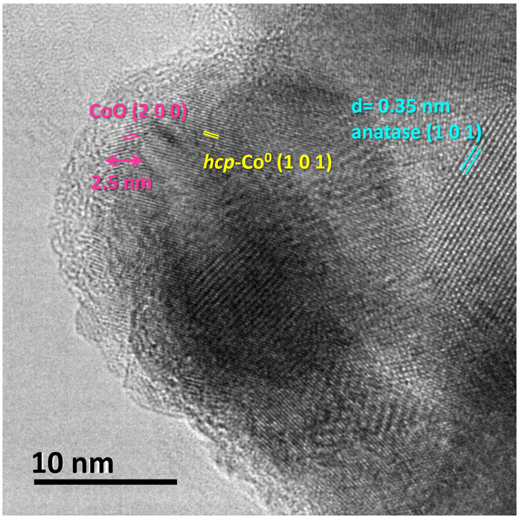

Figure 4.8. HRTEM micrograph of reduced and passivated Co-Ru/Ti-L catalyst showing the 2.5 nm thick CoO layer covering the surface of Co^0 nanoparticles.

The Co^0 particle sizes obtained by H_2 chemisorption are 3-7 times larger than those measured by direct imaging (Table 4.4). This apparent discrepancy is related to the SMSI effect which takes place during the reduction stage of activation where partially reduced TiO_x species migrate on top of the Co^0 nanoparticles suppressing their H_2 (and CO) chemisorption capacity [32]. The ratio between the Co^0 particle size obtained by H_2 chemisorption and by direct observation (STEM), $d(Co^0)_{H2}/d(Co^0)_{TEM}$, can be taken as an indirect estimation of the extent to which the SMSI effect occurred on the different catalysts. As shown in Table 4.4, this ratio increases from 3.7 for Co-Ru/Ti-L to 6.7 for Co-Ru/Ti-H, indicating that the SMSI is exacerbated by the increase in surface area of the TiO_2-anatase support, in line with the trends previously observed for Ru/TiO_2 [20] and Pt/TiO_2-SiO_2 [21] catalysts.

Finally, CO adsorption followed by IR spectroscopy has been used for identification of the amount and the nature of surface cobalt species present in the H_2-reduced Co-Ru/TiO_2 samples with extreme surface areas. The IR spectra of CO adsorption at saturation coverage (Figure 4.9) shows two bands at 2065 and 1982 cm^{-1} for the high surface area Co-Ru/Ti-H sample, and a broad asymmetric band peaking at 2065 cm^{-1} and a tail at lower frequency (~2014 cm^{-1}) for the low surface area Co-Ru/Ti-L sample. The IR band at 2065 cm^{-1} corresponds to CO interacting with both *fcc* and *hcp* Co^0 surface sites [33], while the IR bands at lower frequency (~2014 and 1982 cm^{-1}) have been linked to coordinatively unsaturated cobalt sites in defects (i.e. steps, edges, and corners) of the Co^0 crystallites or at the interface between cobalt and the metal oxide support where CO coordinates in a *tilt* configuration [4]. In the case of TiO_2-supported catalysts, the low frequency IR component at 1982 cm^{-1} might be associated to Co^0 species in contact with TiO_x species characteristic of the SMSI state [19]. Thus, the IR-CO results point towards a higher amount of metal-oxide surface patches in the catalyst based on the high surface area TiO_2-anatase resulting in different surface cobalt topologies for catalysts experiencing distinct SMSI extents. On the other hand, the amount of cobalt species titrated by CO is about 1.9 times higher in Co-Ru/Ti-L than in Co-Ru/Ti-H, according to the respective areas of the cobalt-related IR-CO bands. This area ratio compares well with the H_2 uptake ratio of 1.4 obtained from H_2 chemisorption for these two catalysts (Table 4.4), thus providing further evidence for the occurrence of a more pronounced SMSI effect in the catalyst supported on the high surface area carrier.

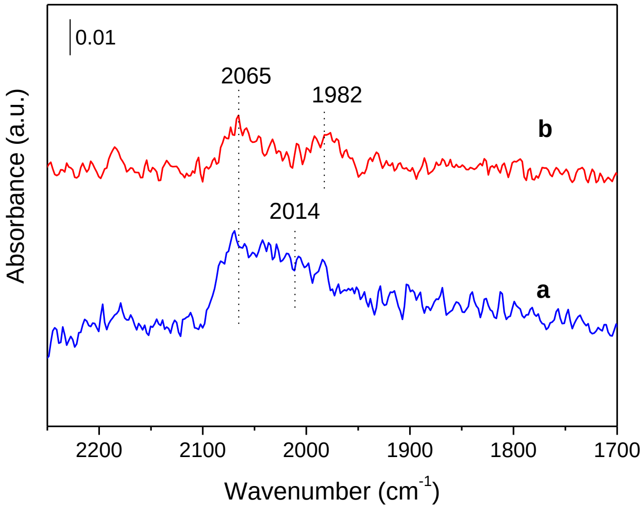

Figure 4.9. IR spectra of CO adsorption at saturation coverage (30 mbar) for Co-Ru/Ti-L (a) and Co-Ru/Ti-H (b) catalysts after reduction in flowing H_2 at 400 °C.

In our earlier work, we reported an enhanced SMSI effect for Co-Ru/TiO_2 catalysts supported on TiO_2-anatase compared to those based on TiO_2-rutile [19]. In the present study, we have shown that, besides the crystalline phase, the TiO_2 surface area exerts a notable influence on the SMSI extent, with higher surface areas (i.e. lower crystallite sizes) leading to a more pronounced SMSI effect. Although the same effect has been previously reported for Ru/TiO_2 [20] and Pt/TiO_2-SiO_2 [21] systems, as mentioned beforehand, its genesis has not yet been clearly established. In the following, we will try to provide a rationale for the experimentally observed dependence of the SMSI extent with the TiO_2 surface area/crystallite size. It is known from earlier works that the SMSI state in TiO_2-supported metal catalysts is tightly linked to the removal of oxygen from the TiO_2 lattice with the consequent formation of Ti^{3+}/oxygen vacancy pairs during reduction in H_2 at high temperature [34]. Indeed, more reducible titania generally induces a larger SMSI effect [35]. On the other hand, the concentration of Ti^{3+}/oxygen vacancy generated upon H_2 reduction was shown to gradually increase with decreasing the crystallite size of the starting TiO_2 material [36,37], as smaller TiO_2 crystals are associated to more defected structures. Therefore, one may anticipate that more partially reduced Ti^{3+} species, which are central to the generation of the SMSI state, would form during reduction of TiO_2 comprising smaller crystallites, that is, higher specific surface areas. In order to experimentally support the above hypothesis, we performed Raman spectroscopy to characterize the structural features of the high surface area (Ti-H) and low surface area (Ti-L) supports in their calcined state as well as after reduction in H_2 at 400°C for 10 h. The corresponding Raman spectra are shown in Figure 4.10a,b. As observed, the calcined Ti-H and Ti-L samples exhibit active Raman bands at ca. 146, 197, 399, 515, and 639 cm^{-1} ascribed to, respectively, the E_g, E_g, B_{1g}, A_{1g}+B_{1g}, and E_g active modes of anatase-TiO_2 [38]. These Raman modes, albeit with decreased intensities, are also observed for the H_2-reduced TiO_2 supports. The weakened intensity of the Raman bands originates from an enhanced nonstoichiometric property (Ti^{3+}/oxygen vacancy) of the H_2-reduced materials [36]. Specifically, the E_g vibration mode is associated with planar O-O interactions and is thus sensitive to the presence of oxygen defects in the TiO_2 lattice. In this respect, a linear correlation has been found between the peak position and the full width at half-maximum (FWHM) of the most intense E_g mode at around 146 cm^{-1} as both parameters increase with the concentration of oxygen vacancies (i.e. Ti^{3+}) in the TiO_2 lattice [39]. In agreement with this, we also observed a linear relationship between the peak position and the FWHM of this E_g band for the Ti-H and

Ti-L samples in their calcined and as-reduced states, as depicted in Figure 4.10c.

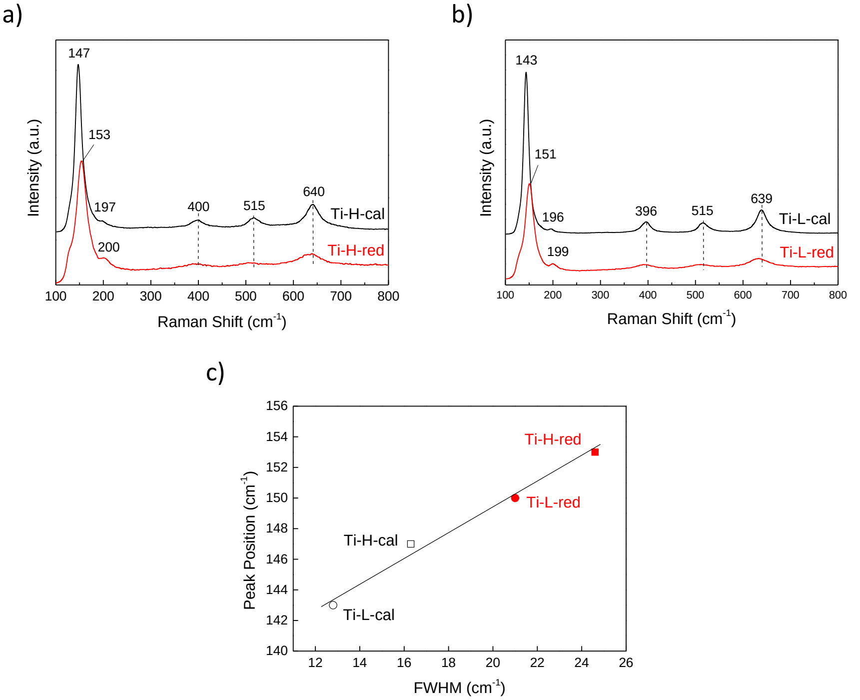

Figure 4.10. Raman spectra for the high surface area Ti-H (a) and the low surface area Ti-L (b) anatase-TiO_2 supports in their calcined state ("-cal") and after reduction in H_2 at 400°C ("-red"); c) correlation between the peak position and the FWHM of the E_g Raman band for the calcined and H_2-reduced Ti-H and Ti-L samples.

The trends in Figure 4.10c indicate an increased concentration of lattice defects in the anatase-TiO_2 supports upon reduction in H_2, as expected. Moreover, the higher wavenumber and FWHM of the E_g Raman band in the high surface area Ti-H sample compared to Ti-L in both their calcined and reduced states clearly sign for a higher concentration of defects (Ti^{3+}/oxygen vacancy) in the former, which can be ascribed to its lower crystallite size [36,37]. According to these results, more partially reduced TiO_x species would form during the reduction in H_2 at 400°C of the Co-Ru/TiO_2 catalysts with increasing the surface area (i.e. with decreasing the crystallite size) of the anatase-TiO_2 support resulting in a higher extension of the SMSI effect, as observed in the present study.

The consequences on the FTS reaction of the enhanced SMSI effect in high surface area Co-Ru/TiO_2 catalysts are analyzed in the following section.

4.3.3. Fischer-Tropsch synthesis on Co-Ru/TiO_2 catalysts

Table 4.5 summarizes the main catalytic properties for FTS of the investigated Co-Ru/TiO_2 catalysts. Initial activities were obtained by extrapolation of the conversion-time-on-stream (TOS) curves at TOS = 0 (not shown). As observed in the table, both the initial CO conversion and cobalt-time-yield (CTY) at constant GHSV progressively increased with the decrease in support surface area, with the low surface area Co-Ru/Ti-L catalyst displaying an initial activity about 1.5 times higher than the high surface area Co-Ru/Ti-H sample. The change in initial CTY with the support surface area parallels the trend in H_2 uptake (Table 4.4) and, thus, in the concentration of surface Co^0 sites available for reaction after H_2 reduction as a result of the SMSI effect. Similar trends are observed for the CTY in the *pseudo*-steady state period (at constant CO conversion of ~10%). However, the relative loss of CTY from the initial to the *pseudo*-steady state (SS) augments from 14.2% to 43.4% with the increase in support surface area (Table 4.5). Considering that the FTS rate of Co-based FTS catalysts displays an apparent negative kinetic dependence with respect to CO [2], this trend likely reflects the increasing resistance for the diffusion of CO through the dense hydrocarbon phase filling the catalyst pores in the *pseudo*-steady state with decreasing the support pore size [6]. Contrarily to the cobalt mass-based activity (CTY), all catalysts display nearly identical values for the initial (TOS$\rightarrow$0) intrinsic activity per exposed Co^0 site (from H_2 chemisorption) or turnover frequency (TOF), as seen in Table 4.5. The obtained initial TOFs ($10\pm1\cdot10^{-2}$ s^{-1}) are in line with those reported for *ex*-nitrate TiO_2-supported Co catalysts at equivalent reaction conditions [5,7,40].

Table 4.5. Initial and *pseudo*-steady state (SS) activities of Co-Ru/TiO_2 catalysts for Fischer-Tropsch synthesis (FTS). Reaction conditions: T= 220 °C, P= 2.0 MPa, H_2/CO= 2 mol/mol. Initial activities were obtained by extrapolating the CO conversion-TOS curves at TOS= 0 at constant GHSV of 11.7 $L_{syngas}/(g_{cat}\cdot h)$, while SS activities were averaged for the next 8 h of reaction after adjusting the GHSV for each catalyst to obtain a CO conversion of ~10%.

Catalyst	CO conversion (%)		$CTY\cdot10^3$ $(mol_{CO}/g_{Co}.h)^a$		$-\Delta CTY^b$ (%)	$TOF\cdot10^2$ $(s^{-1})^c$	
	Initial	SS	Initial	SS		Initial	SS
Co-Ru/Ti-H	7.4	9.3	100.0	56.6	43.4	9.3	5.3
Co-Ru/Ti-M	10.3	11.5	141.1	108.6	23.0	10.9	8.4
Co-Ru/Ti-L	10.8	9.9	156.3	134.1	14.2	9.8	8.4

[a] CTY= cobalt-time-yield (activity per total mass of cobalt).

[b] Relative loss of CTY (in %) from the initial (TOS→ 0) to the *pseudo*-steady state (SS).

[c] TOF= turnover frequency (activity per surface Co^0 sites as measured by H_2 chemisorption).

According to the characterizations discussed before, all three Co-Ru/TiO_2 catalysts display comparable Co^0 particle sizes of about 7-9 nm (based on STEM) and very high and alike degrees of cobalt reduction (ca. 90%). As mentioned in the introduction, a decrease in TOF for Co^0 nanoparticles sizing less than 6-8 nm has been reported for silica- and carbon-supported cobalt catalysts [3,4]. Although an equivalent particle size-TOF dependence has not yet been unambiguously demonstrated for TiO_2-supported cobalt catalysts, a significant impact of particle size on TOF for similarly-sized Co^0 particles in the 7-9 nm range, as for the present Co-Ru/TiO_2 catalysts, is not expected. Taking this into account, the fact that all catalysts display nearly the same initial TOF strongly suggests that the different extents of SMSI originated from the distinct support surface areas do not affect the initial intrinsic activity of the exposed metal cobalt sites. Differently, it can be seen in Table 4.5 that the TOF for Co-Ru/Ti-H in the *pseudo*-steady state ($5.3\cdot10^{-2}$ s^{-1}) is about 1.6 times lower than the TOF for Co-Ru/Ti-M and Co-Ru/Ti-L ($8.4\cdot10^{-2}$ s^{-1}). However, we have recently shown that the SMSI effect in Co-Ru/TiO_2 systems is partially reverted during the FTS reaction, likely due to water-assisted re-oxidation of the TiO_x patches decorating the Co^0 nanoparticles, resulting in an increase in the amount of exposed Co^0 sites [19]. In consequence, the true concentration of active Co^0 sites in the Co-Ru/TiO_2 catalysts under FTS conditions is not known with certainty making the comparison of *pseudo*-steady state TOFs based on H_2 chemisorption data questionable. Therefore, a net influence of the extent of the SMSI decoration effect (directly linked to the TiO_2 surface area) on the TOF of the exposed Co^0 centers in the *working* catalysts cannot be definitively concluded from our results. Nonetheless, large differences in TOF among the studied Co-Ru/TiO_2 catalysts during FTS reaction seem unlikely at the view of their almost identical initial TOF (at zero TOS) in spite of the notable differences in SMSI extent observed in their as-reduced state.

The selectivity to the different hydrocarbon fractions in the *pseudo*-steady state obtained for the Co-Ru/TiO_2 catalysts is compared in Table 4.6 at constant CO conversion (10 ± 1%). The selectivity to CO_2 was in all cases below 1%, as expected from the well known low activity of cobalt for the competing water gas shift reaction (WGSR). Results in Table 4.6 show no practical differences in the distribution of hydrocarbon products for the catalysts based on medium and low surface area TiO_2-anatase supports, both giving selectivities to methane (C_1) and liquids (C_{5+}) of ca. 12-13% and 74%, respectively. Comparatively, the catalyst supported on the high surface area TiO_2 displays higher selectivity to C_1 (16%) and lower to C_{5+} (57%), implying that chain growth processes are inhibited in this catalyst experiencing the largest SMSI effect.

Table 4.6. Product distributions obtained in the *pseudo*-steady state on Co-Ru/TiO_2 catalysts at CO conversion of 10 ± 1%. Reaction conditions: T= 220 °C, P= 2.0 MPa, H_2/CO= 2 mol/mol, GHSV= 5.3 (for Co-Ru/Ti-H), 8.2 (for Co-Ru/Ti-M), and 11.0 (for Co-Ru/Ti-L) $L_{syngas}/g_{cat}\cdot h$.

Catalyst	Selectivity (%C)			Parameter χ[a]
	C_1	C_2-C_4	C_{5+}	(10^{-16} m)
Co-Ru/Ti-H	16.0	27.2	56.8	80
Co-Ru/Ti-M	12.2	13.9	73.9	97
Co-Ru/Ti-L	12.8	13.3	73.9	159

[a] Structural parameter modeling mass transport limitations in cobalt-catalyzed FTS (see text).

At constant reaction conditions and identical support identity, the distribution of hydrocarbons in FTS is mainly determined by the size of the cobalt nanoparticles [3,4], with more extended metal surfaces prevailing in larger particles favoring chain growth and hence C_{5+} selectivity, and by mass transport effects [17]. In our case, the relatively small differences in Co^0 particle size between the three investigated catalysts (ca. 8 ± 1 nm) hardly explain, by themselves, the significantly lower C_{5+} selectivity (ca. 17% in absolute terms) displayed by the high surface area Co-Ru/Ti-H catalyst. On the other hand, the crucial role played by mass transport limitations on the C_{5+} selectivity of cobalt-based FTS catalysts under realistic conditions, particularly for catalyst pellet sizes commonly employed in fixed bed reactors, was highlighted several decades ago in the studies by Iglesia and co-workers [17,41]. According to the model developed by these authors, the C_{5+} selectivity passes a maximum with increasing the severity of intraparticle diffusion resistance described by the structural parameter χ defined as in the following equation (4.1) [17]:

$$\chi = R_0^2 \cdot \varepsilon \cdot \theta_{Co} / r_p \qquad \text{Eq.4.1}$$

where R_0 is the mean radius of catalyst pellets, ε is the pellet void fraction (porosity), θ_{Co} is the density of cobalt sites per unit area, and r_p refers to the mean radius of the catalyst pores. According to this model [17], the C_{5+} selectivity first raises with increasing diffusion limitations up to values of the structural parameter χ of around $170\cdot10^{16}$ m as re-adsorption of α-olefins on the active sites and their participation in new chain growth processes become increasingly favored. Above this value of χ (that is, under more severe mass transport restrictions), a further increase of the structural parameter does not longer change the probability for α-olefin re-adsorption and, instead, the resistance to the transport of CO through the liquid phase filling the pores becomes the limiting factor leading to a gradual decline of the C_{5+} selectivity as χ increases.

In our case, the χ values calculated for the Co-Ru/TiO_2 catalysts fall in the range of $80\cdot10^{16}$-$160\cdot10^{16}$ m (Table 4.6) where C_{5+} selectivity is mostly driven by the resistance to the diffusion of α-olefins [17]. Interestingly, the parameter χ increases in the order: Co-Ru/Ti-H < Co-Ru/Ti-M << Co-Ru/Ti-L that is, with decreasing the support surface area or, equivalently, with increasing the average pore diameter. This trend looks at first sight surprising as a more restricted diffusion could be expected, *a priori*, for catalysts with smaller pores. However, taking into account that the radius of pellets (R_0) used in the catalytic experiments is the same for all three catalysts and that the mean catalyst pore radius (r_p) in the denominator of Eq. (4.1) varies only in a relatively short range (3.2-3.9 nm), it comes that the density of surface active Co^0 sites per unit area, given by the term θ_{Co} in Eq. (4.1), is the most determinant factor influencing the final values of the parameter χ in our catalysts. In fact, the trend for θ_{Co} is the same as that of χ, increasing from Co-Ru/Ti-H ($1.88\cdot10^{17}$ at-Co^0/m^2) to Co-Ru/Ti-M ($2.58\cdot10^{17}$ at-Co^0/m^2) and further to Co-Ru/Ti-L ($6.56\cdot10^{17}$ at-Co^0/m^2). The significantly higher value of θ_{Co} (and of χ) obtained for the low surface area Co-Ru/Ti-L sample originates from its higher concentration of surface Co^0 sites (due to the lower SMSI effect in this catalyst) and its lower specific surface area, as discussed previously on the basis of H_2 chemisorption and N_2 adsorption results. The increasing α-olefin diffusion resistance with decreasing the surface area of the TiO_2-anatase support inferred from the calculated χ values is fully consistent with the variations in the olefin-to-paraffin (O/P) ratio of the produced hydrocarbons. In fact, as observed in Figure 4.11, the O/P ratio for C_2-C_4 and C_5-C_8 hydrocarbons exhibits a decreasing trend with the parameter χ that reflects an increasing probability for α-olefins to undergo secondary reactions such as re-adsorption and hydrogenation as their transport within the catalyst pellets becomes more impeded. In turn, the lower O/P ratio obtained for C_5-C_8 in comparison to C_2-C_4 could be anticipated considering the higher resistance to the diffusion of longer chain α-olefins [17]. It is also worth of noting from the data in Figure 4.11 that the O/P ratio for the C_5-C_8 fraction diminishes more rapidly with increasing χ than that of C_2-C_4 (for instance, the C_2-C_4-to-C_5-C_8 O/P ratio amounts to 1.3 for Co-Ru/Ti-H and 1.6 for Co-Ru/Ti-L), indicating that differences in diffusion resistance between the catalysts become more pronounced with increasing the chain length of the α-olefin product.

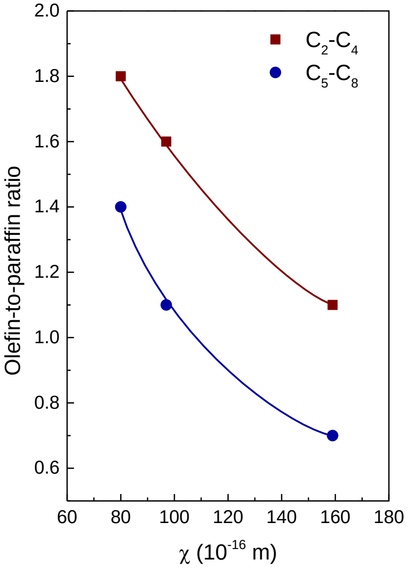

Figure 4.11. Change in olefin-to-paraffin ratio for the C_2-C_4 and C_5-C_8 hydrocarbon fractions as a function of the diffusion-related structural parameter χ.

Nonetheless, even though the hydrocarbon selectivities and O/P ratios follow the general trends expected from the values of the parameter χ, the remarkably lower C_{5+} selectivity observed for Co-Ru/Ti-H relative to the other two catalysts (Table 4.6) can hardly be accounted for by considering only mass transport issues. It is known from preceding surface science studies on model catalysts and theoretical calculations that CO dissociation and chain growth in FTS have distinct site requirements on cobalt catalysts [42]. Thus, while dissociation of CO is found to proceed readily on defected sites such as step edge sites on the surface of cobalt particles, chain growth involves rather large ensembles of Co^0 atoms on closed-packed terraces. Decoration of cobalt nanoparticles by the TiO_x overlayer should expectedly decrease the size of the Co^0 ensembles and, consequently, disfavor chain growth (e.g. C-C bond formation) processes. Therefore, a smaller size for the chain growth ensembles could be envisaged for the Co-Ru/Ti-H sample exhibiting the most pronounced SMSI effect which, besides a lower resistance to the diffusion of α-olefins as discussed before, would contribute to the much lower C_{5+} selectivity of this catalyst.

Overall, the results presented in this study point towards a significant influence of the extent of SMSI, determined by the support surface area in the studied Co-Ru/TiO_2-anatase catalysts, on the cobalt-time-yield (without affecting initial TOFs) as well as on the hydrocarbon selectivity by modifying, respectively, the density of surface active Co^0 sites and the size of the ensembles where chain growth events preferentially take place.

4.4. Conclusions

TiO_2-anatase materials with specific surface areas of 53 (Ti-L), 117 (Ti-M), and 148 (Ti-H) m^2/g were hydrothermally synthesized by adjusting the conditions of the hydrothermal and/or calcination treatments, and applied as supports for preparing Co-Ru/TiO_2 catalysts (nominal loadings of 10 wt% Co and 0.5 wt% Ru) for Fischer-Tropsch synthesis (FTS). The specific surface area of the TiO_2 support was shown to influence the extent of the SMSI effect in the Co-Ru/TiO_2 catalysts after their reduction in H_2 at 400°C for 10 h. As-reduced catalysts displayed equivalent Co^0 particle sizes (7-9 nm) as determined by direct imaging (STEM) and degrees of cobalt reduction (about 90%), thus discarding any significant impact of these parameters on the observed catalytic performances. Lower H_2 uptakes, translating into larger relative differences between the Co^0 particle sizes measured by H_2 chemisorption and electron microscopy (STEM), and lower intensities of the cobalt-carbonyl bands in IR-CO surface titration experiments unambiguously evidenced a more pronounced SMSI decoration effect for catalysts prepared from higher surface area TiO_2 supports. This behavior can be related to a higher concentration of structural defects (i.e. Ti^{3+}/oxygen vacancy) in the high surface area TiO_2 samples comprising small crystallites, as supported by Raman spectroscopy, that results in the formation of more partially reduced TiO_x species involved in the generation of the SMSI state during the H_2 reduction treatment. In consequence, the cobalt-time-yield (activity per total mass of cobalt) progressively decreased with the increase in TiO_2 surface area. Different extents of SMSI, however, did not apparently affect the initial activity of the catalysts per exposed Co^0 site as all three catalysts exhibited analogous initial TOFs ($10\pm1\cdot10^{-2}$ s^{-1}). On the other hand, a definitive conclusion on possible differences in TOF in the *pseudo*-steady state could not reached due to the partial reversibility of the SMSI effect that hampers an accurate determination of the concentration of surface Co^0 sites in the *working* catalysts. The Co-Ru/Ti-

H catalyst, which experienced the largest SMSI extent, did also show the lowest selectivity to the desired liquid (C_{5+}) fraction. Thus, at constant CO conversion of about 10%, the C_{5+} selectivity was ~57% for Co-Ru/Ti-H and ~74% for both Co-Ru/Ti-M and Co-Ru/Ti-L. Such significantly lower C_{5+} selectivity of Co-Ru/Ti-H was accounted for by considering the combined action of two effects, both having a negative impact on the chain growth probability: on one hand, a lower extent of α-olefin re-adsorption and insertion into the growing chains, as inferred from the values of the structural parameter χ, and on the other hand, to a greater reduction in the size of the Co^0 ensembles on the terraces of the nanoparticles (on which chain growth are believed to occur) due to the larger SMSI extent experienced by the catalyst supported on the high surface area TiO_2-anatase. In conclusion, we have shown in this work that the surface area of the TiO_2 carrier influences the extent of the SMSI effect in Co-Ru/TiO_2 catalysts and that this has a direct impact on both the activity and selectivity for the FTS reaction.

Acknowledgments

Financial support by the MINECO of Spain through the Severo Ochoa (SEV 2012-0267) and ENE2014-5761-R projects is gratefully acknowledged. The authors also thank the Microscopy Service of the Universitat Politècnica de València for its assistance in microscopy characterization. F. Bertella (Science without Frontiers − Process no. 13705/13-0) thanks CAPES for a predoctoral fellowship.

4.5. References

[1] M.E. Dry, J. Chem. Technol. Biotechnol. 77 (2002) 43–50.
[2] A.Y. Khodakov, W. Chu, P. Fongarland, Chem. Rev. 107 (2007) 1692–1744.
[3] G.L. Bezemer, J.H. Bitter, H.P.C.E. Kuipers, H. Oosterbeek, J.E. Holewijn, X. Xu, F. Kapteijn, A. J. Van Dillen, K.P. de Jong, J. Am. Chem. Soc. 128 (2006) 3956–3964.
[4] G. Prieto, A. Martínez, P. Concepción, R. Moreno-Tost, J. Catal. 266 (2009) 129–144.
[5] T.O. Eschemann, J.H. Bitter, K.P. de Jong, Catal. Today 228 (2014) 89–95.
[6] A. Martínez, G. Prieto, J. Rollán, J. Catal. 263 (2009) 292–305.
[7] G. Prieto, M.I.S. De Mello, P. Concepción, R. Murciano, S.B.C. Pergher, A. Martínez, ACS Catal. 5 (2015) 3323–3335.
[8] C. Liu, Y. Zhang, Y. Zhao, L. Wei, J. Hong, L. Wang, S. Chen, G. Wang, J. Li, Nanoscale 9 (2017) 570–581.
[9] T.O. Eschemann, J. Oenema, K.P. De Jong, Catal. Today 261 (2016) 60–66.
[10] G.L. Bezemer, P.B. Radstake, U. Falke, H. Oosterbeek, H.P.C.E. Kuipers, A.J. Van Dillen, K.P. De Jong, J. Catal. 237 (2006) 152–161.
[11] K. Shimura, T. Miyazawa, T. Hanaoka, S. Hirata, Appl. Catal. A Gen. 494 (2015) 1–11.
[12] G.R. Johnson, A.T. Bell, ACS Catal. 6 (2016) 100–114.
[13] G. Prieto, P. Concepción, R. Murciano, A. Martínez, J. Catal. 302 (2013) 37–48.
[14] J.A. Delgado, C. Claver, S. Castillón, D. Curulla-Ferré, V. V. Ordomsky, C. Godard, Appl. Catal. A Gen. 513 (2016) 39–46.
[15] J.Y. Park, Y.J. Lee, P.R. Karandikar, K.W. Jun, K.S. Ha, H.G. Park, Appl. Catal. A Gen. 411–412 (2012) 15–23.
[16] O. Borg, P.D.C. Dietzel, A.I. Spjelkavik, E.Z. Tveten, J.C. Walmsley, S. Diplas, S. Eri, A. Holmen, E. Rytter, J. Catal. 259 (2008) 161–164.
[17] E. Iglesia, Appl. Catal. A Gen. 161 (1997) 59–78.
[18] R.C. Reuel, C.H. Bartholomew, J. Catal. 85 (1984) 78–88.
[19] F. Bertella, P. Concepción, A. Martínez, Catal. Today (2016), http://dx.doi.org/10.1016/j.cattod.2016.08.008.
[20] A.M. Abdel-Mageed, D. Widmann, S.E. Olesen, I. Chorkendorff, J. Biskupek, R.J. Behm, ACS Catal. 5 (2015) 6753–6763.
[21] M. Bonne, P. Samoila, T. Ekou, C. Especel, F. Epron, P. Marécot, S. Royer, D. Duprez, Catal. Commun. 12 (2010) 86-91.
[22] M. Wu, G. Lin, D. Chen, G. Wang, D. He, S. Feng, R. Xu, Chem. Mater.

14 (2002) 1974–1980.
[23] D. Zhang, L. Qi, J. Ma, H. Cheng, J. Mater. Chem. 12 (2002) 3677–3680.
[24] C. Sanchez, J. Livage, M. Henry, F. Babonneau, J. Non. Cryst. Solids 100 (1988) 65–76.
[25] M. Thommes, K. Kaneko, A. V. Neimark, J.P. Olivier, F. Rodriguez-Reinoso, J. Rouquerol, K.S.W. Sing, Pure Appl. Chem. 87 (2015) 1051–1069.
[26] Y. Yue, Z. Gao, Chem. Commun. (2000) 1755–1756.
[27] H. Luo, C. Wang, Y. Yan, Chem. Mater. 15 (2003) 3841–3846.
[28] J. Hong, E. Marceau, A.Y. Khodakov, L. Gaberová, A. Griboval-Constant, J.S. Girardon, C. La Fontaine, V. Briois, ACS Catal. 5 (2015) 1273–1282.
[29] J. Li, G. Jacobs, Y. Zhang, T. Das, B.H. Davis, Appl. Catal. A Gen. 223 (2002) 195–203.
[30] J.A. Delgado, C. Claver, S. Castillón, D. Curulla-Ferré, V. V. Ordomsky, C. Godard, Appl. Catal. A Gen. 513 (2016) 39–46.
[31] Q. Cai, J. Li, Catal. Commun. 9 (2008) 2003–2006.
[32] S.J. Tauster, Acc. Chem. Res. 20 (1987) 389–394.
[33] D. Song, J. Li, Q. Cai, J. Phys. Chem. C 111 (2007) 18970–18979.
[34] G.L. Haller, D.E. Resasco, Adv. Catal. 36 (1989) 173-235.
[35] S.J. Tauster, S.C. Fung, J. Catal. 55 (1978) 29-35.
[36] J. Zheng, L. Liu, G. Ji, Q. Yang, L. Zheng, J. Zhang, ACS Appl. Mater. Interfaces 8 (2016) 20074-20081.
[37] Z. Xu, J. Shang, C. Liu, C. Kang, H. Guo, Y. Du, Mater. Sci. Eng. B 56 (1999) 211-214.
[38] T. Ohsaka, F. Izumi, Y. Fujiki, J. Raman Spectrosc. 7 (1978) 321-324.
[39] J.C. Parker, R.W. Siegel, Appl. Phys. Lett. 57 (1990) 943-945.
[40] T.O. Eschemann, K.P. de Jong, ACS Catal. 5 (2015) 3181–3188.
[41] E. Iglesia, S.L. Soled, J.E. Baumgartner, S.C. Reyes, J. Catal. 153 (1995) 108–122.
[42] C.J. Weststrate, P. van Helden, J.W. Niemantsverdriet, Catal. Today 275 (2016) 100–110.

4.6. Supporting Information

4.6.1. Crystalline Co phases in the H_2-reduced catalysts studied by in situ H_2-XRD

4.6.1.1. Experimental

In situ H_2-XRD experiments were performed in order to assess the crystalline phases present in the as-reduced catalysts. The measurements were performed in a Panalytical X'Pert PRO diffractometer using monochromatized Mo K_α radiation and operated at 45 kV and 40 mA. The samples were loaded in a XRK-900 Anton Paar cell and flushed with a gas stream comprising 10 vol% H_2 diluted in N_2. In these experiments, the X-ray diffractograms were first recorded at 30 °C (corresponding to the calcined state of the catalysts) and then the temperature was raised to 400 °C under the diluted H_2 flow with a ramping of 2°C/min. XRD patterns were recorded at selected times after reaching the reduction temperature. No appreciable changes in the diffractograms were noticed already from the first pattern taken after 1 h of reduction at 400°C. The presented H_2-XRD data correspond, thus, to the measurements performed after 2 h of reduction.

4.6.1.2. XRD patterns of as-reduced catalysts

The *in situ* H_2-XRD patterns for the Co-Ru/TiO_2 catalysts after 2 h of reduction at 400°C are presented in Figure 4.S1. For the sake of clarity, only the 2θ region for which the main Co^0 diffractions appear (40°-50°) is shown in the figure. Although relatively low Co loading and overlapping with the intense TiO_2 peaks prevents a clear identification of the crystalline cobalt phases, the presence of weak diffractions at 44.2° (2θ)

of *fcc*-Co^0 (JCPDS 00-15-0806) and at 44.8° and 47.5° (2θ) of *hcp*-Co^0 (JCPDS 00-005-0727) is inferred in all three as-reduced catalysts. It is worth underlying that no reflections belonging to the spinel Co_3O_4 phase (the only crystalline Co phase observed in the calcined samples, Figure 4.4 in the manuscript) were detected after reduction in H_2 at 400°C, indicating a high extent of Co reduction, in agreement with the H_2-TPR profiles (Figure 4.6).

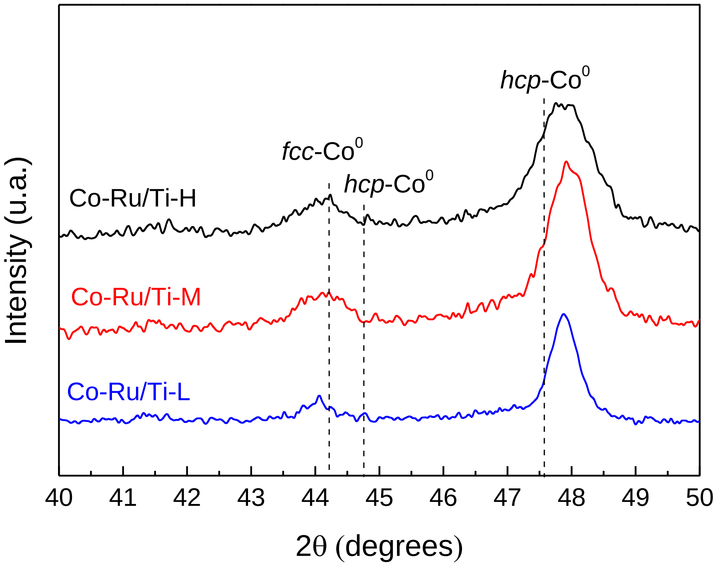

Figure 4.S1. XRD patterns recorded after *in situ* reduction of Co-Ru/TiO_2 catalysts in diluted H_2 flow (10 vol% H_2 in N_2) at 400 °C for 2 h.

CHAPTER 5

INFLUENCE OF RU PROMOTION ON CO/TIO$_2$ CATALYSTS FOR FISCHER-TROPSCH SYNTHESIS

In Chapters 3 and 4, the influence of the SMSI effect respect to titania crystalline phase and anatase surface area on Co-Ru/TiO_2 catalysts have been studied. In order to gain further insights on this complex catalytic system, in this chapter the influence of adding Ru as promoter of cobalt in Co/TiO_2-anatase catalysts is investigated. The catalytic consequences of increasing the Ru concentration in these catalysts is discussed.

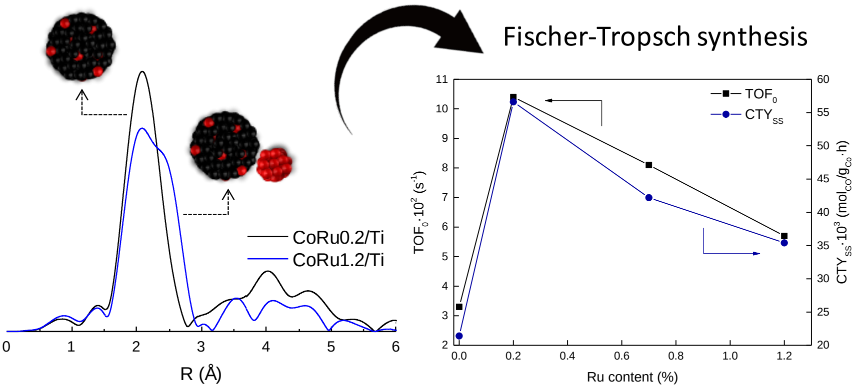

5.1. Introduction

Cobalt supported on porous inorganic oxides (most commonly SiO_2, Al_2O_3, and TiO_2) or carbon materials (carbon nanotubes or nanofibers) are suitable catalysts for the conversion of synthesis gas (syngas) to high quality, almost sulfur-free liquid fuels through the low temperature Fischer-Tropsch synthesis (FTS) process [1, 2]. Since the last few decades, FTS is experiencing a renewed interest due to the shortage in oil reserves and the possibility of obtaining syngas from alternative abundant resources such as natural gas and biomass which, by having a lower carbon footprint than oil, contribute to alleviate CO_2 emissions to the atmosphere. Due to the inherent kinetic limitation of the FTS reaction preventing the formation of gasoline- or diesel-range hydrocarbons in high selectivity, the Co-based catalyst and process conditions are typically adjusted to maximize the formation of long-chain *n*-paraffins (so-called FT waxes) which, after separation, are selectively hydrocracked to the targeted liquid fuel, predominantly to the most demanded diesel fuel [3].

Metallic cobalt atoms exposed on the surface of the supported Co nanoparticles are known to be the active sites for dissociation of H_2 and CO molecules in the syngas feed, formation of CH_x monomers, and C-C chain growth leading to higher (C_{2+}) hydrocarbons [4]. Nonetheless, the detailed FTS chemistry at the atomic level and the specific surface Co^0 atoms (or ensembles of atoms) involved in these reaction steps are still a matter of debate [5-7]. Among the most relevant catalyst design parameters influencing the activity, selectivity, and stability for FTS of supported Co catalysts are the metal loading, the size of the supported cobalt particles (i.e. dispersion), the degree of cobalt reduction (DOR) achieved after the H_2 reduction step typically performed prior the FTS reaction, the texture, morphology, and chemical identity of the support, and the presence of metal and/or metal oxide promoters [8-12]. Regarding cobalt particle size, while a constant intrinsic activity or turnover frequency (TOF) for the surface Co^0 atoms has been reported for cobalt particles larger than 6-8 nm irrespective of the support [4], a drastic decline in TOF with decreasing the particle size below this critical value was found for cobalt supported on carbon nanofibers [13] and silica-type supports [14].

Small amounts of noble metal promoters (most commonly Ru, Re, and Pt) are typically added to the Co catalyst in order to improve the degree of cobalt reduction or the metal dispersion, thereby increasing the concentration of surface Co^0 sites available for reaction [8, 9, 15]. As a consequence, a significant enhancement in the activity per total mass of cobalt (CTY: cobalt-time-yield) and, in some cases, in the intrinsic activity per cobalt metal site (TOF) have been reported. Improvements in selectivity to the C$_{5+}$ hydrocarbon fraction upon promotion with noble metals have also been claimed [16], although the promotion effect on selectivity is generally less pronounced than on activity [9, 15, 17].

The improvements in activity by promotion with noble metals have been associated to several different aspects. On one hand, some authors have attributed the increase in the number of active sites mainly to a higher degree of cobalt reduction (DOR) rather than to an increase in dispersion [8, 18]. The higher DOR is a result of the enhanced activity of noble metals to activate hydrogen, becoming a source for hydrogen spillover to cobalt oxides and hence, promoting its reduction at lower temperature [9].

On the other hand, others have associated the improvements in activity for noble metal-promoted Co catalysts to both an enhanced DOR and a higher cobalt dispersion [19-22]. In case of Al_2O_3-supported catalysts, the presence of noble metals greatly improves the reduction of small cobalt particles interacting strongly with the support, increasing the number of active cobalt metal sites [19, 23, 24]. The same behavior has been observed for Co nanoparticles supported on carbon nanotubes [17]. Besides, a higher content of metallic cobalt with *hcp* structure, which has been reported to be more active than *fcc* Co [25], has also been indicated to contribute to the increase in activity of Ag-promoted Co/TiO_2 catalysts in comparison with the unpromoted counterpart [15].

In case of Ru-promoted catalysts, several authors reported a higher activity for Co in bimetallic Co-Ru particles in comparison to monometallic Co particles [16, 22, 26-28]. In an early work, Iglesia and co-workers [16] reported a two-fold increase in CTY and 2-4 times higher TOFs for Ru-promoted Co/TiO_2 catalysts. This was attributed to a synergism between Co and Ru in bimetallic Co-Ru nanoparticles, where Ru assists in removing adsorbed carbon and oxygen species from the surface of Co particles impeding their deactivation in the initial stages of the FTS reaction. Interestingly, some authors have observed a Ru-enrichment on the surface of bimetallic Co-Ru nanoparticles for catalysts containing ≤ 0.2 wt% Ru [16, 28, 29], which facilitates hydrogen spillover to cobalt promoting its reduction and, in this way, improving the activity [29]. However, an increase in Ru concentration results in segregation of isolated Ru nanoparticles over the support, presenting no contribution [28] or even decreasing the catalytic activity [18, 22].

Furthermore, it has been reported that the optimum amount of Ru as promoter depends on the employed support [18], albeit with contradictory results. While some authors have reported, for silica based catalysts, slight improvements in CO conversion with the increase in Ru loading [18], others have shown either a detrimental [26] or a neutral [29] effect on activity above a certain Ru concentration. Conflicting results have also been described for alumina-supported Co catalysts, for which some authors reported a decrease in CO conversion at higher amounts of Ru [18, 22, 23], while others did not observe any clear influence of Ru concentration on catalysts activity [28].

Thus, due to its high cost [9], it is important to determine the appropriate amount of Ru to use during catalyst preparation in order to take full advantage of its promoter effect. For titania-based catalysts, where low Ru loadings (≤ 0.2 wt%) have been commonly used in most of the previous works [8, 15, 16], there are no studies, to the best of our knowledge, addressing in detail the effect of Ru concentration on the FTS performance. Besides, titania-supported metal catalysts can undergo the well-known strong metal-support interaction (SMSI) effect, by which partially reduced TiO_x species generated during reduction in H_2 at high temperatures migrate from the support and (partly) cover the surface of the supported metal nanoparticles inhibiting their capacity to chemisorb H_2 and CO [30, 31]. Due to this, the CoRu/TiO_2 system is challenging to characterize as the SMSI effect can be reverted, at least in part, under reaction conditions by re-oxidation of the TiO_x decorating species with water generated in the FTS reaction [31, 32]. This makes tricky to determine the true amount of surface Co^0 sites available for reaction in the *working* catalyst, which may significantly differ from that determined for the H_2-reduced catalyst by *ex-situ* H_2 chemisorption measurements.

Based on the above premises, here we investigate the influence of Ru addition and its concentration (0.2, 0.7, and 1.2 wt%) in Co (ca. 12 wt%) catalysts supported on high surface area TiO_2-anatase and the consequences on the activity and selectivity for FTS. In order to shed light on the origin of the observed Ru promotion effects, the catalysts were characterized by both conventional techniques (e.g. XRD, N_2 adsorption, H_2-TPR, H_2 chemisorption, HAADF-STEM) and by *in situ* CO-FTIR, XPS, and XAS spectroscopies.

5.2. Experimental

5.2.1. Synthesis of anatase support

Pure TiO_2-anatase support was synthesized by a hydrothermal method using titanium (IV) butoxide (97%, Aldrich) and acetic acid (99.5%, Aldrich) as reagents. In short, 9.6 mL of titanium (IV) butoxide were added dropwise to 28 mL of acetic acid solution (1.5 mol/L) under magnetic stirring at room temperature. Afterward, the mixture was introduced into a Teflon-lined stainless steel autoclave of 200 mL capacity and hydrothermally treated at 120 °C for 24 h. Subsequently, the solid was recovered by centrifugation, washed 5 times with ethanol in a process involving redispersion and centrifugation, dried at 60 °C overnight, and finally calcined in flowing air at 400 °C for 4 h using a heating rate of 1 °C/min.

5.2.2. Synthesis of CoRu/TiO_2 catalysts

The catalysts were prepared by incipient wetness co-impregnation of the calcined TiO$_2$-anatase support with an aqueous solution containing $Co(NO_3)_2 \cdot 6H_2O$ (Aldrich) and $Ru(NO)(NO_3)_3$ (Aldrich), targeting a nominal cobalt loading of 10 wt% and nominal Ru concentrations of 0.5, 1.5, and 2.5 wt%. The impregnated materials were dried at 100 °C overnight, and subsequently calcined in flowing air at 300 °C for 3 h. The catalysts were labeled according to their final Ru contents (measured by ICP-OES) as CoRu0.2/Ti, CoRu0.7/Ti, and CoRu1.2/Ti corresponding to the nominal contents of 0.5, 1.5, and 2.5 wt% Ru, respectively. For comparison purposes, a catalyst without Ru was additionally prepared (Co/Ti) following the same methodology described above for Ru-promoted samples.

5.2.3. Characterization techniques

Cobalt and ruthenium loadings were obtained by Inductively Coupled Plasma-Optical Emission Spectrometry (ICP-OES) in a Varian 715-ES spectrometer after dissolving the samples in an acid mixture of HNO_3:HF:HCl (1:1:3 volume ratio).

X-ray powder diffraction (XRD) was performed on the calcined materials using a Philips X’Pert diffractometer using monochromatized CuK$_\alpha$ radiation (λ = 0.15406 nm). Average TiO$_2$ particle sizes were calculated from the most intense (1 0 1) reflection of anatase (2θ = 25.3°) using the Scherrer’s equation, assuming a shape factor k = 0.9.

In situ H$_2$-XRD measurements were performed to assess the crystalline phases present in the as-reduced catalysts. The measurements were performed in a Panalytical Empyrean diffractometer using Cu-K$_\alpha$ radiation. The samples were loaded in a XRK 900 Anton Paar reaction chamber and flushed with a gas stream comprising 10 vol% H_2 diluted in N_2. In these experiments, the X-ray diffractograms were first recorded at 25 °C (corresponding to the calcined state of the catalysts) and then the temperature was raised to 400 °C under the diluted H_2 flow with a ramping of 2 °C/min. XRD patterns were recorded at selected times after reaching the reduction temperature.

The N_2 adsorption isotherms were measured in a Micromeritics ASAP-2420 equipment at liquid N_2 temperature (-196 °C). Prior the analyses, the samples were degassed at 300 °C under vacuum overnight. Specific surface areas were determined following the Brunauer-Emmett-Teller (BET) method, pore size distributions were derived by applying the Barrett-Joyner-Halenda (BJH) approach to the adsorption branch of the isotherms, and total pore volumes were obtained at a relative pressure of 0.98.

Morphological analysis of the support was performed by field emission scanning electron microscopy (FESEM) using a ZEISS Ultra-55 microscope.

H_2 temperature-programmed reduction (H_2-TPR) was carried out using a Micromeritics Autochem 2910 device. Typically, 55 mg of catalyst were firstly flushed with an Ar flow at room temperature for 30 min, and subsequently, the gas atmosphere was switched to a mixture of H_2 diluted (10 vol%) in Ar. Next, the reduction took place by linearly increasing the temperature up to 900 °C at a heating rate of 10 °C/min and the H_2 consumption monitored using a thermal conductivity detector (TCD) previously calibrated using the reduction of a standard CuO sample as reference. A 2-propanol/$N_{2(liq)}$ trap located downstream the analyzer was used to retain water and to ensure that only H_2 reaches the detector. In order to determine the degree of cobalt reduction (DOR), additional experiments were carried out in the same equipment. First, the catalysts were reduced *in situ* at the same conditions applied prior the FTS reaction (i.e. at 400 °C for 10 h under flowing pure H_2). Then, after switching to the diluted H_2 stream (10 vol% H_2 in Ar), the temperature was increased from 400 °C to 900 °C at a heating rate of 10 °C/min while monitoring the H_2 signal in the TCD. The DOR was then calculated from the amount of H_2 consumed assuming that this corresponds to the reduction of CoO that remained on the catalyst after the 400 °C reduction treatment.

The amount of surface cobalt metal sites was measured by H_2 chemisorption at 100 °C in a Quantachrome Autosorb-1C instrument by extrapolating the total gas uptakes in the adsorption isotherms at zero pressure [33]. Before measurements, approx. 300 mg of catalyst were reduced under pure H_2 flow at 400 °C for 10 h. From the total amount of chemisorbed H_2, the mean cobalt particle size ($d(Co^0)_{H2}$) was estimated taking into account the Co content (from ICP-OES) and the DOR, assuming spherical particles and an adsorption stoichiometry H/CO of 1.

Direct measurement of cobalt particle sizes was performed by transmission electron microscopy in a JEOL-JEM 2100F microscope operating at 200 kV in scanning transmission mode (STEM) using a high-angle annular dark field (HAADF) detector which provides contrast that has a strong dependence on atomic number. Energy dispersive X-ray spectroscopy (EDS) was used to confirm the presence and location of Co and Ru particles in the samples using a X-Max 80 detector from Oxford Instruments equipped with Aztec software. Before microscopy observation, the samples were first reduced *ex situ* under a flow of pure H_2 at 400 °C and passivated at room temperature under a flow of 0.5 vol%

O_2/N_2. Afterward, the materials were suspended in isopropanol and ultrasonicated for one minute. Then, a drop was extracted from the top side of the suspension and deposited on a carbon-coated copper grid. Average cobalt particle sizes ($d(Co^0)_{STEM}$) were evaluated after measuring 200-300 particles from several micrographs taken at different positions on the TEM grid, and after correcting for the presence of a 2.5 nm thick CoO passivation outlayer.

CO-FTIR spectra were recorded with a Nexus 8700 FTIR spectrometer using a DTGS detector and acquiring at 4 cm^{-1} resolution. An IR cell allowing *in situ* treatments in controlled atmospheres and temperatures in the 25-500 °C range was connected to a vacuum system with gas dosing facility. For IR studies, the samples (pre-reduced *ex situ* at 400 °C for 10 h in pure H_2 flow and subsequently passivated) were pressed into self-supported wafers of approx. 13 mg, and reduced again in the IR cell at 400 °C for 2 h in flowing H_2. Afterwards, the samples were cooled down to 60 °C under dynamic vacuum and syngas (14 mL/min) was passed through the cell at atmospheric pressure. Next, the temperature was increased stepwise up to the FTS reaction temperature (60 °C → 160 °C → 200 °C → 220 °C) and the spectra recorded after 10 min at each intermediate temperature and after 4 h at the reaction temperature of 220 °C. After each measurement, the sample was cooled for 5 minutes and the spectrum recorded again in order to monitor the strength of CO adsorption and thermal stability of the IR bands. At the end of analysis, the IR cell was evacuated at 220 °C and a final spectrum was recorded. Spectra analysis was done using the Origin software.

CO-FTIR spectra with syngas at a higher pressure of 9 bar were recorded in the same equipment described above but using a AABSPEC catalytic cell. For IR studies, pre-reduced and passivated samples were reduced again in the cell at 275 °C for 2 h in flowing H_2. Afterwards, the samples were cooled down to 100 °C and the gas atmosphere was switched to syngas. Next, the cell was pressurized up to 9 bar and the temperature was increased stepwise (100 and 160 °C) up to the FTS reaction temperature of 220 °C and the CO-FTIR spectra recorded after each intermediate step and after 4 h of reaction at 220 °C.

X-ray photoelectron spectra (XPS) were collected on a SPECS spectrometer equipped with a 150-MCD-9 detector and a non-monochromatic and monochromatic AlK_α (1486.6 eV) X-ray source. Spectra were recorded using an analyzer pass energy of 30 eV, an X-ray power of 200 W and under an operating pressure of 10^{-9} mbar. During data processing of the XPS spectra, binding energy (BE) values were referenced to C1s peak (284.5 eV). Spectra treatment was performed using the CASA software. Around 20 mg of sample were pre-reduced at 400 °C in H_2 flow (5 ml/min) for 5 h in a high pressure catalytic reactor (HPCR) connected directly to the XPS analysis chamber, thus avoiding direct exposure of the sample to air. The FTS reaction was performed in the HPCR at 220 °C operating at 9 bar and 10 ml/min of syngas for 3 h. The reaction products were analyzed by online mass spectrometry.

X-ray absorption experiments at the Ru K-edge (22117 eV) were carried out at the BM23 beamline of the European Synchrotron Radiation Facility (ESRF, Grenoble, France). The white beam was monochromatized using a Si (111) double crystal cooled with liquid nitrogen; harmonic rejection was performed using two Pt-coated Si mirrors. The spectra were collected in fluorescence mode using a SSD detector. The CoRu/Ti catalysts were placed in powder form inside a catalytic cell and reduced in flowing H_2 at 400 °C for 3 h at atmospheric pressure. Subsequently, the temperature was decreased to 100 °C for data acquisition in order to avoid thermal effects on the collected spectra and to improve signal quality. Afterwards, a flow of syngas with $H_2/CO = 2$ (molar ratio) was passed through the cell, the temperature raised to 220 °C at ambient pressure, and the spectra measured after 3 h at these conditions (FTS). XAS experiments at Ru K-edge were also performed at higher pressure (7 bars) during FTS reaction at the BL22 (CLÆSS) beamline of ALBA synchrotron (Cerdanyolla del Vallès, Spain) [34]. The white beam was monochromatized using a Si (111) double crystal; harmonic rejection was performed using Rh-coated silicon mirrors. The spectra were collected in fluorescence mode by means of a fluorescence SSD detector. The catalysts, in the form of self-supported pellets of optimized thickness, were located inside an in-house built multipurpose cell described by Guilera [35] allowing *in situ* experiments. Three scans were acquired at each measurement step to ensure spectral reproducibility and good signal-to-noise ratio. The extraction of the $\chi(k)$ function was performed using Athena code; analysis of the EXAFS data was done using the Arthemis software [36]. Ab initio phase and amplitudes were calculated by FEFF6 code and successfully checked with Ru metal powder. For each sample, the averaged $k^3\chi(k)$ function was Fourier transformed in a determined $\Delta k = 2.6 – 12.0$ Å^{-1} interval. To reduce the number of variables and the correlation between them, a co-refinement approach was adopted, fitting all spectra of reduced samples at the same time in different k-weights. The fits were performed in R-space in the $\Delta R = 1.4 – 3.0$ Å range, resulting in a number of independent points equal to 37.2. The passive electron amplitude reduction factor was fixed to that found for metallic Ru ($S_0^2 = 0.72$).

5.2.4. Fischer-Tropsch synthesis experiments

FTS experiments were carried out in a fixed-bed stainless steel reactor (internal diameter of 10 mm and length of 40 cm) loaded with 0.5 g of catalyst (0.25-0.42 mm pellet size), diluted with SiC granules (0.6-0.8 mm) to reach a total bed volume of 6.4 cm^3. Before reaction, the catalysts were reduced *in situ* at ambient pressure in flowing H_2 at 400 °C for 10 h (1 °C/min). After reduction, the reactor was cooled down to 100 °C under flowing H_2, the gas atmosphere changed to syngas with H_2/CO molar ratio of 2 ($CO:H_2:Ar$ volume ratio of 3:6:1, Ar used as internal standard for GC analyses), the pressure increased up to 20 bar, and the temperature raised up to 220 °C (2 °C/min). Two thermocouples connected to independent PID controllers were used to control the temperature through the catalytic bed. After the reaction temperature was established, a third vertically sliding thermocouple was employed to check the absence of temperature gradients (T = 220 ± 1 °C) along the bed. A constant gas hourly space velocity (GHSV) of 11.7 $L_{syngas}/(g_{cat}\cdot h)$ was stablished during the first 8 h of reaction in order to compare the activity of catalysts at quasi-differential conditions (CO conversion < 10%) and, hence, to ensure a low water partial pressure in the catalytic bed. Subsequently, the GHSV was adjusted for each catalyst to reach a constant CO conversion of 10 ± 2% in the *pseudo*-steady state and kept at this condition for an additional period of ca. 8 h. The stream leaving the reactor was depressurized and periodically analyzed on line by gas chromatography in a Varian 450 chromatograph equipped with TCD and FID detectors and three columns. Heavier products and water were condensed in two consecutive traps (at 150 °C and 100 °C, respectively), both at 20 bar, and after weighted and diluted with CS_2, the hydrocarbon fractions collected in the traps were analyzed off line in the same GC. The final product distribution was obtained upon combining the on line and off line GC analyses through the common product methane, resulting in carbon mass balances of 100 ± 2%. Product selectivities are given on a carbon basis.

5.3. Results and discussion

5.3.1. Characterization of the TiO_2-anatase support

The XRD pattern of the calcined support (Figure 5.1) confirms that the synthesized TiO_2 material consists of pure anatase (JCPDS 00-021-1272) with an average crystallite size of ca. 10 nm, as calculated by the Scherrer equation. As already indicated in the literature, the use of acetic acid during hydrothermal synthesis preferentially leads to the crystallization of the anatase phase [37, 38]. Moreover, as we showed in a recent study [39], the use of a synthesis temperature of 120 °C, an acetic acid concentration of 1.5 mol/L, and calcination in flowing air at 400 °C, as applied in the present case, results in pure TiO_2-anatase crystallites with high surface area.

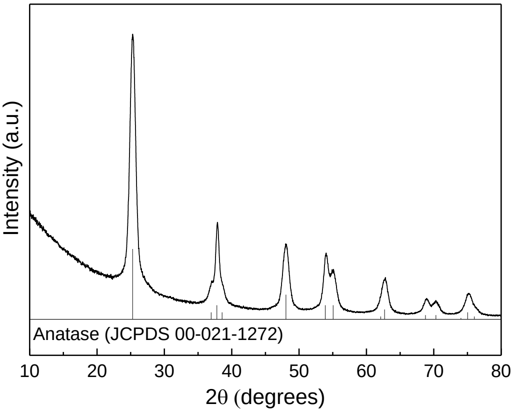

Figure 5.1. X-ray diffraction pattern of calcined TiO_2-anatase support.

The calcined anatase support presented a type IV adsorption-desorption isotherm (Figure 5.2), characteristic of mesoporous solids, similar to other TiO_2 reported in literature [40-42], with a large hysteresis loop at high relative pressure related to capillary condensation, showing a mixture between H1 (typical of materials exhibiting uniform mesopores) and H2 (relative to pore blocking effects) type pores [43]. Besides, the support presents high specific surface area (158 m^2/g, Table 5.1), mean pore diameter of 9.8 nm, and total pore volume of 0.28 cm^3/g, as expected from the applied synthesis conditions [39].

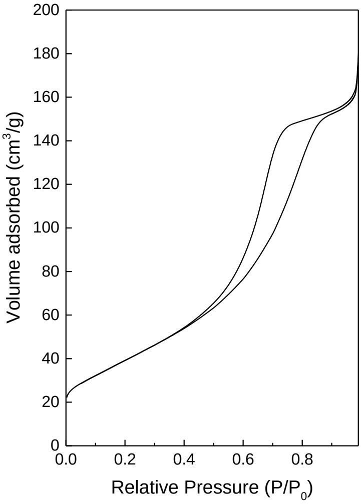

Figure 5.2. N_2 adsorption-desorption isotherm for calcined TiO_2-anatase support.

As evidenced by the representative FESEM image shown in Figure 5.3, the TiO_2-anatase support comprises small rice-like crystallites with sizes ranging from 10 to 30 nm, in fair agreement with XRD. The TiO_2-anatase morphology, as well as its crystallite size, are mainly controlled by the employed synthesis conditions, as reported previously [38, 39].

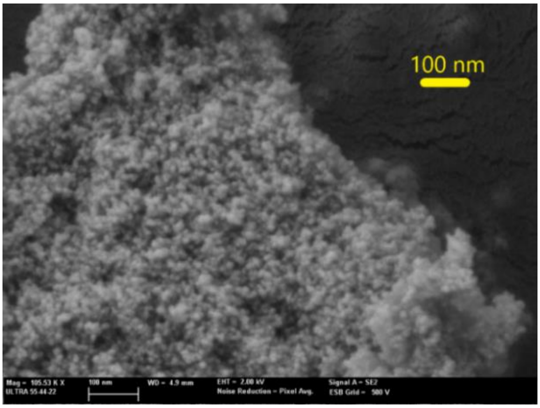

Figure 5.3. Representative FESEM image for calcined TiO_2-anatase support.

5.3.2. Characterization of CoRu/TiO2 catalysts

The X-ray diffraction patterns of calcined CoRu/Ti and Co/Ti catalysts are presented in Figure 5.4. The diffraction peaks related to the Co_3O_4 spinel phase (JCPDS 00-042-1467) are marked for better visualization. Despite that in all calcined catalysts the Co_3O_4 crystalline phase was unambiguously identified, a reliable measurement of its crystallite size by XRD line broadening analysis was not possible due to the low relative intensity of the Co_3O_4 peaks and overlapping with the reflections of the highly crystalline anatase phase. In spite of the low quantity of Ru used in this work, reflections of RuO_2 (JCPDS 00-040-1290) could be identified in the catalyst CoRu1.2/Ti with higher Ru loading (inset in Figure 5.4). It is worth mentioning that no changes in the TiO_2 crystalline phase (anatase) or in its mean crystallite size were noticed upon impregnation of the support with the metal precursors and calcination.

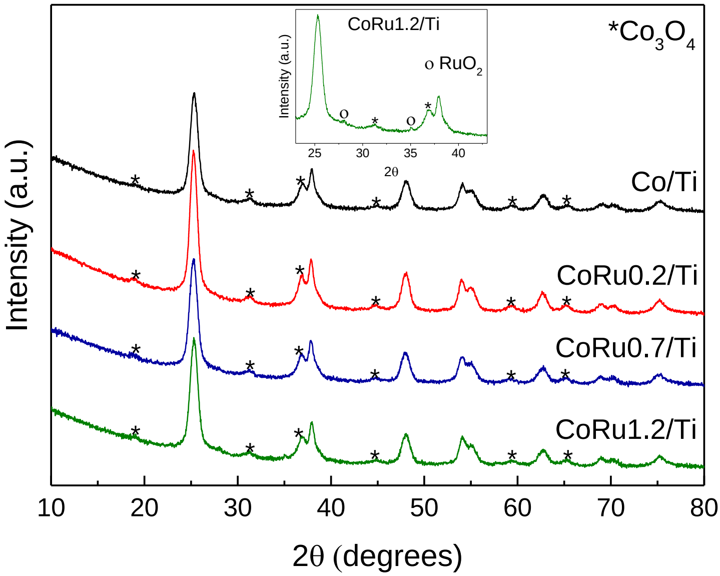

Figure 5.4. X-ray diffraction patterns of calcined Co/TiO_2 and CoRu/TiO_2 catalysts. The characteristic diffraction lines of Co_3O_4 spinel (JCPDS 00-042-1467) are marked (*) for an easier identification. The inset shows the reflections related to RuO_2 (marked with o) (JCPDS 00-040-1290) in the CoRu1.2/Ti catalyst.

As shown in Figure 5.5a, the N_2 adsorption isotherms for the calcined catalysts can also be classified as type IV, characteristic of mesoporous solids [43], resembling the isotherm of the TiO_2 support (Figure 5.2). The catalysts showed unimodal pore size distributions with maximum diameters centered at approximately 9-10 nm (Figure 5.5b), reflecting minor changes with respect the pristine support. The textural properties of the catalysts derived from N_2 adsorption isotherms are summarized in Table 5.1. The BET surface area of the catalysts experienced a decrease of 22-24% relative to the support. However, when these values are corrected per mass of TiO_2 (values between parenthesis), the reduction is much less pronounced and below 10% in all cases. In addition, the mean pore diameter and total pore volume of the catalysts showed minor deviations with respect to the support, indicating a negligible pore blockage by the supported metal oxides.

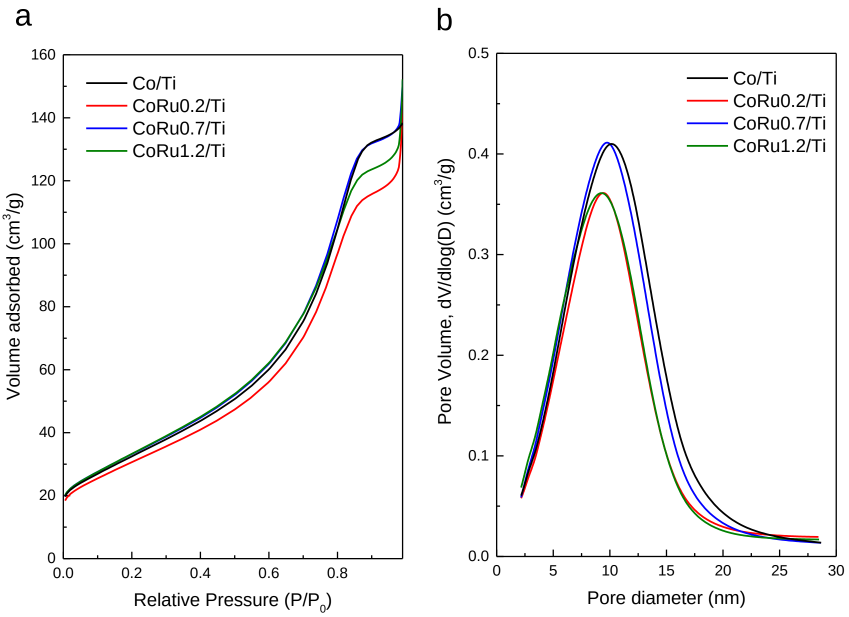

Figure 5.5. N_2 adsorption isotherms (a) and corresponding pore size distributions (b) for calcined Co/TiO_2 and CoRu/TiO_2 catalysts.

As shown in Table 5.1, the Co contents determined by ICP-OES (11.4-12.2 wt%) exceeded by about 20% the nominal value (10 wt%) for all catalysts. The Ru contents (0.2-1.2 wt%), however, are 50-60 % inferior than the theoretical values (0.5-2.5 wt%), which is explained by the formation of volatile RuO_x species during calcination in air in presence of Co_3O_4 [27].

Table 5.1. Textural properties derived from N_2 adsorption isotherms and metal contents (from ICP-OES) for Co/TiO_2 and $CoRu/TiO_2$ catalysts.

Catalyst	BET area [a] (m^2/g)	Pore diameter (nm)	Total pore volume [a] (cm^3/g)	Metal content (wt %)	
				Co	Ru
TiO_2	148	9.1	0.25	-	-
Co/Ti	112 (134)	9.9	0.21 (0.25)	12.2	-
CoRu0.2/Ti	113 (135)	9.7	0.20 (0.24)	11.8	0.2
CoRu0.7/Ti	112 (134)	9.8	0.22 (0.26)	11.4	0.7
CoRu1.2/Ti	116 (141)	9.7	0.21 (0.25)	11.8	1.2

[a] Values in parentheses correspond to the data recalculated per mass of TiO_2 support.

Figure 5.6 shows the H_2-TPR profiles of Ru-promoted and unpromoted Co/TiO_2 catalysts. In line with the literature [15, 27], the reduction of Co_3O_4 takes place in two main steps, the first corresponding to the reduction of Co_3O_4 to CoO, and the high-temperature feature to the reduction of CoO to Co^0. For the Ru-containing catalysts, the temperature of maximum H_2 consumption for the first and second reduction steps were 100-124 °C (T1) and 226-274 °C (T2), respectively. However, for the Co/Ti catalyst the temperatures of maximum H_2 consumption for the two reduction steps were observed at 262 °C (T1) and 443 °C (T2), which are remarkable higher than those obtained for CoRu/Ti catalysts. A small third reduction feature can be perceived at higher temperatures for the $CoRu/TiO_2$ catalysts (T3= 395-398 °C), which is ascribed to the reduction of Co^{2+} species displaying a stronger interaction with the TiO_2 support. In the case of Co/Ti, this feature is enclosed in the second reduction peak (T2= 443 °C). Therefore, the presence of Ru promotes the reduction of cobalt oxides leading to a significant shift of both reduction peaks to lower temperatures, in conformity with the literature [15, 29]. Besides, an even higher shift of T1 and T2 to lower temperatures is observed with the increase in Ru content from 0.2 to 0.7 wt%, in agreement with previous studies [26, 28]. On the other hand, no significant differences in the reduction profiles are observed for catalysts CoRu0.7/Ti and CoRu1.2/Ti, indicating that an increase in Ru loading from 0.7 to 1.2 wt% Ru does not further increase the reducibility of cobalt oxides. A similar trend was also reported at increasing Ru loadings for RuCo/Al_2O_3 catalysts [8, 23].

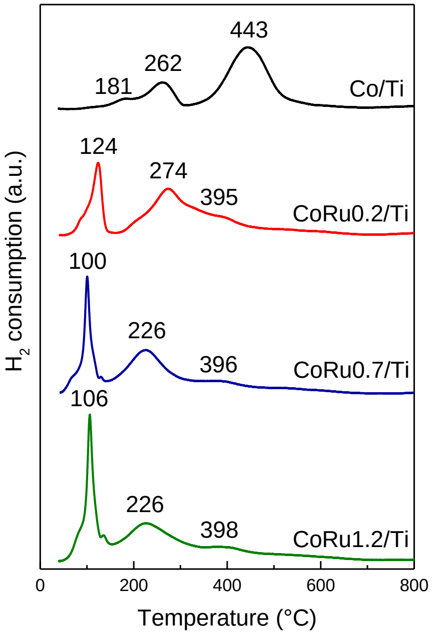

Figure 5.6. Temperature-programmed reduction profiles of Co/TiO_2 and CoRu/TiO_2 catalysts.

In spite of the differences in reduction temperatures between the Ru promoted and unpromoted samples, as inferred from the respective H_2-TPR profiles, all catalysts presented similar and high DOR values (88-93%) after reduction in pure H_2 at 400 °C for 10 h (Table 5.2). However, as fairly reported in literature [30, 31, 44, 45], when submitted to a hydrogen flow at high temperatures, titania-supported metal nanoparticles experience the so-called strong metal-support interaction (SMSI) effect, by which partially reduced TiO_x species migrate from the support and decorate the surface of the supported nanoparticles. Considering this, it is likely that some of the H_2 consumed during the second H_2-TPR measurements (from 400 to 900 °C) performed to calculate the degree of cobalt reduction (DOR, see section 5.2.3) should be related to the partial reduction of TiO_2. Due to this, the calculated DOR values presented in Table 5.2 are probably underestimated and should thus be very close to 100%, as commonly observed for TiO_2-supported Co catalysts [46, 47]. Therefore, in this study we assumed 100% cobalt reduction in all the catalysts for calculating Co^0 particle sizes from H_2 chemisorption data and TOFs.

Table 5.2. Properties of cobalt in the Co/TiO_2 and CoRu/TiO_2 catalysts.

Catalyst	H_2 uptake (µmol/g_{cat})	DOR[a] (%)	Co^0 particle size (nm)	
			$d(Co^0)_{H2}$	$d(Co^0)_{STEM}$
Co/Ti	8.9	89.2	111.7	9.6
CoRu0.2/Ti	17.6	88.3	54.6	7.2
CoRu0.7/Ti	39.1	92.0	23.7	6.2
CoRu1.2/Ti	32.4	92.9	29.7	6.3

[a] DOR: degree of cobalt reduction.

The average size of the supported cobalt nanoparticles in the reduced catalysts was calculated from both H_2 chemisorption and direct observation by STEM. Irrespective of the technique, the mean Co^0 particle size decreased with raising the Ru content up to 0.7 wt% and then barely changed when the Ru loading was further increased to 1.2 wt% (Table 5.2). The decrease in the average Co^0 particle size upon addition of Ru can also be inferred by analyzing the Co^0 particle size distributions derived from STEM measurements (Figure 5.7). Indeed, as seen in Figure 5.7 (bottom), the Ru promoted catalysts contain a significantly higher proportion of Co^0 nanoparticles sizing less than 6 nm (24-48%) in comparison to the unpromoted Co/Ti sample (9%). Therefore, an increase in Ru content up to 0.7 wt% is concluded to improve the cobalt dispersion, probably as a result of the Ru-assisted reduction of the smaller cobalt nanoparticles interacting strongly with the TiO_2 support, as suggested in the literature [8] and also as inferred from the H_2-TPR profiles discussed above. In addition, other authors explained the increase in Co dispersion by an increase in the concentration of CoO nucleation sites in presence of Ru leading to the formation of smaller cobalt NPs [20].

It is remarkable that the Co^0 particle sizes derived from H_2 chemisorption experiments are significantly greater than those directly measured by STEM. This apparent discrepancy is attributed to the reduction in the H_2 chemisorption capacity of cobalt due to the SMSI decoration effect [30, 31].

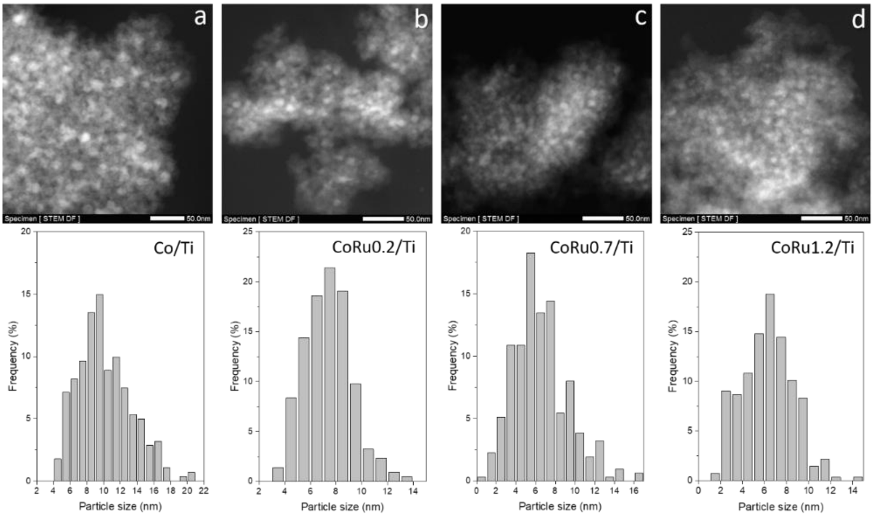

Figure 5.7. HAADF-STEM micrographs (top) for H$_2$-reduced and passivated Co/Ti (a), CoRu0.2/Ti (b), CoRu0.7/Ti (c) and CoRu1.2/Ti (d) catalysts. The respective Co^0 particle size histograms are represented beneath its representative corresponding image.

Additionally, EDS mapping was performed in order to study the spatial distribution of Co and Ru over the support particles (Figure 5.8). Although cobalt appears well distributed in all catalysts, some agglomerated regions can be perceived, as commonly reported for *ex*-nitrate impregnated Co catalysts [10]. In the case of Ru-promoted samples, while a uniform distribution of Ru species was apparent for the catalyst with the lowest Ru loading (CoRu0.2/Ti), some agglomerated Ru regions were evidenced for the catalysts loaded with 0.7 and 1.2 wt% Ru (Figure 5.8c,d), suggesting the presence of isolated (not interacting with Co) metallic Ru particles.

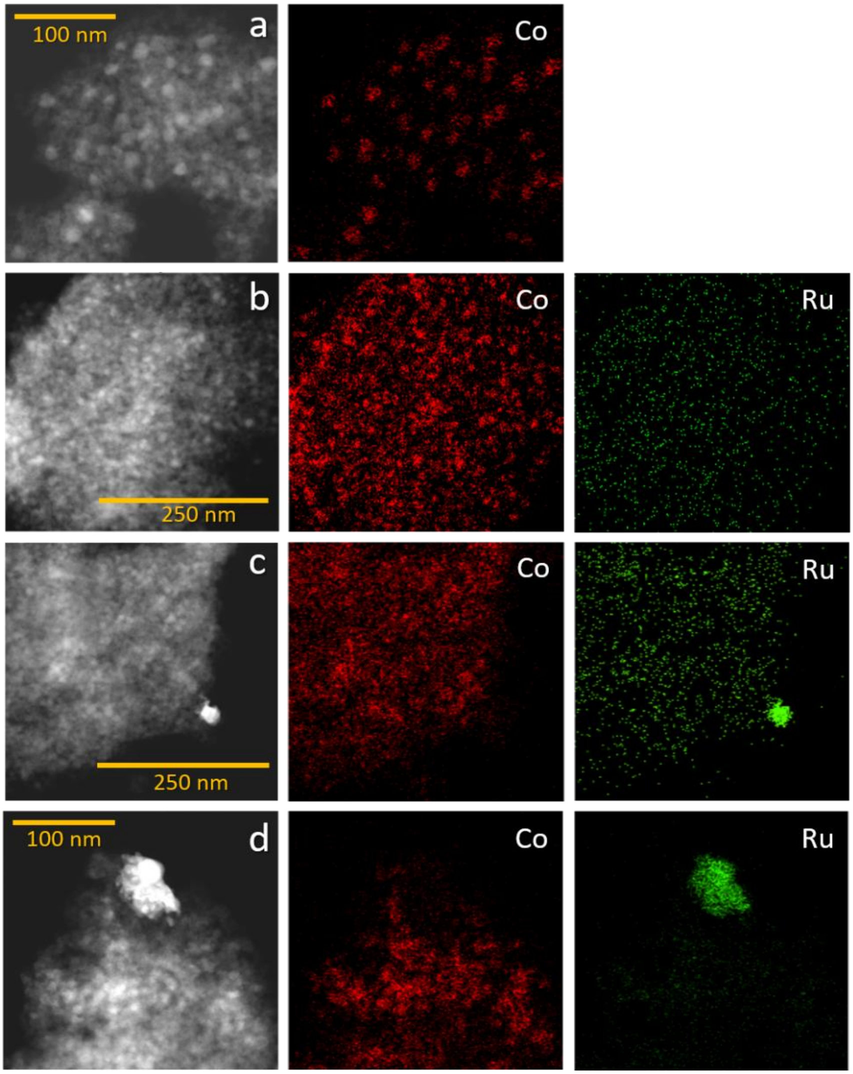

Figure 5.8. EDS elemental mapping for H_2-reduced and passivated Co/Ti (a), CoRu0.2/Ti (b), CoRu0.7/Ti (c) and CoRu1.2/Ti (d) catalysts.

In an earlier work, Iglesia and co-workers [16] studied the influence of adding small amounts of Ru to Co/TiO_2 and Co/SiO_2 catalysts (atomic Ru/Co ratios < 0.008). In that work, these authors related the higher FTS activity of Ru-promoted catalysts to a synergic effect between

Co and Ru in bimetallic Co-Ru particles. In a later work, Hong and co-workers [27] also attributed the increase in activity observed upon addition of 0.2 wt% Ru to a Co/SiO_2 (10 wt% Co) catalyst to the formation of bimetallic Co-Ru particles in which, according to *in situ* XAS measurements, Ru was embedded as individual atoms or small clusters [27]. In both works, the authors attributed the enhanced catalytic activity of the promoted catalysts to the presence of Ru atoms in close contact with Co in the bimetallic Co-Ru particles, resulting in a higher Co^0 site density during reaction [16, 27].

It seems, then, that an intimate contact between Co and Ru in bimetallic particles is of primordial importance to attain the desired promotion effect. In order to ascertain whether bimetallic Co-Ru phases were present in our CoRu/TiO_2 catalysts, the samples were characterized by XAS, a powerful element-sensitive technique that provides information on the local and electronic structure of minority metal atoms [48]. The results of the XAS characterization are discussed in the following section.

5.3.3. In situ characterization of as-reduced CoRu/Ti catalysts by XAS

The three Ru-containing catalysts were studied by X-ray absorption spectroscopy (XAS) on the Ru K-edge to obtain information on the speciation of Ru atoms in catalysts reduced *in situ* under H_2 flow at 400 °C for 3 h. Figure 5.9 presents the normalized XANES spectra of the Ru-promoted catalysts as well as of bulk Ru powder used as reference for metallic Ru species (Ru^0). For all the as-reduced Ru-promoted catalysts, the absorption edge in the XANES spectra is positioned at 22117 eV, indicating that Ru atoms are predominantly present as Ru^0.

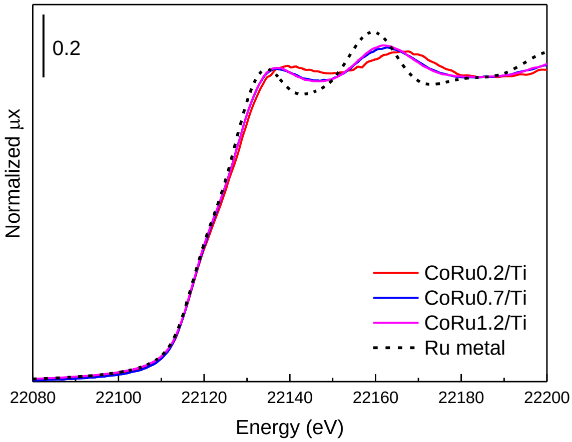

Figure 5.9. Normalized XANES spectra at Ru K-edge for as-reduced CoRu/TiO_2 catalysts.

As observed in Figure 5.9, the intensity of two first oscillations in the XANES spectra of the CoRu/TiO_2 catalysts appears flattened with respect to the Ru reference, signing for a smaller size of the metallic Ru species in the former samples [49]. Interestingly, the oscillations for CoRu0.2/Ti are shifted by ca. 5 eV with respect to those of CoRu0.7/Ti and CoRu1.2/Ti catalysts, suggesting a different neighborhood for Ru atoms in the low (0.2 wt%) and high (0.7-1.2 wt%) loaded samples. For a deeper analysis, the fine structure was investigated and the k^3-weighted, phase-uncorrected χ(k) functions and Fourier transformed spectra of the as-reduced catalysts and the reference Ru^0 sample are shown in Figure 5.10a and 5.10b, respectively.

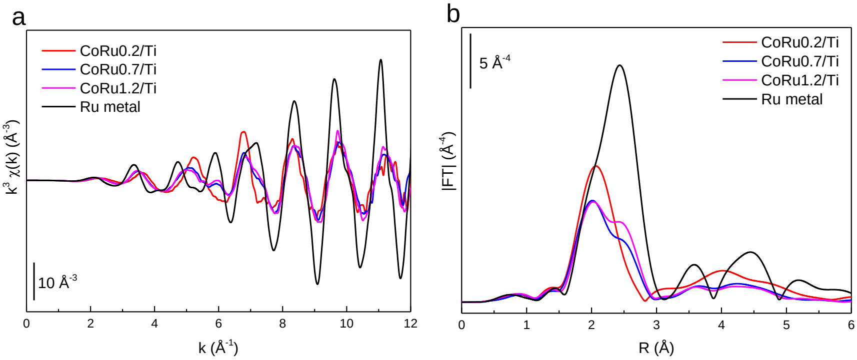

Figure 5.10. k^3-weighted, phase-uncorrected χ(k) functions (a) and |FT| of the EXAFS spectra (b) of as-reduced CoRu/TiO$_2$ catalysts.

It can be seen in Figure 5.10a that at low k-values (2 to 8 Å^{-1}) the catalyst promoted with 0.2 wt% Ru is completely in antiphase (first two oscillations peaking, respectively, at 3.62 and 5.21 Å^{-1}) with respect to the Ru^0 reference (first three oscillations with maxima at 3.32, 4.69, and 5.87 Å^{-1}, respectively). At higher k-values, however, the oscillations resemble those characteristic for metallic Ru atoms, albeit with lower intensity. On the other hand, at low k-values the samples with higher Ru contents (CoRu0.7/Ti and CoRu1.2/Ti) display an intermediate behavior between the reference Ru metal and the CoRu0.2/Ti sample, signing for two different local environments for Ru atoms in the former catalysts. Additional information can be gathered by analyzing the |FT| k^3-weighted χ(k) functions presented in Figure 5.10b, where the position and intensity of the peaks in the |FT| curves reflect the coordination and distances around Ru atoms. For CoRu0.2/Ti catalyst, the first shell is basically composed by a single peak centered at 2.1 Å (not corrected in phase) related to Ru-Co bonds, which indicates that Ru is alloyed with Co in this catalyst. Nonetheless, due to a certain asymmetry in the right-tail end of the first shell peak, the contribution of minority Ru-Ru species cannot be discarded.

In addition to the Ru-Co contribution at 2.1 Å seen for CoRu0.2/Ti, the catalysts with higher Ru contents exhibit a shoulder in the first shell peak at a longer distance (2.4 Å, not corrected in phase) that corresponds to the Ru-Ru distance in metallic Ru species. This is also confirmed by the presence of broad peaks at 3.56 and 4.38 Å attributed to higher coordination shells of Ru metal (Figure 5.10b). The rest of features observed in the |FT| spectra of these samples resemble those of the reference Ru metal powder.

The quantitative results derived from the analysis of the above EXAFS data are gathered in Table 5.3. The reference bulk Ru^0 sample shows a Ru coordination number of 12 with a Ru-Ru distance of 2.67 Å, characteristic of *hcp* Ru metal. To minimize the problems associated to the known strong correlation between the Debye-Waller factor and the amplitude during the analysis of EXAFS data [50], we adopted a co-refinement fit of the spectra resulting in only one Debye-Waller factor (σ^2) and photoelectron energy origin correction (ΔE_0) values for each neighbor contribution (i.e. one for Ru-Co and another for Ru-Ru). The first shell of the CoRu0.2/Ti catalyst is compatible with a Ru-Co alloy model, resulting in an average coordination number ($N_{Ru\text{-}Co}$) of 8.3 ± 0.8 with neighbors located at a distance of ca. 2.50 Å, which is significantly shorter than that of Ru metal (2.67 Å) and very close to the Co-Co distance in metallic Co particles (2.49 Å). This result clearly reinforces the formation of a Ru-Co alloy phase. Similar distances for alloyed Ru-Co have been reported in the literature [16]. Besides Ru-Co, it is also possible to include a Ru-Ru contribution in the |FT| spectrum of sample CoRu0.2/Ti without compromising the fitting goodness, resulting in $N_{Ru\text{-}Ru}$ of 1.6 (Table 5.3). Importantly, the fact that a similar fitting quality is obtained by considering only Ru-Co or both Ru-Co and Ru-Ru contributions suggests that, if present, only a small fraction of Ru is contributing to the formation of very small (subnanometric) Ru^0 clusters according to their low Ru-Ru coordination number ($N_{Ru\text{-}Ru}$ = 1.6 ± 0.5). On the other hand, the |FT| spectra of the catalysts with higher Ru loadings can be well fitted considering the contributions from both Ru-Co alloy (at 2.1 Å) and Ru-Ru metal (at 2.4 Å). As seen in Table 5.3, the average Ru-Co coordination number decreases along with a concomitant increase in Ru-Ru coordination number as the Ru loading in the CoRu/TiO$_2$ catalysts increases from 0.7 to 1.2 wt%. These results support the idea that, as the Ru content increases, Co-Ru alloying is less favored and segregation of metallic Ru species is promoted. Moreover, the fact that for both CoRu0.7/Ti and CoRu1.2/Ti samples the $N_{Ru\text{-}Ru}$ and $R_{Ru\text{-}Ru}$ values are lower than those expected for bulk metallic Ru (Table 5.3) points to the formation of very small metallic Ru clusters and/or nanoparticles for which quantum size effects are expected to appear [51].

Table 5.3. Summary of optimized parameters by fitting EXAFS data of catalysts measured at 100 °C after H_2 reduction at 400 °C and during catalysis (220 °C, 1 bar)[a].

Sample	Path	N	R (Å)	$\sigma^2_{Ru\text{-}Co}$ (Å^2)	$\sigma^2_{Ru\text{-}Ru}$ (Å^2)	$\Delta E_{0\ Ru\text{-}Co}$ (eV)	$\Delta E_{0\ Ru\text{-}Ru}$ (eV)	R_{factor}
Ru metal	Ru-Ru	12	2.673 ± 0.006	-	0.0030 ± 0.0011	-	5.0 ± 1.2	0.0069
CoRu0.2/Ti	Ru-Co	8.3 ± 0.8	2.498 ± 0.012	0.0076 ± 0.0012	0.0052 ± 0.0006	-1.6 ± 1.6	5.0 ± 0.6	0.0047
	Ru-Ru	1.6 ± 0.5	2.674 ± 0.028					
CoRu0.2/Ti - FTS	Ru-Co	6.9 ± 0.7	2.501 ± 0.012	0.0076 ± 0.0012	0.0052 ± 0.0006	-1.6 ± 1.6	5.0 ± 0.6	0.0055
	Ru-Ru	0.8 ± 0.4	2.711 ± 0.054					
CoRu0.7/Ti	Ru-Co	5.1 ± 0.5	2.504 ± 0.013	0.0076 ± 0.0012	0.0052 ± 0.0006	-1.6 ± 1.6	5.0 ± 0.6	0.0035
	Ru-Ru	4.6 ± 0.4	2.643 ± 0.006					
CoRu1.2/Ti	Ru-Co	4.4 ± 0.4	2.506 ± 0.013	0.0076 ± 0.0012	0.0052 ± 0.0006	-1.6 ± 1.6	5.0 ± 0.6	0.0045
	Ru-Ru	5.8 ± 0.3	2.647 ± 0.005					
CoRu1.2/Ti-FTS	Ru-Co	3.7 ± 0.3	2.514 ± 0.013	0.0076 ± 0.0012	0.0052 ± 0.0006	-1.6 ± 1.6	5.0 ± 0.6	0.0078
	Ru-Ru	4.5 ± 0.3	2.652 ± 0.005					

[a] The fits were performed on the first coordination shell (ΔR = 1.4-3.0 Å) over FT of the $k^1k^2k^3$-weighted χ(k) functions performed in the Δk = 2.6-12.0 Å^{-1} interval, resulting into a number of independent parameters of 2ΔRΔk/π = 46.5. Non optimized parameters are recognizable by the absence of the corresponding error bar. S_0^2 = 0.72.

Metal particle sizes and morphology in the nanometer range might be estimated from EXAFS results if some precautions are taken into account [52, 53]. Assuming a cubo-octahedral morphology and considering a narrow size distribution for the small Ru species, an average size for the Ru^0 clusters of 0.8-0.9 nm and 0.9-1.0 nm (considering the fitting errors and that all Ru atoms are involved in Ru-Ru species) were estimated for, respectively, CoRu0.7/Ti and CoRu1.2/Ti catalysts from their Ru-Ru average coordination numbers [54, 55]. It is also important to highlight that not all Ru atoms in these catalysts are present as monometallic clusters/nanoparticles as part of Ru is alloyed with Co forming bimetallic Co-Ru nanoparticles. However, the different Ru contents and similar XANES spectra (preventing a linear correlation approach) of CoRu0.7/Ti and CoRu1.2/Ti samples make unfeasible the estimation of the fraction of Ru atoms involved in either monometallic or bimetallic (Co-Ru) species.

5.3.4. Catalytic behavior of Co/TiO$_2$ and CoRu/TiO$_2$ catalysts in Fischer-Tropsch synthesis

As shown in Table 5.4, the Ru-promoted catalysts presented higher initial (extrapolated to zero TOS) and *pseudo*-steady state cobalt-time-yield (CTY) and TOF values than the Ru-free catalyst. Previous studies also reported an increase of 2-4 times in FTS activity for TiO$_2$-supported Co catalysts upon promotion with low amounts of Ru ($\leq$ 0.2 wt%) [15, 16]. Among the CoRu/TiO$_2$ samples studied here, that with the lowest Ru content (CoRu0.2/Ti) exhibited the highest activity, with initial and *pseudo*-steady state CTY and TOF values that are 2-4 times higher than those of Co/Ti, in close agreement with the mentioned in earlier works. Both CTYs and TOFs progressively declined with increasing the Ru content in our CoRu/TiO$_2$ catalysts from 0.2 to 1.2 wt% (Table 5.4). Although several authors did also report lower CO conversions at increasing Ru loadings [18, 22, 23, 26], others did not observe significant changes in activity above a certain Ru concentration [17, 19, 28, 29] and, thus, this issue remains unclear. The decrease in FTS activity at high Ru contents has been mainly attributed to a decrease in the degree of cobalt reduction (DOR) and, hence, in the amount of active metallic Co sites, due to the segregation of isolated Ru particles which are thus no longer in direct contact with Co atoms [18, 22]. This explanation, in principle, should not be valid for our catalysts as they all exhibit DOR values close to 100% (Table 5.2).

Table 5.4. Activity (expressed as CTY and TOF) of Co/Ti and CoRu/Ti catalysts for Fischer-Tropsch synthesis (FTS). Reaction conditions: T= 220 °C, P= 20 bar, H_2/CO = 2 mol/mol. Initial CTYs and TOFs were obtained by extrapolating the CO conversion-TOS curves at TOS$\rightarrow$0 at a constant GHSV of 11.7 $L_{syngas}/(g_{cat}\cdot h)$. *Pseudo*-steady state (SS) activities were averaged for the last 8 h of reaction after adjusting the GHSV for each catalyst in order to keep a constant CO conversion of ca. 10%.

Catalyst	$CTY\cdot10^3$ $(mol_{CO}/g_{Co}\cdot h)$[a]		$TOF\cdot10^2$ (s^{-1})[b]	
	Initial	SS	Initial	SS
Co/Ti	24.3	21.4	3.3	2.9
CoRu0.2/Ti	100.0	56.6	10.4	5.9
CoRu0.7/Ti	87.4	42.2	8.1	3.9
CoRu1.2/Ti	62.8	35.4	5.7	3.2

[a] CTY = cobalt-time-yield (activity per total mass of cobalt). [b] TOF = turnover frequency (activity per surface Co^0 site) calculated from STEM-derived Co^0 particle sizes assuming spherical particle morphology.

Besides, an increase in Co dispersion when increasing the Ru content has been reported by some authors [17, 19]. In the present study, a decrease in the average Co^0 particle size (i.e., an increase in metal dispersion) was observed by STEM when increasing the Ru concentration from 0 to 0.7 wt%, while a further increment in Ru content up to 1.2 wt% did not appreciably change the size of the Co^0 nanoparticles (Table 5.2). Moreover, the STEM images revealed a larger fraction of Co^0

nanoparticles sizing less than 6 nm (displaying lower TOF [13, 14]) for the high-loaded Ru-promoted catalysts (48% for CoRu0.7/Ti and 44% for CoRu1.2/Ti against 24% for CoRu0.2/Ti and 9% for Co/Ti). The much higher proportion of these intrinsically less active small-sized Co^0 nanoparticles in the CoRu0.7/Ti and CoRu1.2/Ti catalysts may explain, at least in part, the observed decrease in activity (both CTY and TOF) at Ru concentrations above 0.2 wt%. This, however, cannot account for the lower CTY and TOF of Co/Ti compared to CoRu/Ti samples. On the other hand, some authors [15] have attributed the increase in activity observed upon promotion of Co/TiO$_2$ with Ag to a larger amount of *hcp*-Co, which is believed to be more active than *fcc*-Co [25, 56]. In order to ascertain whether this might be a factor contributing to the higher activity of Ru-promoted catalysts, the Co crystalline phases present in the Co/Ti and CoRu0.2/Ti catalysts exhibiting the lowest and highest activity, respectively, were analyzed by *in situ* H$_2$-XRD at 400 °C. The obtained XRD patterns are shown in Figure 5.11, along with the theoretical diffraction lines for *hcp* (JCPDS 00-005-0727) and *fcc* (JCPDS 00-015-0806) metal Co phases. Although small diffraction peaks at 41.7 and 44.8° related to *hcp*-Co were detected in both as-reduced Co/Ti and CoRu0.2/Ti samples, no diffractions associated to *fcc*-Co could be evidenced suggesting that, if present, it should be in amounts below the detection limit of the technique. Therefore, we cannot attribute the differences in activity to a distinct proportion of *hcp* and *fcc* Co phases in our catalysts, although an unambiguous conclusion is hard to be reached based only on the presented *in situ* H$_2$-XRD results.

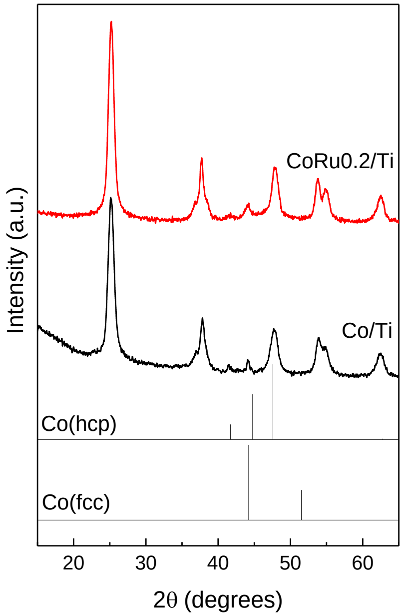

Figure 5.11. XRD patterns recorded after *in situ* reduction of Co/Ti and CoRu0.2/Ti catalysts in diluted H_2 flow at 400 °C for 3 h.

In other studies, the increase in activity of Ru promoted Co catalysts has been attributed to a synergistic effect between Co and Ru atoms in bimetallic nanoparticles, by which Ru inhibits the deactivation of nearby surface Co^0 sites by facilitating the removal of surface C and O species from CO dissociation, limiting the deposition of carbonaceous species [16]. The EXAFS results discussed beforehand unambiguously indicated the formation of alloyed Co-Ru particles after reduction in H_2 at 400 °C. It was also seen that part of the Ru segregated and formed isolated small Ru species sizing about 1 nm and some relatively large agglomerates when raising the Ru content from 0.2 to 0.7 wt%. A further increase in Ru concentration from 0.7 to 1.2 wt% resulted in even larger Ru particles and agglomerates, as identified by STEM and XRD. In order to ascertain whether or not the isolated Ru particles are contributing significantly to the FTS of the catalysts, an additional Co-free Ru/TiO_2 loaded with 0.4 wt% Ru was prepared and evaluated for FTS at same reaction conditions applied for CoRu/TiO_2 catalysts. At these conditions, the monometallic Ru/TiO_2 catalyst presented a CO conversion of only ca. 0.1% of CO conversion, indicating that the FTS activity associated to the isolated Ru sites is negligible compared to that of Co sites in CoRu0.7/Ti and CoRu1.2/Ti catalysts.

All the catalysts studied in this work, including the non-promoted one (Co/Ti), presented DOR values close to 100%. Moreover, significant differences in the prevailing crystalline phase of metallic cobalt (*hcp* vs. *fcc*) could not be evidenced for the as-reduced catalysts (*in situ* H_2-XRD). Therefore, neither the DOR or Co^0 crystalline phase may, in principle, account for the differences in FTS activity observed by Ru addition to Co/Ti and by increasing the Ru concentration in the Ru-promoted catalysts.

Table 5.5 presents the hydrocarbon selectivity in the *pseudo*-steady state for Co/Ti and CoRu/Ti catalysts at constant CO conversions of 10 ± 1%. In spite of some differences in product distribution among the catalysts are evidenced in Table 5.5, the effect of Ru promotion and Ru concentration on selectivity is less pronounced than on activity (Table 5.4). Nonetheless, the Ru-promoted catalysts systematically exhibited a higher selectivity to the target C_{5+} fraction (52.1 – 56.8%) in comparison to the monometallic Co/Ti catalyst (50.8%), as also observed in previous works [16, 17, 22]. Conversely, the selectivity to the C_2-C_4 fraction decreased with Ru promotion (from 32.3% to 27.2-29.9%) while methane selectivity was similar for the non-promoted and promoted catalysts (17 ± 1%) (Table 5.5).

Table 5.5. Hydrocarbon selectivity obtained in the *pseudo*-steady state on Co/Ti and CoRu/Ti catalysts at CO conversion of 10 ± 1%. Reaction conditions: T= 220 °C, P= 20 bar, H_2/CO= 2 mol/mol, GHSV= 1.7 (for Co/Ti), 5.3 (for CoRu0.2/Ti), 3.8 (for CoRu0.7/Ti) and 3.1 (for CoRu1.2/Ti) $L_{syngas}/(g_{cat}\cdot h)$.

Catalyst	Selectivity (% C)			Parameter χ[a]
	C_1	C_2-C_4	C_{5+}	(10^{-16} m)
Co/Ti	16.9	32.3	50.8	317
CoRu0.2/Ti	16.0	27.2	56.8	403
CoRu0.7/Ti	18.0	29.9	52.1	472
CoRu1.2/Ti	16.4	27.6	56.0	460

[a] Structural parameter modeling mass transport limitations in cobalt-catalyzed FTS (see text).

In earlier studies, the increase in C_{5+} selectivity observed for catalysts promoted with Ru has been attributed to different factors: 1) a higher Co^0 site density [16], 2) a higher re-adsorption of α-olefins and further participation in chain growth events [22], and 3) an enrichment of Ru on the surface of Co NPs, due to the high selectivity to long chain hydrocarbons inherent to Ru sites [17]. Since the FTS selectivity is known to be controlled to a large extent by mass transfer limitations, we determined the diffusion-related structural parameter χ proposed by Iglesia and co-workers [4, 57] defined according to Eq.5.1:

$$\chi = R_0^2 \cdot \varepsilon \cdot \theta_{Co}/r_p \qquad \text{(Eq.5.1)}$$

where R_0 is the mean radius of catalyst pellets, ε is the porosity (pellet void fraction), θ_{Co} is the cobalt site density per unit area, and r_p is the mean pore radius. According to this model [4], the selectivity to C_{5+} initially increases with increasing χ (i.e. with increasing diffusion limitations) as α-olefin re-adsorption and participation in chain growth processes becomes favored. Then, the C_{5+} selectivity reaches a maximum at an intermediate value of χ of approx. $200 \cdot 10^{16}$ m, above which value it starts to drop as diffusion of CO through the catalyst pores (filled with liquid hydrocarbons) becomes severely limited. As a result, the true H_2/CO ratio around the Co particles within the pores increases promoting chain termination via hydrogenation of the growing chains enhancing the formation of lighter hydrocarbons. As observed in Table 5.5, the parameter χ raises with the Ru content from 0 (Co/Ti) to 0.7 wt% (CoRu0.7/Ti) and then slightly decreases when the concentration is further increased to 1.2 wt% (CoRu1.2/Ti). Given that all catalysts display alike pore diameters (arising from the common TiO_2-anatase support, Table 5.1) and the same pellet size, the increase in χ with Ru promotion should be mainly ascribed to a higher density of Co sites per unit area (θ_{Co}) in the promoted catalysts as a consequence of their higher Co dispersions (i.e. lower Co particle sizes, as measured by STEM) and lower BET surface areas relative to the non-promoted Co/Ti catalyst. As seen in Table 5.5, all catalysts exhibit χ values above $200 \cdot 10^{16}$ m and, according to the model developed by Iglesia, they fall in the range where the FTS selectivity is controlled by the intra-pore CO diffusion rather than by α-olefin re-adsorption.

In order to assess the relevance of mass transport limitations on the observed product selectivities, the olefin-to-paraffin (O/P) ratio for the C_2-C_4 and C_5-C_8 hydrocarbon fractions is plotted as a function of the parameter χ in Figure 5.12.

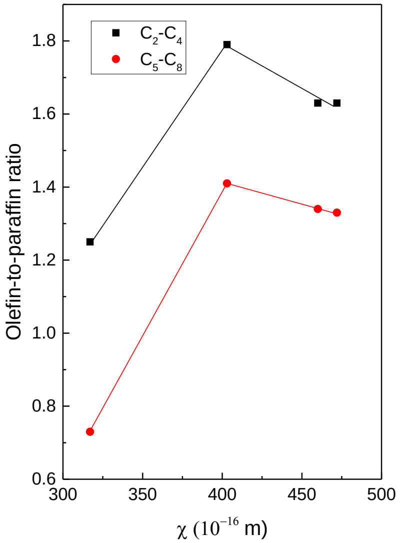

Figure 5.12. Trends in olefin-to-paraffin ratio for the C_2-C_4 and C_5-C_8 hydrocarbon fractions as a function of the diffusion-related structural parameter χ.

As seen in Figure 5.12, the Ru-promoted catalysts presented higher O/P ratios for the analyzed fractions compared to the non-promoted catalyst. This trend seems at first sight surprising given the known high hydrogenation capacity of Ru [9]. Nevertheless, the low olefin content for the Co/Ti catalyst could be related, at least in part, to the lower GHSV used for this catalyst to achieve 10% CO conversion, as the hydrogenation of the olefins becomes favored at increasing bed residence times.

On the other hand, for Ru-promoted catalysts, the increase in Ru content from 0.2 to 0.7-1.2 wt% translated into lower olefin-to-paraffin ratios (Figure 5.12). This could be related to the higher χ values presented by the CoRu0.7/Ti and CoRu1.2/Ti catalysts and the consequently higher restrictions for the diffusion of CO within the catalysts pores, resulting in higher H_2/CO ratios around the active Co sites that enhance hydrogenation reactions favoring lighter hydrocarbons. Additionally, the presence of isolated Ru particles in the high Ru-loaded catalysts, evidenced by EXAFS and STEM, might also contribute to their lower O/P ratios by promoting the activation of H_2 and its diffusion via spillover to the Co particles and subsequent hydrogenation and desorption as paraffins of the intermediate hydrocarbon species. Moreover, as observed in Figure 5.12, the O/P ratio is lower for C_5-C_8 in comparison to C_2-C_4 irrespective of the catalyst, which is explained by a higher restriction for the diffusion of olefins, promoting their hydrogenation, with increasing the olefin chain length [16].

Despite no clear consequences of the SMSI effect on selectivity have been established in the literature for Co/TiO_2 catalysts, decoration of Co^0 surface sites by partially reduced titania species results in a reduced amount of available Co^0 sites and may, hence, indirectly affect the product selectivity. From surface science studies, it is known that dissociation of CO proceeds readily on defected sites, such as steps, edges and corners on the surface of cobalt particles, while chain growth require rather large ensembles of Co^0 atoms on terraces [5, 7]. Hence, the decoration of Co^0 surface sites by TiO_x species might probably reduce the size of the Co^0 ensembles and, consequently, limit chain growth processes ultimately lowering the selectivity to C_{5+}. The SMSI effect will be addressed in more detail in the following section based on *in situ* spectroscopic characterizations.

Aiming at shedding more light on the effect of Ru promotion on FTS performance, we performed an *in situ* spectroscopic study using EXAFS, XPS, and CO-FTIR techniques to characterize the catalysts at different stages. These results will be presented and discussed in the next section.

5.3.5. In situ XAS characterization of CoRu/Ti catalysts during FTS at atmospheric pressure

The Ru local environment in CoRu/Ti catalysts with extreme Ru loadings (0.2 and 1.2 wt%) was investigated under FTS conditions (220 °C, 1 bar) after *in situ* H_2 reduction and the results are summarized in Table 5.3. The k^3-weighted $\chi(k)$ functions were Fourier-transformed and the |FT| plots for CoRu0.2/Ti and CoRu1.2/Ti catalysts after reduction in H_2 and during FTS reaction are presented in Figure 5.13. In addition, the fits of CoRu0.2/Ti and CoRu1.2/Ti catalysts before and during FTS reaction are shown in Figure 5.S1 in Supplementary Material. Both catalysts showed lower amplitude of |FT| signal during reaction with syngas compared to the as-reduced counterparts. At first glance, the values of both $N_{Ru\text{-}Co}$ and $N_{Ru\text{-}Ru}$ decrease during FTS (Table 5.3), which would indicate a change in the Ru environment under reaction conditions. However, the thermal disorder imposed by the reaction temperature on EXAFS spectra should be considered since it strongly affects the coordination numbers through the correlation between Debye-Waller factor (DWF) and amplitude of the EXAFS signal [50]. Nevertheless, by constraining the Debye-Waller factors for Ru-Co and Ru-Ru contributions, the resultant coordination numbers are smaller than for the as-reduced samples. On the other hand, guessing the DWF for both paths results in fit instability and, therefore, higher errors. Consequently, the Ru local order in CoRu nanoparticles is only suffering a disordering effect (increasing in static disorder) rather than a loss of neighbors, which is supported by the fact that the obtained Ru-Co and Ru-Ru distances are slightly modified (bond elongation) when in contact with the syngas feed. It is well known that the presence of hydrides and carbides can affect significantly the metal bond length [58] so that the presence of adsorbed species in our samples could explain these assumptions.

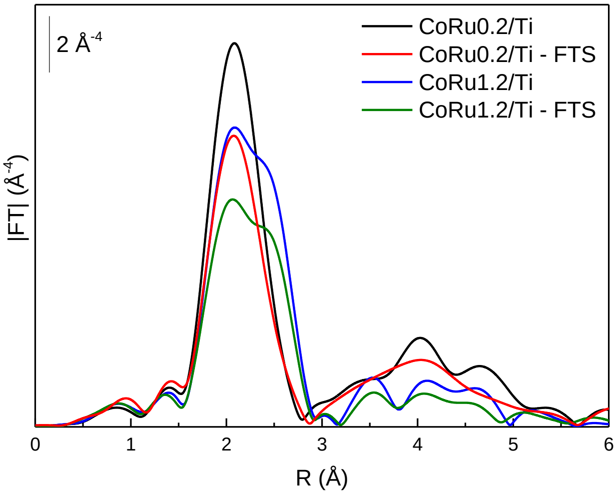

Figure 5.13. Moduli of Fourier transform of the EXAFS spectra of CoRu/Ti catalysts in their as-reduced form and under FTS reaction conditions.

Interestingly, for CoRu0.2/Ti catalyst, at longer distances (higher shells) the shape of multiple scattering contributions does not resemble those in the as-reduced sample. This observation could be related to a change in Ru local order during reaction. However, considering that in CoRu1.2/Ti the Ru loading is ca. 5 times higher than in CoRu0.2/Ti, the changes in higher shells in the former catalyst would not be as perceptible as in CoRu0.2/Ti sample. Finally, the goodness of fits is evidenced by the significant small values of R-factors (Table 5.3) before and after exposure of catalysts to FTS conditions.

To evaluate the influence of syngas pressure on the Ru local environment, *in situ* XAS was also performed under syngas flow at a pressure of 7 bar and 220 °C for the catalysts promoted with 0.2 and 1.2 wt% Ru. Nevertheless, no significant differences were noticed with respect to the results obtained at atmospheric pressure and, thus, we consider the general features observed at atmospheric pressure discussed before to be valid irrespective of the reaction pressure.

5.3.6. In situ CO-FTIR characterization of Co/Ti and CoRu/Ti catalysts during FTS at atmospheric pressure

FTIR spectroscopy of CO adsorption (CO-FTIR) is a very sensitive technique to characterize the nature of surface metal species, as in the case of cobalt in Co-based FTS catalysts [14]. Here we also performed CO-FTIR experiments at room temperature and increasing CO doses in an attempt to characterize the surface Co sites in the H_2-reduced Ru-promoted Co/TiO_2 catalysts as a function of the Ru content. Unfortunately, no relevant information could be derived from these experiments due to a too low intensity of the Co-CO IR bands as, due to the SMSI effect, only part of the surface Co atoms in the H_2-reduced catalysts are exposed to the CO probe molecule.

Next, we carried out *in situ* CO-FTIR experiments under flowing syngas at 1 bar and at the reaction temperature of 220 °C to study the evolution of the surface Co sites during FTS. In spite that higher pressures (typically 20 bar) are employed in industrial FTS processes, CO-FTIR at 1 bar has revealed very successful to derive relevant structure-performance relationships for supported Co FTS catalysts [11], where CO acts as both probe molecule and reactant. Figure 5.14 presents the CO-FTIR spectra recorded under syngas flow (1 bar) at increasing temperatures from 60 to 200 °C (spectra a-c) and after 1 and 4 h of reaction at 220 °C (spectra d-e) for CoRu0.2/Ti after *in situ* reduction in H_2. Additionally, the spectra of the sample cooled for 5 min after being heated to 160 and 200 °C were also recorded in order to better visualize the Co^0-CO bands and shown as dashed lines in Figure 5.14. At the end of the experiment, the catalytic cell was evacuated and a final spectrum was recorded under vacuum at 220 °C (spectrum f).

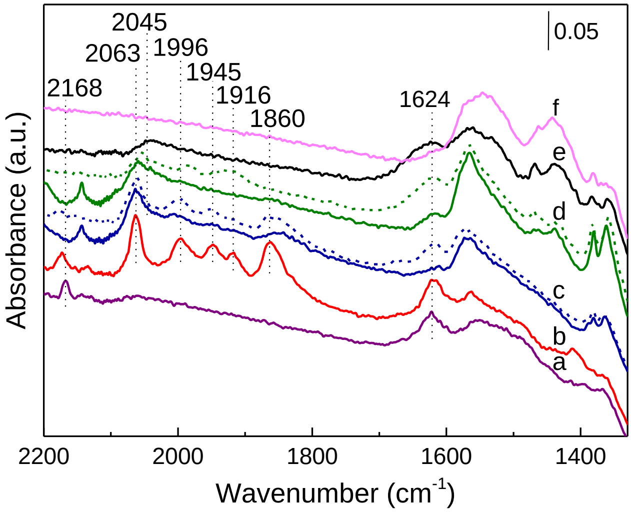

Figure 5.14. CO-FTIR spectra of CoRu0.2/Ti catalyst under syngas flow (1 bar) at increasing temperature: 60 °C (a), 160 °C (b), 200 °C (c), after 1 h at 220 °C (d), after 4 h at 220 °C (e), and after evacuation at 220 °C (f). The dashed lines correspond to the spectra recorded after cooling the samples (see text).

At 60 °C under syngas atmosphere (spectrum a), IR bands related to surface intermediate hydrocarbon (C_xH_y) species formed by hydrogenation of adsorbed CO can be observed in the 1410-1370 cm^{-1} region [59, 60]. Also, an IR band at 2168 cm^{-1} due to CO adsorbed on oxidized cobalt species ($CO\text{-}Co^{n+}$) can be seen [61, 62]. These oxidized cobalt species have already been observed in the CoRu0.2/Ti catalyst after *in situ* reduction in the IR cell (before introducing syngas), and may come from residual cobalt oxide patches on the catalyst surface due to a non-complete surface reduction under the experimental conditions of the IR set up. However, partial cobalt surface oxidation by oxygen species formed upon CO dissociation cannot be completely ruled out. The absence of IR bands associated to Co^0 (2060-1750 cm^{-1} range) could be explained by partial coverage of Co^0 NPs by a TiO_x layer, i.e. the so called SMSI effect, and/or by a blockage of Co surface sites by the detected adsorbed intermediate C_xH_y species.

Upon increasing the temperature to 160 °C (spectrum b), intense and well resolved IR bands in the cobalt-carbonyl region (i.e. 2060-1860 cm^{-1}) become preeminent with maxima at 2063, 1996, 1945, 1916, and 1860 cm^{-1}. This spectrum is markedly different from those usually observed in literature for cobalt-based catalysts, where linear carbonyls (IR bands near 2050-1990 cm^{-1}) and CO adsorbed on multifold metal Co sites (ca. 1800 cm^{-1}) are predominantly formed [14].

In literature, the band at approx. 2060 cm^{-1} has been assigned to different CO adsorption modes on cobalt, such as CO linearly adsorbed on metallic cobalt [62], surface polycarbonyl species $Co(CO)_x$ ($x > 1$) at corner sites on the cobalt nanoparticles [29, 63], partially hydrogenated Co(H)-CO species [62], and CO adsorbed on Co^0 with less marked electron-donor character (i.e. $Co^{\delta+}$) [64], as those at the Co-support interface in small Co^0 NPs [14]. Moreover, the bands in the 2000-1750 cm^{-1} region have been normally attributed to CO interacting with more defected metallic cobalt surface sites as well as to CO adsorbed on Co^0 in a bridge configuration [62, 65]. In these cases, a high thermal stability of the associated IR bands would be expected. However, this is not the case for our catalysts, for which the IR bands at 1996, 1945, 1916, and 1860 cm^{-1} are no longer observed at 200 °C and decomposed into new IR bands at 1984 and 1921 cm^{-1} at 220 °C (see spectrum d). Similar IR bands (2060, 1950, 1900, 1790 cm^{-1}) have been observed in previous studies for a Co/Al_2O_3 catalyst after prolonged exposure to CO atmosphere, and have been assigned to cobalt polycarbonyl species [61]. Likewise, other authors have attributed IR bands at 2040, 1900, 1840, and 1750 cm^{-1} to $Co(CO)_4$ carbonyl species adsorbed on Co^0 [66]. In addition, IR bands in the 2100-1700 cm^{-1} region have also been ascribed to mononuclear and polynuclear cobalt carbonyls, in which the authors have correlated the frequencies in the 2100-2000 cm^{-1} range to the stretching modes of linear carbonyl species and the low frequency bands at 1850-1865 and 1830-1810 cm^{-1} to µ2 and µ3 bridging carbonyls, respectively [67].

Considering the exposed above, and taking into account their low thermal stability, we attribute the IR bands observed at low frequency (2000-1860 cm^{-1} region, spectra b and c in Figure 5.14) to polycarbonyls adsorbed on Co clusters of low nuclearity. These CO species are volatile and can easily decompose into linear monocarbonyls (IR bands at 1984 and 1921 cm^{-1}) at increasing temperatures (see spectra d).

It has been reported that the formation of polycarbonyl(s) on cobalt catalysts depends on the surroundings of the cobalt ions on the catalyst surface [61]. Bearing in mind the presence of partially reduced TiO_x species decorating the surface of cobalt NPs in the reduced samples, and considering that under reaction conditions these TiO_x overlayers can be removed, at least in part, from the Co surface due to oxidation by water (a FTS product) [32], we propose a dynamic process by which removal of TiO_x species from the cobalt NPs (i.e. breaking of Co-O-Ti bonds) during FTS is accompanied by the formation of polycarbonyl(s) on the newly generated unsaturated cobalt sites.

Finally, an increase in intensity of the IR bands in the low frequency region due to adsorbed water (1624 cm^{-1}) along with development of bands in the 1590-1350 cm^{-1} region that suggests the formation of formate, carboxylate, and hydrocarbon species [59, 60, 68, 69] is observed when the temperature in the IR cell reaches the reaction temperature of 220 °C (spectrum d). These species are partially removed upon evacuation at high temperature, indicating their rather low interaction with the catalyst surface (spectrum f). On the other hand, the disappearance of the IR band at 2168 cm^{-1} at 220 °C indicates that the oxidized cobalt species observed at low temperature (60 °C) are reduced to Co^0 under FTS conditions. In addition, after 4 h of reaction at 220 °C the initial IR band at 2060 cm^{-1} shifted to lower frequencies (i.e. 2045 cm^{-1}), signing for a surface reconstruction of Co^0 nanoparticles encompassing a change in morphology towards more open planes, creating new unsaturated Co^0 sites as those present in defects of the crystallites (e.g. corners, edges, steps) [14, 70].

The CoRu1.2/Ti catalyst exhibited IR features during the temperature-resolved FTIR experiments in flowing syngas (Figure 5.15) similar to those discussed above for CoRu0.2/Ti. Thus, besides presenting alike IR bands, the shift of the IR band from 2063 cm^{-1} to 2045 cm^{-1} with the progress of the reaction at 220 °C on CoRu1.2/Ti also evidences surface reconstruction of the Co^0 NPs towards more defected surfaces in this catalyst.

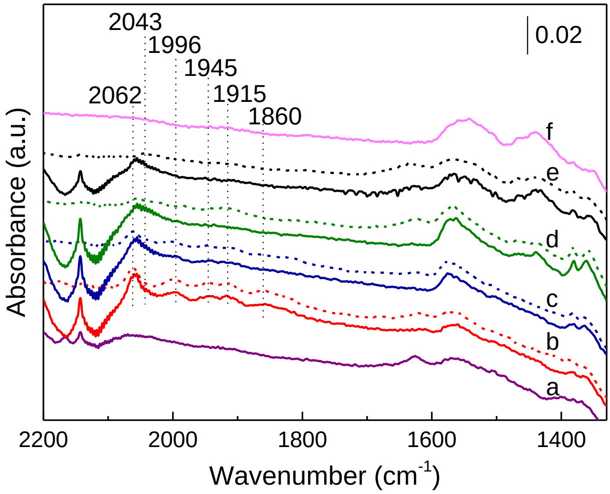

Figure 5.15. CO-FTIR spectra of CoRu1.2/Ti catalyst under syngas atmosphere at increasing temperature: 60 °C (a), 160 °C (b), 200 °C (c), after 1 h at 220 °C (d), after 4 h at 220 °C (e), and after evacuation (f). The dashed lines correspond to the spectra recorded after cooling the samples.

On the other hand, the unpromoted Co/Ti catalyst showed a different behavior (Figure 5.16). At 60 °C (spectrum a), an IR band at 2173 cm^{-1} of CO adsorbed on cobalt oxides that remained unreduced after the *in situ* H_2 reduction treatment, along with bands in the 1410-1370 cm^{-1} region due to surface C_xH_y intermediate species, are detected. Differently from the Ru-promoted catalysts, increasing the temperature in the IR cell to 160 °C (spectrum b, Figure 5.16) did not produce any noticeable change in the IR bands for Co/Ti catalyst. However, at 200 °C (spectrum c), cobalt carbonyl (IR band at 2063 cm^{-1}) and polycarbonyl (bands at 2008, 1997, 1945 and 1845 cm^{-1}) species are observed. After 1 h at 220 °C (spectrum d), the polycarbonyl species are completely desorbed to the gas phase, while intense IR bands associated to intermediate species (formates, carboxylates, and/or hydrocarbons) [59, 60, 69] are seen in the low frequency region (1590-1350 cm^{-1}). The fact that the IR bands related to these intermediate species persist after evacuation (spectrum f) indicates that they are strongly adsorbed on the catalyst surface. Moreover, the band at 2063 cm^{-1} remained unaltered even after reaction for 4 h at 220 °C (spectrum e), indicating that no surface reconstruction of Co^0 NPs occurred for the Ru-free catalyst.

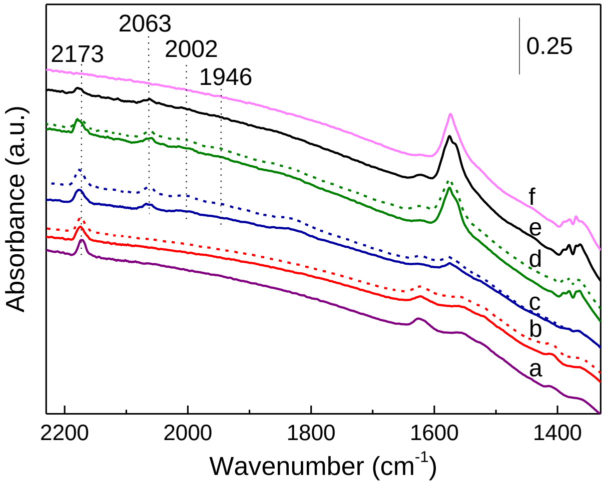

Figure 5.16. CO-FTIR spectra of Co/Ti catalyst under syngas atmosphere at increasing temperature: 60 °C (a), 160 °C (b), 200 °C (c), after 1 h at 220 °C (d), after 4 h at 220 °C (e) and after evacuation (f). The dashed lines correspond to the spectra recorded after cooling the samples.

At variance with the Ru-promoted catalysts, the IR band of CO adsorbed on cobalt oxide (2173 cm^{-1}) can still be perceived during reaction at 220 °C on Co/Ti (Figure 5.16). This fact can be directly related to the absence of Ru in this sample and its role on facilitating the removal of C and O species from the catalyst surface, thus keeping cobalt in its reduced state [16]. Similarly, the absence of Ru might also account for the stronger interaction of the intermediate hydrocarbon species observed after evacuation (spectrum f), which desorption would be enhanced by the high hydrogenating ability of Ru sites.

In summary, based on the above *in situ* FTIR study, the lower activity of the Co/Ti catalyst with respect to the Ru-promoted counterparts could be related to the presence of inactive cobalt oxides and of strongly adsorbed species, both factors resulting in a lower amount of active surface Co^0 sites available for reaction. This result reinforces the relevant role of Ru in keeping the surface of cobalt NPs clean from oxygen and carbon species during FTS reaction [15, 16]. However, the contrasting FTS activity of CoRu0.2/Ti and CoRu1.2/Ti catalysts cannot be explained based on the nature of cobalt sites exposed during reaction, since both samples showed similar evolution of cobalt species during the *in situ* FTIR experiments. Although a lower intensity of the IR bands (at 220 °C) for CoRu1.2/Ti compared to CoRu0.2/Ti (see Figures 5.14 and 5.16) might suggest a lower amount of cobalt metal sites available for CO adsorption and reaction in the former catalyst, the low inherent optical transmission of all catalysts makes quantification not straightforward.

5.3.7. In situ CO-FTIR characterization of Co/Ti and CoRu/Ti catalysts during FTS at high pressure

In an attempt to gain deeper insights into the effect of Ru promotion in Co/TiO$_2$ catalysts under reaction conditions and to explain the observed differences in activity, the catalysts Co/Ti, CoRu0.2/Ti and CoRu1.2/Ti were additionally characterized by *in situ* FTIR with syngas flow at 9 bar and, thus, at more realistic FTS conditions. In principle, we expected that higher working pressures will increase CO conversion rates and, as a result, the structural changes experienced by the catalysts under reaction conditions would be more pronounced and easier to follow by FTIR spectroscopy. The FTIR experiments at 220 °C under syngas flow and a pressure of 9 bar were performed in an especially designed high pressure IR catalytic cell. The temperature-resolved CO-FTIR results obtained for the unpromoted Co/Ti catalyst are presented in Figure 5.17.

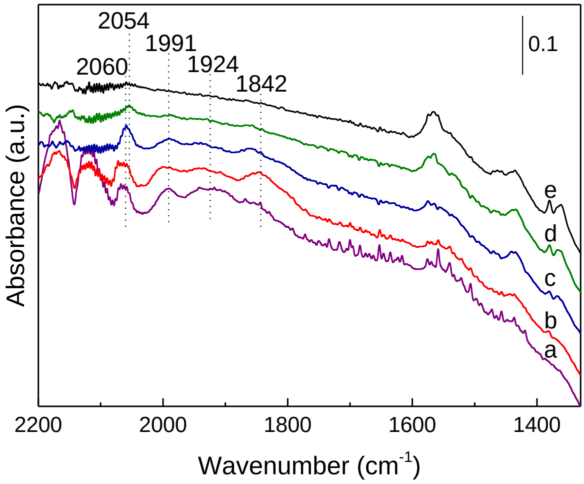

Figure 5.17. CO-FTIR spectra of Co/Ti catalyst under syngas flow at 9 bar at increasing temperatures: 100 °C (a), 160 °C (b), 220 °C (c), after 2 h at 220 °C (d), and after 4 h at 220 °C (e).

Divergently from the spectra collected for the Co/Ti catalyst at atmospheric pressure (Figure 5.16), the cobalt carbonyl band at 2060 cm^{-1} and the bands of cobalt polycarbonyls at 1991, 1924, and 1842 cm^{-1} are readily detected at 100 °C (spectrum a), signing for an enhanced reactivity at the higher syngas pressure, as anticipated. However, we surprisingly found that the intensity of the IR band at 2060 cm^{-1}, still observed after reaching the reaction temperature of 220 °C (spectrum c), significantly declined after 2 h of reaction at this temperature (spectrum d) and completely vanished after reaction with syngas for 4 h (spectrum e). The IR bands of surface intermediate species (1590-1350 cm^{-1} region), however, were still detected and even increased in intensity during reaction at 220 °C. With respect to the CoRu0.2/Ti catalyst (spectra not shown), a small band at 2053 cm^{-1} could still be observed under FTS conditions, although experimental problems related to gas phase subtraction resulted in uncertainties in the accurate identification and position of the IR bands.

Thus, unfortunately and contrary to our initial expectations, the high pressure FTIR spectroscopic study did not provided any additional information on the samples, probably due to the higher reactivity of the catalysts at 9 bar and, consequently, to the increased amount of hydrocarbon intermediates adsorbed on Co sites preventing their titration by CO. Besides, the specific design of the IR catalytic cell, in which IR windows with small diameters had to be used to withstand the high pressure, did also contribute to reduce the intensity of the IR bands.

Continuing the efforts to understand the catalytic behavior of the catalysts investigated in this study, XPS characterization was performed and the obtained results are presented in the following section.

5.3.8. In situ XPS characterization of Co/Ti and CoRu/Ti catalysts during FTS at high pressure

XPS is a very powerful technique with high surface sensitivity, especially when considering Auger XPS peaks. Therefore, the catalysts were characterized by XPS using a high pressure cell (HPC) attached to the analysis chamber, enabling the sample to be evacuated after *in situ* reaction and transferred safely to the analysis chamber without being exposed to ambient air. In these experiments, the FTS reaction was carried out at 220 °C under syngas flow at both 9 bar and atmospheric pressure while monitoring the gas phase products leaving the reaction chamber by on line mass spectrometry to check for the formation of hydrocarbons and, thus, to verify the occurrence of catalysis.

The Co/Ti and CoRu/Ti catalysts were first analyzed in their as-reduced state and after *in situ* reaction with syngas at atmospheric pressure and 220 °C. However, for all catalysts no changes in the Co2p and Co Auger spectra could be observed between the as-reduced and reacted samples, suggesting the absence of significant reaction at this condition, as corroborated by the absence of hydrocarbons in the online MS analyses. Therefore, the results obtained at a syngas pressure of 9 bar are discussed next.

Figure 5.18 (top) shows the XPS C1s spectra for Co/Ti (a), CoRu0.2/Ti (b), and CoRu1.2/Ti (c) catalysts after reduction (H_2) and after reaction (FTS). The deconvoluted C1s XPS peak of Co/Ti (d), CoRu0.2/Ti (e), and CoRu1.2/Ti (f) catalysts after FTS are presented at the bottom of the figure. The deconvolution shows different types of surface carbon species, i.e. aliphatic C-C (284.5 eV), C-O(H) (285.3 eV) [71], oxygenated compounds (288.7 eV) [72], and cobalt carbide species (282.5 eV) [73, 74].

This agrees with the nature of the intermediate species detected in the previous FTIR experiments under flowing syngas at atmospheric pressure, as well as with the EXAFS results performed under FTS conditions, from which the presence of adsorbed species is inferred from the small changes in Ru coordination number during reaction.

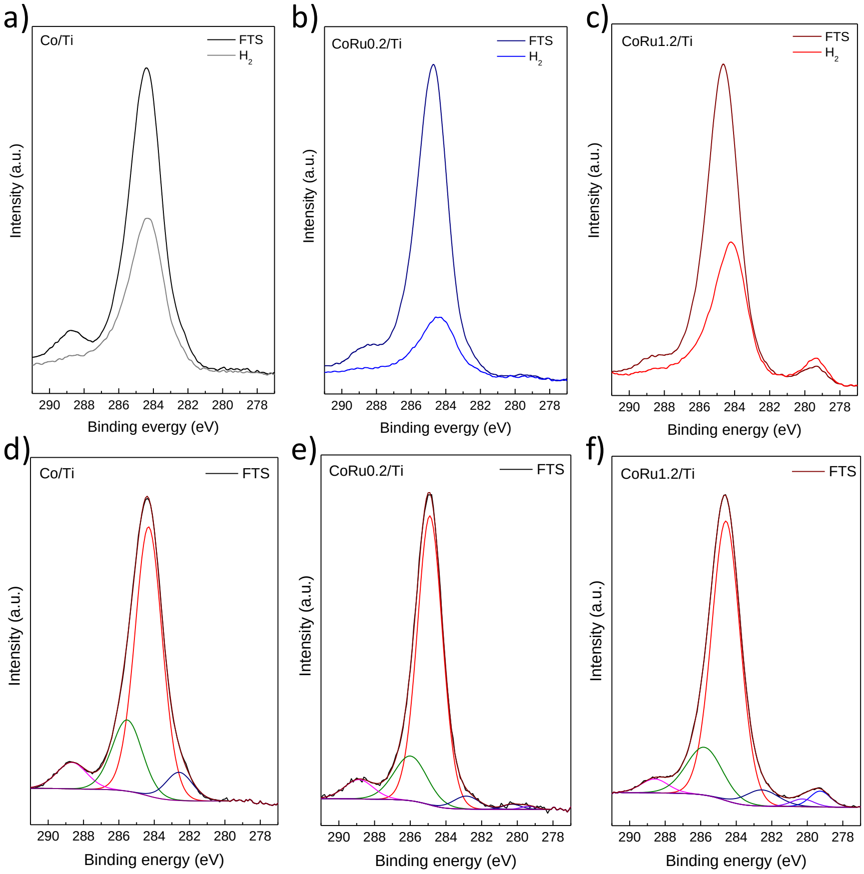

Figure 5.18. XPS spectra (C1s) of Co/Ti (a), CoRu0.2/Ti (b), and CoRu1.2/Ti (c) catalysts after reduction (H$_2$) and after reaction (FTS) (top), and deconvolution of the C1s component for Co/Ti (d), CoRu0.2/Ti (e), and CoRu1.2/Ti (f) catalysts after FTS (bottom).

The Co/Ti atomic ratios for the as-reduced (H_2) catalysts (Table 5.6) are compatible with a higher amount of exposed Co in the catalyst without Ru (0.032) compared to those promoted with Ru. For the later, the atomic Co/Ti ratio decreased from 0.029 to 0.020 with the raise in Ru concentration from 0.2 to 1.2 wt%. This trend might suggest a more pronounced SMSI effect (i.e. more surface Co sites covered by TiO_x species) at higher Ru contents. However, taking into account that the penetration depth of the X-rays in the XPS analyses is ~6 nm, and that the TiO_x overlayer should be very thin, establishing a direct correlation between the surface Co/Ti ratio and the SMSI extent is not obvious at all. On the other hand, the Ru/Ti atomic ratio in the H_2-reduced catalysts increased from 0.002 to 0.016 with the raise in Ru loading from 0.2 to 1.2 wt% (Table 5.6), as expected.

While only minor variations in the Co/Ti and Ru/Ti ratios were observed after reaction with syngas at 220 °C and 9 bar for Co/Ti and CoRu1.2/Ti, both ratios experienced a significant increase after reaction in the case of CoRu0.2/Ti (Table 5.6). Since the lab-scale XPS analyses are not sensitive enough to detect changes in the TiO_x overlayer (especially at low TiO_x coverages), the variations in surface atomic ratios seen for CoRu0.2/Ti may point to morphological changes experienced by the Co nanoparticles promoted by the disruption of Co-O-Ti linkages as a consequence of the SMSI reversion under reaction conditions. In fact, if the polycarbonyl species observed in the FTIR study are formed during the re-oxidation of TiO_x patches, this dynamic process could possibly lead to changes in the morphology of the nanoparticles that could ultimately affect the Co/Ti and Ru/Ti surface atomic ratios.

Table 5.6. Atomic surface ratios derived from XPS for as-reduced catalysts (H$_2$) and after 3 h of reaction with syngas at 220 °C and 9 bar (FTS).

Catalyst	C/Co		Co/Ti		Ru/Ti	
	H$_2$	FTS	H$_2$	FTS	H$_2$	FTS
Co/Ti	19.8	40.0	0.032	0.035	-	-
CoRu0.2/Ti	12.9	56.6	0.029	0.037	0.002	0.005
CoRu1.2/Ti	39.4	111.0	0.020	0.020	0.016	0.016

Moreover, a closer analysis of the Ru3d$_{5/2}$ XPS spectra for the as-reduced CoRu0.2/Ti and CoRu1.2/Ti catalysts revealed two components at 279.2 eV and 280.3 eV (Figure 5.19) that can be assigned to Ru-Ru and Co-Ru species, respectively. The formation of isolated Ru nanoparticles (Ru-Ru) was also evidenced by EXAFS (Figure 5.10). Moreover, the contribution of the isolated Ru-Ru species is incremented with the increase in Ru loading, in consistence with the results obtained by EDS elemental mapping (Figure 5.8). However, it is tricky to follow the evolution and nature of Ru species (Ru-Co and Ru-Ru) under reaction conditions by XPS due to the overlapping of the Ru3d$_{5/2}$ signal with the C1s carbide component, making deconvolution of the Ru peak uncertain. In any case, in spite of the bulk character of the technique, the EXAFS results did not reveal significant changes in the Ru environment for these samples before (as-reduced) and after *in situ* FTS reaction, as discussed previously.

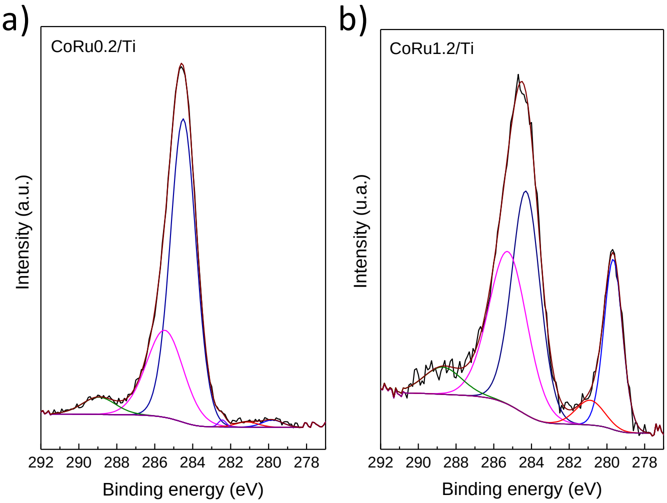

Figure 5.19. Ru3d$_{5/2}$ peak of XPS spectra for as-reduced CoRu0.2/Ti (a) and CoRu1.2/Ti (b) catalysts.

Fitting of the Co2p$_{3/2}$ XPS signal is complex due to both the asymmetric shape of the metallic cobalt XPS peak and the presence of two plasmon loss peaks at 3.0 eV and 5.0 eV above the main signal [75] contributing by ca. 11 and 8%, respectively, to the total peak area. Both plasmon peaks are located at the same binding energy (BE) than Co(OOH) and Co_3O_4 compounds. Since a quantitate assessment of the presence or absence of oxidized Co species is rather difficult, the XPS data will be discussed on a qualitative basis. In this work, the Co2p XPS peak for all catalysts could be fitted with five components located at 775.8, 777.8, 779.0, 780.6, and 783.5 eV. A representative deconvolution of the Co2p$_{3/2}$ peak for the CoRu0.2/Ti catalyst is shown in Figure 5.20. The signal at 777.8 eV is ascribed to Co^0 [76], whereas the small contribution at 775.8 eV is related to a cobalt LMM Auger transition [75]. The component at 779.0 eV can be assigned to oxidized cobalt species. However, since this BE value is lower than that typically reported for Co^{2+} in CoO or CoOOH phases [77], it is likely that the peak at 779.0 eV would correspond to $Co^{\delta+}$ species at the Co-TiO_x interface, as also proposed in the literature [78]. Finally, the components at higher BE (780.6 and 783.5 eV) correspond to plasmon loss peaks overlapped with cobalt oxidized species [75]. Peak areas for components related to Co^0 and Co-O-Ti interface sites are presented in Table 5.7.

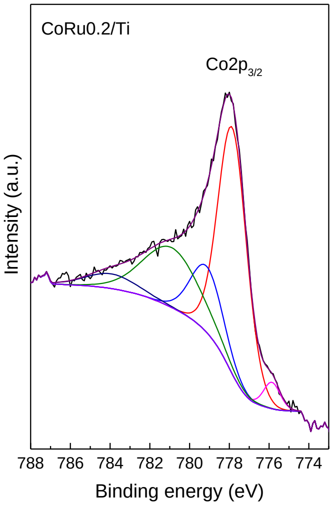

Figure 5.20. Deconvolution of $Co2p_{3/2}$ peak of XPS spectra for the as-reduced CoRu0.2/Ti catalyst.

Table 5.7. Peak areas of XPS components at 777.8 eV (Co^0) and 779.0 eV (interface Co) for as-reduced catalysts (H_2) and after reaction with syngas at 220 °C and 9 bar (FTS).

Catalyst	Co^0 peak area (%)		Co-O-Ti peak area (%)	
	H_2	FTS	H_2	FTS
Co/Ti	45.6	55.5	20.4	16.0
CoRu0.2/Ti	54.0	55.3	16.3	12.9
CoRu1.2/Ti	58.6	55.2	17.4	12.9

For the as-reduced catalysts, a higher amount of surface metallic cobalt at increasing Ru loadings was inferred from the peak areas of Co^0 XPS component (Table 5.7). After reaction with syngas (FTS), the surface Co^0 content raised for Co/Ti catalyst, remained almost constant for CoRu0.2/Ti, and decreased for CoRu1.2/Ti. Moreover, the proportion of cobalt in interface sites (Co-O-Ti) decreased after reaction for all catalysts. The increase in Co^0 area together with the lower amount of cobalt in interface sites after FTS could be related with the reversibility of the SMSI effect, by which TiO_x species decorating the Co^0 NPs are re-oxidized by water and partially removed during reaction. However, this is not obvious at all since, besides Co interacting with the TiO_x outlayer (SMSI), Co atoms at the interface with the TiO_2 support (hence, not related to the SMSI) may also contribute to the XPS signal at 779.0 eV.

Since the overlapping of plasmon loss peaks with the component related to oxidized cobalt species hinders its correct quantification, we used the modified Auger parameter (α’), which is very sensitive to the chemical state of the element [79], to characterize the chemical state of cobalt in our catalysts. The modified Auger parameter can be calculated according to equation 5.2:

$$\alpha' = KE\ (Co_{LMM}) + BE\ (Co\ 2p_{3/2}) \qquad \text{(Eq.5.2)}$$

where KE (Co_{LMM}) is the kinetic energy of the Co_{LMM} Auger electron and BE (Co $2p_{3/2}$) is the binding energy of Co $2p_{3/2}$ photoelectron (777.8 eV).

In this case, analyzing α’ and comparing the obtained value with the reference compounds in the so-called Wagner plots can give precise information about chemical states of the selected element. In the particular case of cobalt, a view of the Wagner plot displayed in Figure 5.21 shows significant differences in α’ for Co^0, CoO and Co_3O_4

compounds, which makes their identification much easier than by conventional XPS analysis based only on BE values. Consequently, the analysis of the Co modified Auger parameter is a very sensitive tool for accurate identification of the oxidation state of cobalt species, which is of particular interest for the catalysts studied in this work.

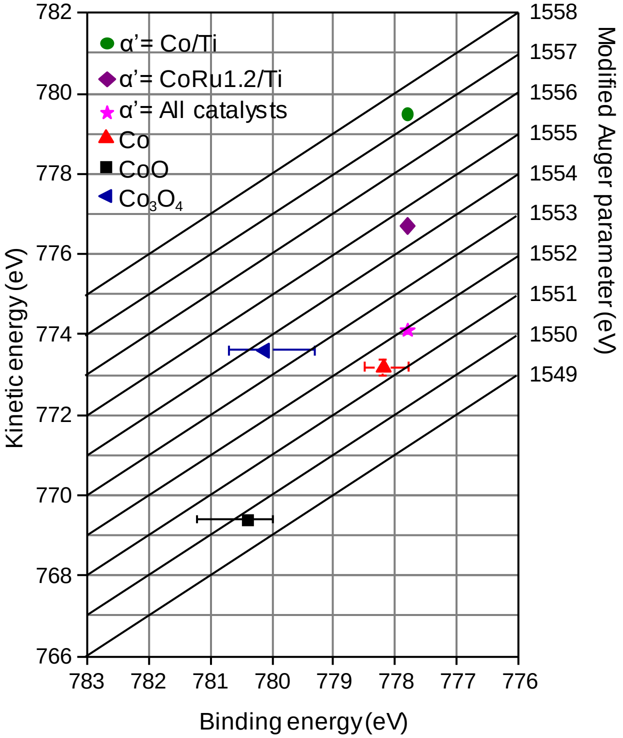

Figure 5.21. Wagner-plots of binding energies, Auger kinetic energies, and modified Auger parameters for reference Co^0, CoO and Co_3O_4 compounds [80] compared with those obtained for the Co catalysts in this work.

The Co Auger peaks of the different samples after FTS are shown in Figure 5.22. All catalysts show a main peak with a maximum at 774.1 eV resulting in an α' of 1551.9 eV, which corresponds to Co^0 (Figure 5.21).

However, for CoRu1.2/Ti catalyst, a shoulder at a higher kinetic energy (KE) of 776.7 eV, equivalent to α' of 1554.4, was detected which can be assigned to Co_3O_4. These results point to the presence of oxidized cobalt species after FTS in the catalyst promoted with 1.2 wt% Ru. At first sight, these data may seem surprising as an increased amount of metallic Co could be expected at higher Ru contents. However, the analysis of both Co-AES and Co2p XPS signals unambiguously point to the presence of oxidized cobalt species during reaction for the CoRu1.2/Ti catalyst.

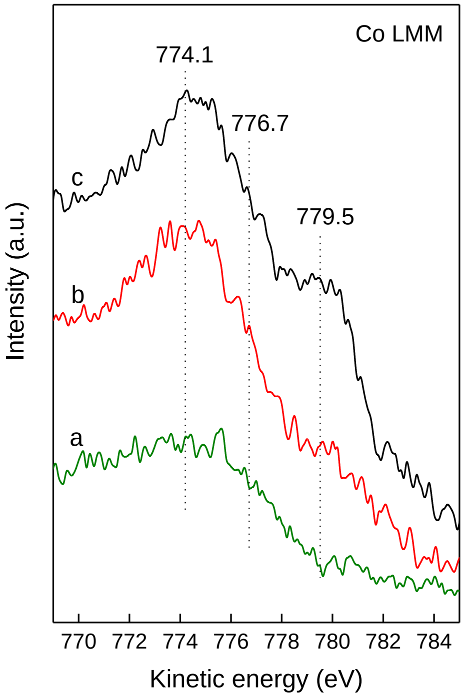

Figure 5.22. Co LMM Auger spectra of CoRu1.2/Ti (a), CoRu0.2/Ti (b) and Co/Ti (c) catalysts after FTS reaction at 220 °C and 9 bar.

Nevertheless, it is not clear why a higher Ru loading results in partial oxidation of Co^0 NPs during reaction. Other authors related the decrease in FTS activity observed at increasing Ru contents to a lower DOR due to segregation of Ru from bimetallic Co-Ru particles [18, 22]. In this sense, it has been suggested that the segregated Ru particles, which are no longer in the surroundings of cobalt, did not significantly influence the reducibility of cobalt oxide NPs [22]. Our spectroscopic results point to a certain re-oxidation of cobalt NPs at high Ru concentrations during FTS reaction (not observed for the as-reduced samples). A possible explanation for this could be that the Ru NPs can also experience the SMSI decoration effect [81]. As a result, the activation of H_2 and its spillover to the Co NPs would be inhibited, thereby increasing the concentration of oxygen species (originated from CO dissociation) on the surface of the cobalt NPs and favoring their (partial) oxidation during FTS reaction, as concluded from XPS.

Finally, a shoulder at KE of 779.5 eV for the Co/Ti catalyst is observed (Figure 5.22), resulting in an α′ of 1557.3 eV. Since this value cannot be ascribed to oxidized or metallic cobalt species, we tentatively assign it to cobalt carbide species. The presence of carbide species in the catalyst without Ru concurs with previous characterizations by XPS (component at 282. 5 eV in the C1s XPS signal) and with the lower desorption ability of surface carbon species detected in the FTIR study at atmospheric pressure. The formation of carbide species is in line with previous works, in where the absence of Ru was shown to result in a higher formation of adsorbed carbonaceous species on cobalt, thus reducing the concentration of Co^0 sites available for reaction [16].

In conclusion, the spectroscopic characterization by XPS pointed to the presence of oxidized cobalt species during FTS reaction at higher Ru loadings, which may account, at least in part, for the lower catalytic activity displayed by the CoRu0.7/Ti and CoRu1.2/Ti catalysts. For the non-promoted catalyst (Co/Ti), its lower FTS activity compared to the Ru-promoted samples can be explained by the presence of adsorbed carbide species lowering the amount of exposed Co^0 sites available for reaction. Therefore, the optimum promotion effect leading to the most active catalyst is achieved at a Ru loading of 0.2 wt% (CoRu0.2/Ti), as at this low concentration all the Ru is in close contact with Co (in bimetallic Co-Ru particles), preventing the formation of detrimental cobalt carbide and/or oxidized cobalt species. Regarding the Ru-promoted catalysts, the surface Co/Ti and Ru/Ti ratios derived from XPS pointed to a higher dynamic behavior of the surface Co species in the CoRu0.2/Ti catalyst, a fact that could be related to the presence of all Ru atoms in close contact with Co in bimetallic Co-Ru NPs. On the other hand, increasing the Ru loading above 0.2 wt% led to segregation of isolated Ru particles which are not in close proximity to Co, resulting in the formation of oxidized cobalt species under reaction conditions.

5.4. Conclusion

The promotion of Co/Ti catalysts with different amounts of Ru (0.2, 0.7, and 1.2 wt%) results in an increase in both catalytic activity (CTY and apparent TOF) and C$_{5+}$ selectivity, both parameters presenting maximum values for the catalyst promoted with the lowest Ru content (CoRu0.2/Ti). The higher activity of the Ru-promoted catalysts in comparison to the non-promoted one can be attributed to the combination of several factors. On one hand, the promoted catalysts all exhibit higher Co dispersions than the non-promoted sample (STEM). Besides, the presence of Ru in close contact with Co in bimetallic Co-Ru

NPs (EXAFS) aids to keep the surface of Co sites in the metallic state avoiding their re-oxidation (CO-FTIR) and preventing the formation of carbide species (XPS) during catalysis. Nevertheless, a certain oxidation of surface cobalt species (inferred from the Auger XPS spectra) occurred under FTS conditions when increasing the Ru content above 0.2 wt%, probably due to segregation of Ru from bimetallic Co-Ru particles, which are no longer aiding in preventing cobalt oxidation. On the other hand, the lower contribution of Co^0 NPs with less than 6 nm in size (STEM) in the catalyst promoted with 0.2 wt% Ru and the absence of oxidized Co species during reaction could explain the superior CTY and apparent TOF of this catalyst with respect to the other Ru-promoted samples. Besides, the Ru-promoted catalysts presented higher selectivity to C_{5+} than the unpromoted counterpart, with a maximum value observed for the catalyst containing 0.2 wt% Ru. Overall, our results clearly demonstrate that an optimum Ru loading is required in order to take full advantage of its promotional effect. In the case of the Co/TiO_2-anatase catalysts investigated in this work, all bearing ca. 12 wt% Co, the optimum is attained at a Ru loading of 0.2 wt%, corresponding to an atomic Ru/Co ratio of ca. 0.01.

Acknowledgments

Financial support by the MINECO of Spain through the Severo Ochoa (SEV2016-0683) and ENE2014-5761-R projects is gratefully acknowledged. The authors also thank the Microscopy Service of the Universitat Politècnica de València for its assistance in microscopy characterization. The XAS experiments at ambient pressure were performed on beamline BM23 at the European Synchrotron Radiation

Facility (ESRF), Grenoble, France. We are grateful to Debora Motta Meira at the ESRF for providing assistance in using beamline BM23. Thanks are also due to ALBA synchrotron for allocating beamtime (XAS experiments at higher pressure) and CLÆSS beamline staff for their technical support during the experiment. F. Bertella (Science without Frontiers − Process no. 13705/13-0) thanks CAPES for a predoctoral fellowship.

5.5. References

[1] A.Y. Khodakov, W. Chu, P. Fongarland, Chem. Rev. 107 (2007) 1692-1744.

[2] H. Xiong, L.L. Jewell, N.J. Coville, ACS Catal. 5 (2015) 2640-2658.

[3] M.E. Dry, J. Chem. Technol. Biot. 77 (2002) 43-50.

[4] E. Iglesia, Appl. Catal. A Gen. 161 (1997) 59-78.

[5] C.J. Weststrate, P. van Helden, J.W. Niemantsverdriet, Catal. Today 275 (2016) 100-110.

[6] C. Ledesma, J. Yang, E.A. Blekkan, A. Holmen, D. Chen, ACS Catal. 6 (2016) 6674-6686.

[7] A. Banerjee, A.P. van Bavel, H.P.C.E. Kuipers, M. Saeys, ACS Catal. 7 (2017) 5289-5293.

[8] G. Jacobs, T.K. Das, Y. Zhang, J. Li, G. Racoillet, B.H. Davis, Appl. Catal. A Gen. 233 (2002) 263-281.

[9] F. Diehl, A.Y. Khodakov, Oil Gas Sci. Technol. 64 (2008) 11-24.

[10] A. Martínez, G. Prieto, J. Rollán, J. Catal. 263 (2009) 292-305.

[11] G. Prieto, M.I.S. De Mello, P. Concepción, R. Murciano, S.B.C. Pergher, A. Martínez, ACS Catal. 5 (2015) 3323-3335.

[12] G. Prieto, A. Martínez, R. Murciano, M.A. Arribas, Appl. Catal. A Gen. 367 (2009) 146-156.

[13] G.L. Bezemer, J.H. Bitter, H.P. Kuipers, H. Oosterbeek, J.E. Holewijn, X. Xu, F. Kapteijn, A.J. van Dillen, K.P. de Jong, J. Am. Chem. Soc. 128 (2006) 3956-3964.

[14] G. Prieto, A. Martínez, P. Concepción, R. Moreno-Tost, J. Catal. 266 (2009) 129-144.

[15] T.O. Eschemann, J. Oenema, K.P. de Jong, Catal. Today 261 (2016) 60-66.

[16] E. Iglesia, S.L. Soled, R.A. Fiato, G.H. Via, J. Catal. 143 (1993) 345-368.

[17] M. Trépanier, A. Tavasoli, A.K. Dalai, N. Abatzoglou, Appl. Catal. A Gen. 353 (2009) 193-202.

[18] S.-H. Song, S.-B. Lee, J.W. Bae, P.S. Sai Prasad, K.-W. Jun, Catal. Commun. 9 (2008) 2282-2286.

[19] A. Kogelbauer, J.J.G. Goodwin, R. Oukaci, J. Catal. 160 (1996) 125-133.

[20] J. Girardon, E. Quinet, A. Gribovalconstant, P. Chernavskii, L. Gengembre, A. Khodakov, J. Catal. 248 (2007) 143-157.

[21] P. Li, J. Liu, N. Nag, P. Crozier, Appl. Catal. A Gen. 307 (2006) 212-221.

[22] J.-Y. Park, Y.-J. Lee, P.R. Karandikar, K.-W. Jun, J.W. Bae, K.-S. Ha, J. Mol. Catal. A Chem. 344 (2011) 153-160.

[23] S.A. Hosseini, A. Taeb, F. Feyzi, F. Yaripour, Catal. Commun. 5 (2004) 137-143.

[24] G. Jacobs, Y. Ji, B.H. Davis, D. Cronauer, A.J. Kropf, C.L. Marshall, Appl. Catal. A Gen. 333 (2007) 177-191.
[25] H. Karaca, O.V. Safonova, S. Chambrey, P. Fongarland, P. Roussel, A. Griboval-Constant, M. Lacroix, A.Y. Khodakov, J. Catal. 277 (2011) 14-26.
[26] C. Pirola, M. Scavini, F. Galli, S. Vitali, A. Comazzi, F. Manenti, P. Ghigna, Fuel 132 (2014) 62-70.
[27] J. Hong, E. Marceau, A.Y. Khodakov, L. Gaberová, A. Griboval-Constant, J.-S. Girardon, C.L. Fontaine, V. Briois, ACS Catal. 5 (2015) 1273-1282.
[28] O.A. Kungurova, A.A. Khassin, S.V. Cherepanova, A.A. Saraev, V.V. Kaichev, N.V. Shtertser, G.K. Chermashentseva, E.Y. Gerasimov, E.A. Paukshtis, O.V. Vodyankina, T.P. Minyukova, G. Abou-Jaoudé, Appl. Catal. A Gen. 539 (2017) 48-58.
[29] N. Tsubaki, S. Sun, K. Fujimoto, J. Catal. 199 (2001) 236-246.
[30] S.J. Tauster, Acc. Chem. Res. 20 (1987) 389-394.
[31] G.L. Haller, D.E. Resasco, Metal-Support Interaction: Group VIII Metals and Reducible Oxides, in: D. Eley (Series Volume Editor), H. Pines, P. B. Weisz (Serial Editors), Advances in Catalysis, Volume 36, 1st Edition, Academic Press, 1989, pp. 173-235.
[32] E. Iglesia, S.L. Soled, R.A. Fiato, J. Catal. 137 (1992) 212-224.
[33] R.C. Reuel, C.H. Bartholomew, J. Catal. 85 (1984) 78-88.
[34] L. Simonelli, C. Marini, W. Olszewski, M. Ávila Pérez, N. Ramanan, G. Guilera, V. Cuartero, K. Klementiev, N.L. Saini, Cogent Physics 3 (2016) 1231987.
[35] G. Guilera, F. Rey, J. Hernández-Fenollosa, J.J. Cortés-Vergaz, J. Phys. Conf. Ser. 430 (2013) 012057.
[36] B. Ravel, M. Newville, J. Synchrotron Radiat. 12 (2005) 537-541.
[37] C. Sanchez, J. Livage, M. Henry, F. Babonneau, J. Non-Cryst. Solids 100 (1988) 65-76.
[38] M. Wu, G. Lin, D. Chen, G. Wang, D. He, S. Feng, R. Xu, Chem. Mater. 14 (2002) 1974-1980.
[39] F. Bertella, P. Concepción, A. Martínez, Catal. Today 296 (2017) 170-180.
[40] P. Yang, D. Zhao, D.I. Margolese, B.F. Chmelka, G.D. Stucky, Chem. Mater. 11 (1999) 2813-2826.
[41] Y. Yue, Z. Gao, Chem. Commun. (2000) 1755-1756.
[42] M.K. Hossain, A.R. Koirala, U.S. Akhtar, M.K. Song, K.B. Yoon, Chem. Mater. 27 (2015) 6550-6557.
[43] M. Thommes, K. Kaneko, A.V. Neimark, J.P. Olivier, F. Rodriguez-Reinoso, J. Rouquerol, K.S.W. Sing, Pure Appl. Chem. 87 (2015).

[44] X.Y. Shi, W. Zhang, C. Zhang, W.T. Zheng, H. Chen, J.G. Qi, J. Microsc. 262 (2016) 203-215.

[45] C.-J. Pan, M.-C. Tsai, W.-N. Su, J. Rick, N.G. Akalework, A.K. Agegnehu, S.-Y. Cheng, B.-J. Hwang, J. Taiwan Inst. Chem. E. 74 (2017) 154-186.

[46] S. Storsater, B. Totdal, J. Walmsley, B. Tanem, A. Holmen, J. Catal. 236 (2005) 139-152.

[47] A. Michalak, M. Nowosielska, W.K. Jóźwiak, Top. Catal. 52 (2009) 1044-1050.

[48] G. Jacobs, W. Ma, P. Gao, B. Todic, T. Bhatelia, D.B. Bukur, B.H. Davis, Catal. Today 214 (2013) 100-139.

[49] E. Groppo, W. Liu, O. Zavorotynska, G. Agostini, G. Spoto, S. Bordiga, C. Lamberti, A. Zecchina, Chem. Mater. 22 (2010) 2297-2308.

[50] M.S. Nashner, A.I. Frenkel, D.L. Adler, J.R. Shapley, R.G. Nuzzo, J. Am. Chem. Soc. 119 (1997) 7760-7771.

[51] A. Frenkel, Zeitschrift für Kristallographie - Crystalline Materials, 222 (2007) 605-611.

[52] J. Wang, Q. Wang, X. Jiang, Z. Liu, W. Yang, A.I. Frenkel, J. Phys. Chem. C 119 (2015) 854-861.

[53] G. Agostini, R. Pellegrini, G. Leofanti, L. Bertinetti, S. Bertarione, E. Groppo, A. Zecchina, C. Lamberti, J. Phys. Chem. C 113 (2009) 10485-10492.

[54] J.M. Montejano-Carrizales, F. Aguilera-Granja, J.L. Morán-López, Nanostruct. Mater. 8 (1997) 269-287.

[55] G. Agostini, A. Piovano, L. Bertinetti, R. Pellegrini, G. Leofanti, E. Groppo, C. Lamberti, J. Phys. Chem. C 118 (2014) 4085-4094.

[56] M. Sadeqzadeh, H. Karaca, O.V. Safonova, P. Fongarland, S. Chambrey, P. Roussel, A. Griboval-Constant, M. Lacroix, D. Curulla-Ferré, F. Luck, A.Y. Khodakov, Catal. Today 164 (2011) 62-67.

[57] E. Iglesia, S.L. Soled, J.E. Baumgartner, S.C. Reyes, J. Catal. 153 (1995) 108-122.

[58] A.L. Bugaev, A.A. Guda, A. Lazzarini, K.A. Lomachenko, E. Groppo, R. Pellegrini, A. Piovano, H. Emerich, A.V. Soldatov, L.A. Bugaev, V.P. Dmitriev, J.A. van Bokhoven, C. Lamberti, Catal. Today 283 (2017) 119-126.

[59] G.R. Fredriksen, E.A. Blekkan, D. Schanke, A. Holmen, Chem. Eng. Technol. 18 (1995) 125-131.

[60] B.C. Smith, Spectroscopy 30 (2015) 40-46.

[61] G. Kadinov, C. Bonev, S. Todorova, A. Palazov, J. Chem. Soc., Faraday Trans. 94 (1998) 3027-3031.

[62] L.E.S. Rygh, O.H. Ellestad, P. Klæboe, C.J. Nielsen, Phys. Chem. Chem. Phys. 2 (2000) 1835-1846.

[63] S. Sun, N. Tsubaki, K. Fujimoto, Appl. Catal. A Gen. 202 (2000) 121-131.

[64] J. Zhang, J. Chen, J. Ren, Y. Sun, Appl. Catal. A Gen. 243 (2003) 121-133.

[65] M. Jiang, N. Koizumi, T. Ozaki, M. Yamada, Appl. Catal. A Gen. 209 (2001) 59-70.

[66] K.M. Rao, G. Spoto, A. Zecchina, J. Catal. 113 (1988) 466-474.

[67] G. Busca, R. Guidetti, V. Lorenzelli, J. Chem. Soc., Faraday Trans. 86 (1990) 989.

[68] V.L. Kuznetsov, M.N. Aleksandrov, L.N. Bulgakova, J. Mol. Catal. 55 (1989) 146-158.

[69] C.G. Visconti, L. Lietti, E. Tronconi, P. Forzatti, R. Zennaro, E. Finocchio, Appl. Catal. A Gen. 355 (2009) 61-68.

[70] L.E.S. Rygh, C.J. Nielsen, J. Catal. 194 (2000) 401-409.

[71] F.-Y. Zhang, S.G. Advani, A.K. Prasad, M.E. Boggs, S.P. Sullivan, T.P. Beebe, Electrochim. Acta 54 (2009) 4025-4030.

[72] M. Li, M. Boggs, T.P. Beebe, C.P. Huang, Carbon 46 (2008) 466-475.

[73] D.X. Ye, S. Pimanpang, C. Jezewski, F. Tang, J.J. Senkevich, G.C. Wang, T.M. Lu, Thin Solid Films 485 (2005) 95-100.

[74] Y. Pei, Y. Ding, H. Zhu, J. Zang, X. Song, W. Dong, T. Wang, L. Yan, Y. Lu, Reac. Kinet. Mech. Cat. 111 (2013) 505-520.

[75] M.C. Biesinger, B.P. Payne, A.P. Grosvenor, L.W.M. Lau, A.R. Gerson, R.S.C. Smart, Appl. Surf. Sci. 257 (2011) 2717-2730.

[76] A. Rodriguez-Gomez, J.P. Holgado, A. Caballero, ACS Catal. 7 (2017) 5243-5247.

[77] J. Wang, P.A. Chernavskii, A.Y. Khodakov, Y. Wang, J. Catal. 286 (2012) 51-61.

[78] V.A. O'Shea, M.C. Galvan, A.E. Prats, J.M. Campos-Martin, J.L. Fierro, Chem. Commun. 47 (2011) 7131-7133.

[79] C.J. Powell, J. Electron. Spectrosc. Relat. Phenom. 185 (2012) 1-3.

[80] NIST: National Institute of Standards and Technology, https://srdata.nist.gov/xps/WagnerPlot.aspx.

[81] A.M. Abdel-Mageed, D. Widmann, S.E. Olesen, I. Chorkendorff, J. Biskupek, R.J. Behm, ACS Catal. 5 (2015) 6753-6763.

5.6. Supporting Information

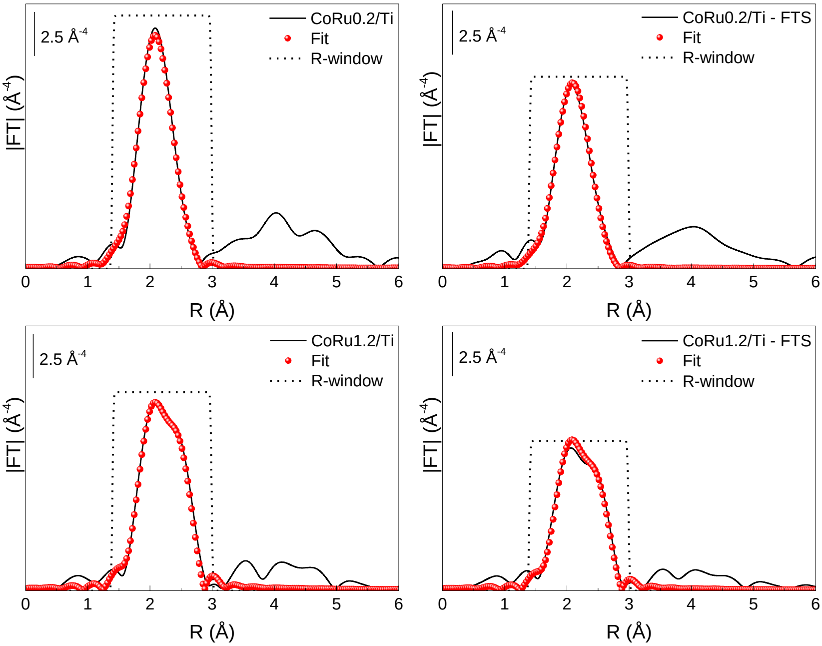

Figure 5.S1. Moduli of Fourier transform of k^3-weighted EXAFS spectra (not phase corrected) and fitting curve of CoRu/Ti catalysts in as-reduced state and under FTS reaction conditions.

CHAPTER 6

IMPROVING THE CATALYTIC ACTIVITY OF CORU/TIO$_2$ CATALYSTS FOR FISCHER-TROPSCH SYNTHESIS BY REDUCTION-OXIDATION-REDUCTION (ROR) TREATMENTS

In the previous chapters, the influence of titania properties (crystalline phase and anatase surface area) were studied taking into account the SMSI effect. Then, in Chapter 5, the Ru content as promoter in Co/TiO_2-anatase catalysts was studied. Since we stablished the factors influencing the CoRu/TiO_2-anatase system, this chapter presents the investigation of ROR (reduction, oxidation and re-reduction) treatments in order to improve the catalytic activity of CoRu/TiO_2 catalysts for Fischer-Tropsch synthesis.

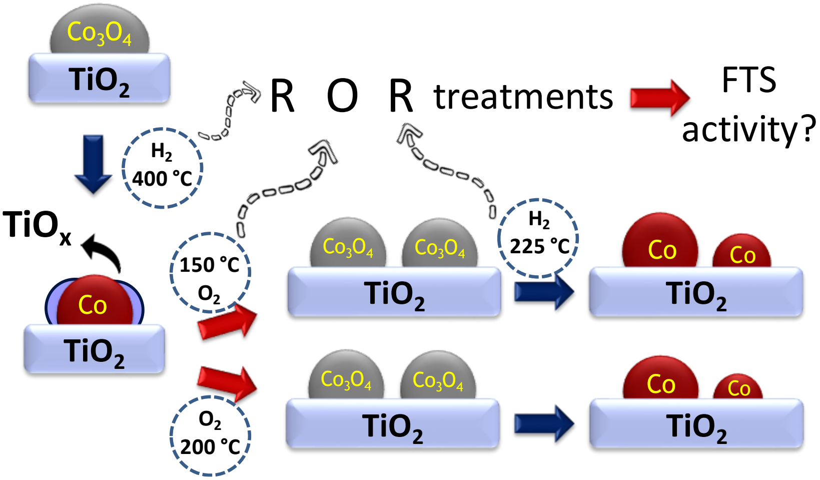

6.1. Introduction

The Fischer-Tropsch synthesis (FTS) is a commercial technology that converts synthesis gas (or syngas), a mixture of CO and H_2, into fuels and chemicals. The FTS is at the core of XTL (X-to-liquids) technologies, in which X represents the source of syngas, traditionally, coal (CTL) or natural gas (GTL), and more recently biomass as a renewable feedstock [1, 2].

Co-based catalysts are preferred over Fe-based systems for producing high quality liquid fuels, particularly diesel, via FTS due to their high activity, high selectivity to higher (C_{5+}) hydrocarbons, and low water-gas shift (WGS) activity [3]. Since metallic cobalt is the active phase for CO hydrogenation, cobalt nanoparticles are typically deposited on supports with high surface area, such as SiO_2, Al_2O_3 and TiO_2 in order to maximize the amount of exposed cobalt metal sites [4].

In this sense, several parameters can be controlled to tune the concentration of Co^0 surface sites, such as Co particle size (i.e. dispersion), degree of cobalt reduction (DOR), the presence of metal promoters and the textural, morphological and chemical properties of the support [3, 5-7]. In fact, it has been reported that the physicochemical characteristics of the support play a major role in the control of size and DOR of supported cobalt nanoparticles (NPs) [4]. Jacobs and co-workers have reported that the interaction between Co nanoparticles and the support increase in the order $SiO_2 < TiO_2 < Al_2O_3$ [5]. For highly interacting supports, such as Al_2O_3 and TiO_2, small amounts of metal promoters are usually added in the catalyst formulation to improve the cobalt reducibility and/or dispersion [8-10].

Interestingly, Iglesia and co-workers [11] reported an increased catalytic activity for Ru-promoted Co/TiO_2 catalysts compared to the non-promoted counterpart, which was attributed to the capacity of Ru for maintaining a higher amount of exposed Co^0 sites during reaction by avoiding the formation of carbonaceous species on the surface of cobalt NPs. They also highlighted the importance of obtaining Co and Ru NPs in close proximity (bimetallic particles) in order to take full advantage of the Ru promoter effect.

However, an important feature of titania-supported metal catalysts is the possible occurrence of the SMSI (strong metal-support interaction) effect during catalyst reduction treatment at high temperature, by which partially reduced titania species (TiO_x) migrate and (partly) cover the surface of the metallic NPs (decoration effect), inhibiting their capacity to chemisorb CO and H_2 [12, 13]. Moreover, the magnitude of the SMSI effect can be controlled by modifying the titania properties. In this sense, a more pronounced SMSI effect for catalysts supported on TiO_2-anatase with respect to those based on rutile-TiO_2 has been reported in literature [14-16]. Besides, for Co catalysts supported on TiO_2-anatase, the extent of the SMSI effect was shown to increase with the support surface area [17-19].

On the other hand, in the case of metals (Co, Ru) supported on titania for FTS, the water generated under reaction conditions can reverse the SMSI effect through oxidation of the decorating TiO_x species and restore, at least partially, the chemisorption capacity of the supported metal NPs [20]. In this sense, Anderson and co-workers [21] have studied the conditions needed to revert the SMSI effect for Pt/TiO_2 and Rh/TiO_2 catalysts. Interestingly, these authors reported that more extreme conditions during re-oxidation are required to eliminate the SMSI state with Pt (400 °C in O_2), while the recovery of the normal state (without SMSI) is almost complete for Rh/TiO_2 catalysts after a re-oxidation treatment at 300 °C.

Soled and co-workers [22] submitted a CoRe/TiO_2 catalyst to reduction, oxidation and re-reduction (ROR) treatments in order to monitor the SMSI effect. In the first reduction treatment (375 °C/2 h), the SMSI state was generated and, then, the catalyst was passivated and subsequently submitted to oxidation with dry air (150 °C/2 h) to revert the decoration effect. Finally, the sample was re-reduced in H_2 at a low temperature of 225 °C for several hours so as to reduce Co oxides to metallic Co while avoiding re-reduction of the TiO_2 support (occurring at higher temperatures) and, thus, the possibility for SMSI. By monitoring the H_2 chemisorption capacity of the samples, the authors observed that the sample submitted to a ROR treatment showed 1.6 higher H_2 uptake than that measured for the catalyst immediately after reduction at 375 °C for 2 h. However, the impact of these treatments on the FTS performance of the catalysts was not addressed in that study.

The ROR treatments are usually employed to regenerate deactivated FTS catalysts. Thus, after a dewaxing process, the spent catalyst is oxidized and subsequently re-reduced to restore its activity [23, 24]. However, some authors observed an increase in cobalt dispersion after ROR treatments, i.e. decrease in the average size of Co NPs, resulting in a lower intrinsic activity (TOF) [25, 26]. This was attributed to the lower TOF of Co particles with sizes below the critical value of 6-8 nm [27, 28].

Lögdberg and co-workers [26], employing a CoRe/TiO_2 catalyst, recently reported an increase in selectivity to C_{5+} after submitting the catalyst to an ROR treatment; however, this catalyst showed an inferior TOF with respect to the sample reduced only once. Besides, the conditions employed for the ROR process (oxidation at 300 °C/16 h and re-reduction at 350 °C/16 h) were more severe than those applied in the work of Soled and co-workers [22], which may have resulted in the reformation of the SMSI effect. However, the authors did not provide details about the SMSI state after the redox treatments.

Based on the exposed above, there is a lack of evidence about the influence of reduction-oxidation-reduction (ROR) treatments and its consequences in the SMSI effect for Co/TiO_2 catalysts. Understanding the parameters influencing the SMSI effect and how they could be controlled is crucial to the design and improvement of this type of catalysts. In this work, we investigated the effect of ROR treatments on the FTS performance of Ru-promoted Co/TiO_2 catalysts. To this purpose, the catalyst was first reduced at 400 °C (leading to the SMSI state), subsequently submitted to an oxidation treatment at a temperature of 150 or 200 °C to revert the SMSI state, and then re-reduced at low temperature (225 °C). The physicochemical properties of the catalysts at different stages of the ROR treatments were determined by conventional *ex situ* techniques as well as by *in situ* spectroscopy, and correlated with their activity and selectivity for the Fischer-Tropsch synthesis.

6.2. Experimental

6.2.1. Synthesis of TiO_2-anatase support

The pure TiO_2-anatase support was prepared by hydrothermal synthesis using titanium(IV) n-butoxide (99 +%, Alfa Aesar) and acetic acid (99.5%, Aldrich) as starting reagents. First, 9.6 mL of the titanium source was added dropwise in 28 mL of acetic acid solution (1.5 mol/L), under magnetic stirring at room temperature. Afterwards, the mixture was transferred to a Teflon-lined stainless steel autoclave of 200 mL capacity and hydrothermally treated at 120 °C for 24 h. Next, the solid was collected by centrifugation, washed 5 times with ethanol in a process involving redispersion and centrifugation, dried in an oven at 60 °C overnight, and finally calcined in flowing air at 400 °C for 4 h, with a heating rate of 1°C/min.

6.2.2. Synthesis of CoRu/TiO_2 catalysts

The catalysts were prepared by incipient wetness co-impregnation of the calcined support with an aqueous solution containing $Co(NO_3)_2 \cdot 6H_2O$ (Aldrich) and $Ru(NO)(NO_3)_3$ (Aldrich) in order to achieve a nominal composition of 10 wt% Co and 0.5 wt% Ru (as a reduction promoter). After impregnation, the material was dried at 100 °C overnight and calcined in flowing air at 300 °C for 3 h.

6.2.3. Reduction, oxidation, re-reduction (ROR) treatments

After calcination, the catalyst was submitted to ROR treatments as indicated in Figure 6.1. First, the calcined sample (Co/Ti-C) was reduced in pure H_2 flow at 400 °C for 10 h (Co/Ti-R). Subsequently, the reduced catalyst was submitted to an oxidizing treatment in flowing air for 2 h at either 150 °C (Co/Ti-RO1) or 200 °C (Co/Ti-RO2). Finally, the Co/Ti-RO1 and Co/Ti-RO2 samples were re-reduced in pure H_2 flow at 225 °C for 2 h to produce, respectively, samples Co/Ti-ROR1 and Co/Ti-ROR2. Dry air was used in each oxidizing treatment and all heating rates were 1 °C/min. After each reduction treatment, the catalysts were passivated with < 1% O_2/N_2 flow.

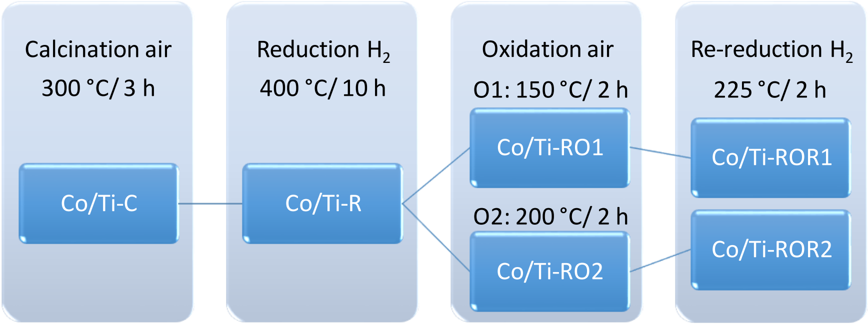

Figure 6.1. Scheme of reduction, oxidation and re-reduction treatments (ROR) applied in the catalyst.

6.2.4. Characterization techniques

The Co and Ru contents were obtained by Inductively Coupled Plasma-Optical Emission Spectrometry (ICP-OES) in a Varian 715-ES spectrometer after dissolving the samples in an acid mixture of HNO_3:HF:HCl (1:1:3 volume ratio).

Crystalline phase identification was performed by X-ray powder diffraction (XRD) on the calcined materials using a Philips X'Pert diffractometer applying monochromatized Cu-K_α radiation (λ = 0.15406 nm). Average TiO_2 particle sizes were calculated from the most intense (101) reflection of anatase (2θ = 25.3°) using the Scherrer equation assuming a shape factor of k = 0.9.

Textural properties were determined from the N_2 adsorption isotherms measured at −196 °C in an ASAP-2420 equipment (Micromeritics). Prior the analysis, the samples were degassed at 300 °C under vacuum overnight. Specific surface areas were determined following the Brunauer-Emmett-Teller (BET) method, pore size distributions were derived by applying the Barrett-Joyner-Halenda (BJH) approach to the adsorption branch of the isotherms, and total pore volumes were obtained at a relative pressure of 0.98.

The morphology of the TiO_2 support was studied by field emission scanning electron microscopy (FESEM) using a ZEISS Ultra-55 microscope. The sample powder was deposited in a double-sided tape and analyzed with metal covering.

The reducibility of cobalt was investigated by H_2 temperature-programmed reduction (H_2-TPR) using a Micromeritics Autochem 2910 device. Typically, 55 mg of catalyst were flushed with an Ar flow at room temperature for 30 min, and subsequently, the gas atmosphere was switched to a mixture of H_2 diluted (10 vol%) in Ar. Next, the reduction took place by linearly increasing the temperature up to 900 °C, with a heating rate of 10 °C/min, while monitoring the H_2 consumption using a thermal conductivity detector (TCD) previously calibrated using a standard CuO sample as reference. A 2-propanol/$N_{2(liq)}$ trap located downstream the analyzer was used to retain water and to ensure that only H_2 reaches the detector. In order to determine the degree of cobalt reduction (DOR), additional experiments were carried out in the same equipment as follows. First, the catalysts were reduced at exactly the same conditions applied prior to the FTS reaction, i.e. in pure flowing H_2 at 400 °C for 10 h. Then, after switching to the diluted H_2 stream (10 vol% H_2 in Ar), the temperature was increased from 400 °C to 900 °C at a heating rate of 10 °C/min while the H_2 signal was monitored by the TCD. The degree of cobalt reduction (DOR) was calculated assuming that this H_2 consumption corresponds to the reduction of CoO that remained after the 400 °C reduction treatment.

The amount of surface cobalt metal sites was measured by H_2 chemisorption at 100 °C in a Quantachrome Autosorb-1C instrument by extrapolating the total gas uptakes in the adsorption isotherms at zero pressure [29]. Before measurements, approx. 300 mg of catalyst were reduced under pure H_2 flow at 400 °C for 10 h. From the total amount of chemisorbed H_2, metal particle sizes ($d(Co^0)_{H2}$) were estimated taking into account the Co content (from ICP-OES) and the degree of cobalt reduction (DOR), assuming spherical particles and an adsorption stoichiometry H:Co of 1:1.

Direct measurement of cobalt particle sizes was performed by transmission electron microscopy in a JEOL-JEM 2100F microscope operating at 200 kV in scanning transmission mode (STEM) using a high-angle annular dark field (HAADF) detector which provides contrast that has a strong dependence on atomic number. Before microscopy observation, the samples were first reduced *ex situ* under a flow of H_2 at 400 °C (Co/Ti-R catalyst) or at 225 °C (Co/Ti-ROR1 and Co/Ti-ROR2 samples) and passivated at room temperature under a flow of < 1 vol% O_2/N_2. Subsequently, the materials were suspended in isopropanol and ultrasonicated for one minute. Then, a drop was extracted from the top side of the suspension and deposited on a carbon-coated copper grid. Average cobalt particle sizes ($d(Co^0)_{STEM}$) were evaluated after measuring 200-300 particles from several micrographs taken at different positions on the TEM grid, and after correcting for the presence of a 2.5 nm thick CoO passivation outlayer.

X-ray absorption (XAS) experiments at the Co K-edge (7709 eV), were performed at the BL22 (CLÆSS) beamline of ALBA synchrotron (Cerdanyolla del Vallès, Spain) [30]. The white beam was monochromatized using a Si (111) double crystal; harmonic rejection has been performed using Rh-coated silicon mirrors. The spectra were collected in transmission mode by means of the ionization chambers filled with appropriate gases (99.9 % N_2 + 0.1 % Kr for I_0 and 73.2 % N_2 + 26.8 % Kr for I_1). Samples in the form of self-supported pellets of optimized thickness were located inside an in-house built multipurpose cell described by Guilera [31] allowing for *in situ* experiments. The Co/Ti-C and Co/Ti-RO1 catalysts were measured in their oxidized state, while Co/Ti-R and Co/Ti-ROR1 were measured in their reduced and passivated form. Subsequently, these catalysts were re-reduced *in situ* with flow of pure H_2 at 400 °C (Co/Ti-R) or 225 °C (Co/Ti-ROR1) for 2 h at atmospheric pressure. Subsequently, the temperature was decreased to 220 °C for data acquisition in order to avoid thermal effects on the collected spectra and to improve signal quality. Afterwards, a flow of H_2 (20 vol% in He) and CO (20 vol% in He), with H_2/CO = 2 (molar ratio), was passed through the cell, the pressure raised to 7 bar at 220 °C (FTS), and the spectra measured after 3 h at these conditions. Several scans were acquired at each measurement step to ensure spectral reproducibility and good signal-to-noise ratio. The data reduction and extraction of the $\chi(k)$ function was performed using Athena code, while EXAFS data analysis was done using the Arthemis software [32]. Phase and amplitudes were calculated by FEFF6 code.

CO-FTIR spectra were recorded with a Vertex 70 FTIR spectrometer using a MCT detector and acquiring at 4 cm^{-1} resolution. The previously reduced (at 400 °C for 10 h or 225 °C for 2 h) and passivated samples were pressed into self-supported wafers of 10 mg/cm^2 and reduced again in the IR cell at 300 °C (Co/Ti-R catalyst) or at 225 °C (Co/Ti-

ROR1 and Co/Ti-ROR2 samples) in H_2 flow for 2 h, followed by vacuum treatment at each reduction temperature for 1 h. Afterwards, the samples were cooled down to 25 °C (Co/Ti-R) or -50 °C (after ROR treatments) under dynamic vacuum, and CO dosed at increasing pressures until saturation. FTIR spectra were recorded after each dosage.

Ambient-pressure X-ray photoelectron spectroscopy (AP-XPS) experiments were performed at the ALBA synchrotron in the CIRCE beamline, which is an undulator beamline with a photon energy range of 100-2000 eV. The beam spot size at the sample was 100×30 µm^2. The AP-XPS endstation, equipped with a PHOIBOS 150 analyzer from SPECS, has been described elsewhere [33]. The data were acquired with an instrumental energy resolution better than 0.3 eV, PE 10 eV, and exit slit 20 µm. The sample (10 mg) was pelletized and mounted onto the sample holder using a resistive button heater for sample heating. The temperature was monitored during all experiments with a K-type thermocouple in direct contact with the sample. First, the catalyst was heated up to 400 °C under 1 mbar of pure H_2 until complete reduction of Co particles (ca. 5.5 h). Subsequently, the temperature was decreased to 100 °C, the gas atmosphere switched to pure O_2 (1 mbar), and the spectra collected at 100, 150, 200, and 250 °C, for approx. 7.5, 6.5, 6 and 2 h, respectively. Afterwards, the gas atmosphere was switched again to pure H_2 (1 mbar) to perform re-reduction of the catalyst, remaining 2 h under H_2 at 200 °C and 3.5 h at 225 °C. Finally, CO and H_2 were fed into the analysis chamber using two leak valves maintaining a total syngas pressure of 1.7 mbar (H_2/CO = 2) inside the chamber during 3 h at 220 °C (FTS). The AP-XP spectra were acquired using two different photon energies, 1000 eV for Co 2p (Co 2p KE = 222 eV) and 680 eV for Ti 2p (Ti

2p KE = 220 eV), in order to ensure a small penetration depth of the incident X-ray for tracking the events occurring on the surface of the catalyst during the redox treatments. XPS data were analyzed using the CASA software. The atomic fraction of each element was obtained from the peak areas, calibrated for the incident photon flux and the corresponding cross sections [34].

6.2.5. Fischer-Tropsch synthesis experiments

FTS experiments were carried out in a fixed-bed stainless steel reactor (internal diameter of 10 mm and length of 40 cm) loaded with 0.7 g of catalyst (0.25-0.42 mm pellet size), diluted with SiC granules (0.6-0.8 mm). Before reaction, the catalysts were reduced *in situ* at ambient pressure in flowing H_2 according to the different reduction treatments applied, i.e. at 400 °C for 10 h (1 °C/min) for catalyst Co/Ti-R, while for the materials submitted to ROR treatments, the first reduction (400 °C/10 h) and subsequent oxidation were carried out *ex situ*. The final re-reduction treatment was performed *in situ* at ambient pressure in flowing H_2 at 225 °C for 2 h (1 °C/min). After the reduction, the reactor was cooled down to 100 °C under flowing H_2 and the gas atmosphere changed to syngas with H_2/CO molar ratio of 2 (CO:H_2:Ar volume ratio of 3:6:1, Ar used as internal standard for GC analyses), the pressure increased up to 10 bar, and the temperature raised up to 220 °C (2 °C/min). To control the temperature through the catalytic bed, two thermocouples connected to independent PID controllers were used. After the reaction temperature was established, a third vertically sliding thermocouple was employed to check the absence of temperature gradients (T = 220 ± 1 °C). Initially, a constant gas hourly space velocity (GHSV) of 6 $L_{syngas}/(g_{cat}\cdot h)$ was stablished. After 8 h on stream, the GHSV was adjusted for each catalyst so as to reach a constant CO conversion of 15 ± 1% in the *pseudo*-steady state, and maintained at this conditions for an additional period of ca. 8 h. The stream leaving the reactor was depressurized and periodically analyzed online by gas chromatography in a Varian 450 chromatograph equipped with TCD and FID detectors and three columns. Heavier products and water were condensed in two consecutive traps (at 150 °C and 100 °C, respectively), both at 10 bar, and after weighted and diluted with CS_2, the hydrocarbon fraction collected in the traps were analyzed offline in the same GC. Product selectivities (given on a carbon basis) were then obtained by combining the online and offline GC analyses through the common product methane. Carbon mass balances of 100 ± 2% were obtained for the experiments reported in this study.

6.3. Results and discussion

6.3.1. *Characterization of TiO_2-support*

The X-ray diffraction pattern of the calcined TiO_2 support (Figure 6.2) confirms the presence of anatase as the unique crystalline phase (JCPDS 00-021-1272), as expected from the use of acetic acid during the hydrothermal synthesis [35]. The mean particle size of TiO_2 calculated by the Scherrer equation was 11 nm, which resulted in a high specific surface area of 151 m^2/g (Table 6.1).

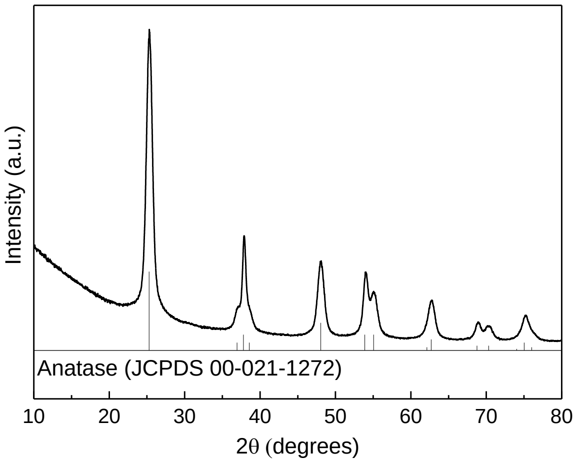

Figure 6.2. X-ray diffraction pattern of the TiO$_2$-anatase support.

The anatase support exhibited a type IV adsorption isotherm (Figure 6.3a), characteristic of mesoporous solids [36], and a pore size distribution centered at 11.4 nm (Figure 6.3b). Besides, the total pore volume measured for the anatase carrier was 0.29 cm^3/g (Table 6.1).

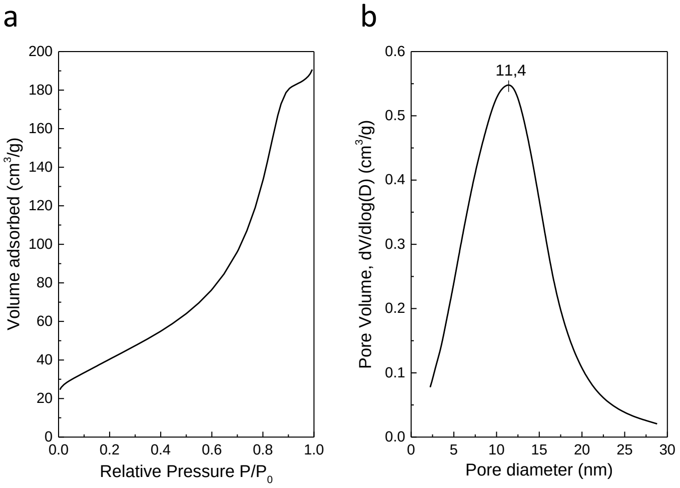

Figure 6.3. N$_2$ adsorption isotherm (a) and corresponding pore size distribution (b) for TiO$_2$-anatase support.

The concentration and nature of acid, as well as temperature and time applied during hydrothermal synthesis dictate the properties of the final TiO$_2$ material, like crystalline phase and morphology [35, 37]. The conditions applied in this work resulted in TiO$_2$-anatase crystallites with rice-like morphology sizing 10 to 30 nm, as observed in the representative FESEM image shown in Figure 6.4.

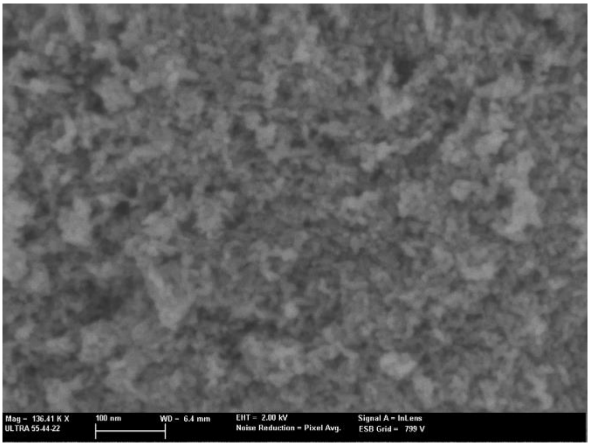

Figure 6.4. Representative FESEM image for the TiO$_2$-anatase carrier.

6.3.2. Characterization of Co/Ti-C catalyst

After impregnation of the TiO$_2$ support with Co and Ru precursor salts and subsequent calcination, the Co/Ti-C catalyst was analyzed by XRD diffraction. The XRD pattern, as shown in Figure 6.5, reveal the reflections corresponding to the Co$_3$O$_4$ spinel phase (JCPDS 00-042-1467). However, a reliable measurement of the mean cobalt particle size (d_{Co}) by line broadening analysis is not possible due to the low intensity of the Co$_3$O$_4$ reflections and overlapping with the anatase diffraction peaks. The TiO$_2$ mean particle size remained the same as before impregnation (11 nm) and no other diffraction lines corresponding to additional titania crystalline phases (rutile and/or brookite) were identified.

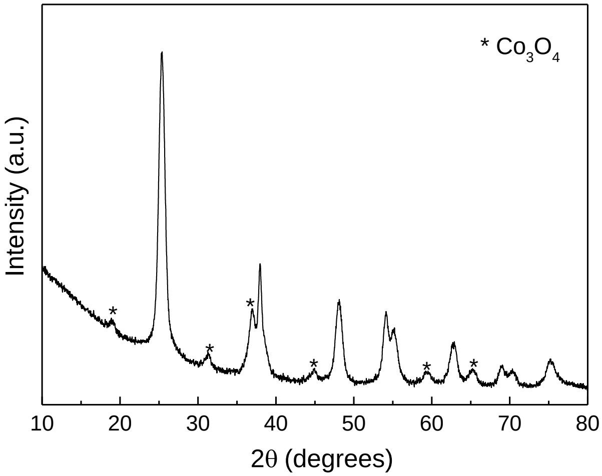

Figure 6.5. X-ray diffraction pattern of the Co/Ti-C catalyst.

The N_2 adsorption isotherm of the Co/Ti-C catalyst (Figure 6.6a) can also be classified as type IV, characteristic of mesoporous solids [36], as for the pristine support. The pore size distribution of the Co/Ti-C sample (Figure 6.6b) exhibits a maximum at 11.7 nm, evidencing minor deviations with respect the TiO_2-anatase carrier. The textural properties of the support and the Co/Ti-C catalyst, derived from the corresponding N_2 adsorption isotherms, are summarized in Table 6.1. A reduction of approx. 24% in surface area is noticed for Co/Ti-C catalyst in comparison with the support. However, after correcting the catalyst surface area per mass of TiO_2, the calculated difference resulted inferior than 10%. A similar trend is observed when considering the total pore volume, both facts pointing to insignificant support pore blockage by the supported Co and Ru oxide phases.

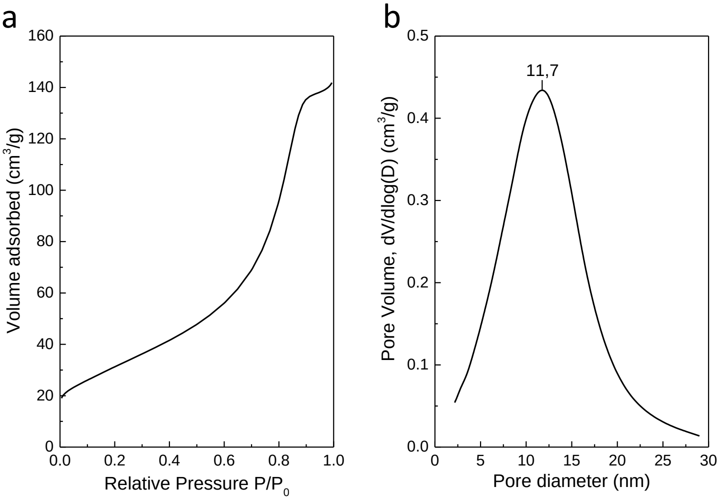

Figure 6.6. N$_2$ adsorption isotherm (a) and corresponding pore size distribution (b) for Co/Ti-C catalyst.

Table 6.1. Textural properties obtained from N$_2$ adsorption isotherm for the TiO$_2$-anatase support and Co/Ti-C catalyst.

Material	BET surface area (m^2/g)	Average pore diameter (nm)	Total pore volume (cm^3/g)
TiO$_2$-anatase	151	11.4	0.29
Co/Ti-C	115 (137)[a]	11.7	0.22 (0.26)[a]

[a] The value in parenthesis correspond to the data recalculated per mass of TiO$_2$ support.

The cobalt metal content measured by ICP-OES for the calcined catalyst (12 wt%) slightly exceeded the nominal content (10 wt% Co), while the final Ru concentration (0.2 wt%) was 40% of the theoretical value (0.5 wt% Ru). This loss of Ru from the catalyst has been attributed to the formation of volatile RuO$_x$ compounds during calcination under air atmosphere [38].

The H_2-TPR profile of the Co/Ti-C catalyst is shown in Figure 6.7. Reduction of cobalt is seen to occur in two main steps: 1) $Co_3O_4 \rightarrow CoO$ (first peak with maximum at 150 °C), and 2) $CoO \rightarrow Co^0$ (second peak with maximum at 305 °C), as commonly observed for ex-nitrate supported Co catalysts [38-40]. The shoulder at approx. 400 °C in the high-temperature reduction peak can be attributed to the reduction of Co^{2+} species interacting strongly with the support. Despite this, the degree of cobalt reduction (DOR) for the calcined catalyst calculated after reduction in pure H_2 flow at 400 °C during 10 h (additional TPR analysis, as detailed in the experimental part) is 88%. However, it is likely that a certain reduction of Ti species in the TiO_2 support (causing the SMSI effect) also took place during the additional TPR measurement, especially at higher temperatures, contributing to the total H_2 consumed and, therefore, underestimating the calculated DOR value. Due to this, in the following we will consider a DOR of 100% after reducing the Co/Ti-C catalyst at 400 °C, in line with other works in the literature which also reported DOR values for Co/TiO_2 catalysts close to 100% [41, 42]. The presence of Ru as promoter, even in amounts as low as 0.2 wt%, certainly contributes to achieve such a high degree of cobalt reduction, as evidenced in Chapter 5.

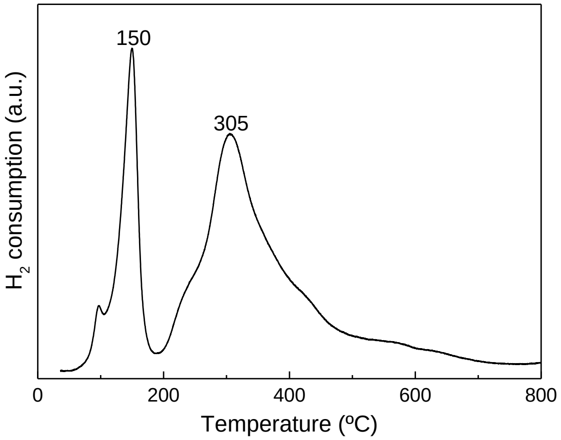

Figure 6.7. H_2-temperature-programmed reduction profile of Co/Ti-C catalyst.

6.3.3. Reduction, oxidation and re-reduction (ROR) treatments

The calcined catalyst was submitted to ROR treatments in order to avoid decoration by TiO_x species (SMSI effect) and by this way, increase the concentration of exposed Co^0 sites. In this section, the *ex situ* characterization of catalysts submitted to the ROR treatments, schematized in Figure 6.1, is presented.

Figure 6.8 shows the XRD patterns of catalysts after reduction at 400 °C and passivation (Co/Ti-R, a), oxidation at 150 °C (Co/Ti-RO1, b) and subsequent re-reduction at 225 °C and passivation (Co/Ti-ROR1, c). For the reduced and passivated Co/Ti-R catalyst, broad and low intense peaks can be detected between 40-45°. In the inset, a comparison with *hcp* and *fcc* Co patterns (JCPDS 00-005-0727 and 00-015-0806, respectively) is shown; however, a clear identification of both crystalline phases is rather difficult due to the low intensity of the diffraction signals. After oxidation at 150 °C (b), the peak related to the metallic Co phase can still be perceived, besides some additional reflections assigned to Co_3O_4 (marked with an asterisk). After re-reduction at 225 °C (c) only the peak related to metallic cobalt phase can be observed.

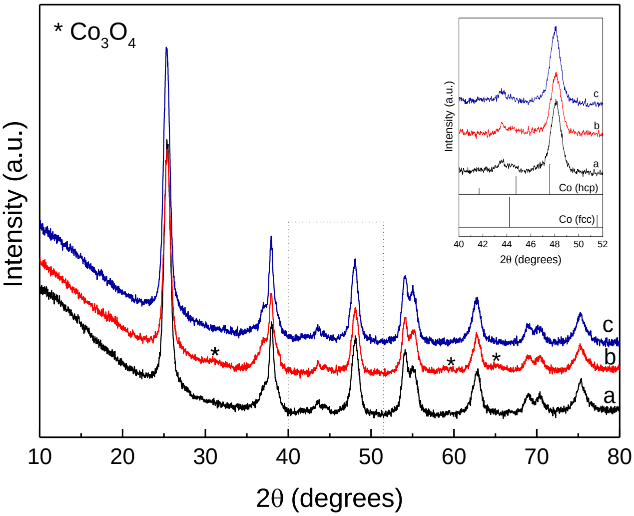

Figure 6.8. X-ray diffraction patterns of Co/Ti-R (a), Co/Ti-RO1 (b) and Co/Ti-ROR1 (c) catalysts.

A similar trend was observed for the catalyst oxidized at 200 °C (Figure 6.9). After oxidative treatment at 200 °C (b) some reflections related to Co_3O_4 can be seen, besides the peak at ca. 44° assigned to metallic cobalt. With subsequent re-reduction at 225 °C (c), the signals related to the spinel phase can no longer be observed and the peak at ca. 44° experience a certain increase in intensity, signing for the re-reduction of cobalt NPs.

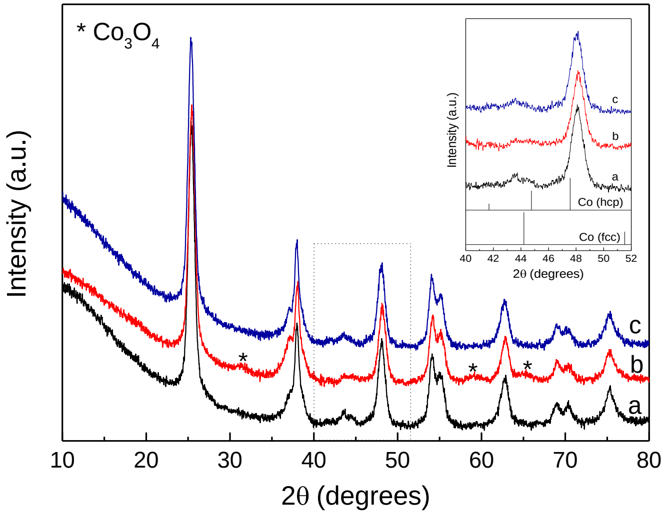

Figure 6.9. X-ray diffraction patterns of Co/Ti-R (a), Co/Ti-RO2 (b) and Co/Ti-ROR2 (c) catalysts.

The above XRD results evidence that the oxidation treatments at 150 and 200 °C in flowing air can lead to partial re-oxidation of Co NPs, but still some remaining metallic cobalt particles could be identified. After re-reduction at 225 °C, only metallic cobalt particles were detected for both catalysts (within the limits of the technique), pointing to the easy re-reduction of Co NPs.

A consequence of the SMSI effect is the suppression of H_2 and CO chemisorption capacity for the supported metal NPs. In order to monitor the influence of the ROR treatments on the SMSI effect, the H_2 chemisorption capacity of the catalysts was determined after each treatment and the results are presented in Table 6.2.

Table 6.2. Cobalt properties in Co/Ti catalysts after reduction, oxidation and re-reduction treatments.

Catalyst	H_2 uptake (μmol/g_{cat})	Co^0 particle size (nm)		$d(Co^0)_{H2}/d(Co^0)_{STEM}$ ratio
		$d(Co^0)_{H2}$	$d(Co^0)_{STEM}$ [a]	
Co/Ti-R	24.6	39.7	8.5 (2.4)	4.67
Co/Ti-ROR1	78.1	12.5	6.5 (1.8)	1.92
Co/Ti-ROR2	90.0	10.8	5.6 (1.6)	1.93

[a] Values in parenthesis indicate the standard deviation.

As observed in Table 6.2, both ROR treatments resulted in higher H_2 chemisorption capacities, with H_2 uptakes 3.2 and 3.6 times higher for catalysts submitted to ROR1 and ROR2 treatments, respectively. These higher chemisorption capacities are probably due to the (partial) reversion of SMSI effect during the oxidative treatments at 150 or 200 °C, resulting in the oxidation of the decorating TiO_x species and consequent increase in the amount of accessible metallic Co sites. After re-reduction at low temperature (225 °C), the cobalt particles undergo re-reduction without further generation of TiO_x species (i.e. SMSI state), maintaining a high density of surface of Co^0 sites in the Co NPs.

The cobalt metal particle sizes were derived from H_2 chemisorption measurements and by direct microscopy observation (STEM) in reduced and passivated catalysts (Figure 6.10 and Table 6.2). The values of Co^0 particle size derived from H_2 chemisorption significantly decreased after ROR treatments as a consequence of the reversibility of the SMSI effect, approaching the real sizes observed by electron microscopy ($d(Co^0)_{STEM}$). On the other hand, the Co^0 particle sizes measured by STEM decreased after applying the ROR treatments, pointing to a certain redispersion of cobalt nanoparticles, concurring with previous observations [25, 26].

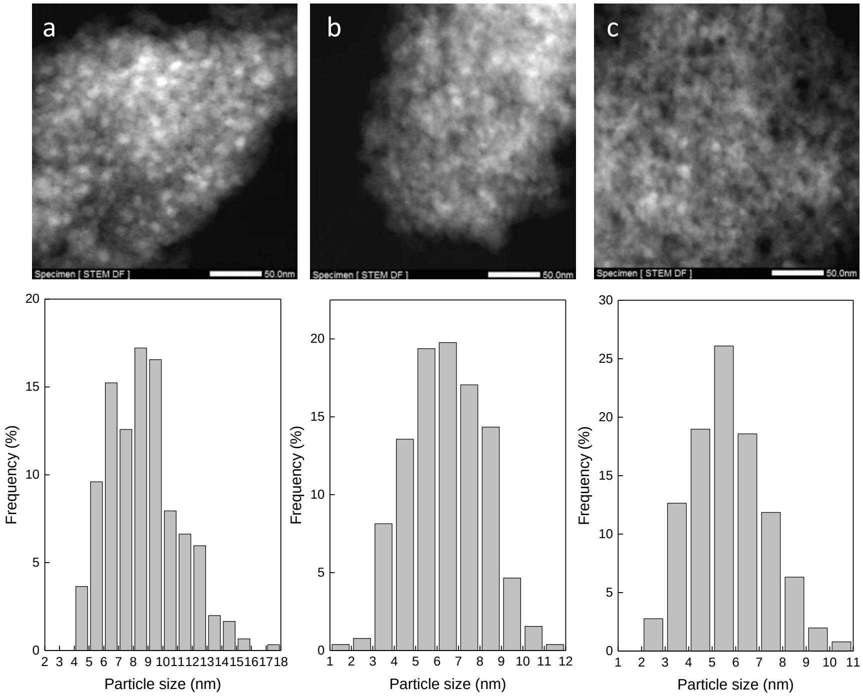

Figure 6.10. HAADF-STEM micrographs (top) for H$_2$-reduced and passivated Co/Ti-R (a), Co/Ti-ROR1 (b) and Co/Ti-ROR2 (c) catalysts. The respective Co^0 particle size histograms are represented beneath its representative corresponding image.

The increase in cobalt dispersion after reduction, oxidation and re-reduction cycles can be explained by the Kirkendall effect [25, 43, 44]. During the first H$_2$ treatment at 400 °C, the Co$_3$O$_4$ particles undergo reduction to the metallic state. With the oxidizing process, a thin oxide layer is created over the cobalt particles forming a hollow structure due to the faster outward diffusion of cobalt with respect to inward diffusion of oxygen (Kirkendall effect). Further re-reduction of cobalt oxide leads to cobalt redispersion as a result of the break-up of hollow spheres into smaller particles [25, 45]. However, for the Co/Ti catalysts investigated in this work, no hollow spheres were detected during microscopy observation probably due to the fact that the samples were in their reduced and passivated state.

Interestingly, the ratio between d(Co^0) calculated by H$_2$ chemisorption and STEM is 4.67 for Co/Ti-R catalyst and decreased to 1.92 and 1.93 for the catalysts submitted to ROR1 and ROR2 treatments, respectively. The similar d(Co^0)$_{H2}$/d(Co^0)$_{STEM}$ ratio for these two samples evidence that the oxidation treatment at 200 °C did not translate into a higher reversibility of the SMSI effect with respect to the oxidation performed at 150 °C. This suggests that the higher H$_2$ uptake obtained for the Co/Ti-ROR2 catalyst is probably due to an increased redispersion (smaller size) of cobalt NPs after the low temperature re-reduction step, as inferred from the corresponding d(Co^0)$_{STEM}$ values in Table 6.2.

The results from Table 6.2 point that both oxidation and re-reduction treatments ROR1 and ROR2 lead to an increase in the concentration of exposed Co^0 sites due to both reversion of the SMSI effect and cobalt redispersion. The latter effect was somewhat more pronounced when the oxidation is performed at 200 °C instead of 150 °C.

6.3.4. In situ characterization of Co/Ti catalysts submitted to ROR treatments by XAS under operational conditions

Since the Co/TiO$_2$ system is rather difficult to be well characterized due to possible interference of the SMSI effect during TPR measurements (to calculate DOR, for instance) and also due to the low intensity and poor resolution of cobalt peaks on X-ray diffraction patterns, we have analyzed the catalysts by X-ray absorption spectroscopy. The element-specific character of this technique makes it possible to follow the changes in cobalt environment without interference of the support.

Figure 6.11 presents the normalized XANES spectra at Co K-edge for the calcined (Co/Ti-C) and Co/Ti-RO1 catalysts.

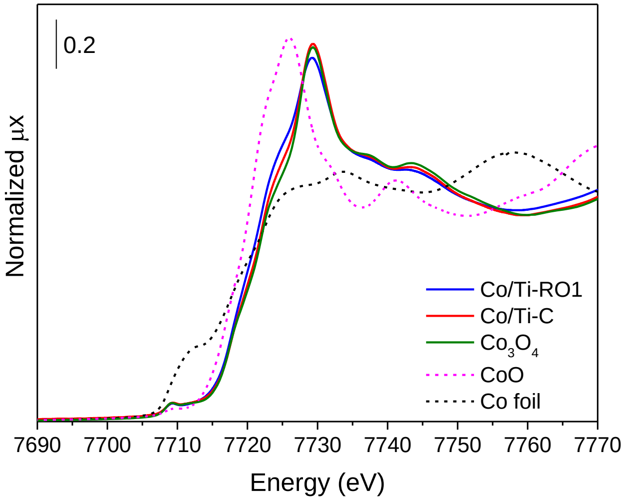

Figure 6.11. Normalized XANES spectra at Co K-edge for oxidized Co/Ti-C and Co/Ti-RO1 catalysts.

By comparing the spectra of catalyst with those of reference compounds (dashed lines), it is clear that cobalt is present as Co_3O_4 in both Co/Ti-C and Co/Ti-RO1 catalysts, in agreement with the corresponding XRD patterns presented in Figures 6.5 and 6.8. For a deeper analysis, the fine structure was Fourier transformed (Figure 6.12) and the spectra of the oxidized catalysts are compared to those of Co_3O_4 spinel and Co metal.

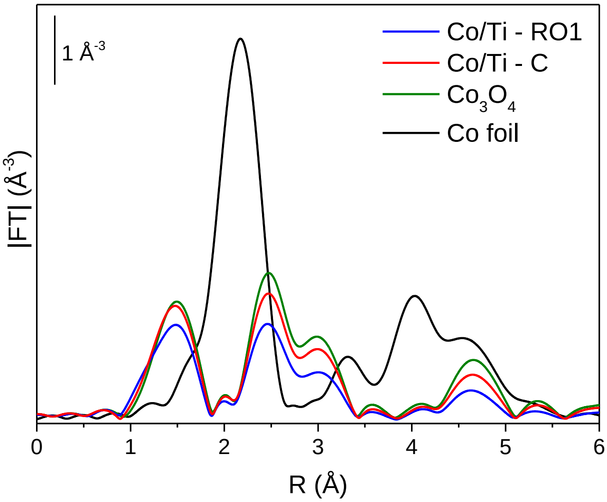

Figure 6.12. |FT| of the EXAFS spectra of oxidized Co/Ti-C and Co/Ti-RO1 catalysts.

The Fourier transform of the EXAFS signal (Figure 6.12) unambiguously show that both catalysts are composed by Co_3O_4, pointing that the oxidation treatment at 150 °C results in complete oxidation of Co^0 NPs to Co_3O_4. Interestingly, the lower amplitude of |FT| for the Co/Ti-RO1 catalyst indicates a smaller cobalt particle size in comparison to Co/Ti-C.

The reduced and passivated catalysts were also analyzed by XAS and the normalized XANES spectra of Co/Ti-R and Co/Ti-ROR1 samples are presented in Figure 6.13.

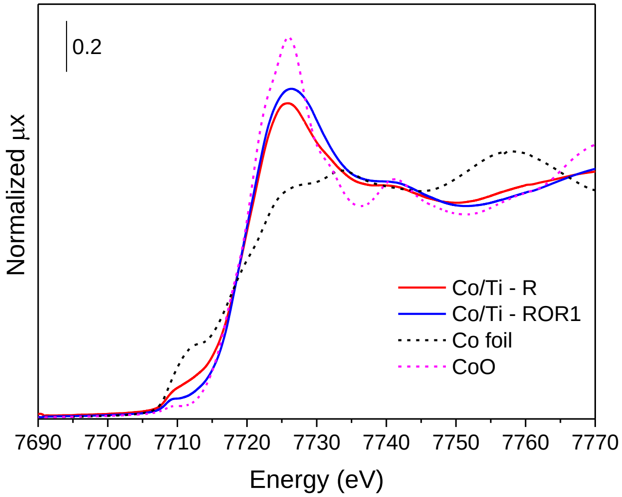

Figure 6.13. Normalized XANES spectra at Co K-edge for reduced and passivated Co/Ti-R and Co/Ti-ROR1 catalysts.

As observed in Figure 6.13, the normalized XANES spectra of Co/Ti-R and Co/Ti-ROR1 catalysts resemble that of the CoO standard, with absorption edge positioned at 7718 eV, indicating that most cobalt atoms are present as Co^{2+}. However, the characteristic XANES features of Co/Ti-R and Co/Ti-ROR1 are much less pronounced with respect to the CoO reference, suggesting a less ordered structure in the formers. Furthermore, the pre-peak at 7710 eV found in spectrum of metallic Co is also observed in the spectra of Co/Ti-R and Co/Ti-ROR1, which indicates that part of the Co atoms are in metallic state.

Figure 6.14 shows the moduli of Fourier transform of reduced and passivated Co/Ti-R and Co/Ti-ROR1 catalysts. Despite of the similitude of the XANES spectra for both catalysts and the reference CoO, the |FT| reveals that the characteristic features of Co/Ti-R and Co/Ti-ROR1 are composed by a complex mixture of contributions from CoO and Co^0, as indicated before from the analysis of the pre-edge feature of XANES spectra.

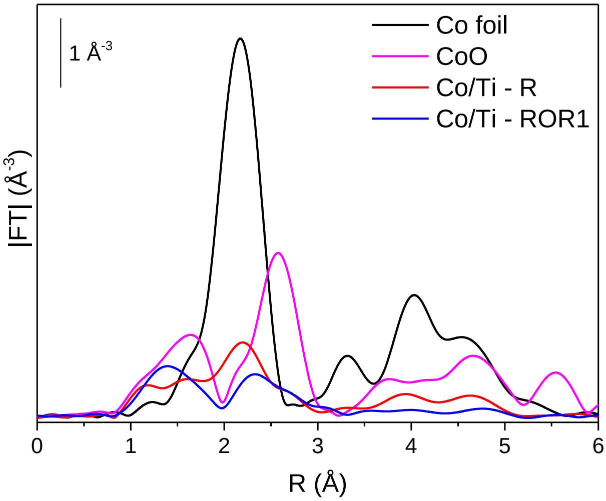

Figure 6.14. |FT| of the EXAFS spectra of reduced and passivated Co/Ti-R and Co/Ti-ROR1 catalysts.

The catalysts were re-reduced *in situ* under H$_2$ flow at selected temperatures (400 °C for Co/Ti-R and 225 °C for Co/Ti-ROR1) for 2 h. Then, the temperature was decreased to 220 °C to avoid different thermal effects on XAS signal and the spectra were measured. Subsequently, the flow was switched to syngas and the spectra were collected after 3 h of *in situ* FTS reaction at 7 bar. Figure 6.15 presents the moduli of Fourier transform of the catalysts after H$_2$ reduction (Co/Ti-R and Co/Ti-ROR1) and during *in situ* FTS reaction (Co/Ti-R-FTS and Co/Ti-ROR1-FTS).

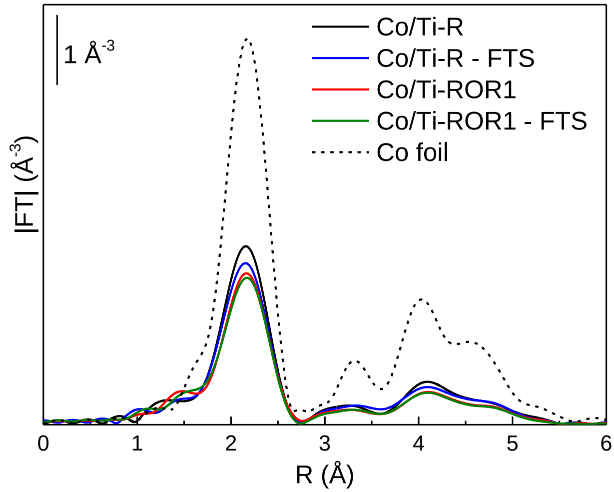

Figure 6.15. Moduli of Fourier transform of the EXAFS spectra of Co/Ti-R and Co/Ti-ROR1 catalysts as-reduced and under FTS reaction conditions.

The |FT| of the EXAFS spectra of as-reduced Co/Ti-R and Co/Ti-ROR1 catalysts (Figure 6.15) resemble to that of Co foil, pointing out that cobalt is in metallic state (Co-Co local environment) in both catalysts before FTS reaction. Furthermore, the different intensity between the spectra of the catalysts and that of Co^0 standard can be explained by the distinct temperature of data collection (room temperature for Co foil versus 220 °C for catalysts), which is a well-known effect affecting EXAFS oscillations [46]. After ROR treatment (as-reduced Co/Ti-ROR1 catalyst), a slight decrease in the first shell intensity can be seen relative to that of the Co/Ti-R sample, which may be indicative of Co redispersion, in agreement with STEM results (Table 6.2). This is supported by the lower cobalt coordination number (Table 6.3) obtained for the catalyst submitted to ROR1 treatment ($N_{Co\text{-}Co} = 6.6$) compared to Co/Ti-R ($N_{Co\text{-}Co} = 7.7$).

The spectra of the catalysts also resemble that of metallic cobalt during FTS reaction. However, slight differences in coordination numbers before and during reaction (Table 6.3) could be perceived for both catalysts, which can be due to static disorder (small changes on surface due to adsorbed products) imposed by FTS conditions [47].

Table 6.3. Summary of optimized parameters by fitting Co K-edge EXAFS data of catalysts during activation and FTS reaction [a].

Catalyst	$N_{Co\text{-}Co}$	$R_{Co\text{-}Co}$ (Å)	σ^2 (Å^2)	ΔE_0 (eV)	R_{factor}
Co foil	12	2.493 ± 0.002	0.0066 ± 0.0003	6.9 ± 0.4	0.0037
Co/Ti-R	7.7 ± 0.5	2.483 ± 0.005	0.0099 ± 0.0005	6.0 ± 0.4	0.0126
Co/Ti-R – FTS	7.2 ± 0.4	2.483 ± 0.004			0.0124
Co/Ti-ROR1	6.6 ± 0.4	2.483 ± 0.004			0.0169
Co/Ti-ROR1 – FTS	6.5 ± 0.4	2.485 ± 0.005			0.0156

[a] The fits were performed on the first coordination shell (ΔR = 1.0-3.0 Å) over FT of the $k^1k^2k^3$-weighted $\chi(k)$ functions performed in the Δk = 2.0-12.0 Å^{-1} interval, resulting into a number of independent parameters of $2\Delta R\Delta k/\pi$ = 49.7 (12.4 for Co foil). The standard Co foil was fitted individually while the catalysts were fitted using a corefinement approach resulting into one $N_{Co\text{-}Co}$ and one $R_{Co\text{-}Co}$ for each sample and one ΔE_0 and σ^2 common for all samples. Non optimized parameters are recognizable by the absence of the corresponding error bar. S_0^2 = 0.91.

In summary, the XAS results indicate that after an oxidative treatment (150 °C) of the pre-reduced catalyst, the Co species can be ascribed to the Co_3O_4 spinel phase. After re-reduction and passivation, the Co spectra is compatible with a contribution from both CoO (due to passivation process) and Co^0. After *in situ* re-reduction in the catalytic cell, only metallic cobalt could be identified in the as-reduced Co/Ti-R and Co-Ti/ROR1 catalysts, confirming that the re-reduction temperature of 225 °C is enough to reduce the Co_3O_4 phase generated in the oxidation treatment of Co-Ti/ROR1 to metallic Co. The analysis of Co coordination numbers indicate that a modest Co redispersion takes place with the ROR treatment, confirming the previous results obtained by STEM. Finally, during FTS reaction, no significant differences in Co coordination numbers of Co/Ti-R and Co/Ti-ROR1 catalysts could be inferred from the *in situ* XAS results.

It is worth mentioning that no contribution of Co-Ru alloy could be detected in our EXAFS data due to the bulk character of XAS technique, since most Co atoms are surrounded by other Co as a result of the dissimilar Co and Ru loadings (12 and 0.2 wt%, respectively).

6.3.5. CO-FTIR characterization of Co/Ti catalysts submitted to ROR treatments

The electronic properties of cobalt catalysts submitted to redox treatments were studied by FTIR spectroscopy with CO as probe molecule (Figure 6.16). The reduced and passivated catalysts were first re-reduced *in situ* (225 °C for Co/Ti-ROR1 and -ROR2 catalysts and 300 °C for Co/Ti-R) and evacuated before CO was introduced in the IR cell at increasing dosages until saturation. For the Co/Ti-R catalyst, the CO-FTIR measurement was performed at room temperature (inset of Figure 6.16), while for Co/Ti-ROR1 and -ROR2 samples (Figure 6.16a and 6.16b, respectively) the CO-FTIR analyses were carried out at -50 °C.

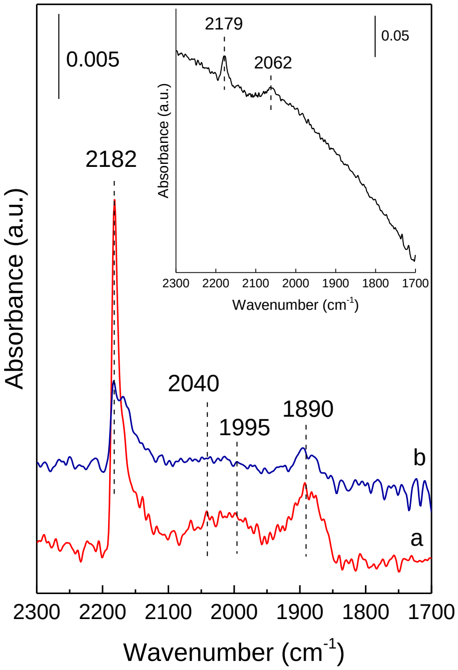

Figure 6.16. CO-FTIR spectra of Co/Ti-ROR1 (a) and Co/Ti-ROR2 (b) catalysts measured at CO saturation coverage and at -50 °C. The inset corresponds to the CO saturation spectrum of Co/Ti-R catalyst analyzed at r.t.

For the Co/Ti-R catalyst (inset of Figure 6.16), IR bands at 2179 and 2062 cm^{-1} were identified. The former band is related to CO adsorbed on oxidized Co species ($CO\text{-}Co^{n+}$) [48], while the assignment of the band at 2062 cm^{-1} is less clear. In fact, this band has been attributed to several CO adsorption modes, such as CO linearly adsorbed on metallic cobalt [48], surface polycarbonyl species $Co(CO)_x$ [49, 50], partially hydrogenated Co(H)-CO structures [48], and CO adsorbed on $Co^{\delta+}$ sites [51].

On the other hand, the catalysts submitted to redox treatments presented, besides the band at 2182 cm^{-1} related to oxidized Co species [48], multiple bands in the Co carbonyl region (2040, 1995 and 1890 cm^{-1}) instead of the single band at 2062 cm^{-1} exhibited by the Co/Ti-R catalyst. The band at 2040 cm^{-1} is assigned to CO linearly adsorbed on metallic cobalt species, while the IR band at 1995 cm^{-1} is attributed to CO adsorbed on low coordination Co^0 sites such as those in steps and corners [52]. This is in consistence with the decrease in size (e.g. increase in dispersion) of the Co NPs observed after the ROR treatments (Table 6.2). The IR band at 1890 cm^{-1} is due to the adsorption of CO in a bridge configuration [48], which suggests a higher concentration of exposed Co^0 sites for catalysts submitted to redox treatments.

The CO-FTIR results point to the presence of oxidized cobalt species for all catalysts, which can be due either to an incomplete cobalt reduction in the IR cell or to the presence of remaining oxidized cobalt species at the surface of the catalyst which did not undergo reduction. However, the concentration of this last species should be relatively low since they were not detected by EXAFS (Figure 6.15). On the other hand, the bands in the Co carbonyl region after redox treatments are different from those present in the spectrum of the Co/Ti-R catalyst, signing for differences in the surface topology of the exposed Co^0 sites. The IR band at 1995 cm^{-1} confirms the lower size of Co^0 NPs in the catalysts submitted to ROR treatments, as discussed above. Moreover, the presence of the IR band at 1890 cm^{-1} suggests a higher amount of exposed cobalt sites after redox treatments, which can be ascribed to the removal of TiO$_x$ species from the cobalt surface (reversion of SMSI) during the oxidation steps.

6.3.6. Characterization by AP-XPS of Co/Ti catalysts submitted to ROR treatments

With the aim of shedding more light on the reversibility of the SMSI effect, we used synchrotron ambient pressure XPS (AP-XPS) to follow the changes in the surface of the supported Co NPs during redox treatments due to the small penetration depth of the X-rays on the surface of the catalyst (ca. 0.7 nm). Figure 6.17 presents the Co/Ti surface molar ratios for the Co/Ti-R catalyst submitted to *in situ* redox treatments. First, the reduced and passivated Co/Ti-R catalyst was re-reduced (400 °C in H_2) in the XPS analysis chamber and the Co 2p and Ti 2p signals recorded. Subsequently, the gas atmosphere was switched to O_2 and the spectra in the Co 2p and Ti 2p regions recorded at increasing temperatures (100, 150, 200, and 250 °C). After complete cobalt oxidation, the gas environment was switched to H_2 and the re-reduction of cobalt species was monitored by acquiring spectra at 200 and 225 °C. Finally, a mixture of H_2+CO (H_2/CO = 2) was passed through the analysis chamber and the FTS reaction was followed by recording the Co 2p and Ti 2p XPS signals at 220 °C (see experimental part for details, Section 6.2.4). The Co and Ti features were quantified and the Co/Ti surface molar ratios for each treatment are shown in Figure 6.17.

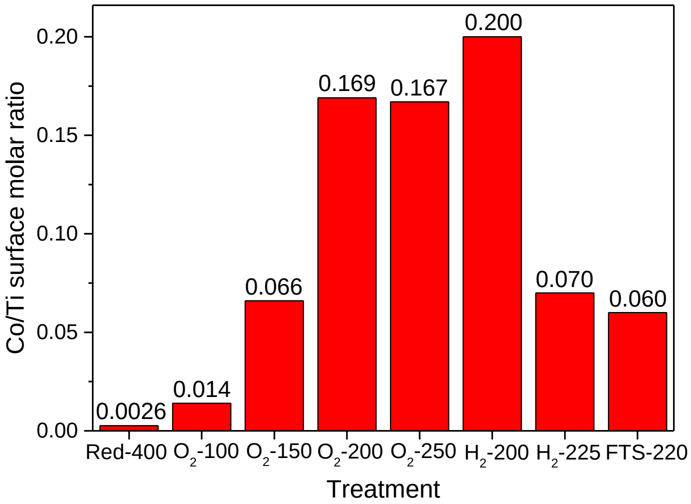

Figure 6.17. Co/Ti surface molar ratios derived from Co 2p and Ti 2p AP-XPS signals measured at different redox treatments and under 1.7 mbar of syngas mixture (1.1 mbar H_2 + 0.6 mbar CO) at 220 °C (FTS).

The Co/Ti ratio obtained for the Co/Ti-R catalyst was remarkably low (0.0026, Figure 6.17), which is due to the decoration of Co^0 surface sites by partially reduced TiO_x species (SMSI effect) [12]. The Co/Ti ratio increased from 0.0026 (as-reduced catalyst) to 0.014 after exposure to O_2 at 100 °C, indicative of an increase in the surface concentration of cobalt. With the subsequent increase in temperature from 100 °C to 150 and 200 °C under O_2, the Co/Ti ratio increased from 0.014 to 0.066 and finally to 0.169, respectively. A further raise in temperature up to 250 °C did not result in an increment in the surface Co/Ti ratio, which remained at 0.167. These results show that the SMSI effect can be reversed by oxidative treatment with O_2 as a consequence of the removal of TiO_x species from the surface of cobalt nanoparticles, translating into an increase in the Co/Ti surface ratios. This process seems to be enhanced with increasing the oxidation temperature, since more cobalt was exposed on the surface in the catalyst oxidized at 200 °C with respect to that treated at 150 °C. The Co/Ti ratio, however, remained constant with the further increase in oxidation temperature to 250 °C (0.167), indicating that oxidation at 200 °C is sufficient to remove the TiO$_x$ species covering (part of) the Co NPs.

Subsequent catalyst re-reduction with H$_2$ at 200 °C resulted in an even higher Co/Ti surface ratio (0.200), which can be ascribed to Co redispersion due to the Kirkendall effect [25, 44], confirming the results obtained by STEM (Table 6.2) and EXAFS (Table 6.3). A further increase in temperature to 225 °C under H$_2$ results in a decrease of the Co/Ti surface ratio to 0.070 due to the reappearance of the SMSI effect, probably as a consequence of the longer exposure times under H$_2$ atmosphere (ca. 5.5 h, see experimental part). Nonetheless, the Co/Ti surface ratio measured under H$_2$ at 225 °C is still approx. 27 times higher than that measured for the catalyst reduced at 400 °C (0.07 and 0.0026, respectively), which clearly indicates that the magnitude of the SMSI effect in the catalysts exposed to ROR treatments is much lower than that in the Co/Ti-R catalyst. Switching the gas atmosphere to syngas at 220 °C (Figure 6.17, FTS-220 column) produced a slight decreased in the Co/Ti ratio to 0.06, which is still 23 times higher than the Co/Ti ratio measured for the catalyst reduced at 400 °C (0.0026).

The analysis of the Co phases in each treatment was performed by a qualitative identification of the Co 2p$_{3/2}$ AP-XPS signal, as shown in Figure 6.18.

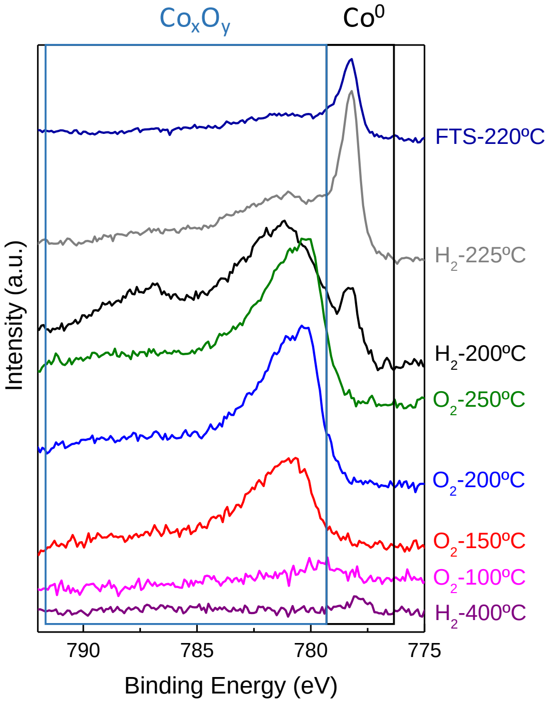

Figure 6.18. Co2p$_{3/2}$ peak of AP-XPS spectra for Co/Ti-R catalyst followed by *in situ* redox treatments.

A very small peak related to Co^0 species (BE = 777.8 eV) [53] is observed for the catalyst reduced in H_2 at 400 °C, which evidences the low amount of Co^0 sites exposed at the surface determined by the SMSI effect. After switching the gas atmosphere to O_2, a poorly defined XPS signal with BE of 779.4 eV, ascribed to partially oxidized cobalt species (Co$^{\delta+}$) [54], is observed at 100 °C (Figure 6.18). However, well defined peaks related to oxidized cobalt species (CoO/Co_3O_4) (BE = 780.7 eV) [55] are clearly observed at temperatures of 150, 200, and 250 °C, indicating the removal (by oxidation) of TiO_x patches from the surface of Co NPs (reversibility of the SMSI effect) and consequent increase in the amount of exposed cobalt species (increase in peak intensity). Switching the atmosphere to

H_2 at 200 °C, the contribution of both oxidized and metallic Co species is evidenced. A further increase in temperature to 225 °C results in a very intense peak at 778.2 eV assigned to Co^0 sites, besides a small contribution of oxidized cobalt species. By comparing the intensity of the Co^0 peak at 225 °C with that of the spectrum measured at 400 °C under H_2, it is clear that the former presents a considerably higher amount of exposed Co^0 sites than the latter, confirming the reversion of the SMSI effect by performing ROR treatments. Finally, under syngas atmosphere at 220 °C, the peak related to Co^0 species is clearly identified, in agreement with the EXAFS results that pointed to the presence of metallic cobalt species under reaction conditions (Table 6.3).

In summary, the AP-XPS analysis revealed a much higher concentration of Co^0 sites exposed on the surface for the catalysts submitted to redox treatments, confirming the reversibility of the SMSI effect. The consequences of the ROR treatments on the FTS performance of CoRu/TiO$_2$ catalysts are discussed in the following section.

6.3.7. Catalytic behavior of Co/Ti catalysts submitted to ROR treatments in Fischer-Tropsch synthesis

The results of the FTS experiments are summarized in Table 6.4. As seen there, the CO conversion is 2.4 and 2.5 times higher for catalysts submitted to ROR1 and ROR2 treatments, respectively, with respect to the catalyst reduced only once at 400 °C (Co/Ti-R). The increase in CO conversion stems from the higher amount of exposed Co^0 surface sites due to the reversion of the SMSI effect with the oxidation treatment and further re-reduction at low temperature (225 °C). The higher concentration of exposed Co^0 sites translated into an increase in activity per total mass of cobalt (CTY) of 2.4 and 2.8 times for Co/Ti-ROR1 and

Co/Ti-ROR2 catalysts, respectively, with respect to Co/Ti-R. However, the catalysts submitted to ROR treatments presented a lower intrinsic activity or TOF (for both initial and *pseudo*-steady state values) than the Co/Ti-R catalyst. The diminution in TOF observed for the catalysts submitted to redox treatments can be related to their higher proportion of cobalt NPs with sizes smaller than the critical value of 6-8 nm (which present lower intrinsic activity [27, 28]) as a result of cobalt redispersion.

Table 6.4. Activities (CTY and TOF) of Co/Ti catalysts after ROR treatments for Fischer-Tropsch synthesis (FTS). Reaction conditions: T= 220 °C, P= 10 bar, H_2/CO = 2 mol/mol. Initial TOF was obtained by extrapolating the CO conversion-TOS curves at TOS→0 at constant GHSV of 6 $L_{syngas}/(g_{cat}\cdot h)$, while *pseudo*-steady state (SS) activities were averaged for the next 8 h of reaction after adjusting the GHSV to reach a CO conversion of ca. 15% for each catalyst.

Catalyst	CO conversion (%)	$CTY_{SS}\cdot 10^3$ $(mol_{CO}/g_{Co}\cdot h)$ [a]	$TOF\cdot 10^2$ (s^{-1}) [b]	
			Initial	SS
Co/Ti-R	12.5	78.6	6.8	5.3
Co/Ti-ROR1	30.2	189.6	5.3	4.0
Co/Ti-ROR2	31.9	219.1	5.0	4.1

[a] CTY = cobalt-time-yield (activity per total mass of cobalt). [b] TOF = turnover frequency (activity per surface Co^0 sites) derived by H_2 chemisorption.

The hydrocarbon selectivities in the *pseudo*-steady state for Co/Ti-R catalyst and for catalysts submitted to ROR treatments are compared in Table 6.5 at a constant CO conversion of 15 ± 1%. The selectivity to methane slightly increased (ca. 3%) for catalysts submitted to ROR treatments, whereas the selectivity to C_2-C_4 hydrocarbons decreased (approx. 4-5%) (Table 6.5). Besides, all catalysts presented high selectivities to the C_{5+} hydrocarbon fraction (74.2-76.6%), with Co/Ti-ROR1 and Co/Ti-ROR2 catalysts displaying slightly higher values in comparison to the Co/Ti-R sample. Lögdberg and co-workers also reported a modest increase in C_{5+} selectivity after submitting a CoRe/TiO_2 catalyst to ROR treatments [26].

Table 6.5. Product selectivity obtained in the *pseudo*-steady state over Co/Ti catalysts submitted to ROR treatments at similar CO conversion (15 ± 1%). Reaction conditions: T= 220 °C, P= 10 bar, H_2/CO= 2 mol/mol, GHSV= 4.6 (for Co/Ti-R), 11.6 (for Co/Ti-ROR1) and 12.6 (for Co/Ti-ROR2) $L_{syngas}/g_{cat}\cdot h$.

Catalyst	Selectivity (% C)			O/P ratio [a]	Parameter χ [b]
	C_1	C_2-C_4	C_{5+}	(wt/wt)	(10^{-16} m)
Co/Ti-R	10.3	15.5	74.2	2.00	63
Co/Ti-ROR1	12.8	11.8	75.4	0.80	201
Co/Ti-ROR2	12.7	10.7	76.6	0.65	232

[a] Olefin-to-paraffin weight ratio for the C_2-C_4 hydrocarbon fraction. [b] Structural parameter modeling mass transport limitations in cobalt-catalyzed FTS (see text).

The slight increase in selectivity to C_{5+} observed in Table 6.5 upon applying ROR treatments to the CoRu/TiO_2 catalyst could be a consequence of reversion of the SMSI effect resulting in larger ensembles of Co^0 atoms on closed-packed terraces on which chain growth is favored [56]. On the other hand, the increase in C_1 selectivity seen upon the ROR treatments may be ascribed to the redispersion of cobalt and the higher intrinsic selectivity to methane (and lower to C_{5+}) reported for small (< 6-8 nm) Co^0 NPs [27, 28]. Therefore, the combination of these two effects (reversion of SMSI and Co redispersion) explains the modest increase in C_{5+} selectivity observed upon the ROR treatments.

On the other hand, the catalysts submitted to ROR treatments exhibited a considerably lower olefin-to-paraffin (O/P) weight ratio for the C_2-C_4 fraction (0.80 and 0.65 for catalysts Co/Ti-ROR1 and -ROR2, respectively) compared to the value of 2 obtained for the Co/Ti-R catalyst (Table 6.5). Since mass transport limitations play an important role on the selectivity of Co-based catalysts under FTS conditions, we calculated the diffusion-related structural parameter χ proposed by Iglesia and co-workers, defined according to equation 6.1 [57]:

$$\chi = R_0^2 \cdot \varepsilon \cdot \theta_{Co}/r_p \qquad \text{Eq.6.1}$$

where R_0 is the mean radius of catalyst pellets, ε is the pellet void fraction (porosity), θ_{Co} is the density of cobalt sites per unit area, and r_p refers to the mean radius of the catalyst pores. According to this model [57], the C_{5+} selectivity first raises with increasing diffusion limitations up to values of the structural parameter χ of around $200 \cdot 10^{16}$ m due to re-adsorption of α-olefins on the active sites and their participation in new chain growth events. Under more severe mass transport restrictions, i.e. in the range of χ above $200 \cdot 10^{16}$ m, the resistance to the diffusion of CO through the catalysts pores (filled with liquid hydrocarbons) becomes the limiting factor leading to a gradual decline of the C_{5+} selectivity as χ increases.

Due to the alike textural properties for the catalysts studied in this work and the equal pellet size (R_0) employed in the FTS experiments, the density of cobalt sites per unit area (θ_{Co}) turns to be the parameter that most influences the final value of χ according to equation 6.1. In this respect, the Co/Ti-R catalyst presented the lowest amount of Co^0 surface sites determined by H_2 chemisorption (Table 6.2) resulting in the lowest value of χ of $63 \cdot 10^{16}$ m, indicative of low diffusional restrictions, and consequently in the highest O/P ratio (Table 6.5). Conversely, the catalysts submitted to ROR treatments exhibited χ values (201 and $232 \cdot 10^{16}$ m) that fall in the region in which the diffusion of CO within the catalysts pores starts to control the product selectivity. In this situation, the true H_2/CO ratio around the Co^0 NPs inside the catalyst pores is higher than that in the syngas feed, thereby promoting the hydrogenation of olefins and the consequent decrease in the O/P ratio, as observed in Table 6.5.

Summing up, a large improvement in activity (CTY, Table 6.4) with a concomitant slight increase in selectivity to C_{5+} hydrocarbons were observed after submitting the catalysts to reduction, oxidation and re-reduction treatments. The increase in activity arise from the reversion of the SMSI effect during the oxidation treatments leading to a greater amount of exposed Co^0 surface sites, while the modest increase in C_{5+} selectivity stems from the opposed influence on selectivity determined by the reversion of the SMSI effect and by Co redispersion. Based on these results, a possible strategy to further increasing the activity (i.e. TOF) and selectivity to the target C_{5+} fraction of the catalysts submitted to ROR treatments would be prepare catalysts containing initially somewhat larger Co particles, thus avoiding or minimizing the formation of intrinsically less active and selective very small (< 6-8 nm) Co^0 nanoparticles.

6.4. Conclusion

The use of powerful spectroscopic techniques combined to lab results pointed that the SMSI state can be reverted by submitting the CoRu/TiO$_2$ catalyst to oxidation and re-reduction treatments, resulting in a remarkable increase of the amount of exposed Co^0 surface sites and, thus, of the FTS activity in terms of CO conversion and CTY. However, cobalt redispersion also occurred during the ROR treatments (due to the Kirkendall effect), leading to a small decrease in TOF. On the other hand, the catalysts submitted to ROR treatments showed a slight improvement in C$_{5+}$selectivity. These results show that, by applying redox treatments under controlled conditions, the detrimental effects originated by the SMSI state can be significantly reduced leading to more active and selective catalysts.

Acknowledgments

Financial support by the MINECO of Spain through the Severo Ochoa (SEV2016-0683) and ENE2014-5761-R projects is gratefully acknowledged. The authors also thank the Microscopy Service of the Universitat Politècnica de València for its assistance in microscopy characterization. Special thanks are also due to ALBA synchrotron for allocating beamtime at CLÆSS (XAS) and CIRCE (XPS) beamlines and also to their staff for their help and technical support during the experiments. F. Bertella (Science without Frontiers − Process no. 13705/13-0) thanks CAPES for a predoctoral fellowship.

6.5. References

[1] E. van Steen, M. Claeys, Chem. Eng. Technol. 31 (2008) 655-666.

[2] H. Jahangiri, J. Bennett, P. Mahjoubi, K. Wilson, S. Gu, Catal. Sci. Technol. 4 (2014) 2210-2229.

[3] A.Y. Khodakov, Catal. Today 144 (2009) 251-257.

[4] J. van de Loosdrecht, F.G. Botes, I.M. Ciobîcă, A. Ferreira, P. Gibson, D. Moodley, A. Saib, J. Visagie, C. Weststrate, H. Niemantsverdriet, Fischer–Tropsch Synthesis: Catalysts and Chemistry, in: J. Reedijk, K. Poeppelmeier (Eds.), Comprehensive Inorganic Chemistry II, Elsevier, 2013, pp. 525-557.

[5] G. Jacobs, T.K. Das, Y. Zhang, J. Li, G. Racoillet, B.H. Davis, Appl. Catal. A Gen. 233 (2002) 263-281.

[6] G. Prieto, A. Martínez, R. Murciano, M.A. Arribas, Appl. Catal. A Gen. 367 (2009) 146-156.

[7] G. Prieto, M.I.S. De Mello, P. Concepción, R. Murciano, S.B.C. Pergher, A. Martínez, ACS Catal. 5 (2015) 3323-3335.

[8] A. Kogelbauer, J.J.G. Goodwin, R. Oukaci, J. Catal. 160 (1996) 125-133.

[9] S.A. Hosseini, A. Taeb, F. Feyzi, Catal. Commun. 6 (2005) 233-240.

[10] W. Ma, G. Jacobs, R.A. Keogh, D.B. Bukur, B.H. Davis, Appl. Catal. A Gen. 437-438 (2012) 1-9.

[11] E. Iglesia, S.L. Soled, R.A. Fiato, G.H. Via, J. Catal. 143 (1993) 345-368.

[12] S.J. Tauster, Acc. Chem. Res. 20 (1987) 389-394.

[13] G.L. Haller, D.E. Resasco, Metal-Support Interaction: Group VIII Metals and Reducible Oxides, in: D. Eley (Series Volume Editor), H. Pines, P. B. Weisz (Serial Editors), Advances in Catalysis, Volume 36, 1st Edition, Academic Press, 1989, pp. 173-235.

[14] Y. Li, B. Xu, Y. Fan, N. Feng, A. Qiu, J.M.J. He, H. Yang, Y. Chen, J. Mol. Catal. A Chem. 216 (2004) 107-114.

[15] A. Yamamoto, J. Ohyama, K. Teramura, T. Shishido, T. Tanaka, Catal. Today 232 (2014) 165-170.

[16] F. Bertella, P. Concepción, A. Martínez, Catal. Today 289 (2017) 181-191.

[17] M. Bonne, P. Samoila, T. Ekou, C. Especel, F. Epron, P. Marécot, S. Royer, D. Duprez, Catal. Commun. 12 (2010) 86-91.

[18] A.M. Abdel-Mageed, D. Widmann, S.E. Olesen, I. Chorkendorff, J. Biskupek, R.J. Behm, ACS Catal. 5 (2015) 6753-6763.

[19] F. Bertella, P. Concepción, A. Martínez, Catal. Today 296 (2017) 170-180.

[20] E. Iglesia, S.L. Soled, R.A. Fiato, J. Catal. 137 (1992) 212-224.

[21] J.B.F. Anderson, R. Burch, J.A. Cairns, Appl. Catal. 25 (1986) 173-180.

[22] S.L. Soled, E. Iglesia, R.A. Fiato, J.E. Baumgartner, H. Vroman, S. Miseo, Top. Catal. 26 (2003) 101-109.

[23] N.E. Tsakoumis, M. Rønning, Ø. Borg, E. Rytter, A. Holmen, Catal. Today 154 (2010) 162-182.

[24] A.M. Saib, D.J. Moodley, I.M. Ciobîcă, M.M. Hauman, B.H. Sigwebela, C.J. Weststrate, J.W. Niemantsverdriet, J. van de Loosdrecht, Catal. Today 154 (2010) 271-282.

[25] M.M. Hauman, A. Saib, D.J. Moodley, E. du Plessis, M. Claeys, E. van Steen, ChemCatChem 4 (2012) 1411-1419.

[26] S. Lögdberg, J. Yang, M. Lualdi, J.C. Walmsley, S. Järås, M. Boutonnet, E.A. Blekkan, E. Rytter, A. Holmen, J. Catal. 352 (2017) 515-531.

[27] G.L. Bezemer, J.H. Bitter, H.P. Kuipers, H. Oosterbeek, J.E. Holewijn, X. Xu, F. Kapteijn, A.J. van Dillen, K.P. de Jong, J. Am. Chem. Soc. 128 (2006) 3956-3964.

[28] G. Prieto, A. Martínez, P. Concepción, R. Moreno-Tost, J. Catal. 266 (2009) 129-144.

[29] R.C. Reuel, C.H. Bartholomew, J. Catal. 85 (1984) 63-77.

[30] L. Simonelli, C. Marini, W. Olszewski, M. Ávila Pérez, N. Ramanan, G. Guilera, V. Cuartero, K. Klementiev, N.L. Saini, Cogent Physics 3 (2016) 1231987.

[31] G. Guilera, F. Rey, J. Hernández-Fenollosa, J.J. Cortés-Vergaz, J. Phys. Conf. Ser. 430 (2013) 012057.

[32] B. Ravel, M. Newville, J. Synchrotron Radiat. 12 (2005) 537-541.

[33] V. Pérez-Dieste, L. Aballe, S. Ferrer, J. Nicolàs, C. Escudero, A. Milán, E. Pellegrin, J. Phys. Conf. Ser. 425 (2013) 072023.

[34] J.J. Yeh, I. Lindau, At. Data Nucl. Data Tables 32 (1985) 1-155.

[35] M. Wu, G. Lin, D. Chen, G. Wang, D. He, S. Feng, R. Xu, Chem. Mater. 14 (2002) 1974-1980.

[36] M. Thommes, K. Kaneko, A.V. Neimark, J.P. Olivier, F. Rodriguez-Reinoso, J. Rouquerol, K.S.W. Sing, Pure Appl. Chem. 87 (2015).

[37] M. Andersson, L. Österlund, S. Ljungström, A. Palmqvist, J. Phys. Chem. B 106 (2002) 10674-10679.

[38] J. Hong, E. Marceau, A.Y. Khodakov, L. Gaberová, A. Griboval-Constant, J.-S. Girardon, C.L. Fontaine, V. Briois, ACS Catal. 5 (2015) 1273-1282.

[39] J. Hong, P.A. Chernavskii, A.Y. Khodakov, W. Chu, Catal. Today 140 (2009) 135-141.

[40] T.O. Eschemann, J. Oenema, K.P. de Jong, Catal. Today 261 (2016) 60-66.

[41] S. Storsater, B. Totdal, J. Walmsley, B. Tanem, A. Holmen, J. Catal. 236 (2005) 139-152.

[42] A. Michalak, M. Nowosielska, W.K. Jóźwiak, Top. Catal. 52 (2009) 1044-1050.
[43] P.A. Chernavskii, G.V. Pankina, V.I. Zaikovskii, N.V. Peskov, P. Afanasiev, J. Phys. Chem. C 112 (2008) 9573-9578.
[44] C.J. Weststrate, M.M. Hauman, D.J. Moodley, A.M. Saib, E. van Steen, J.W. Niemantsverdriet, Top. Catal. 54 (2011) 811-816.
[45] S. Sadasivan, R.M. Bellabarba, R.P. Tooze, Nanoscale 5 (2013) 11139-11146.
[46] G. Dalba, P. Fornasini, J. Synchrotron Radiat. 4 (1997) 243-255.
[47] A.L. Bugaev, A.A. Guda, A. Lazzarini, K.A. Lomachenko, E. Groppo, R. Pellegrini, A. Piovano, H. Emerich, A.V. Soldatov, L.A. Bugaev, V.P. Dmitriev, J.A. van Bokhoven, C. Lamberti, Catal. Today 283 (2017) 119-126.
[48] L.E.S. Rygh, O.H. Ellestad, P. Klæboe, C.J. Nielsen, Phys. Chem. Chem. Phys. 2 (2000) 1835-1846.
[49] S. Sun, N. Tsubaki, K. Fujimoto, Appl. Catal. A Gen. 202 (2000) 121-131.
[50] N. Tsubaki, S. Sun, K. Fujimoto, J. Catal. 199 (2001) 236-246.
[51] J. Zhang, J. Chen, J. Ren, Y. Sun, Appl. Catal. A Gen. 243 (2003) 121-133.
[52] L.E.S. Rygh, C.J. Nielsen, J. Catal. 194 (2000) 401-409.
[53] A. Rodriguez-Gomez, J.P. Holgado, A. Caballero, ACS Catal. 7 (2017) 5243-5247.
[54] V.A. de la Peña O'Shea, M.C. Álvarez-Galván, J.M. Campos-Martin, N.N. Menéndez, J.D. Tornero, J.L.G. Fierro, Eur. J. Inorg. Chem. 2006 (2006) 5057-5068.
[55] J. Wang, P.A. Chernavskii, A.Y. Khodakov, Y. Wang, J. Catal. 286 (2012) 51-61.
[56] C.J. Weststrate, P. van Helden, J.W. Niemantsverdriet, Catal. Today 275 (2016) 100-110.
[57] E. Iglesia, Appl. Catal. A Gen. 161 (1997) 59-78.

CHAPTER 7

GENERAL CONCLUSIONS

The most relevant conclusions derived from the results presented in this doctoral thesis are summarized below:

- Both anatase and rutile titania polymorphs employed as supports for CoRu-based catalysts experienced the SMSI effect during reduction in H_2 at 400 °C. However, the extent of the SMSI was higher for catalysts supported on the anatase phase with respect to those supported on rutile. As a result, the former catalysts presented a lower amount of exposed Co^0 sites translating into an inferior catalytic activity for FTS with respect to rutile-based catalysts. Moreover, the materials based on rutile presented, at constant CO conversion, higher selectivity to C_{5+} hydrocarbons due to an enhanced mass transfer and probably also to a lower surface acidity of this TiO_2 polymorph compared to anatase.
- The textural properties, and more specifically the surface area, of anatase-TiO_2 used as support for CoRu-based catalysts significantly influenced the extent of the SMSI effect after H_2 reduction. Therefore, increasing the anatase surface area led to a more pronounced SMSI effect, resulting in a progressive decrease of catalytic activity (CTY). This behavior is ascribed to a higher concentration of structural defects in the high surface area anatase-TiO_2 support, which promotes the formation of partially reduced TiO_x species from the support involved in the generation of the SMSI state. Moreover, the anatase support with high surface area led to lower selectivity to the C_{5+} hydrocarbon fraction due to the combination of an enhanced SMSI effect and a lower intraparticle diffusion resistance.

- The promotion with Ru and the Ru concentration (in the range of 0.2-1.2 wt%) significantly influenced the catalytic performance for FTS of Co/TiO_2-anatase catalysts. Thus, the Ru-promoted catalysts displayed higher catalytic activity (both CTY and TOF) as well as higher C_{5+} selectivity compared to the non-promoted counterpart. Both activity and C_{5+} selectivity exhibited maximum values for the catalyst promoted with the lowest amount of Ru (0.2 wt%), for which all Ru species were alloyed with Co forming bimetallic Co-Ru nanoparticles. The higher activity of the Ru-promoted catalysts is ascribed to an enhanced Co dispersion and to the effect of Ru on facilitating the removal of C and O species (from CO dissociation) from the surface of the Co NPs avoiding their reoxidation and formation of detrimental carbide species during catalysis. However, the later synergic effect was less pronounced when increasing the Ru content beyond 0.2 wt% due to segregation of some Ru species from the bimetallic Co-Ru nanoparticles which, in addition to a higher proportion of very small Co^0 nanoparticles at high Ru loadings, decreased the catalyst activity in terms of both CTY and TOF. These results show that an optimum Ru loading is required in order to take full advantage of its promotional role as promoter.
- Reduction-oxidation-reduction (ROR) treatments substantially improved the catalytic activity (CO conversion and CTY) of CoRu/TiO_2-anatase catalysts by reverting the SMSI effect that takes place during reduction of the catalysts in H_2 at high temperature (400 °C), resulting in an increase in the concentration of exposed Co^0 surface sites. However, cobalt redispersion also occurred during the ROR treatments, probably through the

Kirkendall effect, resulting in too small (< 6 nm) Co^0 particles, which are known to be intrinsically less active for FTS, and therefore in slightly lower TOFs compared to the catalyst that was simply reduced once at 400 °C. Moreover, the catalysts submitted to redox treatments also presented a slightly higher selectivity to C_{5+} when compared to the untreated catalyst at the same CO conversion level. The modest increase in C_{5+} selectivity upon performing the ROR treatments is explained by the combination of two factors presenting opposite effects, namely reversion of the SMSI effect and cobalt redispersion. The results of this study clearly indicate that performing ROR treatments prior catalysis could represent a suitable strategy to improve the activity and selectivity of TiO_2-supported Co catalysts by avoiding (or minimizing) detrimental effects related to the SMSI state.